



**NATIONAL TECHNICAL UNIVERSITY OF ATHENS**

SCHOOL OF MINING AND METALLURGICAL ENGINEERING

DEPARTMENT OF METALLURGY AND MATERIALS SCIENCE

LABORATORY OF PHYSICAL METALLURGY

**The effect of Ultra-Fast Heat treatments on the microstructure evolution of  
Automotive Steels**

DOCTORAL THESIS

**ALEXANDROS C. BANIS**

Supervisor

Associate Professor Dr.-Ing. Spyros Papaefthymiou

ATHENS 2021





**NATIONAL TECHNICAL UNIVERSITY OF ATHENS**

SCHOOL OF MINING AND METALLURGICAL ENGINEERING

DEPARTMENT OF METALLURGY AND MATERIALS SCIENCE

LABORATORY OF PHYSICAL METALLURGY

**The effect of Ultra-Fast Heat treatments on the microstructure evolution of  
Automotive Steels**

DOCTORAL THESIS

**ALEXANDROS C. BANIS**

Supervisor

Associate Professor Dr.-Ing. Spyros Papaefthymiou

ATHENS 2021





**NATIONAL TECHNICAL UNIVERSITY OF ATHENS**  
SCHOOL OF MINING AND METALLURGICAL ENGINEERING  
DEPARTMENT OF METALLURGY AND MATERIALS SCIENCE  
LABORATORY OF PHYSICAL METALLURGY

**The effect of Ultra-Fast Heat treatments on the microstructure evolution of  
Automotive Steels**

DOCTORAL THESIS

**ALEXANDROS C. BANIS**

The Supervising Committee

Associate Professor Dr.-Ing. Spyros Papaefthymiou

Professor Dr. Georgios Fournalaris

Professor Dr. Elias Chatzitheodoridis

ATHENS 2021



The research described in this thesis was conducted in the Laboratory of Physical Metallurgy and Center of Electron Microscopy of the School of Mining and Metallurgical Engineering, NTUA.

Part of this research was also conducted in the Department of Electrical Energy, Metals, Mechanical Constructions & Systems, Ghent University via the Erasmus+ Program with the support of Prof. Roumen H. Petrov.

This thesis was supervised by the supervisor:

Associate Professor Dr. -Ing. Spyros Papaefthymiou

National Technical University of Athens

And the members of the supervising committee:

Professor Dr. Georgios Fournalaris

National Technical University of Athens

Professor Dr. Elias Chatzitheodoridis

National Technical University of Athens

The examination committee:

Professor Dr. Angeliki Lekatou

University of Ioannina

Professor Dr. Nikolaos Michailidis

Aristotle University of Thessaloniki

Professor Dr. Gregorios Chaidemenopoulos

University of Thessaly

Assistant Professor Dr. Petros Tsakiridis

National Technical University of Athens



*This thesis is dedicated to my parents Constantinos and Charikleia,  
and my brother George with all my love*

ὡς δ' ὅτ' ἀνὴρ χαλκεὺς πέλεκυν μέγαν ἤε σκέπαρνον  
εἰν ὕδατι ψυχρῷ βάπτῃ μεγάλα ἰάχοντα  
φαρμάσσων: τὸ γὰρ αὖτε σιδήρου γε κράτος ἐστίν.

*Ομήρου Οδύσσεια, Ραψωδία Ι, Στίχος 390*

As when a man who works as a blacksmith plunges a screaming great ax blade or plane  
into cold water, treating it for temper,  
since this is the way steel is made strong.

*Homer's Odyssey, Rhapsody I, Line 390*



# Acknowledgments

I would like to express my deep gratitude to my promotor Assoc. Professor Dr.-Ing. Spyros Papaefthymiou for his supervision and mentoring throughout my research. Our cooperation through these years as an undergraduate and as a Ph.D. student has been impeccable and has led to the achievement of important milestones in our research. I am looking forward to our further cooperation in the future.

I would also like to thank my co-promotor and head of the Laboratory of Physical Metallurgy, Professor Dr. Georgios Fournalis, for setting the foundations and the knowledge needed in my research through his lectures. He is responsible for intriguing me into the world of Physical Metallurgy, and for that, I am grateful.

My gratitude also goes to my co-promotor, Professor Dr. Elias Chatzitheodoridis. His guidance was important to my research, and his suggestions were gladly received for future work.

Furthermore, I would like to express my sincere gratitude to Professor Dr.ir. Roumen H. Petrov from Ghent University for his mentoring during my stay in Ghent. His guidance through these ten months has been crucial in my research, as well as his teachings and support. Alongside Prof. Petrov, I would like to also thank Professor Dr. ir. Leo Kestens and Professor Dr. ir. Patricia Vermeulen for their support and cooperation during my research at Ghent University.

My thanks are also addressed to Professor Papaefthymiou's team, Dr. Evangelos Gavalas, Dr. Marianthi Bouzouni and Ph.D. student Sofia Papadopoulou. Our collaboration and discussions on the research topic have been very fruitful and helpful for this thesis. Their contribution to the heat-treating experiments, simulation analysis, and EBSD analysis has been most valuable for my research.

I would also like to thank my friends and colleagues from the Laboratory of Physical Metallurgy. Specifically, I would like to thank Assistant Professor Dr. Petros Tsakiridis for his training on the microscopes and the fruitful discussions. My dearest friends and Ph.D. student Anastasia Alexandratou and Dr. Stavros Deligiannis for their mental and scientific support through all these years, the long discussions, and all the good and bad times we shared trying to overcome all the problems that occurred during our researches. I would also like to thank my colleague Ph.D. student Angelos Kaldellis for his support and, finally, Mr. Ioannis Charlabitas for our deep discussions and for just being around.

I am also grateful to my friends/technicians/colleagues from Ghent University for their assistance and beers that we shared and made my stay in Ghent delightful. Specifically, I would like to thank the Ph.D. students Eliseo Hernandez Duran, Ksenija Nikolic, Florian Vercruysse, Sarath Chandran, Luca Corallo, Edvin Armis, and Drs. Vitaliy Bliznuk and Hadi Pirgazi. My deepest thanks are also dedicated to Ilse Vercruysse for her overall assistance during my stay in Ghent.

My supervisor, Assoc. Professor Dr.-Ing. S. Papaefthymiou, and the Erasmus+ program are also acknowledged for giving me the opportunity to conduct part of my research in Ghent. Additionally, my supervisor and the

Erasmus+ program are acknowledged for giving me the chance to complete my diploma thesis in RWTH Aachen during my undergraduate studies, under the guidance of Assoc. Prof. Dr.-Ing. S. Papaefthymiou and the co-supervision of Professor W. Bleck and Dr. J. Roik. My time there has been catalytic in my decision to pursue a Ph.D.

Also, I want to thank my dearest friends that I have known for most of my life for their support and for being around helping me go through this research and listening to me complain about almost everything. I wish you success and happiness in your lives.

Last but not least, there are not enough words to thank enough my parents Constantinos and Charikleia, as well as my brother, George. They have been the pillars that keep me standing in life and have made me the person I am today. I owe them everything for their endless and unconditional love, and I wish to make them all proud of me.



# 1. Table of Contents

1.	Table of Contents .....	1
2.	List of Abbreviations .....	4
3.	Σύνοψη στα Ελληνικά .....	9
3.1.	Περίληψη.....	9
3.2.	Εισαγωγή.....	9
3.2.1.	Σκοπός.....	10
3.3.	Πειραματικό μέρος.....	11
3.4.	Αποτελέσματα .....	16
3.4.1.	Ανάλυση των παραμέτρων τάχιστων θερμικών κατεργασιών σε εργαστηριακό επίπεδο μέσω διαστολομετρίας.....	16
3.4.2.	Ο σχηματισμός μπαινίτη και υπολειπόμενου ωστενίτη κατά την εφαρμογή τάχιστων θερμικών κύκλων σε σωλήνες χωρίς ραφή (σε πιλοτικό επαγωγικό φούρνο ραγδαίας αναθέρμανσης)	22
3.4.3.	Η εφαρμογή τάχιστων θερμικών κύκλων σε συμβατικό τύπο χάλυβα της αυτοκινητοβιομηχανίας εργαστηριακά σε θερμομηχανικό προσομοιωτή Gleeble.....	25
3.5.	Συζήτηση των αποτελεσμάτων.....	35
3.5.1.	Σχηματισμός Μαρτενσίτη.....	35
3.5.2.	Χημική Σύσταση Πρότερου Ωστενίτη .....	35
3.5.3.	Σχηματισμός μπαινίτη .....	38
3.5.4.	Υπολειπόμενος ωστενίτης .....	38
3.5.5.	Εξέλιξη του μεγέθους κόκκου των κύριων φάσεων της μικροδομής.....	39
3.5.6.	Ανακρυστάλλωση του φερρίτη.....	41
3.5.7.	Επίδραση της μικροδομής στις μηχανικές ιδιότητες .....	42
3.6.	Συμπεράσματα.....	42
3.7.	Ενδεικτική Βιβλιογραφία .....	44
4.	Abstract.....	47
5.	Introduction .....	49
5.1.	Trends in the automotive industry .....	49
5.2.	Generations of AHSS .....	49
5.2.1.	Conventional Steels .....	50
5.2.2.	High Strength Steels .....	51
5.2.3.	Advanced High Strength Steels.....	52
5.3.	The Ultra-Fast Heat Treatment as an alternative process to produce new AHSS grades.....	55
6.	Theoretical Background .....	57
6.1.	Steel and its phases .....	57
6.1.1.	Phase diagram.....	57

## 1. Table of Contents

---

6.1.2.	Ferrite .....	58
6.1.3.	Austenite.....	58
6.1.4.	Martensite.....	58
6.1.5.	Bainite.....	59
6.1.6.	Cementite.....	60
6.2.	Phase Transformations .....	61
6.2.1.	Diffusion transformations.....	61
6.2.2.	Alloying elements.....	64
6.2.3.	Crystallography of iron.....	69
6.2.4.	Recrystallization of Ferrite .....	72
6.2.5.	Austenitization.....	74
6.2.6.	Transformation during cooling.....	75
6.3.	State of the Art: Ultra-fast Heating as a thermal treatment method .....	81
6.3.1.	The introduction of Ultra-fast heating .....	81
6.3.2.	The effect of heating rate in an annealing treatment .....	81
6.3.3.	The effect of the initial microstructure .....	82
6.3.4.	Nucleation of austenite .....	83
6.3.5.	Growth of austenite .....	84
6.3.6.	Effect of Ultra-Fast Heating on Recovery and Recrystallization .....	86
6.3.7.	Effect of Ultra-Fast Heating on Grain Refinement.....	87
6.3.8.	Production of AHSS via Ultra-Fast Heating .....	88
7.	Experimental Implementation .....	89
7.1.	Thermal Treatments.....	89
7.1.1.	Dilatometry.....	89
7.1.2.	Pilot-scale induction heating machine .....	90
7.1.3.	Gleeble Thermo-Mechanical Simulator .....	91
7.2.	Material Characterization .....	92
7.2.1.	Sample preparation.....	92
7.2.2.	Scanning Electron Microscope (SEM).....	93
7.2.3.	Electron Back-Scatter Diffraction (EBSD) .....	93
7.2.4.	Transmission Electron Microscopy (TEM).....	97
7.2.5.	X-Ray Diffraction (XRD).....	98
7.3.	Simulation software.....	98
7.3.1.	Parent austenite reconstruction software ARPGE .....	98
7.4.	Mechanical properties.....	99
7.4.1.	Tensile tests .....	99
7.4.2.	Hardness test.....	103
8.	Experimental Results.....	104

---

8.1.	The effect of the thermal treatment’s parameters .....	104
8.1.1.	Introduction .....	104
8.1.2.	Implementation .....	104
8.1.3.	Effect of the Chemical Composition .....	105
8.1.4.	Effect of the heating time .....	115
8.1.5.	Comparison of an ultra-fast heating cycle with a conventional heating cycle .....	125
8.2.	The formation of bainite and retainment of austenite in industry-scale samples .....	133
8.2.1.	Introduction .....	133
8.2.2.	Materials and methods.....	133
8.2.3.	Results .....	136
8.3.	The Ultra-Fast Heat Treatment as a method to produce commercial DP Steels .....	157
8.3.1.	Introduction .....	157
8.3.2.	Materials and methods.....	157
8.3.3.	Results .....	162
9.	Discussion.....	198
9.1.	Discussion on the effect of the heating parameters .....	198
9.2.	Discussion on the formation of bainite and the retainment of austenite in large-scale samples under UFH cycles .....	201
9.3.	Discussion on the application of UFH on a commercial DP steel grade.....	203
10.	Conclusions .....	205
11.	References .....	207
12.	Curriculum Vitae .....	219

## **2. List of Abbreviations**

<b>A<sub>e1</sub></b>	The temperature in which the ferrite-to-austenite transformation initiates
<b>A<sub>e3</sub></b>	The temperature in which the ferrite-to-austenite transformation ends
<b>Al</b>	Aluminum
<b>APF</b>	Atomic Packing Factor
<b>B</b>	Bainite
<b>BF</b>	Bright Field
<b>B<sub>f</sub></b>	Bainitic Transformation Finishing Temperature
<b>BH</b>	Bake Hardening
<b>B<sub>s</sub></b>	Bainitic Transformation Starting Temperature
<b>C</b>	Carbon
<b>CALH</b>	Continuous Annealing Line Heating
<b>CCT</b>	Continuous Cooling Transformation
<b>CH</b>	Conventional Heating
<b>CI</b>	Confidence Index
<b>CP</b>	Complex Phase
<b>Cr</b>	Chromium
<b>DP</b>	Dual-Phase
<b>EBSD</b>	Electron BackScatter Diffraction

<b>EDS</b>	Energy Dispersive Spectroscopy
<b>EDXS</b>	Energy Dispersive X-ray Spectroscopy
<b>F</b>	Ferrite
<b>FB</b>	Ferrite-Bainite
<b>Fe</b>	Iron
<b>GAIQ</b>	Grain Average Image Quality
<b>GB</b>	Grain Boundary
<b>GPa</b>	Giga Pascal
<b>HAGB</b>	High Angle Grain Boundary
<b>HSLA</b>	High Strength - Low Alloy
<b>IF</b>	Interstitial Free
<b>IM</b>	Initial Microstructure
<b>IPF</b>	Inverse Pole Figure
<b>IQ</b>	Image Quality
<b>IS</b>	Isotropic Steel
<b>K-S</b>	Kurdjumov-Sachs
<b>kV</b>	KiloVolts
<b>LAGB</b>	Low Angle Grain Boundary
<b>LOM</b>	Light Optical Microscope

## *2. List of Abbreviations*

---

<b>M</b>	Martensite
<b>Mf</b>	Martensitic Transformation Finishing Temperature
<b>mm</b>	millimeter
<b>MMnS</b>	Medium Manganese Steels
<b>Mn</b>	Manganese
<b>Mo</b>	Molybdenum
<b>MPa</b>	Mega Pascal
<b>Ms</b>	Martensitic Transformation Starting Temperature
<b>Nb</b>	Niobium
<b>ND</b>	Normal Direction
<b>N-W</b>	Nishiyama-Wasserman
<b>°C</b>	Celsius degrees
<b>P</b>	Pearlite
<b>PAG</b>	Parent Austenite Grain
<b>PH</b>	Press Hardening
<b>PIPS</b>	Precision Ion Polishing System
<b>Q&amp;P</b>	Quench & Partitioning
<b>R</b>	Plastic Strain Ratio
<b>RA</b>	Retained Austenite

<b>RexF</b>	Recrystallized Ferrite
<b>S</b>	Sulfur
<b>saed</b>	Selected Area Electron Diffraction
<b>SC</b>	Spheroidized Cementite
<b>SE</b>	Secondary Electrons
<b>s</b>	Seconds
<b>SEM</b>	Scanning Electron Microscope
<b>SGB</b>	Sub-Grain Boundaries
<b>Si</b>	Silicon
<b>STEM</b>	Scanning Transmission Electron Microscope
<b>TD</b>	Transverse Direction
<b>TE</b>	Total Elongation
<b>t-EBSD TKD</b>	Transmission Electron BackScatter Diffraction / Transmission Kikuchi Diffraction
<b>TEM</b>	Transmission Electron Microscope
<b>Ti</b>	Titanium
<b>TRIP</b>	Transformation Induced Plasticity
<b>TTT</b>	Time-Temperature-Transformation
<b>TWIP</b>	TWinning Induced Plasticity
<b>ULC</b>	Ultra-Low Carbon

## *2. List of Abbreviations*

---

<b>UFH</b>	Ultra-fast Heating
<b>USC</b>	Undissolved Spheroidized Cementite
<b>UTS</b>	Ultimate Tensile Strength
<b>V</b>	Volts
<b>XRD</b>	X-Ray Diffraction
<b>YS</b>	Yield Strength
<b><math>\alpha</math></b>	ferrite
<b><math>\gamma</math></b>	austenite
<b><math>\Delta G</math></b>	Gibbs Energy change
<b><math>\Delta R</math></b>	Planar Anisotropy Parameter
<b><math>\theta</math></b>	cementite
<b><math>\mu\text{m}</math></b>	micrometer



### 3. Σύνοψη στα Ελληνικά

#### 3.1. Περίληψη

Αυτή η διατριβή έχει ως στόχο τη λεπτομερή κατανόηση των φαινομένων μετασχηματισμού που λαμβάνουν χώρα όταν εφαρμόζονται υψηλοί ρυθμοί θέρμανσης σε τύπους χαλύβων της αυτοκινητοβιομηχανίας. Επικεντρώνεται στην εξέλιξη της μικροδομής μέσω των σταδίων θέρμανσης και ψύξης της θερμικής επεξεργασίας. Με την κατανόηση αυτών των φαινομένων, οι κατεργασίες Ultra-Fast Heating μπορούν να ελεγχθούν καλύτερα με σκοπό τη βελτιστοποίηση των υπάρχοντων βαθμών και τη σχεδίαση νέων. Τέτοιοι βαθμοί μπορούν να ενσωματωθούν στους τρέχοντες Προηγμένους Χάλυβες Υψηλής Αντοχής 3<sup>rd</sup> γενιάς που συνίστανται από παρόμοιες μικροδομές και παρουσιάζουν ιδανικές μηχανικές ιδιότητες. Για το σκοπό αυτό, μελετάται η επίδραση του ρυθμού θέρμανσης, μέσω της χρήσης τεχνικών χαρακτηρισμού, στη σφαιροποίηση και διάλυση του σεμεντίτη, στην ανακρυστάλλωση του φερρίτη και στην πυρήνωση και ανάπτυξη του ωστενίτη, τα οποία τελικά οδηγούν στο σχηματισμό μπαινίτη και μαρτενσίτη, και σε υπολειπόμενο ωστενίτη κατά την βαφή. Από τα πειράματα, προκύπτει το συμπέρασμα ότι σε τάχιστες θερμικές επεξεργασίες, λόγω της καθυστερημένης και ατελούς διαλυτοποίησης του σεμεντίτη, εμφανίζεται ετερογένεια στη χημική σύσταση και στο μέγεθος κόκκου του πρότερου ωστενίτη. Αυτή η ετερογένεια έρχεται να εξηγήσει τον σχηματισμό του μπαινίτη παράλληλα με τον μαρτενσίτη και τη διατήρηση του ωστενίτη. Γενικά, οι χάλυβες που έχουν υποστεί τάχιστη θερμική κατεργασία εμφανίζουν καλύτερη αναλογία αντοχής / ολκιμότητας από τους συμβατικούς θερμαινόμενους χάλυβες. Αυτές οι μηχανικές ιδιότητες προκύπτουν από τις εκλεπτυσμένες μικτές μικροδομές τους. Αντιθέτως, στους χάλυβες που έχουν υποστεί συμβατικές θερμικές κατεργασίες, η μικροδομή αποτελείται μόνο από μαρτενσίτη, και έτσι η ολκιμότητα τους αναμένεται σχετικά χαμηλή. Αποδεικνύεται επίσης ότι η αντοχή του χάλυβα μπορεί να αυξηθεί χωρίς σημαντικές απώλειες στην ολκιμότητα, όταν εφαρμόζονται υψηλοί ρυθμοί θέρμανσης. Η πειραματική προσέγγιση που χρησιμοποιείται σε αυτή τη διατριβή, επιβεβαιώνει μέσω τεχνικών χαρακτηρισμού την ικανότητα παραγωγής μικτών μικροδομών σε ένα μόνο βήμα, εξηγώντας τον ταυτόχρονο σχηματισμό μπαινίτη και μαρτενσίτη, και τη διατήρηση του ωστενίτη σε εξαιρετικά γρήγορους κύκλους θέρμανσης, όπως έχει προβλεφθεί μέσω πειραμάτων προσομοίωσης.

#### 3.2. Εισαγωγή

Τις τελευταίες δεκαετίες, οι βιομηχανίες παραγωγής χάλυβα μαζί με την αυτοκινητοβιομηχανία προωθούν την προσθήκη κραματικών στοιχείων και την εφαρμογή θερμικών κατεργασιών, με σκοπό την παραγωγή τύπων χάλυβα με τις επιθυμητές ιδιότητες, ώστε να εφαρμοστούν στην άτρακτο (body-in-white) των οχημάτων. Έτσι, προέκυψαν οι Ανεπτυγμένοι Χάλυβες Υψηλής αντοχής με σκοπό τη βέλτιστη αναλογία αντοχής/ολκιμότητας, οι οποίοι χρησιμοποιούνται μέχρι σήμερα για την κατασκευή των οχημάτων. Τα τελευταία χρόνια, ωστόσο, και σύμφωνα με τις οδηγίες της Ε.Ε. [1], εγείρεται επιτακτική επίσης η ανάγκη για τη μείωση των ρύπων CO/CO<sub>2</sub> που παράγονται από τα αυτοκίνητα. Ως αποτέλεσμα, η αυτοκινητοβιομηχανία αναζητεί νέες μεθόδους παραγωγής και κατεργασίας χαλύβων ώστε να μειωθεί η διατομή των χρησιμοποιούμενων υλικών

και, συνεπώς, το βάρος του οχήματος, χωρίς όμως να τίθεται ζήτημα μείωσης της ασφάλειας των επιβατών. Η επιβολή τάχιστων θερμικών κύκλων (Ultra-Fast Heating – UFH), η οποία μελετάται από διαφορετικές επιστημονικές ομάδες σε όλο τον κόσμο τα τελευταία χρόνια [2-11] μπορεί να προσφέρει μία εναλλακτική νέα μέθοδο για την επίτευξη χαλύβων υψηλότερης αντοχής για χρήση στην αυτοκινητοβιομηχανία. Αν και η επιβολή ραγδαίων ρυθμών θέρμανσης έχει χρησιμοποιηθεί βιομηχανικά στο παρελθόν για επιφανειακή σκλήρυνση, η εφαρμογή της ως μέθοδος θερμικής κατεργασίας χαλύβων βρίσκεται ακόμα υπό μελέτη. Σύμφωνα με αυτή τη μέθοδο, το υλικό θερμαίνεται με πολύ υψηλούς ρυθμούς θέρμανσης (100-1000 °C/s) μέχρι την επιθυμητή θερμοκρασία ( $>A_{c1}$ ) και ύστερα από ελάχιστη παραμονή σε αυτή τη θερμοκρασία ( $<3$  sec) ψύχεται ραγδαία σε θερμοκρασία δωματίου. Αυτό έρχεται σε αντίθεση με τις θερμικές κατεργασίες που χρησιμοποιούνται μέχρι σήμερα για την παραγωγή τύπων χάλυβα, π.χ. διφασικοί χάλυβες, στις οποίες εφαρμόζονται αρκετά πιο αργοί ρυθμοί αναθέρμανσης ( $\sim 10$  °C/s), ενώ και ο χρόνος παραμονής στην επιθυμητή θερμοκρασία είναι σημαντικά μεγαλύτερος (4-10 min), ενώ η αρχική διφασική (ωστενιτική-φερριτική) μικροδομή παρουσιάζει ομοιογένεια στην περιεκτικότητα σε άνθρακα (και σε λοιπά κραματικά στοιχεία), κάτι το οποίο δε συμβαίνει στην περίπτωση του ωστενίτη, που προκύπτει μετά τη ραγδαία αναθέρμανση.

### 3.2.1. Σκοπός

Σκοπός της Διατριβής είναι η διερεύνηση παραγωγής χαλύβων με χαρακτηριστικά αντίστοιχα με εκείνα Προηγμένων Χαλύβων 3ης Γενιάς ύστερα από την εφαρμογή τάχιστων θερμικών κύκλων.

Συγκεκριμένα, μελετήθηκε διεξοδικά η εξέλιξη της μικροδομής. Αναζητήθηκε η ύπαρξη μπαινίτη και υπολειπόμενου ωστενίτη, που αποτελούν βασικά συστατικά των εν λόγω χαλύβων. Κατά την πειραματική έρευνα, με χαρακτηρισμό και ανάλυση της μικροδομής, εκτός του μαρτενσίτη, ο οποίος αποτελεί βασικό συστατικό της μικροδομής, παρατηρήθηκε όντως και η ύπαρξη μπαινίτη, αλλά και μικροποσότητας υπολειπόμενου ωστενίτη. Ο σχηματισμός μπαινίτη (και ωστενίτη) δεν αναμενόταν λόγω του ελάχιστου διαθέσιμου χρόνου της θερμικής κατεργασίας. Συνεπώς, αποδεικνύεται πειραματικά ότι είναι δυνατόν να προκύψουν σε μικρό χρονικό διάστημα και χωρίς την εφαρμογή περισσότερων βημάτων τέτοιου τύπου χάλυβες, οι οποίοι μέχρι σήμερα επιτυγχάνονται με συμβατικές, χρονοβόρες μεθόδους, και σύνθετους θερμικούς κύκλους.

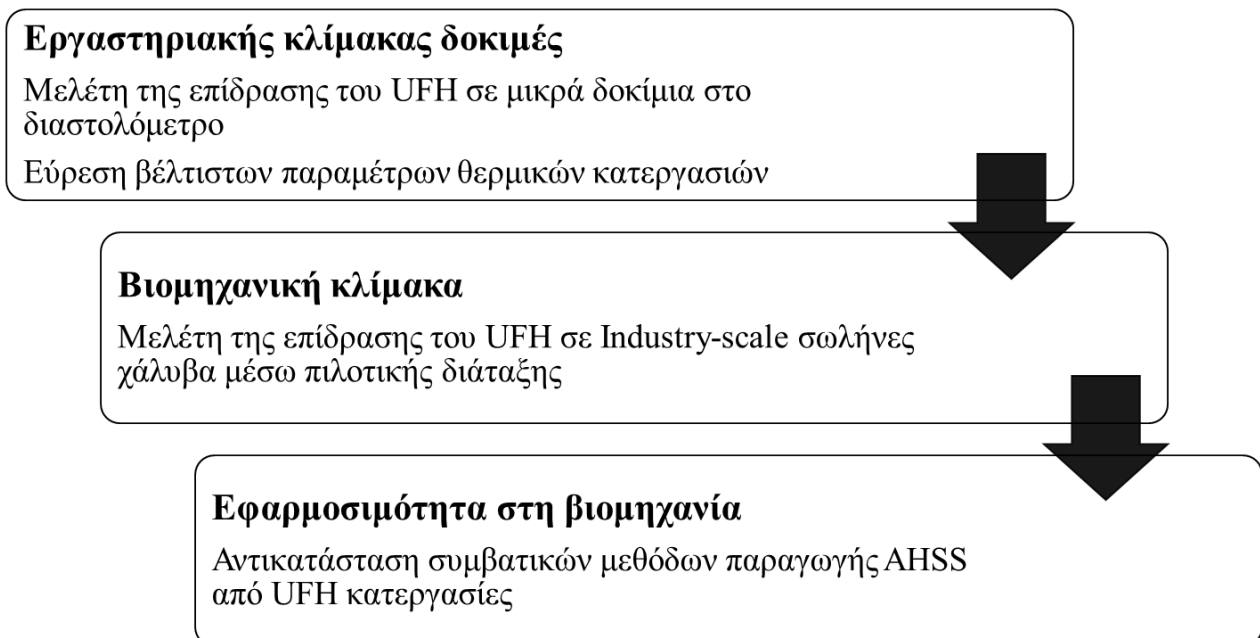
Η μελέτη αποσκοπεί, επίσης, στη διεύρυνση και στον εμπλουτισμό της υπάρχουσας γνώσης σχετικά με τις ραγδαίες (UFH) κατεργασίες και τους μηχανισμούς των μετασχηματισμών, που συμβαίνουν κατά τη διάρκεια τάχιστης αναθέρμανσης και υπό καθεστώς αμελητέου χρόνου για διάχυση. Συγκεκριμένα, με την εφαρμογή υψηλών ρυθμών θέρμανσης, η επίδραση της UFH μελετάται στη διάλυση του σεμεντίτη, στη διάχυση του άνθρακα, στην πυρήνωση του ωστενίτη και στις διεργασίες επαναφοράς και ανακρυστάλλωσης. Αναλόγως, μελετώνται τα προϊόντα που σχηματίζονται κατά την ψύξη.

Η παρούσα μελέτη εντάσσεται στο επιστημονικό έργο της ερευνητικής ομάδας του Καθηγητή κ. Παπαευθυμίου πάνω στην εφαρμογή τάχιστων θερμικών κύκλων σε χάλυβες. Συμπληρώνει τη διατριβή της

Δρ. Μπουζούνη με θέμα τη μοντελοποίηση και την ανάλυση των φαινομένων, που συναντώνται σε αυτές τις κατεργασίες.

### 3.3. Πειραματικό μέρος

Ο σχεδιασμός των πειραμάτων ήταν τέτοιος ώστε να μελετηθεί πλήρως η επίδραση των τάχιστων θερμικών κύκλων στη μικροδομή και τις μηχανικές ιδιότητες των χαλύβων και κατά πόσο είναι δυνατή η εφαρμογή τους στη βιομηχανία. Για αυτόν τον λόγο, πραγματοποιήθηκαν πειράματα σε δοκίμια μικρού μεγέθους, εργαστηριακής κλίμακας, όπου ήταν δυνατός ο έλεγχος των διαφόρων παραμέτρων της θερμικής κατεργασίας. Μετά τον προσδιορισμό της επίδρασης των διαφόρων παραμέτρων, έγιναν δοκιμές σε βιομηχανικής κλίμακας σωλήνες και μελετήθηκε η μικροδομή τους ύστερα από την επιβολή τάχιστων θερμικών κύκλων. Τέλος, εφαρμόστηκαν ραγδαίοι θερμικοί κύκλοι σε εμπορικούς χάλυβες με σκοπό να μελετηθεί η δυνατότητα παραγωγής AHSS. Συγκεκριμένα, επιλέχθηκαν οι διφασικοί χάλυβες για τον λόγο ότι χρησιμοποιούνται ως επί το πλείστον στην αυτοκινητοβιομηχανία σήμερα.



Η αρχική προσέγγιση έγινε εργαστηριακά με χρήση διαστολομετρίας. Περιλαμβάνει τη μελέτη μικρών δοκιμίων (διαμέτρου 3 mm, μήκους 10 mm) από χαμηλά κραματωμένο χάλυβα μέσης περιεκτικότητας σε άνθρακα και χαμηλή περιεκτικότητα σε χρώμιο και μολυβδαίνιο. Σε αυτά τα δοκίμια, οι θερμικές κατεργασίες έγιναν σε διαστολόμετρο για τον ακριβή έλεγχο των μετασχηματισμών φάσης και των παραμέτρων των θερμικών κατεργασιών. Ο σκοπός αυτής της προσέγγισης ήταν η μελέτη της επίδρασης κάθε παραμέτρου της θερμικής κατεργασίας ξεχωριστά. Με αυτά τα αποτελέσματα μπόρεσε να προσδιοριστεί με μεγαλύτερη ακρίβεια η βέλτιστη θερμική κατεργασία σε βιομηχανικής κλίμακας δοκίμια (σωλήνες χωρίς ραφή ίδιου χάλυβα πάχους τοιχώματος 2,5 mm, διαμέτρου 35 mm και μήκους 110 mm). Συγκεκριμένα, οι παράμετροι που μελετήθηκαν είναι η περιεκτικότητα του υλικού σε Cr, Mn και Mo (σύσταση 42CrMo4 και C45), η αρχική μικροδομή, η θερμοκρασία ανόπτησης, ο χρόνος παραμονής σε αυτή τη θερμοκρασία (σύσταση 42CrMn6),

### 3. Σύνοψη στα Ελληνικά

ενώ τέλος έγινε σύγκριση ενός τάχιστου θερμικού κύκλου με έναν συμβατικό, όμοιο με αυτούς που χρησιμοποιούνται στη βιομηχανία (σύσταση 42CrMn6).

Οι χημικές συστάσεις των δοκιμών αναγράφονται αναλυτικότερα στον **Πίνακα 3.1**. Επίσης, οι αρχικές μικροδομές αποτελούνται από φερρίτη και σεμεντίτη, είτε σφαιροποιημένο είτε σε πλακοειδή μορφή, ενώ οι θερμικοί κύκλοι που εφαρμόστηκαν αναγράφονται στον **Πίνακα 3.2**.

**Πίνακας 3.1:** Οι χημικές συστάσεις κατά βάρος % των δοκιμών που χρησιμοποιήθηκαν κατά τη διαστολομετρία.

	C	Mn	Si	Cr	Mo	P	S	Fe
42CrMo4	0.43	1	0.35	1.1	0.25	<0.04	<0,04	balance
C45	0.43	0.5-0.8	<0.4	<0.4	<0.03	<0.035	<0.04	balance
42CrMn6	0.43	1.43	0.4	1.23	0.1	<0.04	<0.04	balance

**Πίνακας 3.2:** Η σύσταση, οι αρχικές μικροδομές και οι παράμετροι των θερμικών κατεργασιών που εφαρμόστηκαν στα δοκίμια διαστολομετρίας.

Όνομα δοκιμίου	Σύσταση	Αρχική μικροδομή	Ρυθμός θέρμανσης (°C/s)	Θερμοκρασία ανόπτησης (°C)	Χρόνος παραμονής (s)	Ρυθμός ψύξης (°C/s)
42CrMo4	<b>42CrMo4</b>	Φερρίτης + Περλίτης	100	1080	3	100
C45	<b>C45</b>					
UF&Q	42CrMn6	Φερρίτης + Σφαιροποιημένος σεμεντίτης (ΣΣ)	300	900	<b>3</b>	100
UF&S&Q					<b>300</b>	
UFHT	42CrMn6	Φερρίτης + Σφαιροποιημένος σεμεντίτης (ΣΣ)	<b>300</b>	<b>1080</b>	<b>2</b>	100
CHT			<b>10</b>	<b>900</b>	<b>300</b>	

Στη συνέχεια πραγματοποιήθηκαν πειράματα σε δοκίμια σωλήνων κανονικού μεγέθους (δείγματα μήκους 110 mm, διαμέτρου 35 mm και πάχους τοιχώματος 2.5 mm), αντίστοιχου με αυτό που χρησιμοποιείται στη βιομηχανία. Σκοπός αυτών των πειραμάτων είναι να μελετηθεί κατά πόσο τα φαινόμενα που παρατηρήθηκαν στις εργαστηριακές δοκιμές εμφανίζονται και σε δοκίμια μεγαλύτερου μεγέθους και να επιβεβαιωθούν τα συστατικά της μικροδομής μέσω διεξοδικού χαρακτηρισμού. Συγκεκριμένα, μέσω ηλεκτρονικής μικροσκοπίας διερχόμενης δέσμης (TEM) επιβεβαιώθηκε η ύπαρξη μπαινίτη και υπολειπόμενου οστενίτη στη μικροδομή, ενώ εξηγήθηκε η αλληλουχία των μετασχηματισμών από τους οποίους προέκυψαν. Η σύσταση του χάλυβα είναι η 42CrMo4 που αναγράφεται στον **Πίνακα 3.1** παραπάνω και η θερμική κατεργασία αναγράφεται στον **Πίνακα 3.3**, ενώ η αρχική μικροδομή αποτελείται από φερρίτη και περλίτη.

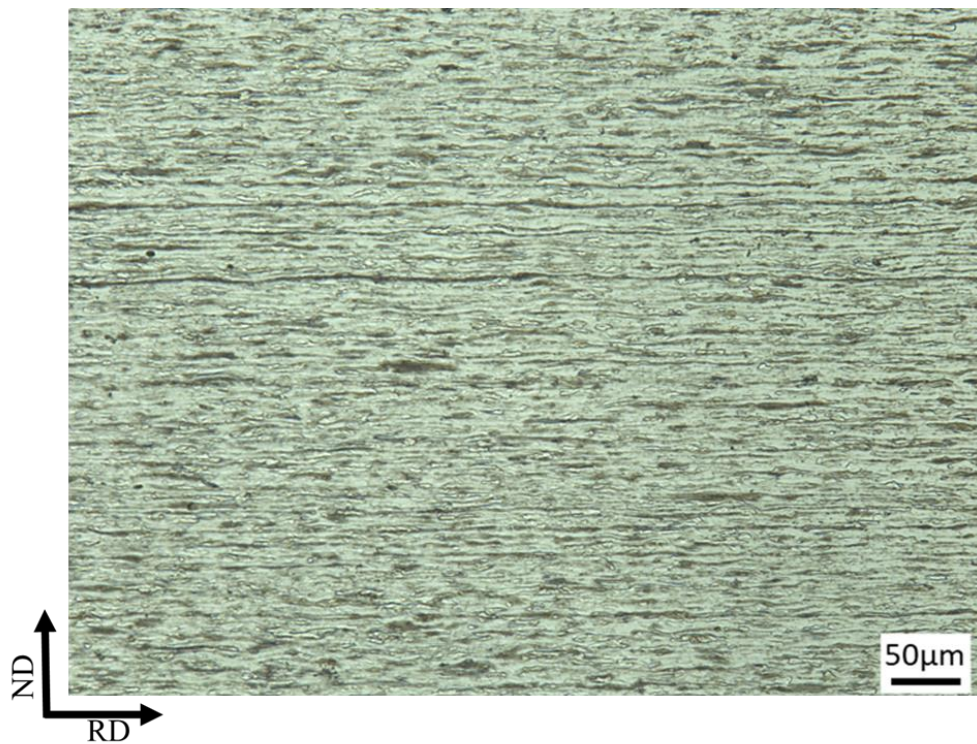
**Πίνακας 3.3:** Η σύσταση, η αρχική μικροδομή και οι παράμετροι της θερμικής κατεργασίας για τα δοκίμια βιομηχανικής κλίμακας.

Όνομα δοκιμίου	Σύσταση	Αρχική μικροδομή	Ρυθμός θέρμανσης (°C/s)	Θερμοκρασία ανόπτησης (°C)	Χρόνος παραμονής (s)	Ρυθμός ψύξης (°C/s)
UFIP	42CrMo4	Φερρίτης + Περλίτης	100	900	-	Βαφή σε νερό

Τέλος, στο επόμενο επίπεδο μελέτης διερευνήθηκε εργαστηριακά σε πειραματική διάταξη Gleeble η πιθανότητα η μέθοδος ραγδαίας αναθέρμανσης να διευρύνει τις δυνατότητες των υπαρχουσών μεθόδων παραγωγής χαλύβων, που χρησιμοποιούνται ευρέως στην αυτοκινητοβιομηχανία. Για τον λόγο αυτό, επιλέχθηκε ένας εμπορικός χάλυβας που χρησιμοποιείται ευρέως στην αυτοκινητοβιομηχανία (**Πίνακας 3.4**) και στον οποίο υποβλήθηκαν οι ραγδαίοι θερμικοί κύκλοι, που φαίνονται στον **Πίνακα 3.5**. Σε αυτά τα πειράματα συμπεριλήφθηκε ένα στάδιο προθέρμανσης (PH), το οποίο δεν επηρεάζει τη μικροδομή, διευκολύνει όμως τη μηχανή να επιτύχει τους τάχιστους ρυθμούς θέρμανσης. Αυτός ο χάλυβας ήταν ψυχρής έλασης με φερριτο-περλιτική μικροδομή, όπως φαίνεται στην **Εικόνα 3.1**. Η μελέτη αποσκοπούσε στο σχηματισμό διφασικής μικροδομής φερρίτη-μαρτενσίτη μέσω τάχιστης θερμικής κατεργασίας και τη σύγκρισή τους με τους ήδη εφαρμοζόμενους διφασικούς χάλυβες με αντίστοιχη αναλογία φάσεων.

**Πίνακας 3.4:** Η χημική σύσταση κατά βάρος % του εμπορικού χάλυβα που χρησιμοποιήθηκε για την παραγωγή UF διφασικού χάλυβα.

C	Si	Mn	Cr	Mo	S	P	Nb+Ti	Fe
0.14	0.24	1.7	0.25	0.25	0.004	0.014	0.05	balance



**Εικόνα 3.1:** Εικόνα από το OM με την αρχική μικροδομή του ψυχρώς ελασμένου χάλυβα που χρησιμοποιήθηκε για την παραγωγή του διφασικού χάλυβα.

**Πίνακας 3.5:** Η αρχική μικροδομή και οι παράμετροι της θερμικής κατεργασίας που εφαρμόστηκαν στα δοκίμια για την παραγωγή του διφασικού χάλυβα.

Όνομα δοκιμίου	Αρχική μικροδομή	Ρυθμός θέρμανσης (°C/s)	Θερμοκρασία ανόπτησης (°C)	Χρόνος παραμονής (s)	Ρυθμός ψύξης (°C/s)
UFH	Φερρίτης + Περλίτης, Έλαση 60%	780	760	0.2	65
CH		10			
CALH				240	

Για την ανάλυση της μικροδομής έγινε χρήση του Οπτικού Μικροσκοπίου (LOM), του Ηλεκτρονικού Μικροσκοπίου Σάρωσης (SEM), εξοπλισμένο με φασματομέτρο ακτίνων X διασπαρμένης ενέργειας (EDS), όπως και του Ηλεκτρονικού Μικροσκοπίου Διερχόμενης δέσμης (TEM). Επίσης, έγινε ανάλυση με τη μέθοδο Περίθλασης Οπισθοσκεδαζόμενων Ηλεκτρονίων (EBSD), καθώς επίσης και ανάλυση με περίθλαση ακτίνων X (XRD). Με συνδυασμό όλων των παραπάνω τεχνικών, καθίσταται δυνατός ο όσο το δυνατόν καλύτερος χαρακτηρισμός των φάσεων και των συστατικών της μικροδομής. Για όλες τις παραπάνω μεθόδους

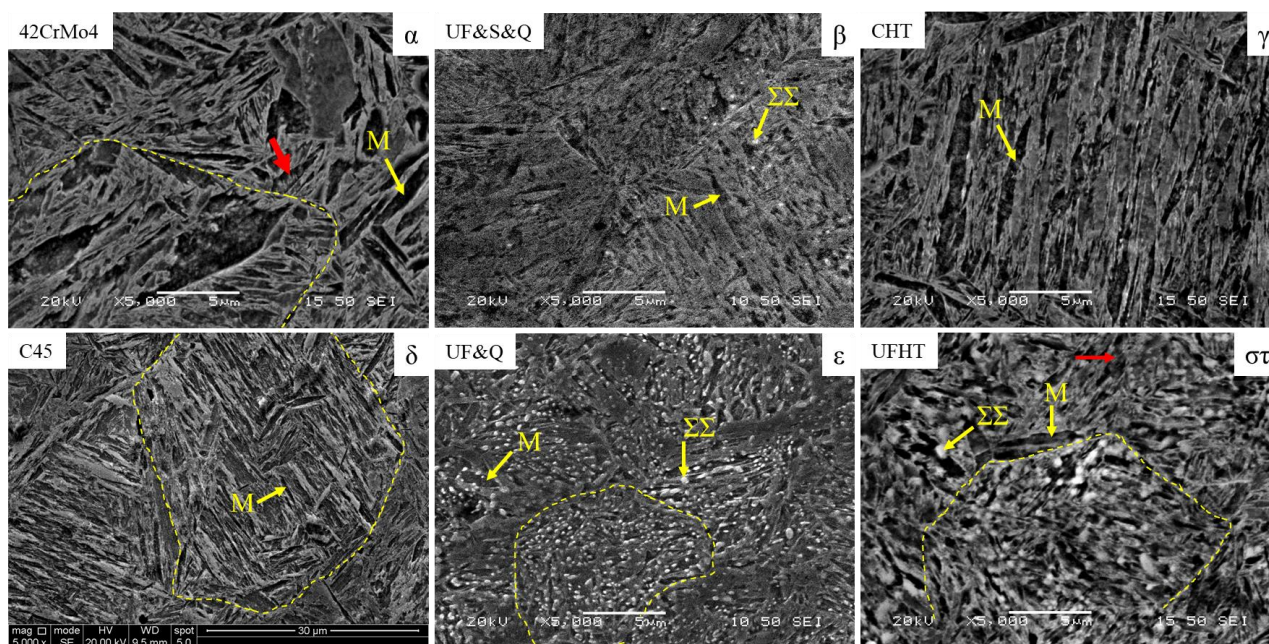
έχει προηγηθεί η κατάλληλη προετοιμασία των δοκιμών. Το λογισμικό ARPGE [13] χρησιμοποιήθηκε για την επανοικοδόμηση των κόκκων του πρότερου ωστενίτη βασιζόμενο στις σχέσεις προσανατολισμού φερρίτη – ωστενίτη κατά Nishiyama – Wasserman (N-W). Με τη χρήση αυτού του λογισμικού έγινε μια προσέγγιση χαρακτηρισμού της μικροδομής στη θερμοκρασία ανόπτησης. Έτσι επετεύχθη η σύνδεση της αρχικής με την τελική μικροδομή και έγινε δυνατή η εξέλιξη των μετασχηματισμών που έλαβαν χώρα. Επίσης, τα διαγράμματα controlled cooling transformation (CCT) σχεδιάστηκαν με τη χρήση των μοντέλων του Kirkaldy [14] και του Bhadeshia [15,16]. Χρησιμοποιώντας δεδομένα από τις παραπάνω μεθόδους, ο σχεδιασμός των διαγραμμάτων CCT δύναται να εξηγήσει τον σχηματισμό των προϊόντων της βαφής. Για τη μελέτη των μηχανικών ιδιοτήτων έγιναν σκληρομετρήσεις κατά την κλίμακα Vickers (HV) και εφελκυσμοί σε δοκίμια μικρού μεγέθους και διατομής τύπου dog-bone.

### 3.4. Αποτελέσματα

#### 3.4.1. Ανάλυση των παραμέτρων τάχιστων θερμικών κατεργασιών σε εργαστηριακό επίπεδο μέσω διαστολομετρίας

Στον πρώτο κύκλο πειραμάτων, στις θερμικές κατεργασίες στο διαστολόμετρο Dil805A της Bähr Co., η θερμοκρασία ανόπτησης ήταν πάνω από την  $Ac_3$  θερμοκρασία. Για αυτόν τον λόγο η μικροδομή αναμένεται να είναι μαρτενιτική, όπως φαίνεται στο SEM (**Εικόνα 3.2**). Συγκεκριμένα, στα δοκίμια όπου η αρχική μικροδομή αποτελείται από περλίτη και φερρίτη (42CrMo4 - **Εικόνα 3.2α** και C45 – **Εικόνα 3.2δ**), φαίνεται πως έχει γίνει πλήρης διαλυτοποίηση του σεμεντίτη. Το ίδιο φαίνεται και για το δοκίμιο αναφοράς που έχει υποστεί αργή θέρμανση με χρόνο παραμονής 300 s (CHT – **Εικόνα 3.2γ**), όπου η διαλυτοποίηση του σφαιροποιημένου σεμεντίτη (ΣΣ) καθίσταται δυνατή. Στο εν λόγω δοκίμιο η μικροδομή αποτελείται από ευμεγέθεις βελόνες μαρτενσίτη (M), όπως αναμένεται από τη συμβατική θερμική κατεργασία στην οποία υπεβλήθη. Αντιθέτως, στα υπόλοιπα δοκίμια των οποίων η αρχική μικροδομή αποτελείται από φερρίτη και σφαιροποιημένο σεμεντίτη, και τα οποία έχουν υποστεί τάχιστη θερμική κατεργασία (UF&S&Q – **Εικόνα 3.2β**, UF&Q – **Εικόνα 3.2ε** και UFHT – **Εικόνα 3.2στ**), φαίνεται πως δεν έχει γίνει πλήρης διαλυτοποίηση του σεμεντίτη. Επίσης, μπορεί να παρατηρηθεί ότι οι βελόνες του μαρτενσίτη είναι μικρότερες στα δοκίμια που έχουν υποστεί UFH σε σχέση με το CHT δοκίμιο, κάτι το οποίο θα αναλυθεί στη συνέχεια. Κάτι αντίστοιχο μπορεί να παρατηρηθεί και για τα όρια του πρότερου ωστενίτη, όπως αυτά φαίνονται στις εικόνες (κίτρινη διακεκομμένη γραμμή). Τέλος, σε κάποια από τα δοκίμια που έχουν υποστεί τάχιστη θερμική κατεργασία, παρατηρούνται κάποιες μπαινιτικές μικροδομές, οι οποίες αναδεικνύονται με κόκκινα βέλη.

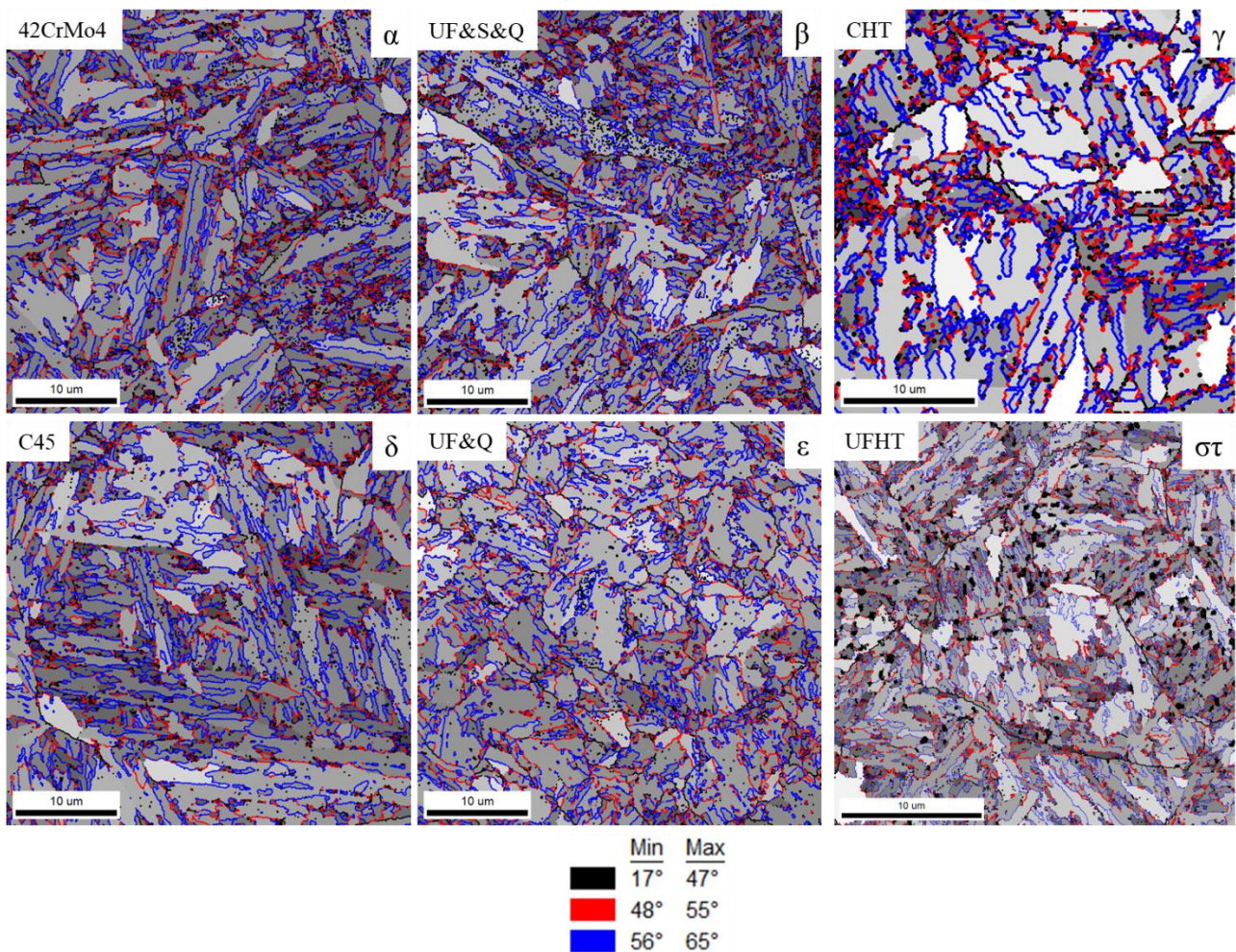




**Εικόνα 3.2:** SE εικόνες από το SEM για τα δοκίμια (α) 42CrMo4, όπου φαίνονται οι βελόνες μαρτενσίτη (M) και πιθανές μπαινιτικές μικροδομές (κόκκινο βέλος), (β) UF&S&Q που αποτελείται από μαρτενσίτη (M) και σφαιροποιημένο σεμεντίτη (ΣΣ), (γ) CHT που είναι πλήρως μαρτενσιτικό, (δ) C45 στο οποίο παρατηρείται κυρίως μαρτενσίτη, (ε) UF&Q του οποίου η μικροδομή αποτελείται από M και ΣΣ και (στ) UFHT στο οποίο, εκτός από M και ΣΣ, παρατηρούνται και μπαινιτικές μικροδομές (κόκκινο βέλος).

Περισσότερες ενδείξεις για την ύπαρξη μπαινίτη δίνονται από το EBSD. Σύμφωνα με τους Zajac et al. [12], και σύμφωνα με τη φύση του μπαινιτικού μετασχηματισμού, οι αποκλίσεις (misorientations) των ορίων των μπαινιτικών πλακιδίων είναι μικρότερες από αυτές των ορίων των μαρτενσιτικών βελονών. Αυτό συμβαίνει λόγω του διατμησιακού μετασχηματισμού του μαρτενσίτη, ο οποίος συμβαίνει ακαριαία και με παραμόρφωση της FCC κυψελίδας του ωστενίτη. Αντιθέτως, ο μετασχηματισμός του άνω μπαινίτη, είναι διαχυσιακός, δηλαδή απαιτείται περισσότερος χρόνος για τη διάχυση του άνθρακα από την κυψελίδα του ωστενίτη και ο μετασχηματισμός σε BCC προκαλεί μικρότερη παραμόρφωση. Σύμφωνα με τους Zajac et al. [12], κατά αυτόν τον τρόπο γίνεται ένας διαχωρισμός αυτών των συστατικών βάσει των συγκεκριμένων αποκλίσεων. Ειδικότερα, όπως φαίνεται στο EBSD, μεγάλες αποκλίσεις με γωνίες  $56^{\circ}$ -  $65^{\circ}$  (μπλε γραμμές) αντιστοιχούν σε βελόνες μαρτενσίτη, ενώ μικρότερες αποκλίσεις με γωνίες  $48^{\circ}$ -  $55^{\circ}$  (κόκκινες γραμμές), αντιστοιχούν σε πλακίδια μπαινίτη. Σε κάθε περίπτωση όμως, αυτή η μέθοδος δίνει ενδείξεις για την ύπαρξη του μπαινίτη και δεν αποτελεί αποδεικτικό στοιχείο, συνεπώς άλλες μέθοδοι πρέπει να χρησιμοποιηθούν συνδυαστικά. Αυτό θα πραγματοποιηθεί στη συνέχεια στα δοκίμια βιομηχανικής κλίμακας. Στα δοκίμια της διαστολομετρίας βρίσκονται παντού ενδείξεις για την ύπαρξη του μπαινίτη. Στους χάρτες για τα δοκίμια όπου υπάρχει αρκετός χρόνος παραμονής (UF&S&Q – **Εικόνα 3.3β** και CHT – **Εικόνα 3.3γ**) το ποσοστό των κόκκινων γραμμών παρατηρείται να είναι μικρότερο, ενώ δεν αναμένεται η ύπαρξη μπαινίτη σε αυτά τα δοκίμια λόγω του αυξημένου χρόνου θέρμανσης.



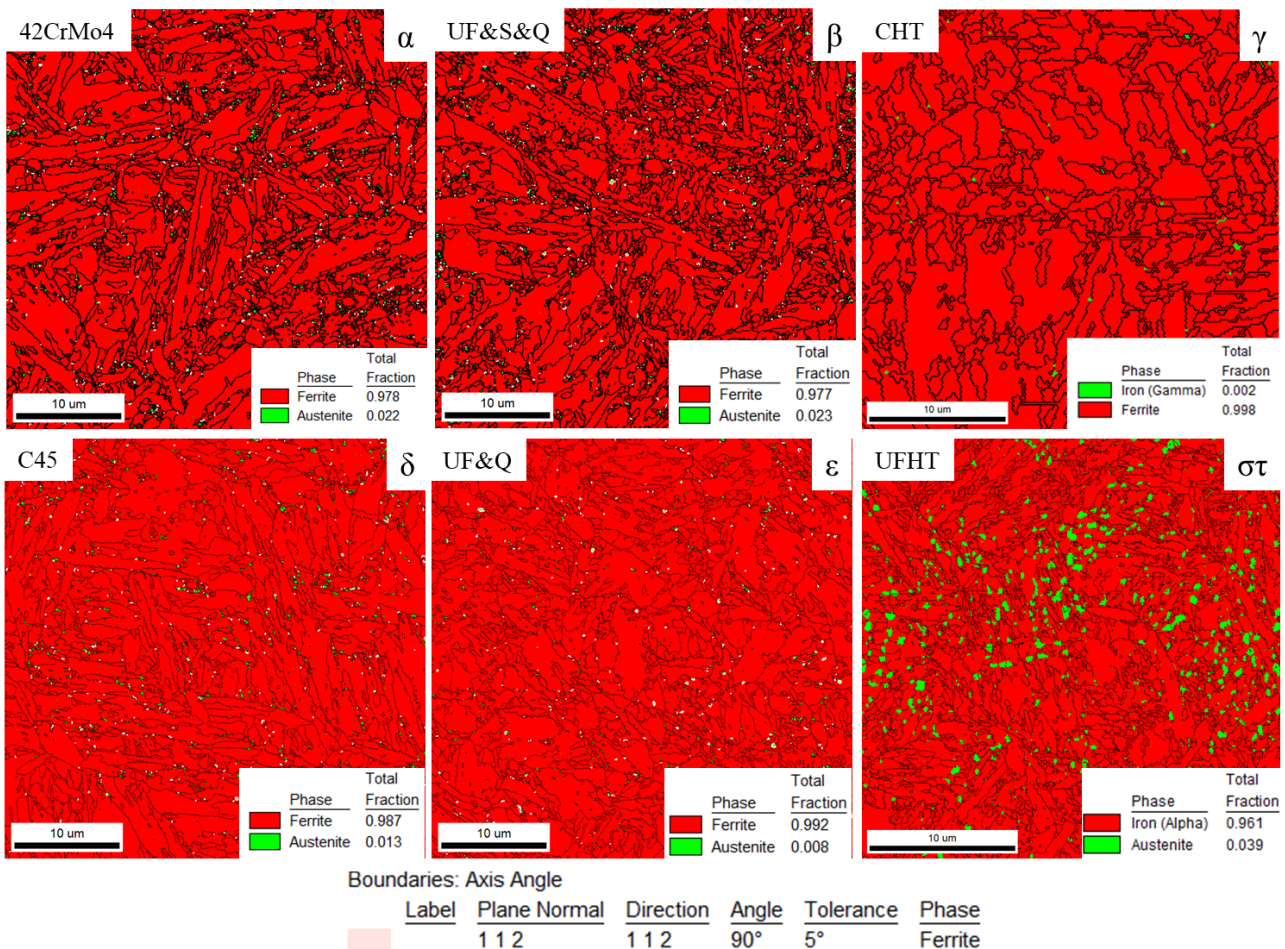


**Εικόνα 3.3:** GAIQ χάρτες από το EBSD. Για χαμηλότερο IQ, το χρώμα του κόκκου είναι πιο σκούρο γκρι, ενώ για πολύ υψηλό IQ, οι κόκκοι εμφανίζονται λευκοί. Τα όρια των κόκκων έχουν σχεδιαστεί με μαύρο χρώμα για γωνίες απόκλισης 17°-47°, με κόκκινο για 48°-55° και με μπλε για 56°-65°. Σύμφωνα με τη βιβλιογραφία [12], αυτές οι γωνίες αντιστοιχούν σε όρια φερρίτη, μαινίτη και μαρτενσίτη αντίστοιχα. Step size: 70 nm.

Εκτός από μαινίτη, η ανάλυση στο EBSD έδειξε και την πιθανή ύπαρξη υπολειπόμενου ωστενίτη. Συγκεκριμένα, στα δοκίμια στα οποία έχει γίνει πλήρης διαλυτοποίηση του σεμεντίτη (42CrMo4 – **Εικόνα 3.4α** και C45 – **Εικόνα 3.4γ**) το κλάσμα όγκου του υπολειπόμενου ωστενίτη είναι πάρα πολύ μικρό, μεταξύ 1-2 %. Αντίστοιχο ποσοστό βρέθηκε και για τα δοκίμια που έχουν ΣΣ στη μικροδομή τους (UF&S&Q – **Εικόνα 3.4β** και UF&Q – **Εικόνα 3.4ε**). Αντιθέτως, στο συμβατικό δοκίμιο (CHT – **Εικόνα 3.4γ**) δεν βρέθηκε υπολειπόμενος ωστενίτης, ενώ στο δοκίμιο που έχει υποστεί τάχιστα θερμική κατεργασία και έχει ΣΣ στη μικροδομή του (UFHT – **Εικόνα 3.4στ**) το ποσοστό του υπολειπόμενου ωστενίτη ήταν αρκετά ψηλότερο, γύρω στο 4 %. Για την αποφυγή σφάλματος, στους χάρτες EBSD έχει προστεθεί και η σχέση Kurdjumov–Sachs (K-S) για ωστενίτη και φερρίτη, η οποία επισημαίνει πως το επίπεδο [1 1 2] του φερρίτη είναι παράλληλο στο επίπεδο [1 1 2] του ωστενίτη, μετατοπισμένου κατά 90°. Παρατηρείται επίσης ότι για τα δοκίμια UF&S&Q και CHT, για τα οποία η μόνη διαφορά στη θερμική κατεργασία είναι ο ρυθμός θέρμανσης, η διαφορά στο ποσοστό του ωστενίτη είναι 2 %, δεδομένου ότι δεν υπολείπεται ωστενίτης στο CHT δοκίμιο. Αντίστοιχα, η μόνη διαφορά στα δοκίμια UF&Q και UFHT, είναι η διαφορετική θερμοκρασία ανόπτησης.



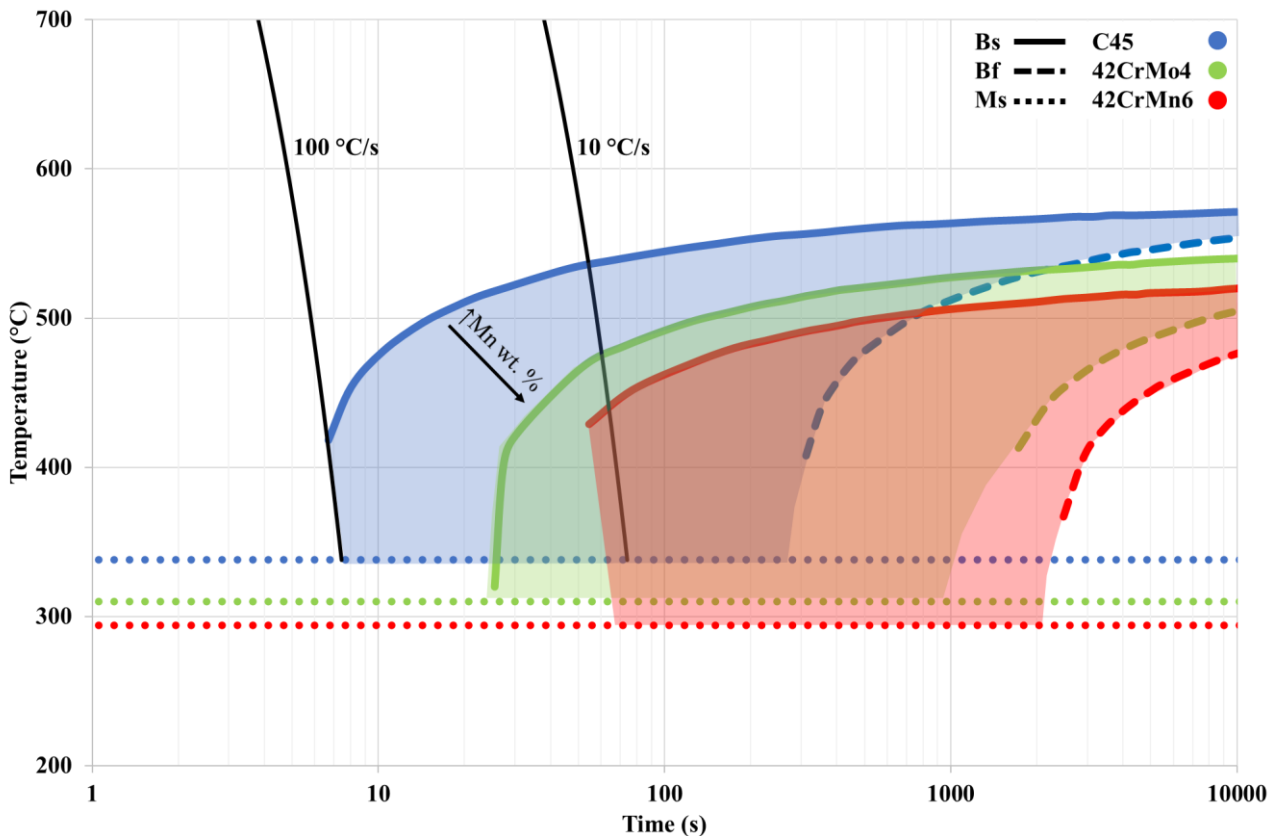
Ωστόσο, η διαφορά στο κλάσμα όγκου του ωστενίτη σε αυτή την περίπτωση είναι μεγαλύτερη και συγκεκριμένα γύρω στο 3 %. Συνεπώς, φαίνεται πως οι γρήγοροι ρυθμοί θέρμανσης είναι απαραίτητοι, ώστε να υπολείπεται ο ωστενίτης, όπως επίσης και ότι η θερμοκρασία απόψησης παίζει σημαντικό ρόλο.



**Εικόνα 3.4:** Χάρτες EBSD όπου με κόκκινο χρώμα εμφανίζονται οι BCC φάσεις (φερρίτης) και με πράσινο χρώμα οι FCC (ωστενίτης). Για τα περισσότερα δοκίμια το ποσοστό του ωστενίτη είναι πολύ μικρό, γύρω στο 1-2 %. Για το UFHT δοκίμιο το ποσοστό του ωστενίτη βρέθηκε στο 4 %. Με λευκό χρώμα έχει σχεδιαστεί η σχέση K-S μεταξύ ωστενίτη και φερρίτη. Step size: 70 nm.

Βάσει των ανωτέρω ευρημάτων, σχεδιάστηκε το διάγραμμα CCT (Εικόνα 3.5) για τις τρεις διαφορετικές συστάσεις με τη χρήση μοντέλων [14-16]. Όπως φαίνεται σε αυτό, η μπαινιτική περιοχή, δηλαδή η περιοχή στην οποία μπορεί να γίνει μετασχηματισμός του ωστενίτη σε μπαινίτη και βρίσκεται μεταξύ των θερμοκρασιών  $B_s$  και  $B_f$ , εξαρτάται κατά μεγάλο βαθμό από τη σύσταση. Καθώς και οι τρεις χάλυβες έχουν την ίδια περιεκτικότητα σε άνθρακα, οι διαφορές οφείλονται στη διαφορετική περιεκτικότητα σε χρώμιο (Cr), Μαγγάνιο (Mn) και μολυβδαίνιο (Mo). Θα πρέπει να σημειωθεί ότι οι μπαινιτικές αυτές περιοχές μπορούν να μετακινηθούν για διαφορετικό μέγεθος πρότερου ωστενίτη, καθώς επίσης και για διακυμάνσεις στην περιεκτικότητα του άνθρακα στη μικροδομή. Και για τις τρεις συστάσεις, η  $B_f$  θερμοκρασία βρίσκεται στα δεξιά του διαγράμματος και, συνεπώς, απαιτείται πολύ αργός ρυθμός ψύξης,  $<10$  °C/s για να είναι πλήρως μπαινιτική η μικροδομή, κάτι το οποίο αποκλείεται στα συγκεκριμένα πειράματα. Από την άλλη, παρατηρείται

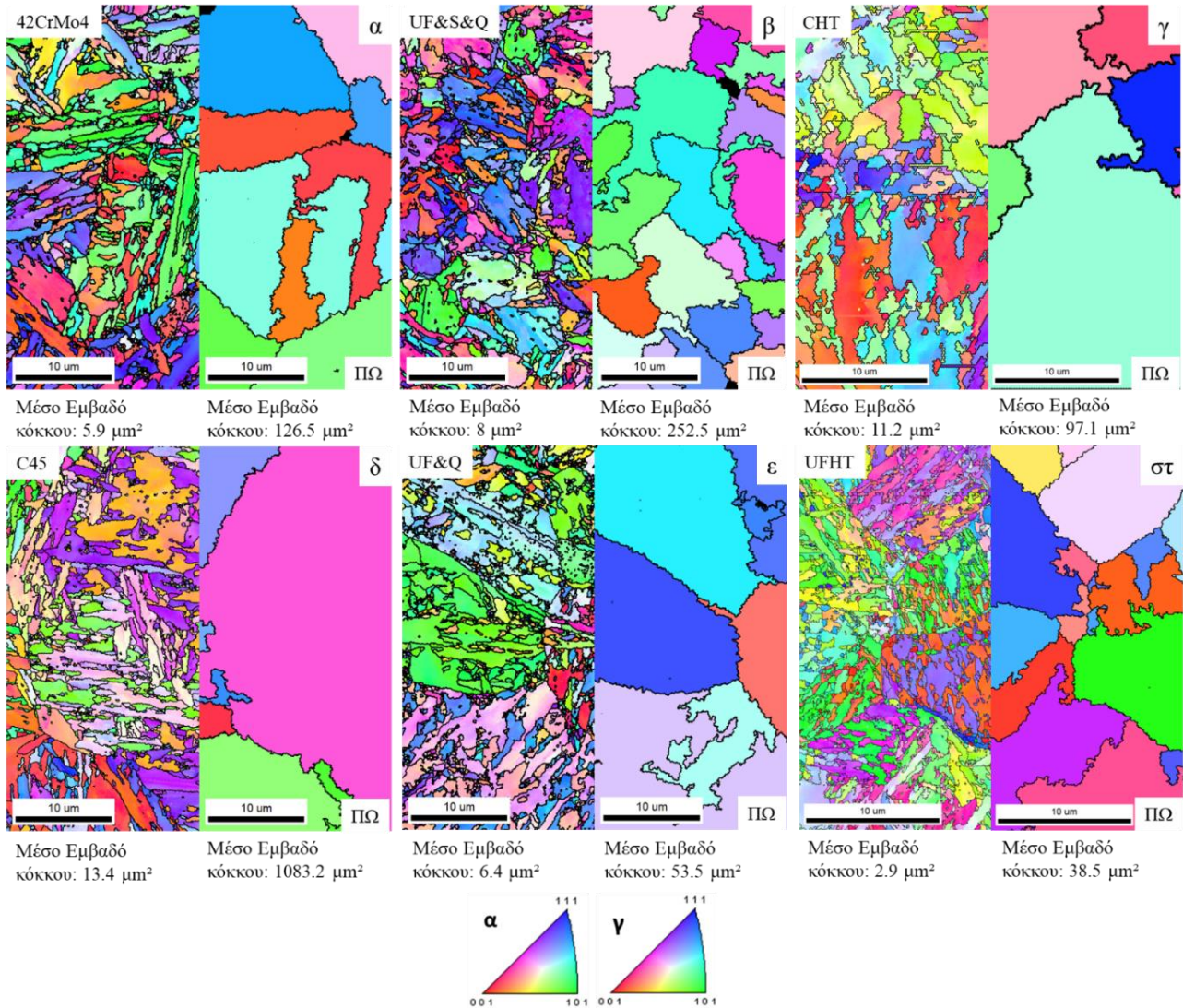
πως η μπεινιτική περιοχή για τη C45 (μπλε) σύσταση βρίσκεται πιο αριστερά στο διάγραμμα σε σχέση με τις άλλες δύο. Αυτό σημαίνει ότι μπορεί να σχηματιστεί μπεινίτης για γρηγορότερους ρυθμούς ψύξης, μέχρι 100 °C/s. Οι άλλες δύο συστάσεις έχουν μεγαλύτερη περιεκτικότητα σε Mn. Αυτό το στοιχείο θεωρείται γ-φερρογόνο και συνεπώς αναστέλλει τον μετασχηματισμό σε μπεινίτη. Για τον λόγο αυτό, οι μπεινιτικές περιοχές για τη σύσταση 42CrMn6 (κόκκινη) και 42CrMo4 (πράσινη) βρίσκονται πιο χαμηλά και πιο δεξιά στο διάγραμμα. Αυτό σημαίνει ότι για τον σχηματισμό του μπεινίτη απαιτούνται πιο αργοί ρυθμοί ψύξης. Για τον ίδιο λόγο μειώνονται και οι τιμές των θερμοκρασιών  $M_s$ .



**Εικόνα 3.5:** Διάγραμμα CCT που σχεδιάστηκε σύμφωνα με τα μοντέλα [14-16]. Σε αυτό έχουν σχεδιαστεί οι μπεινιτικές περιοχές για τις τρεις διαφορετικές συστάσεις και για συγκεκριμένο μέγεθος κόκκου πρότερου ωστενίτη. Με αντίστοιχα χρώματα έχουν προστεθεί και οι υπολογισμένες θερμοκρασίες  $M_s$  για την κάθε σύσταση.

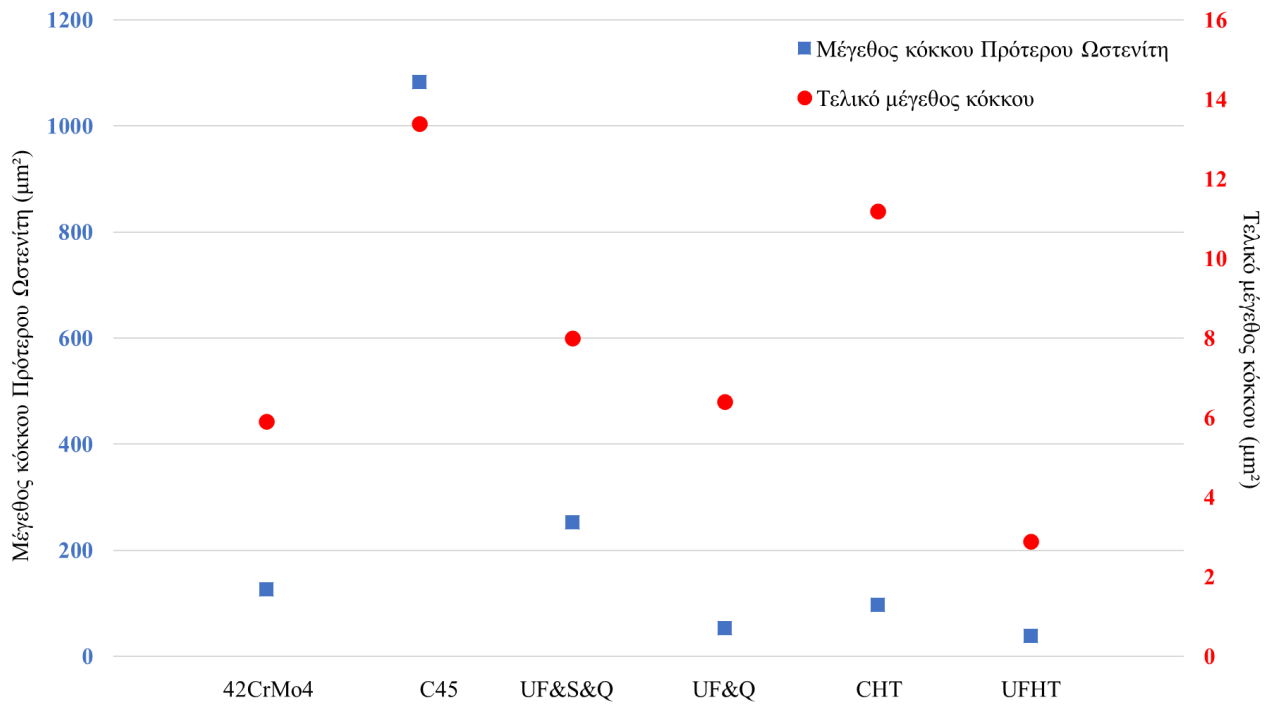
Τέλος, από την ανάλυση στο EBSD μελετήθηκε το μέγεθος των κόκκων της μικροδομής (**Εικόνα 3.6**) μετά τη βαφή (αριστερό μέρος κάθε εικόνας) αλλά και των κόκκων πρότερου ωστενίτη (δεξί μέρος κάθε εικόνας), όπως αυτοί κατασκευάστηκαν με τη χρήση του προγράμματος ARPGE [13]. Σε συνδυασμό με το διάγραμμα της **Εικόνας 3.7**, μπορεί να παρατηρηθεί ότι το μέγεθος του κόκκου του πρότερου ωστενίτη είναι μεγαλύτερο στα δοκίμια όπου υπάρχει αρκετός χρόνος θέρμανσης (UF&S&Q, CHT). Επίσης, στα δοκίμια στα οποία έχει γίνει πλήρης διαλυτοποίηση του σεμεντίτη (42CrMo4, C45), το μέγεθος του πρότερου ωστενίτη είναι μεγαλύτερο σε σχέση με τα δοκίμια στα οποία υπάρχει σφαιροποιημένος σεμεντίτης μετά τη θερμική κατεργασία (UF&S&Q, UF&Q, UFHT). Τέλος, το δοκίμιο C45 έχει μεγαλύτερο μέγεθος πρότερου ωστενίτη σε σχέση με το 42CrMo4, παρόλο που έχουν την ίδια αρχική μικροδομή και θερμική κατεργασία. Όπως είναι λογικό, σύμφωνα με τον μηχανισμό του μαρτενσιτικού μετασχηματισμού [17], όσο μικρότερο είναι το

μέγεθος του πρότερου ωστενίτη, τόσο μικρότερο αναμένεται το μέγεθος των βελονών μαρτενσίτη στην τελική μικροδομή μετά τη βαφή. Η πιο εκλεπτυσμένη μικροδομή συναντάται στο δοκίμιο UFHT, παρόμοια με το δοκίμιο UF&Q, η μόνη διαφορά των οποίων είναι η θερμοκρασία ανόπτησης. Όμως, η διαφορά στο τελικό μέγεθος κόκκου θεωρείται αμελητέα και εντός του στατιστικού σφάλματος, που μπορεί να προκύψει από την ανάλυση στο EBSD.



**Εικόνα 3.6:** Χάρτες IPF όπου φαίνεται ο προσανατολισμός του πλέγματος σε κάθε κόκκο. Στο αριστερό μέρος κάθε εικόνας φαίνεται η τελική μικροδομή των δοκιμίων ενώ στο δεξιό μέρος φαίνονται οι κόκκοι του πρότερου ωστενίτη, όπως αυτοί προσομοιώθηκαν με τη χρήση του προγράμματος ARPGE [13]. Κάτω από κάθε εικόνα αναγράφεται το μέσο εμβαδόν των κόκκων, όπως αυτό υπολογίστηκε από το λογισμικό του EBSD. Step size: 70 nm.





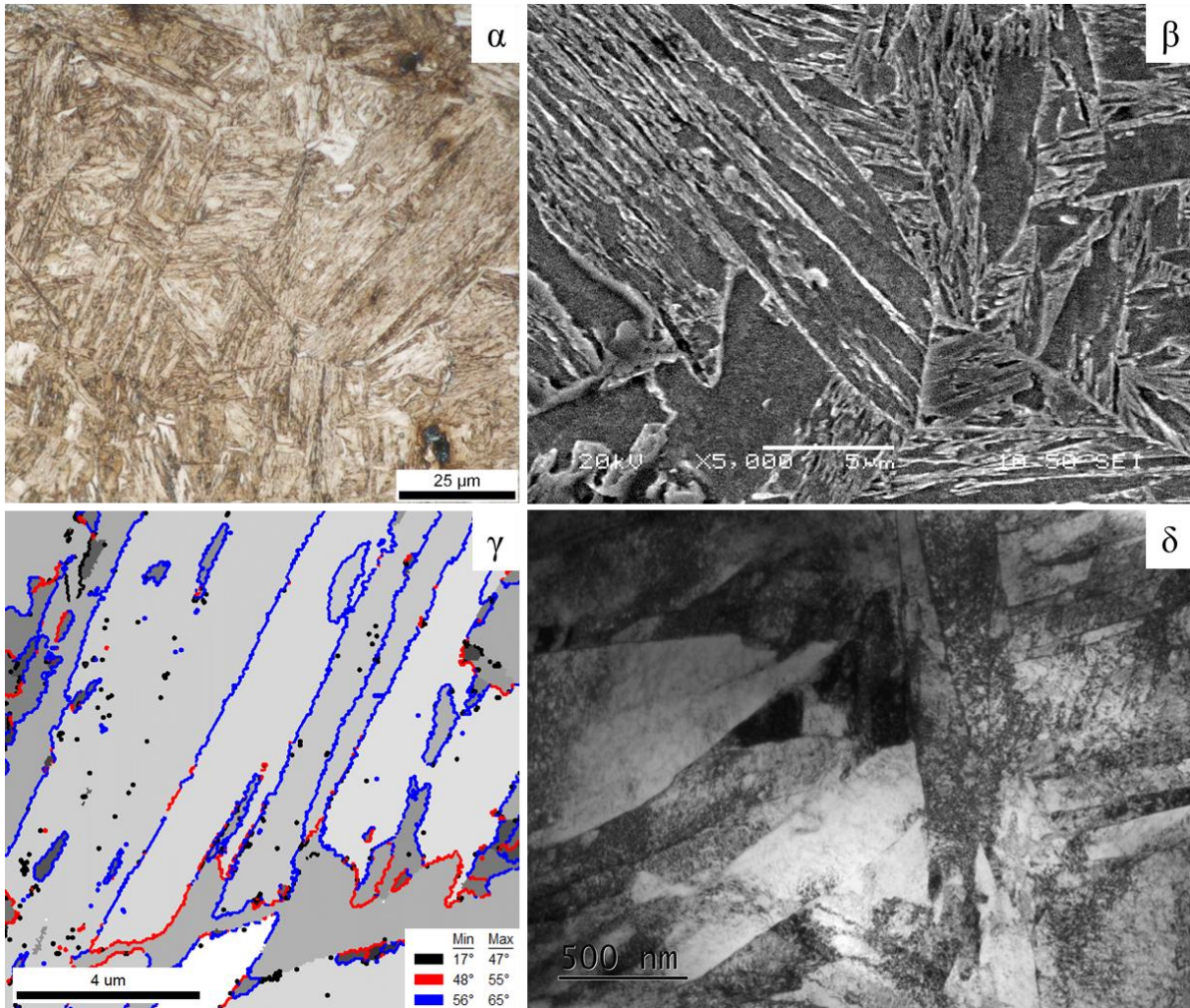
**Εικόνα 3.7:** Διάγραμμα με το υπολογισμένο μέγεθος κόκκου σε εμβαδόν για το κάθε δοκίμιο. Στον αριστερό άξονα (μπλε) αντιστοιχούν οι μετρήσεις για το εμβαδόν των κόκκων του πρότερου ωστενίτη, ενώ στον δεξιό άξονα (κόκκινο) αντιστοιχούν οι μετρήσεις για το εμβαδόν των κόκκων της τελικής μικροδομής, μετά τη βαφή.

### 3.4.2. Ο σχηματισμός μπαινίτη και υπολειπόμενου ωστενίτη κατά την εφαρμογή τάχιστων θερμικών κύκλων σε σωλήνες χωρίς ραφή (σε πιλοτικό επαγωγικό φούρνο ραγδαίας αναθέρμανσης)

Η συγκεκριμένη προσέγγιση είχε ως σκοπό τη μελέτη των τάχιστων θερμικών κατεργασιών σε σωλήνες μεγάλου μεγέθους, αντίστοιχου με αυτό που χρησιμοποιείται στη βιομηχανία. Από την προηγούμενη προσέγγιση βρέθηκαν ενδείξεις για την ύπαρξη μπαινίτη και υπολειπόμενου ωστενίτη στη μικροδομή. Σε αυτόν τον κύκλο ήταν δυνατή η απόδειξη της ύπαρξής τους μέσω της χρήσης του TEM.

Πρώτον, όπως φαίνεται από τις **Εικόνες 3.8α, β**, από το οπτικό μικροσκόπιο και το SEM αντίστοιχα, η μικροδομή του δοκιμίου που μελετήθηκε είναι κυρίως μαρτενσιτική. Βελόνες μαρτενσίτη παρατηρούνται με διαφορετικά πάχη και μήκη, ανάλογα με το πότε σχηματίστηκαν [18]. Όπως αναφέρθηκε και παραπάνω, καθώς ο μαρτενσιτικός μετασχηματισμός συμβαίνει ακαριαία και είναι διατμησιακός, οι γωνιακές αποκλίσεις αναμένονται υψηλές. Αυτό επιβεβαιώνεται από το EBSD (**Εικόνα 3.8γ**), όπου με μπλε χρώμα φαίνονται οι αποκλίσεις μεταξύ 58° και 65°. Σύμφωνα με τη βιβλιογραφία [12] αυτές οι γωνίες αντιστοιχούν σε βελόνες μαρτενσίτη, ενώ χαμηλότερες αποκλίσεις αντιστοιχούν σε μπαινίτη και φερρίτη. Επίσης, μαρτενσιτικές βελόνες παρατηρήθηκαν και στο TEM (**Εικόνα 3.8δ**). Βασικό τους χαρακτηριστικό είναι η εντόνως παραμορφωμένη τους δομή, με υψηλά ποσοστά ελαστικής παραμόρφωσης λόγω στρέβλωσης του κρυσταλλικού πλέγματος. Αυτή η έντονη παραμόρφωση παρατηρείται με σκούρο χρώμα από το TEM, καθώς εμποδίζεται η περίθλαση των ηλεκτρονίων. Επίσης, καθώς η αρχική μικροδομή αποτελείται από φερρίτη και

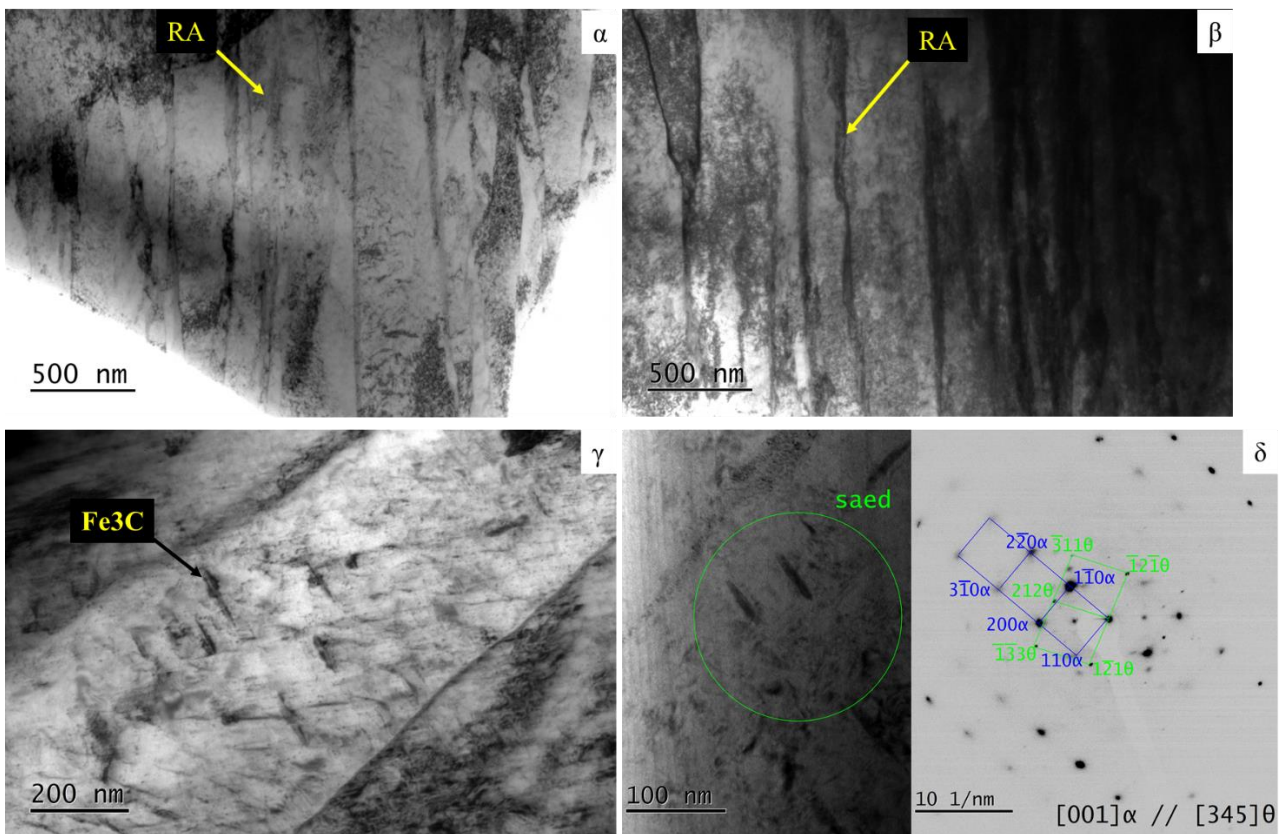
περλίτη, όπως φάνηκε προηγουμένως στο δοκίμιο 42CrMo4, έχει επιτευχθεί πλήρης διαλυτοποίησή του και συνεπώς δεν συναντάται στη μικροδομή.



**Εικόνα 3.8:** (α) Μεταλλογραφία στο OM όπου φαίνεται πως η δομή είναι κυρίως μαρτενσιτική, (β) οι βελόνες του μαρτενσίτη παρατηρήθηκαν και στο SEM, (γ) οι βελόνες του μαρτενσίτη στο EBSD χαρακτηρίζονται από μικρό IQ και μεγάλες γωνιακές αποκλίσεις. Step size: 15 nm. (δ) στο TEM, οι βελόνες του μαρτενσίτη διακρίνονται από το σχήμα, το μέγεθος και το μεγάλο ποσοστό διαταραχής.

Οι μαρτενσιτικές βελόνες μπορούν να διαχωριστούν από τα πλακίδια του μπαινίτη με διάφορους τρόπους. Ο μπαινίτης, λόγω της υψηλότερης θερμοκρασίας στην οποία σχηματίζεται, αποκτά πλακοειδή μορφή και μεγαλύτερο πλάτος από τις βελόνες του μαρτενσίτη. Επίσης, για τον ίδιο λόγο, και επειδή επιτυγχάνεται διάχυση του άνθρακα, τα πλακίδιά του είναι λιγότερο παραμορφωμένα. Όσον αφορά στη διάχυση του άνθρακα, αυτή επιτυγχάνεται, κυρίως, κοντά στα όρια των πλακιδίων του κατώτερου μπαινίτη. Λόγω της χαμηλής διαλυτότητας του άνθρακα στην κρυσταλλική δομή του μπαινιτικού φερρίτη, ο άνθρακας αποβάλλεται μέσω διάχυσης από τα πλακίδια και συγκεντρώνεται στα όρια μεταξύ των πλακιδίων. Η υψηλότερη περιεκτικότητα του άνθρακα σε αυτά τα σημεία μπορεί να οδηγήσει στη σταθεροποίηση του οστενίτη με αποτέλεσμα αυτός να υπολείπεται. Σε περιπτώσεις όπου η περιεκτικότητα του άνθρακα στο υλικό είναι υψηλότερη, είναι δυνατός και ο σχηματισμός σεμενίτη στις διεπιφάνειες μεταξύ των πλακιδίων [19].

Τέτοιες μορφολογίες παρατηρούνται στο υλικό, στις **Εικόνες 3.9α, β**. Συγκεκριμένα, παρατηρήθηκαν ευμεγέθη πλακίδια, παράλληλα μεταξύ τους μεταξύ των οποίων βρίσκονται λεπτά υμένια -φίλμ υπολειπόμενου ωστενίτη, όπως θα αναλυθεί παρακάτω. Επιπλέον, λόγω του ότι δεν υπάρχει χρόνος για τη διάχυση του άνθρακα σε μεγάλες αποστάσεις, αυτός 'εγκλωβίζεται' εντός του πλακιδίου του μπαινίτη. Ωστόσο, πάλι λόγω της χαμηλής διαλυτότητας του άνθρακα στη BCC δομή, αυτός κατακρημνίζεται υπό τη μορφή παράλληλων σωματιδίων σεμεντίτη. Τέτοιες μικροδομές παρατηρήθηκαν επίσης στο υλικό, όπως φαίνεται στις **Εικόνες 3.9γ,δ**. Στην **Εικόνα 3.9δ** έχει προστεθεί και το διάγραμμα περίθλασης ηλεκτρονίων της επιλεγμένης περιοχής (selected area electron diffraction - saed), στο οποίο διαχωρίζεται ο φερρίτης (μπλε) από τον σεμεντίτη (πράσινο).

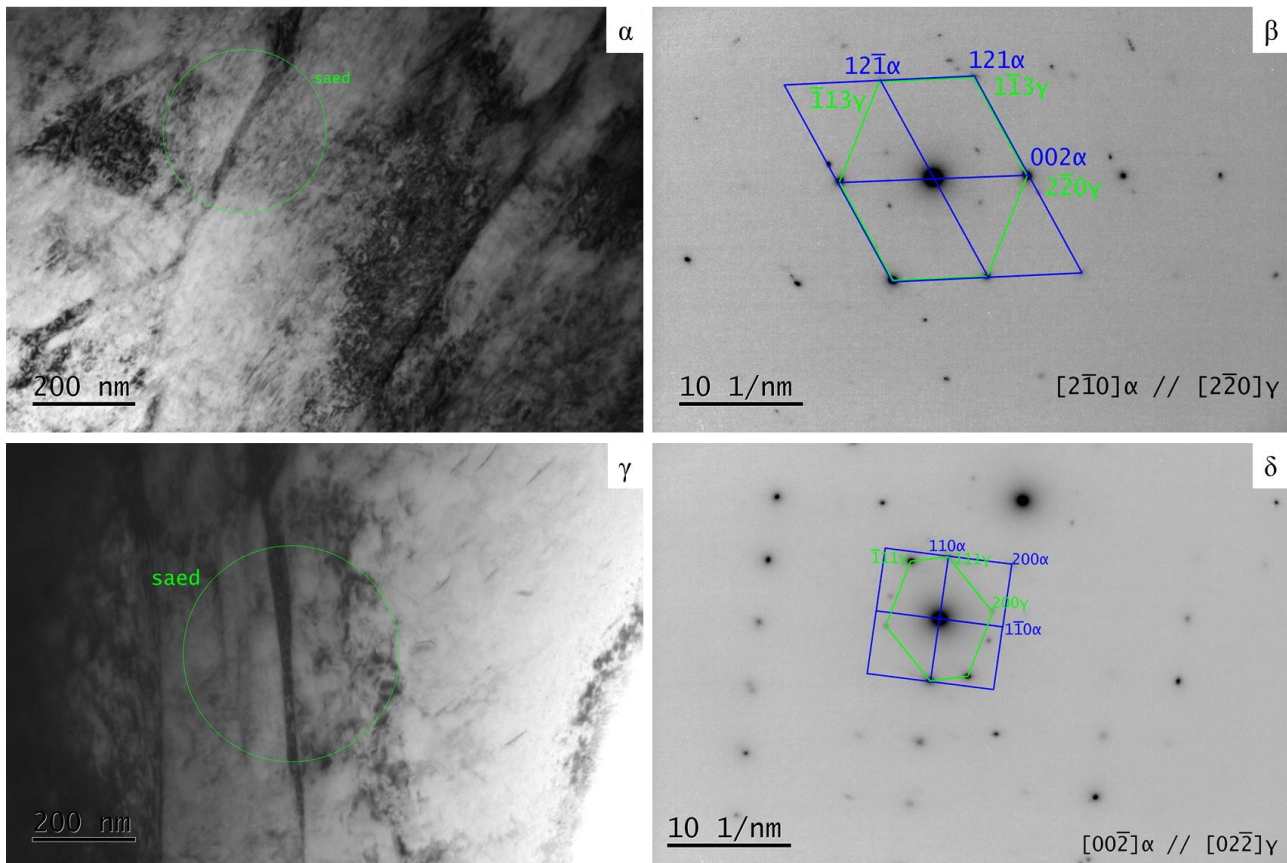


**Εικόνα 3.9:** Εικόνες TEM που δείχνουν την ύπαρξη μπαινίτη στη μικροδομή. Ο μπαινίτης διακρίνεται από το μεγαλύτερο πάχος πλακιδίου, την παραλληλία των πλακιδίων και την ύπαρξη υπολειπόμενου ωστενίτη στο ενδιάμεσό τους, όπως επίσης και από την ύπαρξη παράλληλων σωματιδίων σεμεντίτη στο εσωτερικό των πλακιδίων. Η επιβεβαίωση για την ύπαρξη του σεμεντίτη έγινε με την ανάλυση του διαγράμματος περίθλασης ηλεκτρονίων που φαίνεται στην εικόνα (δ).

Όπως αναφέρθηκε, ο ωστενίτης μπορεί να υπολείπεται μεταξύ των πλακιδίων του μπαινίτη λόγω της διάχυσης του άνθρακα στην περιοχή μεταξύ των πλακιδίων. Στον μπαινίτη, τα πλακίδια σχηματίζονται σχεδόν ταυτόχρονα το ένα δίπλα στο άλλο και με την πάροδο του χρόνου επιμηκύνονται. Αντίθετα, στον μαρτενσιτικό μετασχηματισμό δεν συμβαίνει κάτι ανάλογο. Σε αυτή την περίπτωση, θα σχηματιστούν οι πρώτες βελόνες μαρτενσίτη ακαριαία κατά τη διάμετρο του κόκκου του πρότερου ωστενίτη και εν συνεχεία θα σχηματίζονται οι επόμενες βελόνες, ώστε να καλυφθεί ο όγκος όλου του κόκκου. Καθώς όμως σχηματίζονται ολοένα και περισσότερες βελόνες εντός του κόκκου, ο ωστενίτης που δεν έχει μετασχηματιστεί ακόμα σε μαρτενσίτη,



εμπλουτίζεται σε άνθρακα, καθώς αυτός πρέπει να κατανομηθεί σε μικρότερο όγκο. Αυτό έχει ως συνέπεια, σε κάποιο σημείο ο ωστενίτης που δεν έχει μετασχηματιστεί να είναι τόσο εμπλουτισμένος σε άνθρακα, ώστε να μπορεί να υπολείπεται, καθώς μεγαλύτερη περιεκτικότητα σε άνθρακα μειώνει τις θερμοκρασίες μετασχηματισμού του μαρτενσίτη. Συνεπώς, υπολειπόμενος ωστενίτης μπορεί να παρατηρηθεί σε μπαινιτικές και μαρτενσιτικές περιοχές του δοκιμίου, όπως φαίνεται στις **Εικόνες 3.10α, β**, όπου συναντάται σε μορφή φιλμ. Στις εικόνες από το TEM έχουν προστεθεί και τα διαγράμματα περίθλασης ηλεκτρονίων των επιλεγμένων περιοχών (saed) για τον διαχωρισμό του ωστενίτη (πράσινο) από τον φερρίτη (μπλέ).



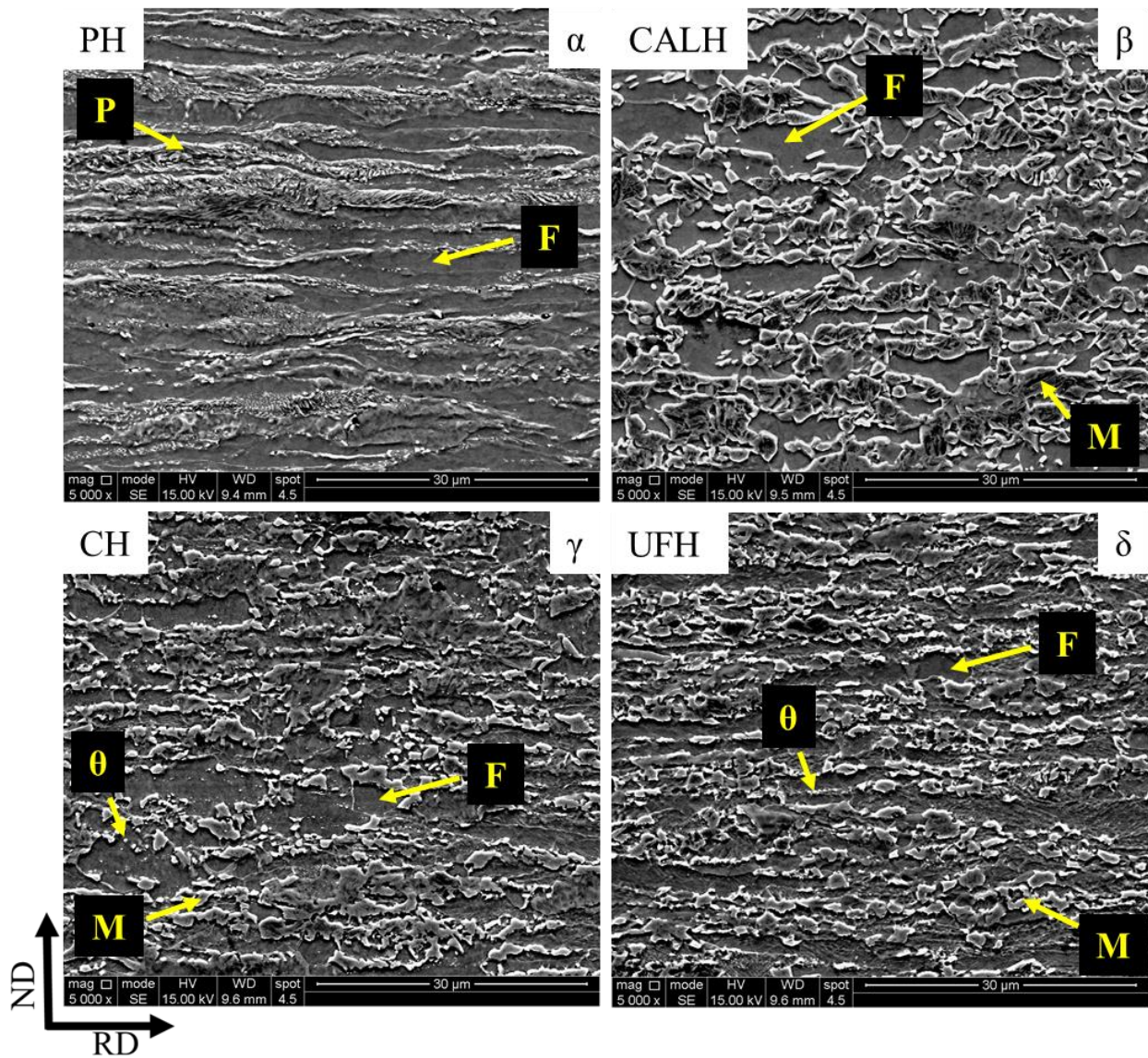
**Εικόνα 3.10:** (α,γ) Εικόνες TEM όπου φαίνεται υπολειπόμενος ωστενίτης στα όρια των βελονών/πλακιδίων. Τα διαγράμματα περίθλασης έχουν προστεθεί (β,δ) για την εξακρίβωση της ύπαρξης του ωστενίτη (πράσινο).

### 3.4.3. Η εφαρμογή τάχιστων θερμικών κύκλων σε συμβατικό τύπο χάλυβα της αυτοκινητοβιομηχανίας εργαστηριακά σε θερμομηχανικό προσομοιωτή Gleeble

Μέχρι στιγμής, μελετήθηκε η επίδραση των παραμέτρων της θερμικής κατεργασίας, της χημικής σύστασης του υλικού και της αρχικής μικροδομής και αποδείχθηκε ότι η τελική μικροδομή μπορεί να αποτελείται από μαρτενσίτη, μπαινίτη, υπολειπόμενο ωστενίτη και, αναλόγως με το υλικό, σφαιροποιημένο σεμεντίτη. Στη συνέχεια, σκοπός είναι να μελετηθεί η εφαρμογή αυτής της μεθόδου σε ένα συμβατικό τύπο χάλυβα για την παραγωγή.

Όπως παρατηρήθηκε από το SEM, το στάδιο της προθέρμανσης (PH) δεν έχει επίδραση στη μικροδομή του υλικού καθώς αυτή είναι παρόμοια με την αρχική μικροδομή (IM) και αποτελείται από φερρίτη (F) και περλίτη

(P), ενώ παραμένει ορατή η επίδραση της έλασης (**Εικόνα 3.11α**). Συγκεκριμένα, είναι ορατές οι ζώνες της έλασης, η παραμόρφωση του φερρίτη και η τύπου ‘pancake’ δομή [20]. Όσον αφορά στο δοκίμιο αναφοράς (CALH), του οποίου η θερμική κατεργασία έχει σκοπό να προσομοιώσει τις κατεργασίες που υποβάλλονται σήμερα στην παραγωγή αντίστοιχων διαφασικών χαλύβων, η μικροδομή είναι τυπική διαφασικού χάλυβα, η οποία αποτελείται από τη μήτρα φερρίτη και νησίδες μαρτενσίτη (M) (**Εικόνα 3.11β**). Για το δοκίμιο CH (**Εικόνα 3.11γ**), του οποίου η θερμική διαφέρει από αυτή του CALH στο ότι λείπει το στάδιο παραμονής στη θερμοκρασία ανόπτησης, η μικροδομή διαφέρει αρκετά. Συγκεκριμένα, ο περλίτης της αρχικής μικροδομής φαίνεται να μην έχει διαλυτοποιηθεί πλήρως καθώς εμφανίζεται σεμεντίτης ( $\theta$ ) σε σφαιροποιημένη, αλλά και πλακοειδή μορφή. Επίσης, παρατηρούνται ακόμα παραμορφωμένοι και επιμηκυσμένοι κόκοι φερρίτη από την ψυχρή έλαση. Τέλος, οι νησίδες του μαρτενσίτη φαίνονται μικρότερες σε αυτό το δοκίμιο. Αντίστοιχα, στο UFH δοκίμιο, όπου ο ρυθμός θέρμανσης είναι πολύ υψηλότερος, το ποσοστό του αδιάλυτου σεμεντίτη φαίνεται να είναι μεγαλύτερο, ενώ οι νησίδες μαρτενσίτη είναι ακόμα πιο εκλεπτυσμένες. Η δομή μοιάζει αρκετά με αυτή του PH δοκιμίου, με τις ζώνες της ψυχρής έλασης να έχουν παραμείνει και ο φερρίτης να παραμένει επιμηκυσμένος και παραμορφωμένος (**Εικόνα 3.11δ**).

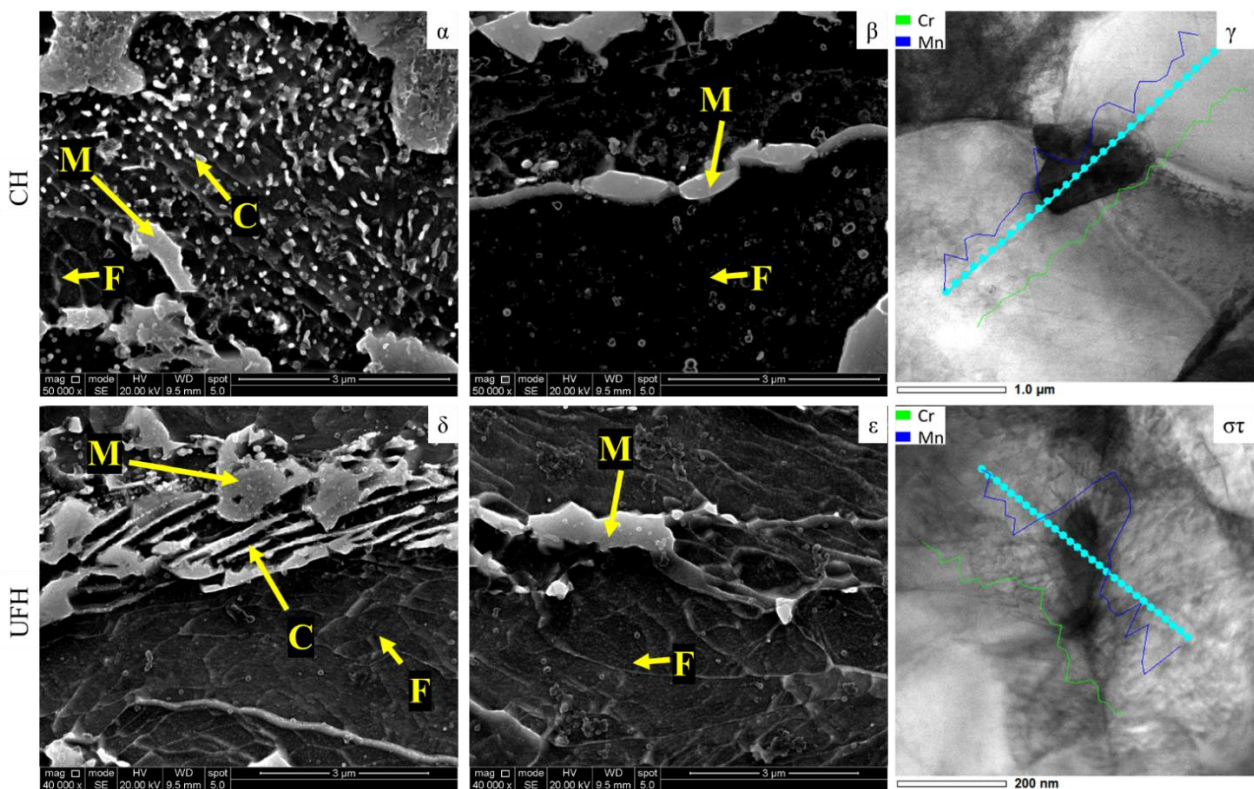


**Εικόνα 3.11:** (α) η μικροδομή του δοκιμίου όπου έχει εφαρμοστεί μόνο το στάδιο της προθέρμανσης. Η μικροδομή αποτελείται από φερρίτη (F) και περλίτη (P) και είναι παρόμοια με αυτή της νυχρώς ελασμένης αρχικής μικροδομής. (β) το δοκίμιο αναφοράς CALH έχει την τυπική μικροδομή διφασικού χάλυβα που αποτελείται από φερρίτη και μαρτενσίτη (M), (γ) στο δοκίμιο CH η μικροδομή είναι παρόμοια με του CALH, με τη διαφορά ότι τα νησίδα μαρτενσίτη είναι πιο εκλεπτυσμένα και υπάρχει αδιάλυτος σεμεντίτης (θ), (δ) για το UFH δοκίμιο, η μικροδομή μοιάζει πιο πολύ με την αρχική παρά με του CALH και αποτελείται από εκλεπτυσμένο φερρίτη, μαρτενσίτη και αδιάλυτο σεμεντίτη.

Με πιο προσεκτική ανάλυση στο SEM (**Εικόνα 3.12**) φαίνεται ότι και στα δυο δοκίμια η ωστενιτοποίηση ξεκινάει όχι μόνο στις διεπιφάνειες φερρίτη/σεμεντίτη (**Εικόνες 3.12α, δ**) αλλά και στις διεπιφάνειες φερρίτη/φερρίτη (**Εικόνες 3.12β, ε**), δηλαδή μεταξύ δύο ή τριών κόκκων φερρίτη (F), χωρίς την ύπαρξη σεμεντίτη στη γύρω περιοχή. Σημειώνεται ότι δεν παρατηρείται ο ίδιος ο ωστενίτης, αλλά ο μαρτενσίτης (M) που είναι προϊόν της βαφής του ωστενίτη. Η φύτρωση του ωστενίτη στις διεπιφάνειες α/θ αναμένεται θερμοδυναμικά καθώς υπάρχει διαφορά στην ενέργεια Gibbs των δύο αυτών φάσεων, και η οποία οφείλεται στη διαφορετική περιεκτικότητα σε άνθρακα [21]. Κάτι τέτοιο όμως δεν συμβαίνει στην περίπτωση της φύτρωσης μεταξύ δύο κόκκων φερρίτη, καθώς έχουν την ίδια μέγιστη διαλυτότητα σε άνθρακα. Σε αυτή την

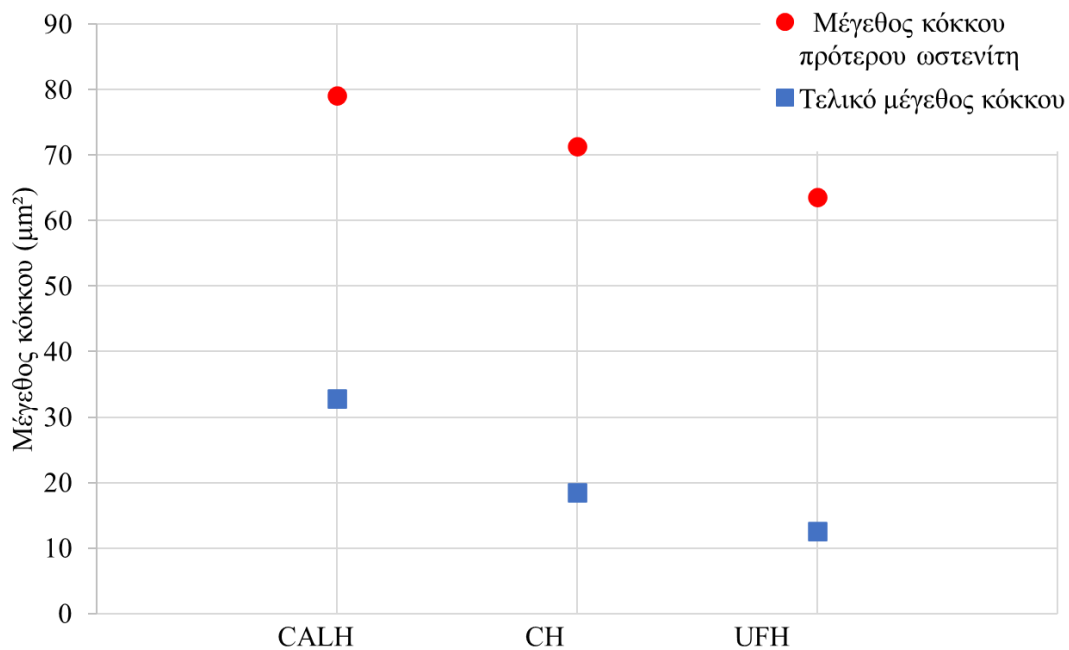


περίπτωση, η κινητήριος δύναμη οφείλεται στον διαφορισμό του άνθρακα και άλλων στοιχείων στα όρια των κόκκων φερρίτη, καθώς μέσω αυτών γίνεται πιο γρήγορα η διάχυση [22]. Συνεπώς, από αυτή τη διαφορά περιεκτικότητας σε άνθρακα μεταξύ των δύο κόκκων φερρίτη και του ορίου μεταξύ τους προκύπτει η απαραίτητη διαφορά στην ενέργεια Gibbs που καθιστά δυνατή θερμοδυναμικά τη φύτρωση του ωστενίτη σε αυτές τις θέσεις [21]. Αυτό παρατηρήθηκε από τη χημική ανάλυση EDS στο STEM. Για αργούς ρυθμούς θέρμανσης (**Εικόνα 3.12γ**) επιτυγχάνεται ομογενοποίηση της χημικής σύστασης μεταξύ των δύο κόκκων φερρίτη και του μαρτενσίτη, ενώ στο UFH δοκίμιο (**Εικόνα 3.12στ**) υπάρχει διαφορά στο ποσοστό του χρωμίου και του μαγγανίου μεταξύ του μαρτενσίτη και των κόκκων φερρίτη λόγω έλλειψης χρόνου για τη διάχυσή τους και τον εμπλουτισμό του φερρίτη σε αυτά τα στοιχεία.



**Εικόνα 3.12:** Εικόνες SEM όπου φαίνεται ότι η πυρήνωση του ωστενίτη και συνεπώς ο σχηματισμός του μαρτενσίτη (M) γίνεται (α,δ) στις διεπιφάνειες α/θ και (β,ε) στις διεπιφάνειες α/α. (γ,στ) Εικόνες STEM με γραμμική χημική ανάλυση EDS όπου φαίνεται η συγκέντρωση του Cr και Mn στις διεπιφάνειες α/α.

Επίσης, έγινε ανάλυση του μεγέθους κόκκου στο EBSD όπως και ανάλυση του μεγέθους κόκκου του πρότερου ωστενίτη με τη βοήθεια του προγράμματος ARPGE [13]. Καθώς η μικροδομή είναι διαφασική, θα πρέπει να σημειωθεί ότι οι τιμές που αναγράφονται στο διάγραμμα της **Εικόνας 3.13** αφορούν στο τελικό μέγεθος του μαρτενσίτη μαζί με τον φερρίτη (μπλε) όπως και στο μέγεθος του πρότερου ωστενίτη μαζί με τον φερρίτη (κόκκινο). Όπως παρατηρείται, και όπως είναι λογικό, όσο μειώνεται ο χρόνος θέρμανσης και ανόπτησης, μειώνεται και το μέγεθος των κόκκων του πρότερου ωστενίτη. Εκλέπτυνση των κόκκων του πρότερου ωστενίτη οδηγεί και σε εκλέπτυνση των μαρτενσιτικών νησίδων, όπως επιβεβαιώνεται και από το διάγραμμα.



**Εικόνα 3.13:** Διάγραμμα με το εμβαδόν των κόκκων της τελικής μικροδομής (μπλε) και των κόκκων πρότερου ωστενίτη (κόκκινο) [13] όπου παρατηρείται μείωση όσο μειώνεται ο χρόνος θέρμανσης. Σε αυτές τις μετρήσεις συμπεριλαμβάνεται και το εμβαδόν των κόκκων φερρίτη.

Όπως φάνηκε από τις μικροδομές των διαφόρων δοκιμίων, ο φερρίτης εμφανίζεται είτε παραμορφωμένος ή όχι. Αυτό μπορεί να παρατηρηθεί καλύτερα στην **Εικόνα 3.14α** για το CH δοκίμιο και στην **Εικόνα 3.14β** για το UFH δοκίμιο. Όπως φαίνεται, κάποιοι κόκκοι φερρίτη φαίνονται αρκετά παραμορφωμένοι, με μεγάλη πυκνότητα διαταραχών και κυρίως στο UFH δοκίμιο, ενώ άλλοι κόκκοι φαίνονται καθαροί από διαταραχές. Κατά τη θέρμανση, λαμβάνει χώρα η διαδικασία της ανακρυστάλλωσης. Σύμφωνα με αυτή, οι διαταραχές μετατρέπονται σε υπο-όρια (SGB) τα οποία μετακινούνται και δημιουργούν νέους κόκκους φερρίτη. Η κινητήριος δύναμη σε αυτή τη διεργασία είναι η μείωση της εσωτερικής ενέργειας με τη δημιουργία νέων, μικρότερων κόκκων φερρίτη καθαρών από διαταραχές. Αυτός ο φερρίτης ονομάζεται ανακρυσταλλωμένος φερρίτης (RexF). Όπως φαίνεται και από τους Kernel Average Misorientation (KAM) χάρτες στο EBSD (**Εικόνες 3.14γ, δ**), η πυκνότητα των διαταραχών στο UFH υλικό είναι αρκετά μεγαλύτερη. Επίσης, τα υπο-όρια που έχουν σχηματιστεί διατηρούν τη φορά της έλασης, ενώ οι υπο-κόκκοι στο CH υλικό είναι πιο ισαξονικοί. Οι κόκκινες γραμμές υποδεικνύουν τα LAGB. Όπως φαίνεται και στην **Εικόνα 3.14ε**, για το CH δοκίμιο, μέσω της μεθόδου t-EBSD, ο σχηματισμός των LAGB προκύπτει από τη συσσώρευση διαταραχών. Σύμφωνα με τις ρυθμίσεις του EBSD, γωνιακές αποκλίσεις μεταξύ  $2 - 5^\circ$  αντιστοιχούν σε διαταραχές, ενώ γωνίες μεταξύ  $5 - 15^\circ$  σε LAGB. Τέλος, οι γωνίες μεταξύ  $15 - 65^\circ$  αντιστοιχούν σε HAGB, δηλαδή σε όρια κόκκου. Σύμφωνα με αυτά, όπως φαίνεται στην εικόνα αυτή, τα LAGB προκύπτουν από την ευθυγράμμιση των διαταραχών και τη μεταβολή της γωνιακής τους απόκλισης πάνω από  $5^\circ$ . Εν συνεχεία, αυτή η απόκλιση θα αυξηθεί και θα επέλθει ο σχηματισμός των νέων ορίων κόκκου. Αυτό το φαινόμενο της ευθυγράμμισης των διαταραχών που οδηγεί σε γωνιακές αποκλίσεις ονομάζεται ‘πολυγωνισμός’ [23] και προκαλεί μεταβολές στον προσανατολισμό της κρυσταλλικής κυψελίδας μέσα στον ίδιο κόκκο. Αυτό φαίνεται στον IPF χάρτη της

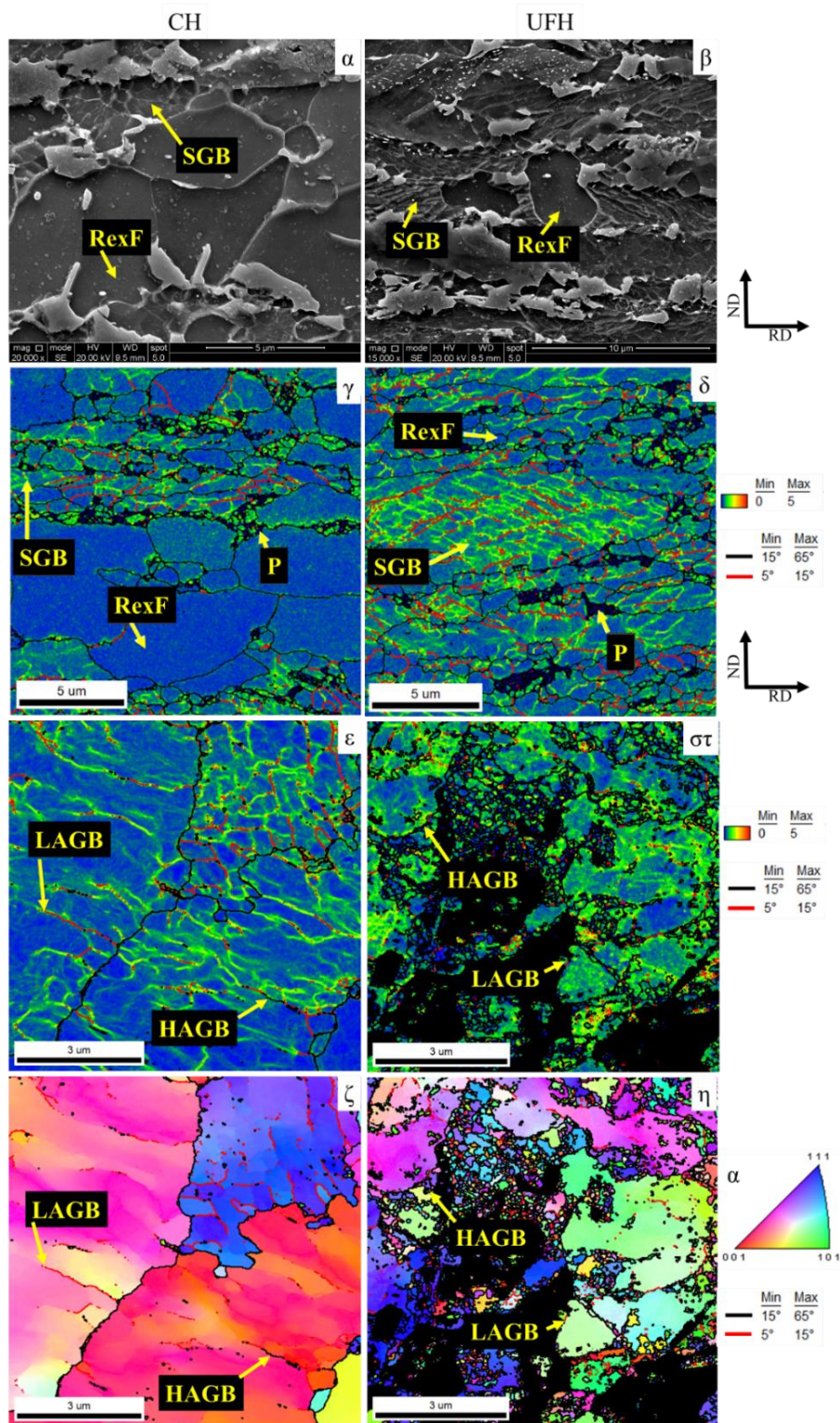
**Εικόνας 3.14ζ** από τις εναλλαγές των χρωμάτων εντός των δύο κόκκων φερρίτη. Σε αρκετά σημεία αυτό το στάδιο της ανακρυστάλλωσης δεν παρατηρήθηκε. Όπως φαίνεται στις **Εικόνες 3.14στ,η** οι διαταραχές είναι ακανόνιστες και δεν έχει επέλθει κάποια ευθυγράμμιση ή σχηματισμός Low Angle Grain Boundaries (LAGB).

Από την ανάλυση στο EBSD προέκυψαν επίσης τα ποσοστά του ανακρυσταλλωμένου και του παραμορφωμένου φερρίτη για κάθε δοκίμιο. Από αυτά τα ποσοστά προέκυψε επίσης και το ποσοστό του μαρτενσίτη. Αυτά τα ποσοστά αναγράφονται στον **Πίνακα 3.6**. Όπως έχει αναφερθεί [24,25], οι γρήγοροι ρυθμοί θέρμανσης επιδρούν στις θερμοκρασίες μετασχηματισμού  $A_1$  και  $A_3$  και συγκεκριμένα τις μετατοπίζουν σε υψηλότερες τιμές. Συνεπώς, παρόλο που η θερμοκρασία απόπτωσης ήταν η ίδια για όλα τα δοκίμια, το δοκίμιο CALH έχει περίπου το διπλάσιο ποσοστό μαρτενσίτη από τα άλλα δύο. Όμως, το υψηλότερο ποσοστό του μαρτενσίτη στο UFH δοκίμιο σε σχέση με το CH δεν συνάδει με αυτή τη θεωρία. Αυτό οφείλεται στο μεγάλο ποσοστό του παραμορφωμένου φερρίτη στο συγκεκριμένο δοκίμιο, καθώς η μεγαλύτερη πυκνότητα διαταραχών ευνοεί τη διάχυση κραματικών στοιχείων και τη φύτρωση του ωστενίτη, κάτι το οποίο δεν μπορεί να γίνει εύκολα στον ανακρυσταλλωμένο φερρίτη.

**Πίνακας 3.6:** Κλάσματα όγκου του ανακρυσταλλωμένου και παραμορφωμένου φερρίτη και του μαρτενσίτη/σεμεντίτη για τα τρία δοκίμια που μελετήθηκαν

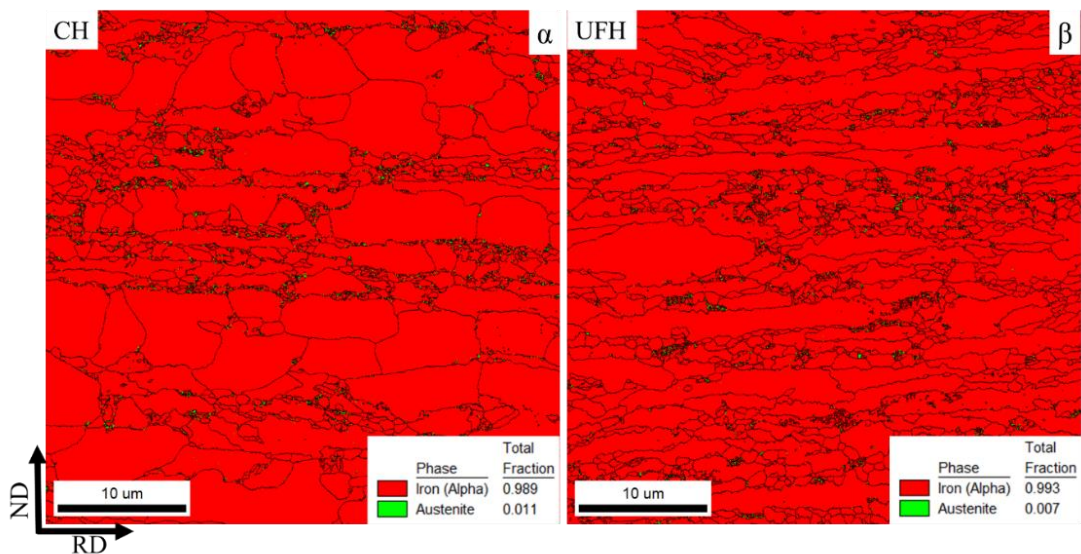
Κλάσμα όγκου %	CALH	CH	UFH
Ανακρυσταλλωμένος φερρίτης	56 %	77 %	24 %
Μη-ανακρυσταλλωμένος φερρίτης	0 %	9 %	55 %
Μαρτενσίτης/σεμεντίτης	44 %	14 %	21 %





**Εικόνα 3.14:** (α,β) Εικόνες SE SEM στις οποίες φαίνονται ανακρυσταλλωμένοι κόκκοι φερρίτη (RexF) και παραμορφωμένοι κόκκοι φερρίτη με υπο-όρια (SGB) και στα δύο δοκίμια. (γ,δ) χάρτης KAM 2<sup>nd</sup> neighbor όπου φαίνεται το αποτέλεσμα των διαταραχών στη μικροδομή και ο σχηματισμός υπο-ορίων. Με σκούρο μπλε φαίνονται οι αδιάλυτες περλιτικές περιοχές (P). Step size: 50 nm. (ε,στ) t-EBSD 2<sup>nd</sup> neighbor KAM χάρτες όπου πάλι φαίνεται ο σχηματισμός ορίων LAGB (κόκκινο) και HAGB (μαύρο) κατά την ανακρυστάλλωση. Step size: 50 nm. (ζ,η) κατά τη μετακίνηση των διαταραχών δημιουργούνται γωνιακές αποκλίσεις και διαφορές στον προσανατολισμό εντός του κόκκου, όπως φαίνεται στον IPF χάρτη. Step size: 20 nm.

Τέλος, η ανάλυση στο EBSD (**Εικόνα 3.15α, β**) έδειξε πολύ μικρά ποσοστά υπολειπόμενου ωστενίτη και στα δύο δοκίμια, αντίστοιχα με τα δοκίμια του 2<sup>ου</sup> κύκλου πειραμάτων, γύρω στο 1 %.



**Εικόνα 3.15:** Χάρτες EBSD με τις φάσεις του φερρίτη (κόκκινο) και του ωστενίτη (πράσινο). Και στα δύο δοκίμια, το ποσοστό του υπολειπόμενου ωστενίτη ήταν πολύ μικρό. Step size: 50 nm.

Επίσης, στα δοκίμια CH και UFH έγιναν δοκιμές εφελκυσμού σε μικρά δοκίμια τύπου dog-bone με διαστάσεις 48 x 12.5 mm. Οι τιμές της συνολικής επιμήκυνσης πρέπει να αντιμετωπίζονται με προσοχή, καθώς τυχόν εγκλείσματα μπορεί να επηρεάσουν σημαντικά το αποτέλεσμα. Για καλύτερα αποτελέσματα και για να μελετηθεί η ανισοτροπία του υλικού, τα δοκίμια του εφελκυσμού κόπηκαν υπό γωνίες 0, 45 και 90° σε σχέση με τη φορά της έλασης. Τα αποτελέσματα αναγράφονται στον **Πίνακα 3.7**. Όπως φαίνεται, τα δοκίμια UFH έχουν μεγαλύτερη UTS από τα CH δοκίμια κατά 150 – 250 MPa ενώ η ολική επιμήκυνση (TE) παραμένει σχεδόν η ίδια. Η αυξημένη αντοχή οφείλεται στο μεγαλύτερο ποσοστό του μαρτενσίτη και στην πιο εκλεπτυσμένη μικροδομή, όπως αναφέρθηκε προηγουμένως. Παρατηρείται, επίσης, ότι όταν ο άξονας του εφελκυσμού είναι παράλληλος με τη φορά της έλασης, η αντοχή είναι υψηλότερη με την μικρότερη όμως TE. Αντιθέτως, στην περίπτωση που ο άξονας του εφελκυσμού βρίσκεται υπό γωνία 45° από τη φορά της έλασης, η αντοχή μειώνεται σημαντικά, όμως η ολική επιμήκυνση είναι η μεγαλύτερη που σημειώθηκε. Ο λόγος για τον οποίο έγιναν δοκιμές εφελκυσμού σε δοκίμια υπό διαφορετικές γωνίες από τη φορά της έλασης είναι για να μελετηθεί η ανισοτροπία του υλικού. Υψηλότερος δείκτης R είναι προτιμότερος και σημαίνει ότι οι ιδιότητες του υλικού έχουν μεγαλύτερη ισοτροπία. Αντιθέτως για το ΔR, μικρότερες τιμές είναι προτιμητέες. Συνεπώς, όπως φαίνεται από τον πίνακα, τα δοκίμια UFH, εκτός από αυξημένη αντοχή εμφανίζουν και καλύτερη ισοτροπία από το CH δοκίμια.

Ο λόγος για τον οποίο παρατηρείται βελτιωμένη ολκιμότητα στη διεύθυνση των 45° φαίνεται στην **Εικόνα 3.16**. Από αυτόν τον IPF χάρτη φαίνεται ότι το μεγαλύτερο κλάσμα όγκου του φερρίτη έχει συγκεκριμένο προσανατολισμό, ο οποίος οφείλεται στην έλλειψη ανακρυστάλλωσής του. Αυτός ο

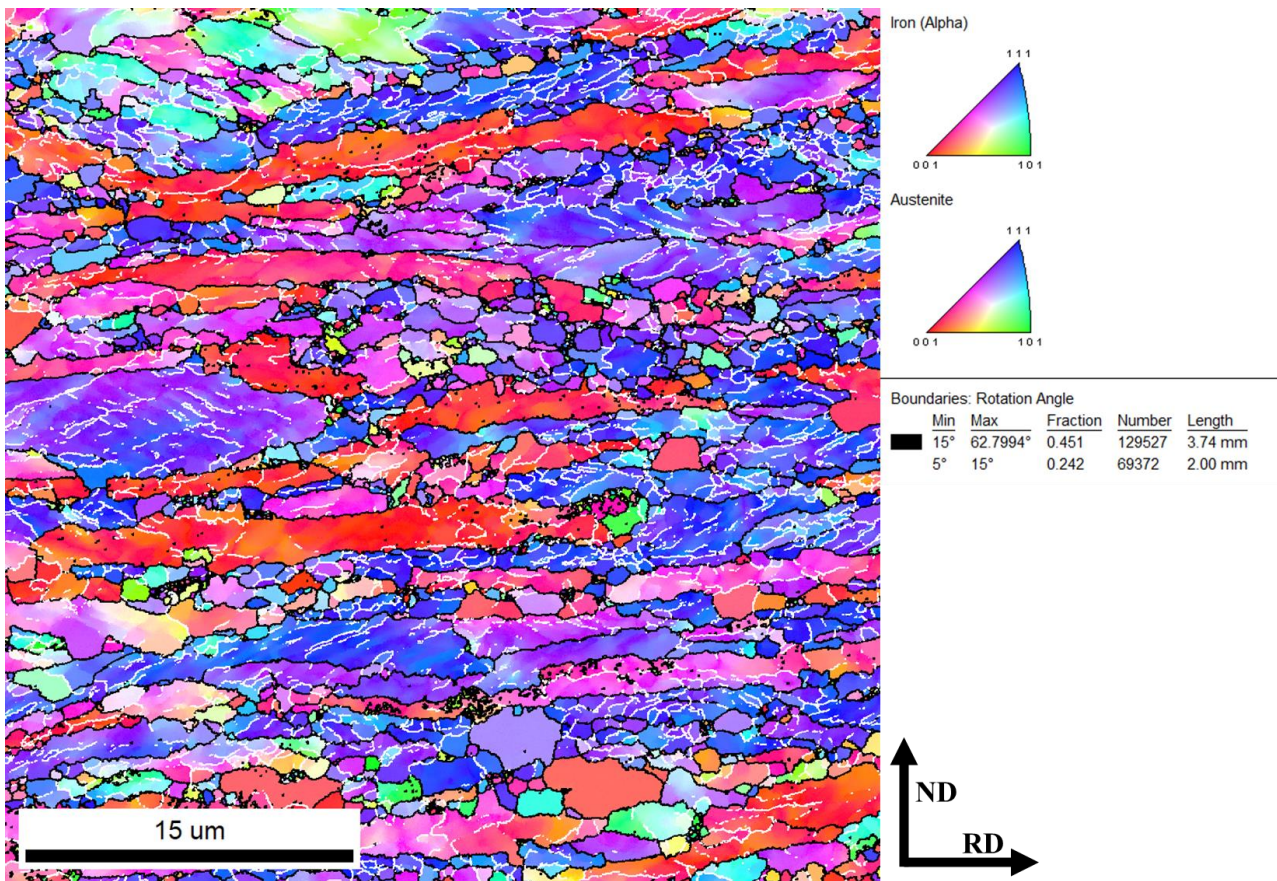


προσανατολισμός συνάδει με τις πιο συνηθισμένες διευθύνσεις ολίσθησης για τη BCC δομή, οι οποίες είναι οι  $\langle \bar{1} 1 1 \rangle$  και  $\langle 1 1 0 \rangle$  [30].

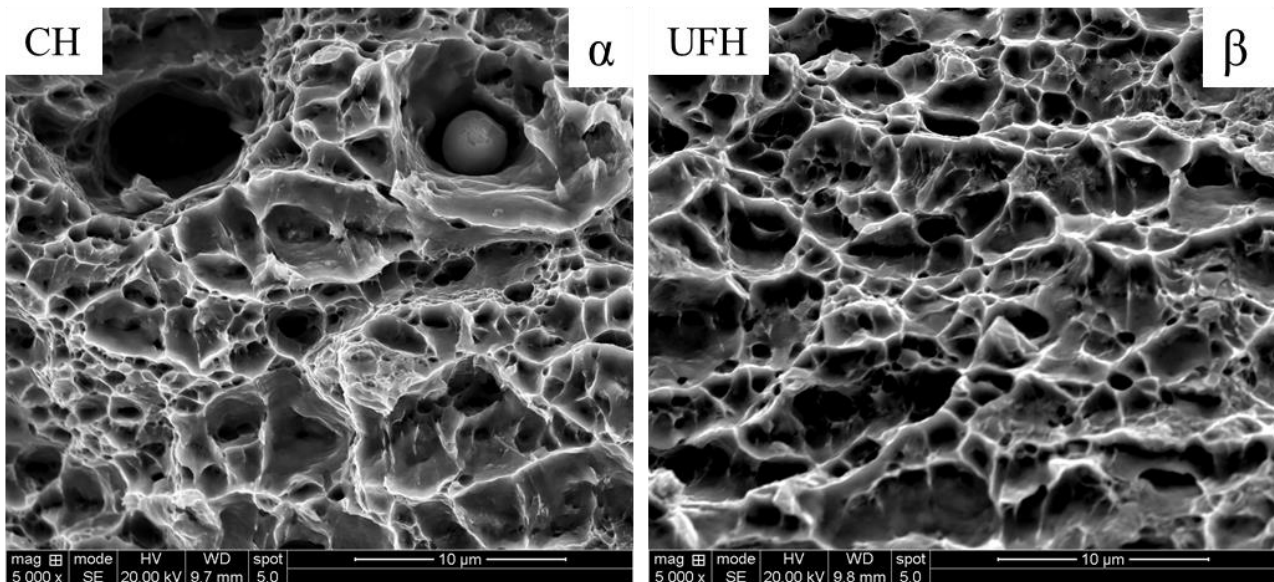
**Πίνακας 3.7:** Οι μηχανικές ιδιότητες των CH και UFH δοκιμίων, όπως αυτές προέκυψαν από τις δοκιμές εφελκυσμού.

	CH			UFH		
	0°	45°	90°	0°	45°	90°
<b>YS (MPa)</b>	453	355	347	570	520	562
<b>UTS (MPa)</b>	697	612	682	973	762	815
<b>UE (%)</b>	7.7	13.1	12.7	8	10	8.7
<b>TE (%)</b>	13.2	24.8	22	13.85	23.9	18
<b>r</b>	0.321	0.883	1.742	0.558	1.671	1.097
<b>R</b>	0.957			1.25		
<b>ΔR</b>	0.149			-0.844		

Από τη θραυστογραφία στα δοκίμια με τις υψηλότερες UTS (**Εικόνες 3.17α, β**) παρατηρείται ότι η θραύση είναι όλκιμη, ενώ υπάρχουν επιφάνειες που αναδεικνύουν θραύση με σχισμό (cleavage fracture) σε μικροκλίμακα. Αυτό φαίνεται από την ύπαρξη οπών (όλκιμη θραύση) και λείων επιφανειών από απόσχιση. Οι οπές αντιστοιχούν σε κόκκους φερρίτη και το μέγεθός τους εξαρτάται από το μέγεθος του φερρίτη. Οι οπές στο UFH δοκίμιο είναι μικρότερες, πράγμα που επιβεβαιώνει και την εκλέπτυνση του φερρίτη στο εν λόγω δοκίμιο. Το ίδιο ισχύει και για τις επιφάνειες απόσχισης, οι οποίες εμφανίζονται στα σημεία που υπάρχουν νησίδες μαρτενσίτη.



**Εικόνα 3.16:** IPF χάρτης του UFH δοκιμίου στον οποίο φαίνεται ο προσανατολισμός των κόκκων. Φαίνεται ότι οι κόκκοι του φερριτή έχουν συγκεκριμένο προσανατολισμό, ο οποίος εξηγεί την αυξημένη ολκιμότητα όταν ο εφελκυσμός γίνεται υπό γωνία 45° από τη φορά της έλασης. Step size: 50 nm.



**Εικόνα 3.17:** Θραυστογραφίες στο SEM όπου παρατηρείται όλκιμη θραύση και για τα δύο δοκίμια με τη δημιουργία σπών και σε μικρό ποσοστό επιφανειών απόσχισης.

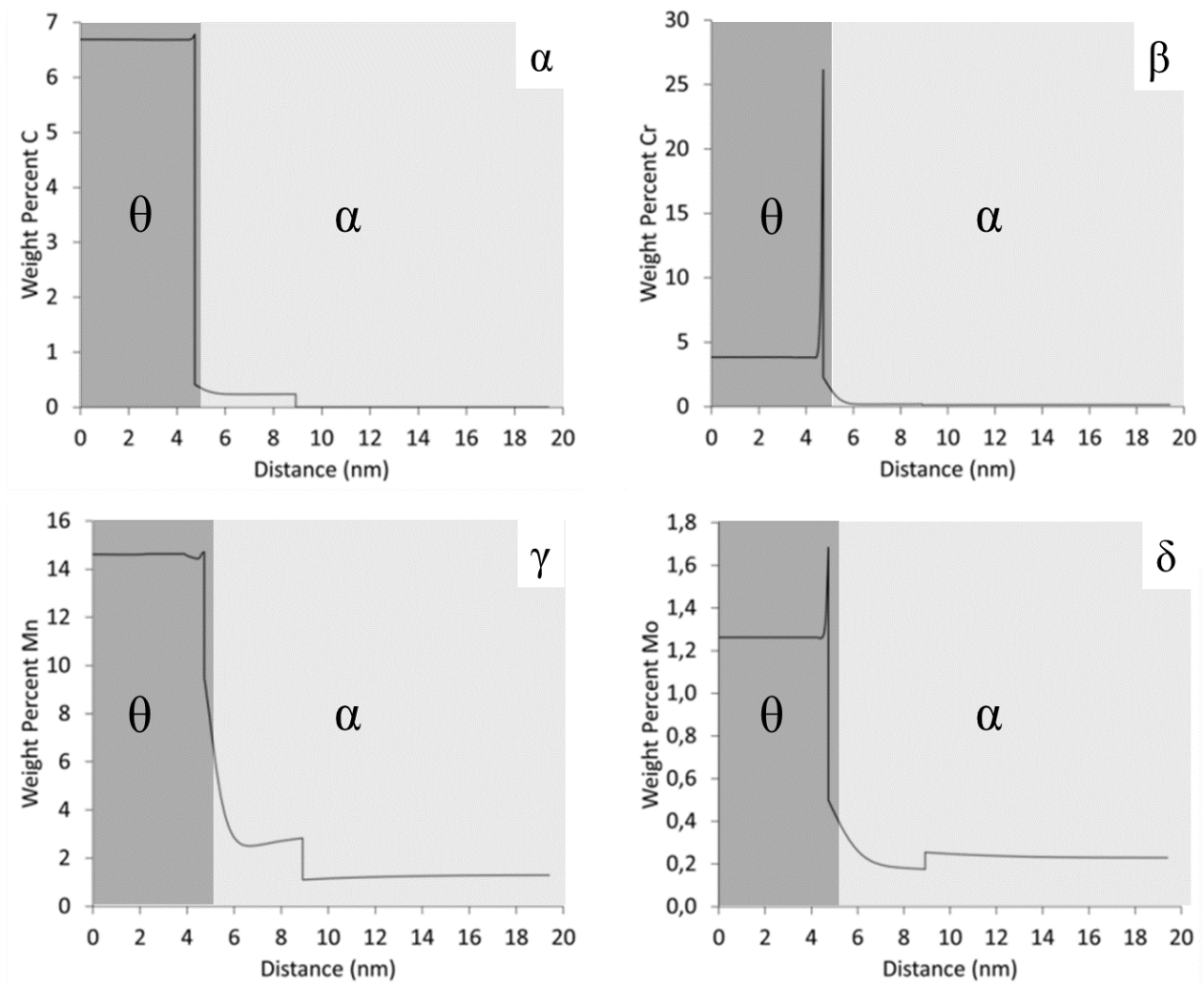
### 3.5. Συζήτηση των αποτελεσμάτων

#### 3.5.1. Σχηματισμός Μαρτενσίτη

Σε όλα τα δοκίμια τα οποία μελετήθηκαν το προϊόν της βαφής που απαντήθηκε σε μεγαλύτερο βαθμό ήταν ο μαρτενσίτης. Αυτό εξηγείται εύκολα από το CCT διαγραμμα της **Εικόνας 3.4**, στην οποία φαίνεται ότι για ρυθμούς ψύξης μεγαλύτερους από 100 °C/s η καμπύλη δεν περνάει από την μαινιτική περιοχή, αλλά μόνο τέμνει την  $M_s$  θερμοκρασία. Το μέγεθος των βελονών του μαρτενσίτη εξαρτάται από το μέγεθος του κόκκου του πρότερου ωστενίτη. Επιπλέον, καθώς ο μαρτενσίτης είναι προϊόν της γρήγορης ψύξης του ωστενίτη, η χημική του σύσταση εξαρτάται και αυτή από τη χημική σύσταση του πρότερου ωστενίτη.

#### 3.5.2. Χημική Σύσταση Πρότερου Ωστενίτη

Όπως παρατηρήθηκε, η φύτρωση του ωστενίτη μπορεί να συμβεί σε δύο σημεία. Κατ' αρχάς, η φύτρωση ξεκινάει στις διεπιφάνειες α/θ, δηλαδή στις διεπιφάνειες του φερρίτη με τον αδιάλυτο σεμεντίτη που βρέθηκε στα περισσότερα δοκίμια. Σε αυτή την περίπτωση, η κινητήριος δύναμη είναι η διαφορά της περιεκτικότητας σε άνθρακα και ο μετασχηματισμός συνοδεύεται από εμπλουτισμό του φερρίτη σε άνθρακα. Αυτός ο εμπλουτισμός συμβαίνει τοπικά επειδή ο χρόνος για τη διάχυση του άνθρακα είναι περιορισμένος. Έτσι, όπως έχει υποστηρίξει στη διατριβή της η Μπουζούνη [26], και όπως φαίνεται στις **Εικόνες 3.17α-δ**, για σφαιροποιημένους κόκκους σεμεντίτη μικρού μεγέθους, η περιοχή γύρω από τον σφαιροποιημένο κόκκο εμφανίζει βάρθρωση στην περιεκτικότητα του άνθρακα και του μαγγανίου, ενώ στοιχεία όπως το χρώμιο και το μολυβδένιο διαφορίζονται στη διεπιφάνεια του σεμεντίτη με τον φερρίτη. Τα συγκεκριμένα διαγράμματα έχουν σχεδιαστεί για τη σύσταση των δοκιμίων CH και UFH. Για τα δοκίμια με σύσταση  $42CrMo4$  ή  $42CrMn6$ , η κλιμάκωση αυτή αναμένεται πιο έντονη, λόγω του μεγαλύτερου ποσοστού άνθρακα και μαγγανίου. Επίσης, αυτός ο διαφορισμός χρωμίου και μολυβδενίου στα όρια του σεμεντίτη καθυστερεί τη διαλυτοποίησή του [26]. Άρα, κάτι τέτοιο συμβαίνει και στα δοκίμια που μελετήθηκαν σε αυτή τη διατριβή, εκτός του δοκιμίου C45, στο οποίο η περιεκτικότητα σε αυτά τα στοιχεία είναι αρκετά μικρότερη.



**Εικόνα 3.17:** Διαγράμματα στα οποία φαίνεται η μεταβολή της περιεκτικότητας του (α) C, (β) Cr, (γ) Mn και (δ) Mo στον φερρίτη (α) σε σχέση με την απόσταση από το σφαιρίδιο του σεμεντίτη (θ). Παρατηρείται ότι για τον άνθρακα και το μαγγάνιο υπάρχει κλιμάκωση στην περιεκτικότητά τους στον φερρίτη ενώ το χρώμιο και το μολυβδένιο διαφορίζονται πάνω στη διεπιφάνεια. Τα διαγράμματα δημιουργήθηκαν με τη χρήση του λογισμικού προσομοίωσης DICTRA [26]. Σύσταση δοκιμών CH, CALH, UFH.

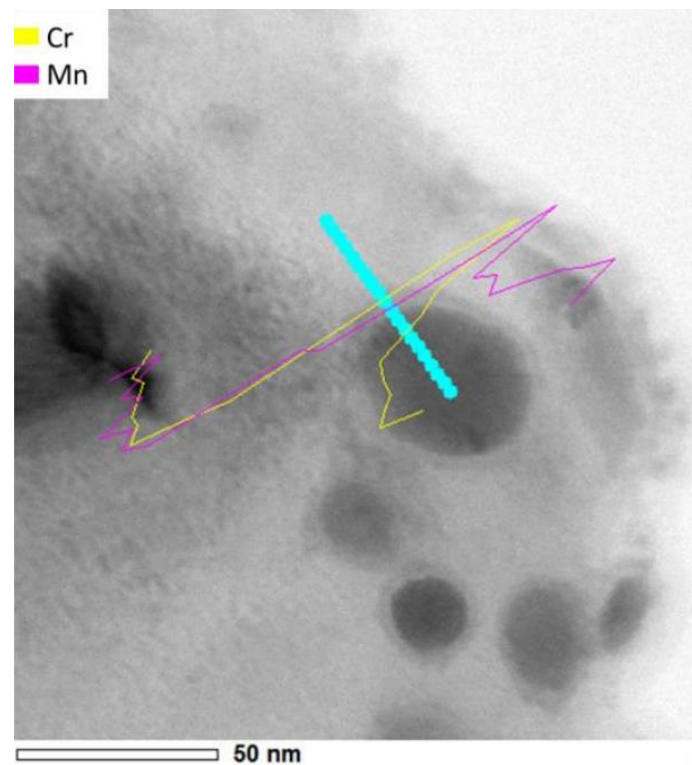
Από την άλλη, βρέθηκε ότι η φύτευση του ωστενίτη συμβαίνει και στα όρια μεταξύ δύο ή τριών κόκκων φερρίτη, χωρίς κάποια παραπλήσια υποφαινόμενη πηγή άνθρακα (σεμεντίτη). Σε αυτή την περίπτωση, ο ωστενίτης που δημιουργείται δεν εμπλουτίζεται σε άνθρακα και ο σχηματισμός του οφείλεται στον διαφορισμό του άνθρακα στα όρια των κόκκων. Συνεπώς, στη θερμοκρασία απόπτησης αναμένονται δύο τύποι πρότερου ωστενίτη, ένας πλούσιος σε άνθρακα (A1) και ο άλλος με περιορισμένο ποσοστό άνθρακα (A2). Οι συστάσεις αυτών των τύπων ωστενίτη υπολογίστηκαν με τη χρήση του DICTRA [26] και αναγράφονται στον **Πίνακα 3.8**.



**Πίνακας 3.8:** Οι περιεκτικότητες του εμπλουτισμένου σε άνθρακα ωστενίτη (A1) και του φτωχού σε άνθρακα ωστενίτη (A2), όπως αυτές υπολογίστηκαν με τη χρήση του λογισμικού DICTRA [26].

Περιεκτικότητα πρότερου ωστενίτη (% κ.β.)	C	Cr	Mn	Mo
A1	0.24	0.18	2.77	0.18
A2	0.18	0.19	3.25	0.17

Για την επιβεβαίωση αυτών των αποτελεσμάτων της προσομοίωσης έγινε χρήση του EDS στο TEM. Όπως φαίνεται στην **Εικόνα 3.18**, η περιεκτικότητα του μαγγανίου (μωβ) μειώνεται όσο αυξάνεται η απόσταση από τον σφαιροποιημένο σεμεντίτη, ενώ το χρώμιο (κίτρινο) φαίνεται να διαφορίζεται στη διεπιφάνεια, όπως προβλέφθηκε από το DICTRA [26].



**Εικόνα 3.18:** Γραμμική χημική ανάλυση EDS στο STEM στην οποία επιβεβαιώνεται η κλιμάκωση στην περιεκτικότητα του μαγγανίου στον φερρίτη όσο αυξάνεται η απόσταση από τον σεμεντίτη και ο διαφορισμός στη διεπιφάνεια α/θ. Δοκίμιο UFH.

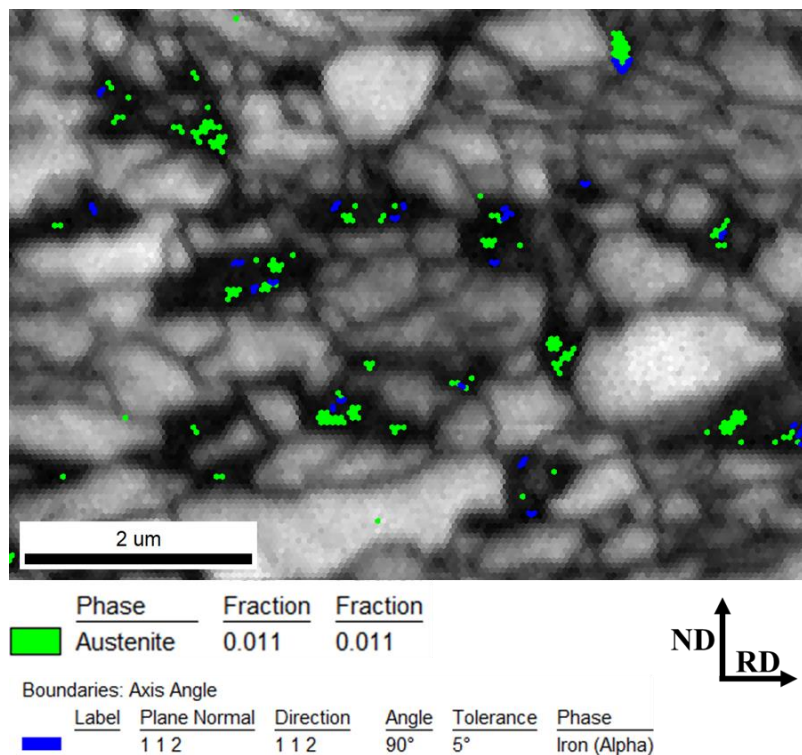
Στην περίπτωση που έχει γίνει πλήρης διαλυτοποίηση του σεμεντίτη (δοκίμια 42CrMo4, C45), αυτή η ετερογένεια οφείλεται στην έλλειψη χρόνου για ομογενοποίηση της σύστασης, η οποία συμβαίνει αφού έχει ξεπεραστεί η θερμοκρασία  $A_{c3}$  ή ύστερα από το πέρας συγκεκριμένου χρόνου στη θερμοκρασία ανόπτησης.

### 3.5.3. Σχηματισμός μπαινίτη

Όπως αναφέρθηκε, βρέθηκαν ενδείξεις για την ύπαρξη μπαινίτη στα δοκίμια στις εργαστηριακής κλίμακας δοκιμές, ενώ η ύπαρξή του παρατηρήθηκε μέσω του TEM στα βιομηχανικής κλίμακας δοκίμια. Η ύπαρξή του οφείλεται στην ετερογένεια του πρότερου ωστενίτη ως προς τη σύσταση. Συγκεκριμένα, ο πρότερος ωστενίτης που σχηματίστηκε μεταξύ κόκκων φερρίτη και είναι φτωχός σε άνθρακα ευνοεί τον σχηματισμό του μπαινίτη. Αυτό συμβαίνει διότι, όπως φαίνεται στο διάγραμμα CCT της **Εικόνας 3.5**, όσο μειώνεται η περιεκτικότητα του άνθρακα στον πρότερο ωστενίτη, τόσο οι μπαινιτικές περιοχές μετατοπίζονται προς τα αριστερά του διαγράμματος και τόσο πιο πιθανός είναι ο σχηματισμός του μπαινίτη για ταχύτερους ρυθμούς ψύξης.

### 3.5.4. Υπολειπόμενος ωστενίτης

Όπως παρατηρήθηκε, είναι δυνατόν να υπολείπεται ο ωστενίτης σε τρεις πιθανές περιπτώσεις. Πρώτον, σε περιοχές κοντά στον αδιάλυτο σεμεντίτη, όπου ο πρότερος ωστενίτης είναι αρκετά εμπλουτισμένος σε άνθρακα και μαγγάνιο [26] η πτώση των τιμών των θερμοκρασιών μετασχηματισμού του μαρτενσίτη μπορεί να οδηγήσει στο να υπολείπεται ο ωστενίτης σε θερμοκρασία περιβάλλοντος. Αυτό φαίνεται στην **Εικόνα 3.19**, για το δοκίμιο UFH. Στον συγκεκριμένο IQ χάρτη του EBSD φαίνεται με πράσινο χρώμα ο υπολειπόμενος ωστενίτης. Φαίνεται ότι βρίσκεται σε περιοχές χαμηλής ποιότητας που αντιστοιχούν στις περλιτικές περιοχές, οι οποίες εμφανίζονται με μαύρο χρώμα.



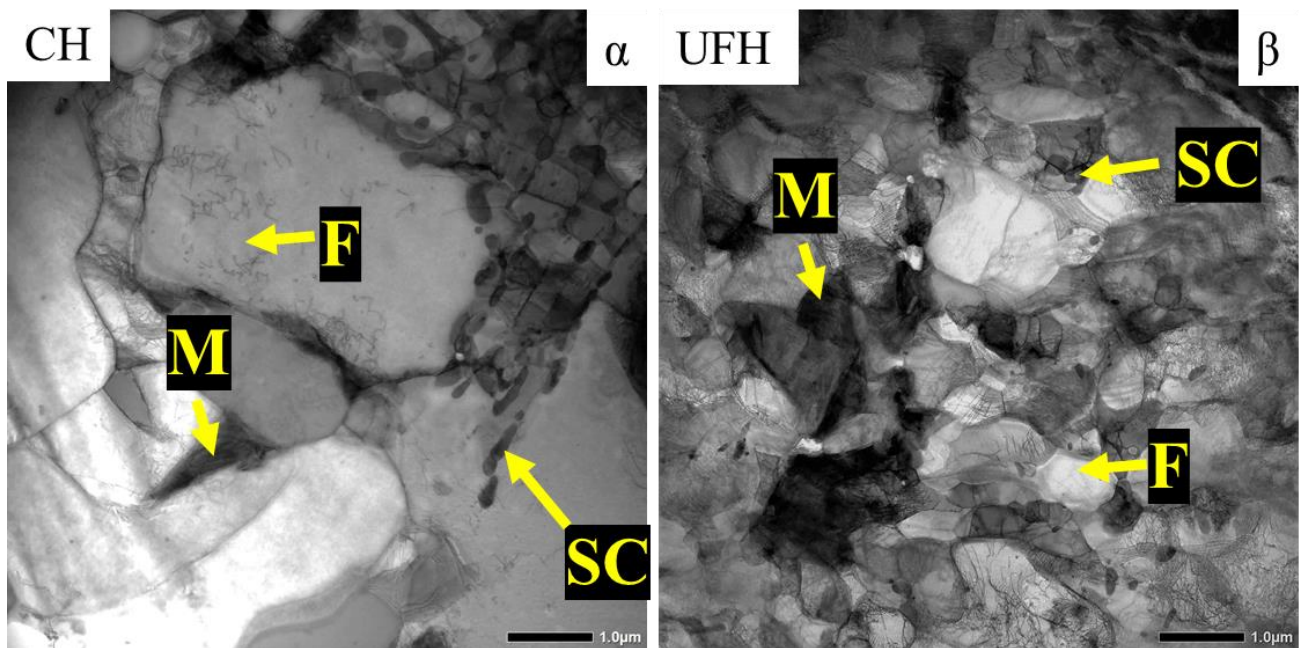
**Εικόνα 3.19:** IQ χάρτης στο EBSD με ενσωματωμένη τη φάση του ωστενίτη (πράσινο). Με μπλε χρώμα έχει προστεθεί η σχέση K-S μεταξύ φερρίτη και ωστενίτη. Ο υπολειπόμενος ωστενίτης βρίσκεται σε περιοχές χαμηλού IQ, οι οποίες αντιστοιχούν σε αδιάλυτες αποικίες περλίτη. Δοκίμιο UFH. Step size: 50 nm.

Δεύτερον, κατά τον σχηματισμό του μπαινίτη, οι περιοχές μεταξύ των πλακιδίων εμπλουτίζονται σε άνθρακα μέσω διάχυσης. Λόγω της σχετικά υψηλής θερμοκρασίας που γίνεται ο σχηματισμός του μπαινίτη, υπάρχει η διαθέσιμη ενέργεια για να επιτευχθεί διάχυση του άνθρακα σε μικρές αποστάσεις. Συνεπώς, μέρος του άνθρακα θα διαφοριστεί στα όρια των πλακιδίων, ενώ το υπόλοιπο θα κατακρημνιστεί, σχηματίζοντας παράλληλα σωματίδια σεμεντίτη. Συνεπώς, λόγω μείωσης της  $M_s$  στα όρια των πλακιδίων, λόγω υψηλής περιεκτικότητας σε άνθρακα, είναι δυνατό να υπολείπεται ο ωστενίτης σε μορφή λεπτών υμενίων (φιλμ) (**Εικόνες 3.9α, β**).

Η τρίτη περίπτωση στην οποία παρατηρήθηκε ο υπολειπόμενος ωστενίτης είναι μεταξύ των βελόνων μαρτενσίτη (**Εικόνα 3.10α**). Αυτό οφείλεται επίσης στην υψηλή περιεκτικότητα σε άνθρακα, η οποία εμφανίζεται στον κόκκο του πρότερου ωστενίτη κατά τη διάρκεια του σχηματισμού των βελόνων μαρτενσίτη.

### 3.5.5. *Εξέλιξη του μεγέθους κόκκου των κύριων φάσεων της μικροδομής*

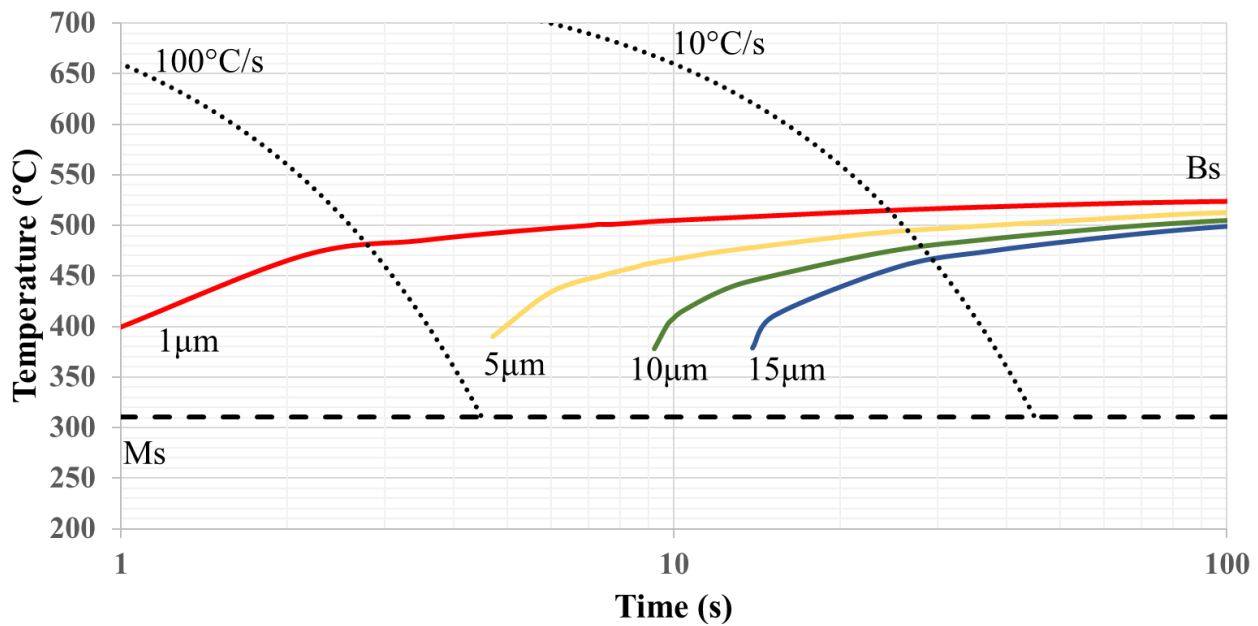
Όσον αφορά στο μέγεθος κόκκου, γενικώς παρατηρήθηκε ότι τα δοκίμια, στα οποία δεν έχει ολοκληρωθεί η διαλυτοποίηση του σεμεντίτη έχουν πιο λεπτομερή μικροδομή. Αυτό οφείλεται στο γεγονός ότι ο αδιάλυτος σεμεντίτης μπορεί να παρεμποδίσει τη μετακίνηση των ορίων του ωστενίτη κατά την ανάπτυξή του μέσω της αγκίστρωσης των ορίων κόκκου (φαινόμενο pinning effect). Σύμφωνα με αυτό, για να διαπεράσει το όριο ένα καρβίδιο ή ένα σωματίδιο σεμεντίτη, απαιτείται μεγάλο ποσό ενέργειας, το οποίο όμως δεν είναι διαθέσιμο. Για αυτόν τον λόγο παρατηρούνται μικροί κόκκοι ανάμεσα στα σωματίδια σφαιροποιημένου σεμεντίτη, όπως στην **Εικόνα 3.20**. Σε αυτές τις εικόνες από το TEM φαίνεται η διαφορά μεταξύ του μεγέθους των κόκκων που βρίσκονται στο ενδιάμεσο των σφαιριδίων σεμεντίτη και των κόκκων που δεν επηρεάζονται από τα αδιάλυτα καρβίδια.



**Εικόνα 3.20:** Η αγκίστρωση που προκαλούν τα σφαιρίδια αδιάλυτου σεμεντίτη (SC) στην ανάπτυξη των κόκκων οδηγεί σε εκλέπτυνση της μικροδομής. Δοκίμιο UFH.

Η εκλέπτυνση των κόκκων του πρότερου ωστενίτη έχει τρία σημαντικά προτερήματα σχετικά με τη μικροδομή και τις ιδιότητες του υλικού. Πρώτον, όπως φαίνεται από το διάγραμμα CCT (Εικόνα 3.21), το οποίο σχεδιάστηκε [14-16] για μία συγκεκριμένη χημική σύσταση και για μεταβλητά μεγέθη πρότερου ωστενίτη, η μπαινιτική περιοχή επηρεάζεται από το μέγεθος του πρότερου ωστενίτη. Αναλυτικότερα, όσο μικρότερος είναι ο πρότερος ωστενίτης τόσο πιο αριστερά στο διάγραμμα μετατοπίζεται η μπαινιτική περιοχή. Αυτό σημαίνει και πάλι πως είναι δυνατός ο μπαινιτικός μετασχηματισμός για γρήγορους ρυθμούς ψύξης, σε κόκκους πρότερου ωστενίτη που έχουν αρκετά μικρό μέγεθος.





**Εικόνα 3.21:** Διάγραμμα CCT το οποίο σχεδιάστηκε [14-16] για τη χημική σύσταση του δοκίμιου και στο οποίο φαίνεται η επίδραση του μεγέθους κόκκου (διάμετρος) του πρότερου ωστενίτη στον σχηματισμό του μαινίτη κατά τη βαφή για συγκεκριμένη σύσταση. Δοκίμιο UFH.

Δεύτερον, η εκλέπτυνση των κόκκων του πρότερου ωστενίτη συμβάλλει στην ισοτροπία των ιδιοτήτων του υλικού. Συγκεκριμένα, μικρότεροι κόκκοι πρότερου ωστενίτη μεταφράζεται σε μικρότερα πακέτα μαρτενσίτη. Αυτά τα πακέτα χαρακτηρίζονται από βελόνες μαρτενσίτη που έχουν τον ίδιο ή παρόμοιο προσανατολισμό. Όταν τα πακέτα είναι μικρότερα και συνεπώς περισσότερα, οι εμφανιζόμενοι προσανατολισμοί θα είναι περισσότεροι και δεν θα έχουν κάποια συγκεκριμένη διεύθυνση, μειώνοντας συνεπώς την ανισοτροπία του υλικού. Αυτό φαίνεται στο UFH δοκίμιο, το οποίο έχει μεγαλύτερο δείκτη R και μικρότερο μέγεθος πρότερου ωστενίτη (**Πίνακας 3.7**). Τέλος, η εκλέπτυνση των κόκκων του πρότερου ωστενίτη οδηγεί σε εκλέπτυνση των βελονών μαρτενσίτη της τελικής μικροδομής, όπως παρατηρήθηκε για όλα τα δοκίμια. Αυτό συμβαίνει διότι η φύτρωση των βελονών μαρτενσίτη ξεκινά από τα όρια κόκκου του πρότερου ωστενίτη [27] και η ανάπτυξή τους δεν μπορεί να συνεχιστεί πέρα από τα όρια του κόκκου.

Επίσης, παρατηρήθηκε ότι το δοκίμιο C45, το οποίο έχει μικρό ποσοστό σε Mn, Mo και Cr, έχει μεγαλύτερο μέσο μέγεθος κόκκου από το δοκίμιο 42CrMo4, παρά την ίδια αρχική μικροδομή και θερμική κατεργασία. Αυτό πιθανώς οφείλεται στον διαφορισμό αυτών των στοιχείων στη διεπιφάνεια του σεμεντίτη με τον φερρίτη, όπως φάνηκε από το DICTRA (**Εικόνα 3.17**). Κατά αυτόν τον τρόπο, καθυστερεί η διαλυτοποίηση του σεμεντίτη μέσω του φαινομένου solute drag effect [28]. Για αυτόν τον λόγο, η διαλυτοποίηση του σεμεντίτη στο δοκίμιο C45 είναι πιο γρήγορη και η ανάπτυξη των κόκκων του ωστενίτη πιο εκτενής.

### 3.5.6. Ανακρυστάλλωση του φερρίτη

Όπως υποδεικνύουν και τα ευρήματα του Cerda [29], γρήγοροι ρυθμοί θέρμανσης αναστέλλουν την έναρξη της διεργασίας της ανακρυστάλλωσης, η οποία πραγματοποιείται σε υψηλότερες θερμοκρασίες. Συνεπώς,

αυτή η διεργασία μπορεί να συμβαίνει παράλληλα με τη διεργασία της ωστενιτοποίησης και εν τέλει, όταν η ανόπτηση γίνεται στη διαφασική περιοχή, η ανακρυστάλλωση του φερρίτη δεν έχει ολοκληρωθεί. Για αυτόν τον λόγο βρέθηκε παραμορφωμένος φερρίτης στα CH και UFH δοκίμια, ενώ στο CALH δοκίμιο η ανακρυστάλλωση έχει ολοκληρωθεί. Η διαφορά στο κλάσμα όγκου του ανακρυσταλλωμένου φερρίτη μεταξύ των δύο πρώτων δοκιμίων, οφείλεται στη μεγάλη διαφορά του ρυθμού θέρμανσης.

### 3.5.7. Επίδραση της μικροδομής στις μηχανικές ιδιότητες

Οι μηχανικές ιδιότητες όπως προέκυψαν από τις δοκιμές εφελκυσμού στα δοκίμια της 3ης σειράς πειραμάτων αφορούσαν τη μέγιστη εφελκυστική αντοχή, το όριο διαρροής και την ολκιμότητα. Παρατηρήθηκε ότι η εκλέπτυνση της τελικής μικροδομής συμβάλλει στην αύξηση της αντοχής του υλικού, χωρίς όμως να μειώνεται η ολκιμότητα. Η αύξηση της αντοχής αυτή (Πίνακας 3.7), μελετήθηκε στο δοκίμιο UFH που έχει πιο λεπτομερή μικροδομή και εμφανίζει υψηλότερη UTS, ενώ η TE παραμένει ίδια με το CH δοκίμιο. Στην αυξημένη αντοχή συμβάλλει επίσης το σχετικά μεγαλύτερο ποσοστό του μαρτενσίτη στο συγκεκριμένο δοκίμιο (UFH). Παρατηρήθηκε επίσης ότι όταν ο άξονας του εφελκυσμού είναι υπό γωνία 45° από τη φορά της έλασης, η TE αυξάνεται σημαντικά ως αποτέλεσμα του κρυσταλλογραφικού προσανατολισμού του φερρίτη. Παρατηρήθηκε (Εικόνα 3.16) ότι οι κόκκοι φερρίτη έχουν συγκεκριμένο προσανατολισμό που συνάδει με τις πιο συνηθισμένες διευθύνσεις ολίσθησης για τη BCC δομή, οι οποίες είναι οι  $\langle \bar{1} 1 1 \rangle$  και  $\langle 1 1 0 \rangle$  [30]. Αυτό σημαίνει ότι το διάνυσμα Burgers για αυτές τις διευθύνσεις είναι παράλληλο στη φορά του εφελκυσμού, όταν αυτός εφαρμόζεται υπό γωνία 45° ως προς τη φορά της έλασης. Συνεπώς, παρατηρείται βελτίωση της ολκιμότητας του υλικού σε αυτή τη διεύθυνση. Συνολικά προκύπτει ότι με την εφαρμογή του UFH, επιτυγχάνεται σημαντική αύξηση της UTS ενώ παράλληλα διατηρείται η TE στα ίδια επίπεδα.

Όσον αφορά στις σκληρομετρήσεις, παρατηρείται ότι το CH δοκίμιο έχει μειωμένη σκληρότητα σε σχέση με το αρχικό υλικό και το UFH. Αυτό οφείλεται στο μεγάλο ποσοστό του ανακρυσταλλωμένου φερρίτη στο CH δοκίμιο. Από την άλλη, η σκληρότητα του UFH οφείλεται στο υψηλότερο ποσοστό του μαρτενσίτη και στην υψηλή παραμόρφωση του φερρίτη.

## 3.6. Συμπεράσματα

Η παρούσα διατριβή έχει ως σκοπό να εξηγήσει την εξέλιξη της μικροδομής, η οποία δίνει τη δυνατότητα ελέγχου θερμικών κατεργασιών και τον σχεδιασμό νέων τύπων χάλυβα που μπορούν να θεωρηθούν ως 3<sup>ης</sup> γενιάς AHSS, όπως οι χάλυβες TRIP και Q&P που χρησιμοποιούνται σήμερα. Η έρευνα εντάσσεται σε μια σύγχρονη παγκόσμια επιστημονική τάση που αφορά στη μελέτη της συνολικής επίδρασης των τάχιστων θερμικών κατεργασιών, υπό διαφορετικά πρίσματα, όπως η κατανόηση των φαινομένων της ανακρυστάλλωσης, της διαλυτοποίησης και κατακρήμνισης καρβιδίων, και η παραγωγή τύπων χάλυβα για την αυτοκινητοβιομηχανία, όπως οι Q&P.

- Τα αποτελέσματα της τρέχουσας μελέτης αφορούν στους μηχανισμούς μετασχηματισμού που παρατηρούνται κατά το στάδιο της αναθέρμανσης, όταν αυτή γίνεται ραγδαία, και στους επακόλουθους μετασχηματισμούς φάσεων κατά τη βαφή, μέσω τεχνικών χαρακτηρισμού.

Συγκεκριμένα, διερευνήθηκαν οι διαφορετικές παράμετροι της θερμικής κατεργασίας επί της μικροδομής που οδηγούν στον ταυτόχρονο σχηματισμό μαρτενσίτη και μπαινίτη, και τη διατήρηση του ωστενίτη και συνεπώς σε βέλτιστες μηχανικές ιδιότητες.

- Η διαλυτοποίηση του σεμεντίτη εξαρτάται από την προσθήκη χρωμίου λόγω της επίδρασης ‘solute drag’, καθώς διαφορίζεται στις διεπιφάνειες α/θ. Στην περίπτωση που η περιεκτικότητα σε χρώμιο είναι χαμηλότερη, η διαλυτοποίηση του σεμεντίτη είναι ταχύτερη και επιτυγχάνεται καλύτερη ομογενοποίηση της χημικής σύστασης της μικροδομής. Παράλληλα, το μαγγάνιο και ο άνθρακας διαφορίζονται στα όρια μεταξύ περλίτη/φερρίτη και φερρίτη/φερρίτη και προσφέρουν την απαιτούμενη θερμοδυναμική κινητήρια δύναμη για την πυρήνωση του ωστενίτη. Στη διαλυτοποίηση του σεμεντίτη συμβάλλει επίσης η μέγιστη θερμοκρασία ανόπτησης, η οποία έχει ισχυρότερη επίδραση από τον ρυθμό θέρμανσης. Ο σφαιροποιημένος σεμεντίτης είτε προέρχεται από την αρχική μικροδομή ή σχηματίστηκε κατά την αναθέρμανση, είναι ενεργειακά σταθερός και μπορεί να διατηρηθεί στην τελική μικροδομή. Αυτό δημιουργεί μια κλιμάκωση της περιεκτικότητας του άνθρακα σε μια ακτίνα γύρω από το σωματίδιο του σεμεντίτη.
- Η μικροδομή επηρεάζεται επίσης από την αυξημένη παραμόρφωση του φερρίτη, καθώς οι διαταραχές λειτουργούν ως διάλυτοι για τη γρήγορη διάχυση του άνθρακα και θα λειτουργήσουν ως θέσεις ετερογενούς πυρήνωσης του ωστενίτη. Ως προς τον φερρίτη, οι μηχανισμοί της επαναφοράς και ανακρυστάλλωσής του μετατοπίζονται σε υψηλότερες θερμοκρασίες και, σε κάποιο σημείο, αλληλοεπικαλύπτονται με τον μηχανισμό της ωστενιτοποίησης, όταν εφαρμόζονται υψηλοί ρυθμοί θέρμανσης. Επομένως, ο μη ανακρυσταλλωμένος φερρίτης συνυπάρχει στη μικροδομή με τον ανακρυσταλλωμένο φερρίτη. Το κλάσμα όγκου του μη ανακρυσταλλωμένου φερρίτη εξαρτάται αποκλειστικά από το ρυθμό θέρμανσης. Το υψηλό κλάσμα μη ανακρυσταλλωμένου φερρίτη επηρεάζει τον κρυσταλλογραφικό ιστό του υλικού. Όταν το κλάσμα του ανακρυσταλλωμένου φερρίτη είναι αρκετά χαμηλό, ο ιστός είναι πολύ παρόμοιος με εκείνον του αρχικού υλικού και επηρεάζει έντονα τις μηχανικές ιδιότητες και την ισοτροπία των ιδιοτήτων του υλικού.
- Η πυρήνωση και η χημική σύσταση του ωστενίτη εξαρτάται σε μεγάλο βαθμό από τους ρυθμούς θέρμανσης. Ο ωστενίτης φυτρώνει όταν το υλικό φθάσει τη θερμοκρασία  $A_{c1}$  κατά προτίμηση σε περιοχές όπου υπάρχει αρκετή διαφορά στην περιεκτικότητα σε άνθρακα. Τέτοιες θέσεις είναι κυρίως οι διεπιφάνειες μεταξύ φερρίτη και πλακοειδή ή σφαιροποιημένου σεμεντίτη, και δευτερευόντως οι διαταραχές ή τα όρια φερρίτη/φερρίτη. Η πυρήνωση του ωστενίτη θα γίνει αρχικά στις πρώτες θέσεις και στη συνέχεια θα ξεκινήσει στις επόμενες θέσεις. Ως εκ τούτου, θα σχηματιστούν δύο τύποι ωστενίτη, αυτοί με υψηλή περιεκτικότητα σε άνθρακα, σε μικρή απόσταση από τον σεμεντίτη, και εκείνοι με χαμηλότερη περιεκτικότητα σε άνθρακα, σχηματισμένοι στις διεπιφάνειες φερρίτη και σε διαταραχές. Η ανάπτυξη του ωστενίτη θα παρεμποδιστεί λόγω των τάχιστων ρυθμών θέρμανσης και λόγω της παρουσίας αδιάλυτου σεμεντίτη. Στην περίπτωση που ο σεμεντίτης είναι πλήρως διαλυτοποιημένος, οι κόκκοι ωστενίτη θα αυξηθούν περισσότερο σε μέγεθος, καθώς η ανάπτυξή τους θα εξαρτηθεί μόνο από τον ρυθμό θέρμανσης. Σε αντίθεση με την συμβατική θερμική κατεργασία, η ετερογένεια της χημικής σύστασης διατηρείται και το μέγεθος των κόκκων ωστενίτη μειώνεται.

- Η σύσταση και το μέγεθος του ωστενίτη επηρεάζει τα προϊόντα της βαφής. Ο μαρτενσίτης σχηματίζεται κατά τη βαφή σε θερμοκρασία δωματίου από τον εμπλουτισμένο σε άνθρακα ωστενίτη. Ο σχηματισμός του μπαινίτη πραγματοποιείται με τους ίδιους ρυθμούς ψύξης στον φτωχό σε άνθρακα ωστενίτη. Η παρουσία του μπαινίτη επιβεβαιώνεται από την ανάλυση στα SEM, EBSD και TEM. Υπολειπόμενος ωστενίτης σε υμένα εμφανίζεται επίσης στις περιοχές πλούσιες σε άνθρακα λόγω της τοπικής μείωσης της θερμοκρασίας Ms.
- Οι μικροδομές που προκύπτουν από UFH μπορεί συνεπώς να αποτελούνται από μαρτενσίτη, υπολειπόμενο ωστενίτη, μπαινίτη, φερρίτη και αδιάλυτο σεμεντίτη, και είναι παρόμοιες με αυτές που συναντώνται στους Προηγμένους Χάλυβες Υψηλής Αντοχής 3<sup>ης</sup> γενιάς. Κατά τη διάρκεια των δοκιμών εφελκυσμού, το υλικό παρουσίασε πολύ καλή αναλογία αντοχής και ολκιμότητας σε σύγκριση με τους συμβατικούς χάλυβες με το ίδιο κλάσμα όγκου μαρτενσίτη. Η αντοχή και η σκληρότητα του υλικού αποδίδονται στον μαρτενσίτη, ενώ η καλή ολκιμότητα αποδίδεται στον υπολειπόμενο ωστενίτη, τον μπαινίτη και τον φερρίτη. Ωστόσο, λόγω του κρυσταλλογραφικού ιστού, αυτές οι ιδιότητες δεν εμφανίζουν ισοτροπία, περιορίζοντας έτσι τις πιθανές εφαρμογές ενός τέτοιου χάλυβα. Η θραύση είναι όλκιμη ως επί το πλείστον, ενώ παρατηρήθηκαν λίγες επιφάνειες θραύσης με απόσχιση.

Η UFH αποτελεί μία ενδιαφέρουσα εναλλακτική στις μεθόδους μέσω των οποίων επιδιώκεται η βελτιστοποίηση των τύπων χάλυβα της αυτοκινητοβιομηχανίας αλλά και τύπων χάλυβα για άλλες εφαρμογές όπου απαιτούνται υψηλές αντοχές. Η πλήρης εξήγηση των μηχανισμών μετασχηματισμού κατά τα στάδια θέρμανσης και ψύξης όταν εφαρμόζονται πολύ υψηλοί ρυθμοί, όπως προκύπτει από την παρούσα διατριβή, δίνει τη δυνατότητα ελέγχου κατεργασιών αυτού του είδους και τον σχεδιασμό νέων κραμάτων. Συμβάλλει, επομένως, στη βελτίωση της μεθόδου UFH ώστε να καταστεί ελκυστική και αξιοποιήσιμη στην αυτοκινητοβιομηχανία.

### 3.7. Ενδεικτική Βιβλιογραφία

1. European Commission Emissions in the automotive sector.  
[https://ec.europa.eu/growth/sectors/automotive/environment-protection/emissions\\_en](https://ec.europa.eu/growth/sectors/automotive/environment-protection/emissions_en). Accessed 16 Nov. 2020
2. Lolla T., Cola G., Narayanan B. et al. (2011) Development of rapid heating and cooling (flash processing) process to produce advanced high strength steel microstructures. *Materials Science and Technology* 27: 863–875. <https://doi.org/10.1179/174328409X433813>
3. Petrov R.H., Kestens L., Kaluba W., et al. (2003) Recrystallization and austenite formation in a cold rolled TRIP steel during ultra fast heating. *Steel Grips* 1: 289–293
4. Kaluba W.J., Taillard R., Foct J. (1998) The bainitic mechanism of austenite formation during rapid heating. *Acta Materialia* 46: 5917–5927. [https://doi.org/10.1016/S1359-6454\(98\)00210-9](https://doi.org/10.1016/S1359-6454(98)00210-9)
5. Liu G., Li J., Zhang S., et al. (2016) Dilatometric study on the recrystallization and austenization behavior of cold-rolled steel with different heating rates. *Journal of Alloys and Compounds* 666: 309–316. <https://doi.org/10.1016/j.jallcom.2016.01.137>

6. Xu D., Li J., Meng Q., et al. (2014) Effect of heating rate on microstructure and mechanical properties of TRIP-aided multiphase steel. *Journal of Alloys and Compounds* 614: 94–101. <https://doi.org/10.1016/j.jallcom.2014.06.075>
7. Wen P., Han J., Luo H., et al. (2020) Effect of flash processing on recrystallization behavior and mechanical performance of cold-rolled IF steel. *International Journal of Minerals and Metallic Materials* 27: 1234–1243. <https://doi.org/10.1007/s12613-020-2023-2>
8. Cerda F.C., Goulas C., Sabirov I. et al. (2016) Microstructure, texture and mechanical properties in a low carbon steel after ultrafast heating. *Materials Science and Engineering: A* 672: 108–120. <https://doi.org/10.1016/j.msea.2016.06.056>
9. Arruda M.V.P., Melo T.M.F., Costa F.S. et al. (2019) Microstructural evolution during continuous annealing of a 980 MPa cold rolled steel grade. *Journal of Physics: Conf Ser* 1270: 12020. <https://doi.org/10.1088/1742-6596/1270/1/012020>
10. Hernandez-Duran E.I., Ros-Yanez T., Castro-Cerda F.M. et al. (2020) The influence of the heating rate on the microstructure and mechanical properties of a peak annealed quenched and partitioned steel. *Materials Science and Engineering: A* 797: 140061. <https://doi.org/10.1016/j.msea.2020.140061>
11. Cryderman R., Garrett D., Schlittenhart Z. et al. (2020) Effects of Rapid Induction Heating on Transformations in 0.6% C Steels. *Journal of Materials Engineering and Performance* 29: 3502–3515. <https://doi.org/10.1007/s11665-020-04632-0>
12. Zajac S., Schwinn V., Tacke K.H. (2005) Characterisation and Quantification of Complex Bainitic Microstructures in High and Ultra-High Strength Linepipe Steels. *MSF* 500-501: 387–394. <https://doi.org/10.4028/www.scientific.net/MSF.500-501.387>
13. Cayron C. (2007) ARPGE: a computer program to automatically reconstruct the parent grains from electron backscatter diffraction data. *Journal of Applied Crystallography* 40: 1183–1188
14. Kirkaldy J.S., Doane D.V. (eds) (1984) *Hardenability Concepts with Applications to Steel*. AIME: Warrendale, Pa, USA
15. Bhadeshia, H. K. D. H. (1982) Thermodynamic analysis of isothermal transformation diagrams. *Metal Science* 16: 159–166. <https://doi.org/10.1179/030634582790427217>
16. Bhadeshia, H. K. D. H. (1981) Driving force for martensitic transformation in steels. *Metal Science* 15: 175–177. <https://doi.org/10.1179/030634581790426714>
17. Bhadeshia, H. K. D. H. (2018) *Geometry of crystals, polycrystals and phase transformations*. CRC Press/Taylor & Francis Group, Boca Raton
18. Bhadeshia, H. K. D. H., Christian J.W. (1990) Bainite in steels. *Metallurgical and Materials Transactions A* 21A: 767–797
19. Takahashi M. (2004) Recent progress: kinetics of the bainite transformation in steels. *Current Opinion in Solid State and Materials Science* 8: 213–217. <https://doi.org/10.1016/j.cossms.2004.08.003>
20. Cardozo J.J., Rivas A.L., Colas R., (2007) Effect of the Annealing Conditions on the Microstructure and Mechanical Properties of a 0.04% C Al Killed Steel. *Materials Science Forum* 539-543:4208-4213 <https://doi.org/10.4028/www.scientific.net/MSF.539-543.4208>

21. Savran V.I. (2009) Austenite Formation in C-Mn Steel. Doctoral Thesis, TU Delft
22. Love G.R. (1964) Dislocation pipe diffusion. *Acta Metallurgica* 12: 731–737
23. Bartuška P., The relation between the polygonization and recrystallization of nickel (1967) *Czechoslovak Journal of Physics B*, 17, 798–804
24. Valdes-Taberero M.A., Vercruyssen F., Sabirov I., et al. (2018) Effect of Ultrafast Heating on the Properties of the Microconstituents in a Low-Carbon Steel. *Metallurgical and Materials Transactions A* 49: 3145–3150. <https://doi.org/10.1007/s11661-018-4658-4>
25. De Knijf D., Puype A., Föjler C. et al. (2015) The influence of ultra-fast annealing prior to quenching and partitioning on the microstructure and mechanical properties. *Materials Science and Engineering: A* 627: 182–190. <https://doi.org/10.1016/j.msea.2014.12.118>
26. Μπουζούνη, Μ., Προσομοίωση των μετασχηματισμών φάσης και της εξέλιξης της μικροδομής σε υποευτηκτοειδείς χάλυβες κατά τη διάρκεια ραγδαίων θερμικών κατεργασιών, Διδακτορική Διατριβή, ΕΜΠ, Αθήνα, 2020
27. Landheer H. (2010) Nucleation of ferrite in austenite: The role of crystallography. Doctoral. TU Delft, Delft, NE
28. Papaefthymiou S., Bouzouni M., Petrov R.H. (2018) Study of Carbide Dissolution and Austenite Formation during Ultra-Fast Heating in Medium Carbon Chromium Molybdenum Steel. *Metals* 8: 646. <https://doi.org/10.3390/met8080646>
29. Castro Cerda F. (2017) Third Generation Advanced High Strength Steels via Ultrafast Heating. Doctoral Thesis, TU Delft
30. Weinberger C.R., Boyce B.L., Battaile C.C. (2013) Slip planes in bcc transition metals. *International Materials Reviews* 58: 296–314. <https://doi.org/10.1179/1743280412Y.0000000015>

## 4. Abstract

This thesis aims to offer a detailed understanding of the transformation phenomena that occur when high heating rates are applied to automotive steel grades. It is focused on the evolution of the microstructure through the heating and cooling stages of the thermal treatment. By comprehending these phenomena, Ultra-Fast Heating treatments are better controlled with the purpose to improve existing grades and design new ones. Such grades can be incorporated into the current 3rd Generation Advanced High Strength Steels that consist of similar microstructures and exhibit desired mechanical properties. To that end, the effect of the heating rate is studied, using characterization techniques, on the cementite spheroidization and dissolution, the recrystallization of ferrite, and the nucleation and growth of austenite, which eventually lead to the formation of bainite and martensite, and the retainment of austenite upon quenching.

To better analyze these mechanisms, three different approaches were made. On the first approach, the goal is to study the effect of the chemical composition, initial microstructure, heating rate, heating time, and soaking time on the microstructure when high heating rates are applied in laboratory-scale samples. The purpose of these experiments is to determine the optimal sample and treatment parameters that will lead to the desired microstructures. Therefore, three different automotive steel grades are used that undergo different UFH treatments on a laboratory scale, and their microstructures are characterized. The results of these experiments set the stepping stone for the second approach, in which, an ultra-fast heating cycle was studied on industry-scale samples with the scope to determine whether such treatments can be applied in the industry. The compositions and thermal treatments are chosen for this set according to the results of the laboratory-scale experiments. The final approach's scope is to check whether such heat treatments can replace currently used conventional steel grades. To that end, high heating rates were applied on commercial steel grades and the microstructure and properties were compared to the conventional ones.

The first approach (Chapter 8.1) comprises a set of three different experiments. Its purpose is to study small-sized samples to comprehend the effect of the parameters mentioned above better. The heat treatments are conducted with the use of dilatometers. Three different automotive grades with medium carbon content were studied, the C45, 42CrMo4, and 42CrMn6. Also, the initial microstructure would consist either of ferrite and pearlite or ferrite and spheroidized cementite. The heating treatments consist of high heating rates (300 °C/s), up to the peak temperature (900-1080 °C), and either short (2 s) or long (300 s) soaking times followed by quenching. For comparison reasons, conventional heating treatments (10 °C/s heating rate) were also studied. The analysis of the microstructure took place with the use of electron microscopy techniques, such as Secondary Electron Microscopy (SEM), Transmission Electron Microscopy (TEM), and Electron BackScatter Diffraction (EBSD). The characterization is focused on the microstructural constituents and their grain size. Simulation software is also used for analyzing the size and composition of the Parent Austenite Grains (PAGs). It is found that the dissolution of cementite is impeded to a large extent, depending on its initial shape and size. This undissolved cementite leads to the refinement of the parent austenite grains and heterogeneity in its chemical composition, creating gradients in the carbon content. These gradients can lead to the formation of

bainite and retained austenite in the final microstructure, as has been indicated. Also, alloying elements, such as chromium and molybdenum, impede cementite dissolution through the solute drag effect. From these results, the optimal parameters were chosen for the second set of experiments on industrial scale samples.

With the optimal parameters determined, high heating rates were applied (Chapter 8.2) on large-scale hollow tube samples, similar to those used in the industry, using a pilot setup designed by the supervisor. This approach aims to study whether such treatments are viable in a production line. The chosen composition is that of the 42CrMo4, with ferrite-pearlite initial microstructure. The heating rate used is 100 °C/s, up to the annealing temperature of 930 °C followed by subsequent quenching in water. The formation of lower bainite alongside the retainment of austenite films found in the dilatometry samples is now confirmed with the TEM. The presence of such constituents is attributed to the chemical heterogeneity that was found in the laboratory-scale samples. Regions that are not enriched in carbon favor bainite formation, while regions in small proximity to carbon sources favor the formation of martensite and retainment of austenite.

The third and final approach (Chapter 8.3) aims to study whether the application of an ultra-fast heat treatment can replace conventional methods currently used in the automotive industry. Therefore, very high heating rates were applied in a commercial steel grade that is thoroughly used in vehicles' bodies. The microstructure features and the studied material properties are compared to the conventional, commercial grade. It is found that the partial spheroidization and dissolution of cementite found in the pearlitic colonies of the initial microstructure favors the refinement of the ferrite, parent austenite grains, and martensite of the final microstructure. The evolution of the microstructure is thoroughly studied. The recovery and recrystallization processes initiate at higher temperatures when high heating rates are applied, which overlap with the austenitization and are incomplete. The nucleation of austenite occurs inside the pearlitic colonies due to the high carbon concentration and ferritic areas without any carbon enrichment. Traces of retained austenite are found inside the partially dissolved pearlitic colonies. The ultra-fast heated samples show increased strength and elongation compared to the conventional ones.

From this thesis, it is concluded that in ultra-fast heat treatments, due to cementite's impeded and incomplete dissolution, heterogeneity in the parent austenite's chemical composition and grain size is formed. This heterogeneity explains the bainite formation alongside martensite and the retainment of austenite. Such grades with mixed microstructures can be incorporated to the 3rd Generation AHSS that exhibit spectacular properties. In general, the ultra-fast heated steels exhibit better strength/ductility ratio than the conventional heated steels. The mechanical properties of these steels result from their refined mixed microstructures. In contrast, in the conventional heated steels, the microstructure consists only of martensite, and thus their ductility is expected relatively low. It is also proven that the strength of the steel can be increased without significant losses in the ductility, when high heating rates are applied. The experimental approach used in this thesis, confirms through characterization techniques the ability to produce mixed microstructures in a single step, by explaining the simultaneous formation of bainite and martensite, and the retainment of austenite in ultra-fast heating cycles, as has been predicted via simulation experiments.



## 5. Introduction

### 5.1. Trends in the automotive industry

Over the last years, the automotive industry is looking for alternative methods to produce better vehicle components to improve safety and reduce weight while maintaining low production costs [1]. Components with higher strengths are intended to improve passenger safety, which is the top priority of the automotive industries according to the imposed regulations. On the other hand, stronger components can reduce the material used with thinner plates, leading to lightweight Body-In-White (BIW) vehicle structures. Reducing weight while maintaining the regulated strength criteria is an essential requisite for modern vehicles. Lower weight means lower fuel consumption and also lower carbon emissions leading to an eco-friendlier way of transportation. This can be very important for the recently introduced electric vehicles that use heavy batteries, and thus the weight reduction is a necessity.

In order to meet these regulations, the Advanced High Strength Steel (AHSS) grades have emerged. It is intended for these grades to cover a wide range of strength/strain ratios making each grade suitable for use as different components. In particular, grades with low strength and high strain capability are being used in the crumple zones, the front and back parts of the vehicle to absorb as much energy as possible from the collision. On the contrary, high strength grades with meager ductility capability are intended for the passenger compartment, where the deformation has to be minimal. To achieve this, two main ideas are applied. The first one is alloying the steel with elements such as carbon, manganese, chromium, molybdenum, aluminum, etc., in different contents. Each alloying element has a different effect either on the microstructure or on the properties, or both.

Nevertheless, alloying the steel with some of these elements can considerably increase the final product's cost, making it non-sustainable for today's market. The other approach is to apply specific thermomechanical treatments (rolling, annealing, tempering) on the steel to affect its microstructure and its constituents. These microstructural constituents can either favor the material's hardness and strength (martensite, cementite), while others tend to favor its ductility and formability (ferrite, bainite). Thus, depending on the component's intended use, a combination of the constituents mentioned above in different fractions can be achieved through thermal treatments. It has to be noted that none of these two approaches are self-sustainable, but they have to be combined to receive the optimal results.

### 5.2. Generations of AHSS

Currently, the 1<sup>st</sup> and 2<sup>nd</sup> Generations of AHSS are used in today's automobiles, which combine thermal treatments and the use of specific alloying elements. These grades are distinguished by their mechanical properties and are categorized in Conventional, 1<sup>st</sup>, 2<sup>nd</sup>, and 3<sup>rd</sup> generation steels as shown in the strength-elongation diagram of **Figure 5.1** [2]. The Interstitial Free (IF) and High Strength Low Alloy (HSLA) steels are lean alloyed steels that show excellent ductility and low strength making them suitable for crumple zones.

On the contrary, Martensitic Steels (MS) and Press Hardened Steels (PHS) offer high strengths but low ductility and formability, as they are quite brittle. To bridge this gap, grades that combine harder and softer phases have emerged, such as the Dual Phase (DP) steels that can show a wide range of strength and ductility, making them the most commonly used steel grades as vehicle components until now. Other grades use induced plasticity mechanisms, which increase their strength while under stress and during collisions. These grades are the TRansformation Induced Plasticity (TRIP) steels and the TWinning Induced Plasticity (TWIP) steels.

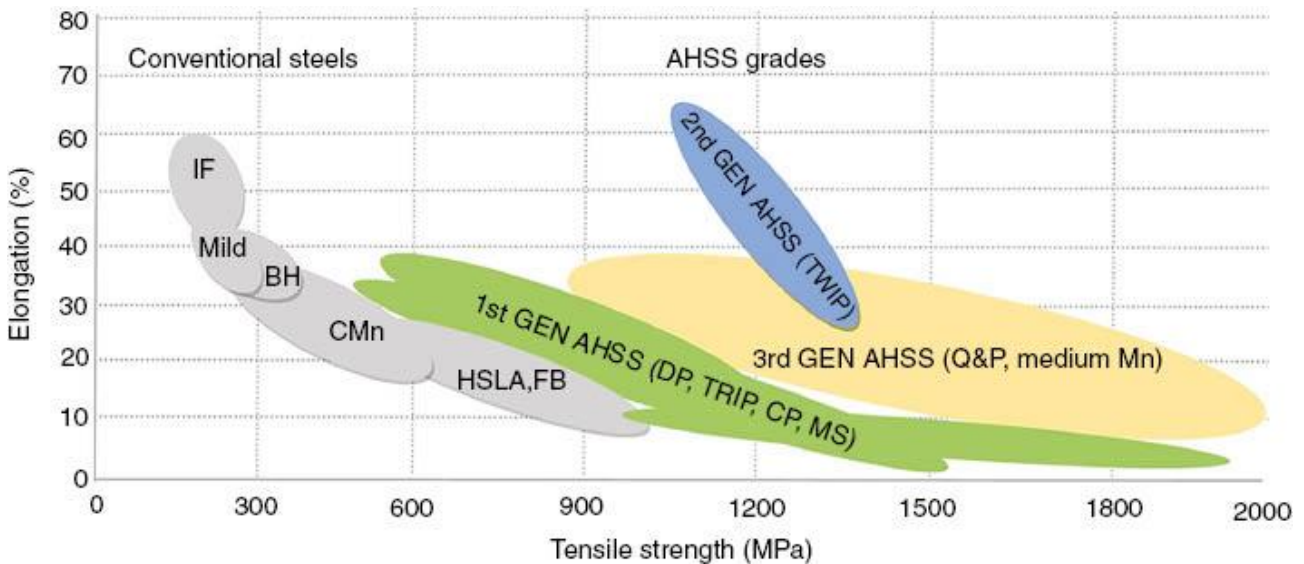


Figure 5.1: The strength-elongation diagram and the categorization of different steel grades in it [2].

### 5.2.1. Conventional Steels

Conventional steels, as called in the automotive industry, are the grades of steels that exhibit lower values of mechanical strength (up to 210 MPa yield strength and up to 300 MPa Fracture strength) but have very high ductility. Their common feature is that they consist of a ferritic microstructure and exhibit excellent properties concerning formability, adhesion. They are distinguished in Interstitial Free (IF) and low carbon (Mild Steels or Low Carbon, LC) steels.

#### 5.2.1.1. IF Steels

IF or Ultra-Low Carbon (ULC) steels have a very low content of interstitial elements ( $C < 30$  ppm,  $N < 30$  ppm) and consist of a ferritic microstructure. They have very high work hardening and formability and excellent weldability due to the meager percentage of carbon in the ferrite lattice. However, as shown in the diagram, IFs have low strength.

#### 5.2.1.2. Mild steels

Mild steels are low carbon or slightly alloyed, hypo-eutectoid steels, with a carbon content not exceeding 0.25 % wt. They are produced with very low production costs and exhibit low tensile strength but excellent ductility, formability, and weldability.

### 5.2.2. High Strength Steels

High-strength steels were developed to achieve higher steel strengths and reduce the overall mass of the vehicle body with the scope to offer more safety. Their microstructure consists mainly of a ferritic matrix. Simultaneously, the strengthening mechanisms are attributed to creating a solid solution, the refinement of the grain size, and the precipitation of secondary phases. This category includes the Carbon-Manganese (C-Mn) steels, Bake Hardening (BH) steels, Isotropic steels (IS), Interstitial Free – High Strength steels (IF-HS), High Strength Low Alloy (HSLA) and Ferritic - Bainitic (FB) steels [3].

#### 5.2.2.1. C-Mn steels

Steels with combined carbon-manganese (C-Mn) additives contain 1.2-1.8 % Mn and about 0.3 % C. Other micro-alloying additives such as Si, Al, Ti, Nb, and V are usually added as protection against oxidation, control the microstructure, and other metallurgical purposes. The total percentage of alloying elements against Fe does not, however, exceed 3 %. Their typical microstructure mainly consists of the ferrite matrix and pearlite. This is a category of steels that exhibit increased resistance to fatigue and have good weldability and formability [4].

#### 5.2.2.2. BH steels

Bake Hardening (BH) steels usually contain a low carbon percentage and have a mainly ferritic microstructure. The additional aging step during their production aims to increase their strength without losing ductility. Aging can occur either during the baking process or during the stay at room temperature for several weeks. A primary condition for their production is the presence of dissolved carbon ( $C < 25$  ppm) in the ferrite lattice after the final annealing, which then diffuses during the aging step. Higher C content is not desirable, as it favors the phenomenon of aging at room temperature [5].

#### 5.2.2.3. High Strength – Low Alloy steels

HSLA steels are a particular class of low-alloy carbon steels containing micro-alloying elements such as V, Nb, or Ti, leading to superior mechanical properties. Their maximum tensile strength can reach 750 MPa while maintaining excellent ductility, weldability, formability, and resistance to corrosion and fatigue [6]. The main factors responsible for their aforementioned excellent properties are the refinement of the ferritic grains, the hardening from precipitation of secondary phases that result from the micro-alloying elements, and the control of the geometry of the inclusions during production [7].

#### 5.2.2.4. Ferritic - Bainitic steels

FB steels are a class of steels selected in the automotive industry to meet specific requirements during their application, such as hole expansion and bending. These steels consist of a very detailed microstructure of ferrite grains and bainite plates. They are usually available as hot rolled products. They have excellent weldability, good crash performance, and good fatigue [3].

### 5.2.3. *Advanced High Strength Steels*

AHSS steels are mainly distinguished from multiphase microstructures consisting of one or more phases other than ferrite or cementite, such as martensite, bainite, austenite, or retained austenite, in volume fractions suitable for the production of components with excellent mechanical properties. All AHSSs are produced by controlling the chemical composition and cooling rates from the austenitic or the intercritical (ferrite-austenite) region, either during hot rolling or in the cooling section of the continuous annealing line.

#### 5.2.3.1. **1<sup>st</sup> Generation Advanced High Strength Steels**

The microstructure of this generation consists of ferrite and martensite/bainite. They were developed to combine strength and ductility. The ferrite matrix is ductile, favoring formability, while martensite and bainite are harder phases that increase strength. Bainite formation is preferred, as it is a more ductile phase compared to martensite. In AHSS, the other phases within the ferrite matrix significantly affect the mechanical properties and formability. The hardening mechanisms are not conventional, such as forming a solid solution or precipitates, but more complicated due to the existence of multiple phases. This class includes DP, TRIP, CP, and martensitic steels (MART) [4].

#### ➤ **Dual-Phase steels**

The microstructure of DP steels consists of martensite islands on a ferritic matrix. They are produced by heat treatments, in which the material is heated within the intercritical region, followed by quenching to room temperature. The difference in the microstructural components' mechanical properties contributes to the strength-ductility combination and gives great strain hardening ability (high  $n$ -value). DP steels have a low yield point and exhibit continuous yielding due to the creation of new dislocations in the ferrite matrix due to the transformation of austenite into martensite, which has high hardness and strength, but low ductility. These characteristics favor the absorption of energy during crash events. Their tensile strength is between 450-1200 MPa and depends on the volume fraction of martensite [29], [40], [48]. Usually, low carbon steels (0.08-0.12 % wt. C) are used, which might contain Mn, Si, and other alloying elements (Mo, Cr, Ni, W) in smaller fractions [8].

#### ➤ **TRansformation Induced Plasticity steels**

TRIP steels are lean alloyed steels with multi-phase microstructures consisting from a ferritic matrix (50 %), bainitic ferrite (35-40 %) and a fraction of retained austenite of up to 10 %-15 %. The production of TRIP steels is similar to that of DP. The annealing occurs within the intercritical region followed by bainitic isothermal quenching at an intermediate temperature within the bainitic region. During isothermal treatment, a most of the austenite transforms into bainite, while a part of it is retained as a consequence of its carbon enrichment above 1 %. During consequent quenching, the fraction of austenite that has not stabilized is transformed into martensite [9], which is not wishful. TRIP-assisted steels' main advantage is the balanced strength-ductility ratio, which is attributed to their microstructure and, more specifically, to the transformation of the retained austenite into martensite during deformation (TRIP effect). The excellent formability of TRIP

steels is attributed to the increasing high work hardening rate, which results from the transformation of the retained austenite into martensite, which also acts as a strain hardening mechanism, resulting in high strength and plasticity. TRIP steels, compared to DP, exhibit better formability for the same tensile strength [10]. However, the disadvantage of TRIP steels is that their strong alloying, required to stabilize the austenite at room temperature, increases the carbon equivalent, decreasing their weldability.

#### ➤ **Complex Phase steels**

The CP steels' microstructure consists of ferrite, martensite, bainite, and tempered martensite [8]. Their chemical composition is similar to that of DP and TRIP, with the difference that the carbon content is lower than 0.15 % in order to reduce the retained austenite fraction. At the same time, they contain alloying elements such as Nb, Ti, and V, which precipitate in the refined ferrite matrix in the form of carbides, nitrides, and carbonitrides. Delayed recrystallization and precipitation contribute to the refinement of the microstructure. CP steels have high strength, higher than 800 MPa, but less formability than TRIPs, while their yield point is higher than that of DP steels. The low content of alloying elements increases the weldability and reduces the cost [3, 8]. They are characterized by high energy absorption, hole expansion, and high residual deformation capacity. In the automotive industry, they are used as reinforcement in the passenger compartment's pillars, in the reinforcement of the doors and other parts of the body.

#### ➤ **Martensitic steels**

Martensitic steels (MART) consist of a matrix rich in martensite and small fractions of ferrite and/or bainite. They are produced by heating in the austenitic region or high in the intercritical region, followed by quenching in water to room temperature [11]. The presence of 0.09-0.23 % carbon increases the hardness of martensite, while alloying elements such as Mn, Si, Cr, Mo, B, V, and Ni improve hardenability [11]. Martensitic steels exhibit a UTS of about 1.2-1.5 GPa (UTS) and may reach 2 GPa [12]. The increase in strength is achieved by strengthening the martensite, accompanied by a loss of ductility. Their low ductility is sufficient for the intended applications in the car body but limits their formability. This led to the development of new forming methods (hot forming, hot stamping) resulting in the development of more advanced types of steel [4].

#### **5.2.3.2. 2<sup>nd</sup> Generation Advanced High Strength Steels**

This generation's steels offer an excellent combination of high strength and ductility due to the retainment of austenite at room temperature. Its stabilization is carried out by the high addition of  $\gamma$ -stabilizing elements, such as Mn [13]. This category includes TWIP and austenitic stainless steels, though they are not currently used in the automotive industry due to their high cost.

#### ➤ **Twinning-induced plasticity steels**

TWIP steels provide a combination of high UTS and excellent ductility [14]. They are austenitic steels, which during deformation, utilize the phenomenon of the formation of twins due to the very low energy of stacking faults, in contrast to TRIP steels, which exploit the mechanism of transformation of austenite into martensite

[29]. As the value of the applied stress to the material increases, the volume fraction of the twins in the microstructure increases, thus impeding the movement of the dislocations, thus increasing the strength through grain refinement hardening. This capability of TWIP steels gives them very high strength and ductility. TWIP steels have exceptionally high manganese content, ~ 22-28 % Mn [8].

### 5.2.3.3. 3<sup>rd</sup> Generation Advanced High Strength Steels

As imposed by the European Commission [1] and must be followed by the steel industry, the overall trend in the automotive industry is to decrease the vehicle weight in order to decrease emissions harmful to the environment. The efforts made by the steel industry in order to meet these requirements is by replacing existing HSS or AHSS grades with new steels that can provide higher mechanical strength values while maintaining competitive ductility levels. This way, less material is used during production without compromising the passengers' safety. Specifically, high-strength steels need to be replaced by steels with a higher UTS while maintaining almost the same ductility. Besides, these new grades must also be competitive cost-wise in order to be able to replace the currently used grades.

#### ➤ Q&P steels

Quenching & Partitioning (Q&P) steels are characterized by an excellent balance of very high tensile strength and good ductility with similar chemical compositions to conventional TRIP steels. They are produced through the Q&P process, consisting of a stage of isothermal quenching and an aging stage (partitioning). At the quenching stage, the steels are in the austenitic region. They are quenched at temperatures between the  $M_s$  and  $M_f$  temperatures to form the desired martensitic volume fraction alongside the existing austenite or ferrite. After the quenching stage, the steels are held at the same temperature, or higher, during the partitioning stage. The main idea of Q&P lies in the fact that the carbon contained in the already formed martensite diffuses through the martensite-austenite interface to the retained austenite. This results in a significant volume fraction of austenite retained at room temperature alongside ferrite; thus, achieving superior mechanical properties compared to conventional TRIP steels [8].

#### ➤ Medium Manganese Steels

MMnS have a manganese content of 3-12% wt. and are distinguished from steels with higher percentages of manganese ( $Mn > 15\%$ ), such as TWIP. They exhibit extremely high strength, higher than 1000 MPa, combined with an excellent ductility, which exceeds 25-30 %, thanks to their complex microstructure. In general, MMnS contain relatively low percentages in alloying elements that stabilize the austenitic phase at room temperature. Except for Mn, carbon does not exceed 0.4 % wt. while aluminum is present in contents around 3 %. With this composition, MMn steels consist of refined ferrite and austenite phases obtained by heat treatments of intercritical annealing. Through the conditions selected for the intercritical annealing and in combination with their chemical composition, the segregations of carbon and manganese from ferrite to austenite is possible, thus increasing its stability at room temperature [8].

These grades are considered the most commonly used grades in the automotive industry, though more grades will not be mentioned in this thesis. A trend can be found in the design of these grades. Specifically, the existence of bainite or retained austenite in the microstructure is preferred to maintain a good strength/ductility ratio, while martensite is essential for increasing the steel's strength. Also, the content of C and Mn is a crucial factor that determines the microstructural constituents and their properties. Considering these ideas for the development of AHSS, new methods emerge to produce new grades with the optimal properties that will meet the requirement imposed by the European Commission [1]. One of these methods is the application of rapid heating rates.

### **5.3. The Ultra-Fast Heat Treatment as an alternative process to produce new AHSS grades**

Over the last years, a new thermal treating process is under meticulous investigation as it intrigues both the automotive industry and academia. This method applies rapid heating rates during the annealing, followed by minimal soaking times and consecutive quenching [15–18]. Even though the application of rapid heating rates has been used in the past for surface hardening processes, it has not been applied yet as a thermal treatment for bulk specimens. The Ultra-Fast Heating (UFH) process attracts so much interest in its complexity to comprehend the phenomena that occur in such short times and the challenge to control such thermal treatments. Short heating times lead to different transformation mechanisms, leading to a heterogeneous microstructure concerning its grain size and chemical composition. Both of these affect the transformations that occur during the quenching, and therefore, heterogeneity is expected in the microstructure of the final product. Refined mixed microstructures consisting of all martensite, bainite, ferrite, retained austenite, cementite, and other carbides are expected from this treatment. Each of these constituents favors different properties of the material. The advantage of UFH treatment is that complex microstructures are achieved in very short times while it would need much longer periods in conventional heating lines. The ability to explain and control the formation of such complex microstructures can constitute an alternative for the production of AHSS steels that can offer new choices of lean alloyed, optimized steel grades and improve the production process of already existing grades.

In frames of the current research, an effort is made to comprehend the phenomena that occur during such short heating times and the microstructure's evolution. To achieve this, scanning and transmission electron microscopy is used alongside electron backscatter diffraction and electron dispersive spectroscopy to analyze the constituents of the final microstructure. Simulation software is used to define the microstructure grain size and composition at peak temperature and better understand the evolution of the microstructure in each stage of the treatment. Finally, an attempt is made to correlate the microstructure with the material's properties and specifically the stress and strain. Three sets of experiments have been conducted, one at small scale samples, using dilatometers for the heat treatment, the second one to study the treatment in large samples in order to check if this treatment can be sustainable in the industry, and finally, an effort is made to produce existing steel grades via UFH.

The purpose of this dissertation is to investigate the production of steels with characteristics similar to those of Advanced 3<sup>rd</sup> Generation Steels, after the application of rapid thermal cycles. In particular, the coexistence of martensite, carbides, lower bainite and traces of retained austenite, which are key components of these steels, was sought. During the experimental research, with the characterization of the microstructure, the presence of bainite and retained austenite was indeed observed, the formation of which was not expected due to the minimum available time of the heat treatment. Therefore, it is proven experimentally that it is possible to produce this type of steels in a short time, which are currently achieved by conventional, time-consuming methods.

The thesis tends also to enhance the overall knowledge on the UFH processes, to provide a better understanding of the transformation mechanisms that occur during rapid heat treatments, and to be the stepping stone on further research that can lead to the improvement of future transportation. In particular, with the application of high heating rates, the effect of UFH is studied on the dissolution of cementite, diffusion of carbon, the nucleation of austenite, and the recovery and recrystallization processes during heating. Depending on these mechanisms, the transformation products are studied upon cooling.

The present study is part of the scientific work of the research team of Assoc. Professor Dr.-Ing. S. Papaefthymiou on the application of rapid thermal cycles in steels. It complements the dissertation of Dr. Bouzouni on the analysis of the phenomena encountered in these treatments via simulation software. Such studied phenomena are the dissolution of cementite and the kinetics of the austenite formation during UFH.



## 6. Theoretical Background

### 6.1. Steel and its phases

Iron (Fe) and carbon (C) are the basic elements of all steel. However, depending on the application, other alloying elements may be added to improve the properties and meet each application's requirements. One way to influence the properties of the final product is by changing the steel's chemical composition with the addition of alloying elements. The other way to affect the properties is by heat treatment, which depends on the fact that iron has different crystallographic lattices at different temperatures. Carbon can be considered a small interstitial atom that fits into the octahedral voids formed in the iron lattice. This results in the strengthening of steel, and it gives the ability to harden by heat treatment.

#### 6.1.1. Phase diagram

The phase diagram is a graph that shows the equilibrium conditions for the thermodynamically distinct phases. Depending on the carbon concentration in the steel, the diagram is divided into four parts:

- hypo-eutectoid steels, which contain less than 0.80 wt. % of carbon;
- eutectoid steel, which contains 0.80 wt. % of carbon;
- hyper-eutectoid steels, which contain more than 0.80 wt. % of carbon;
- cast irons, which contain more than 2 wt. % of carbon.

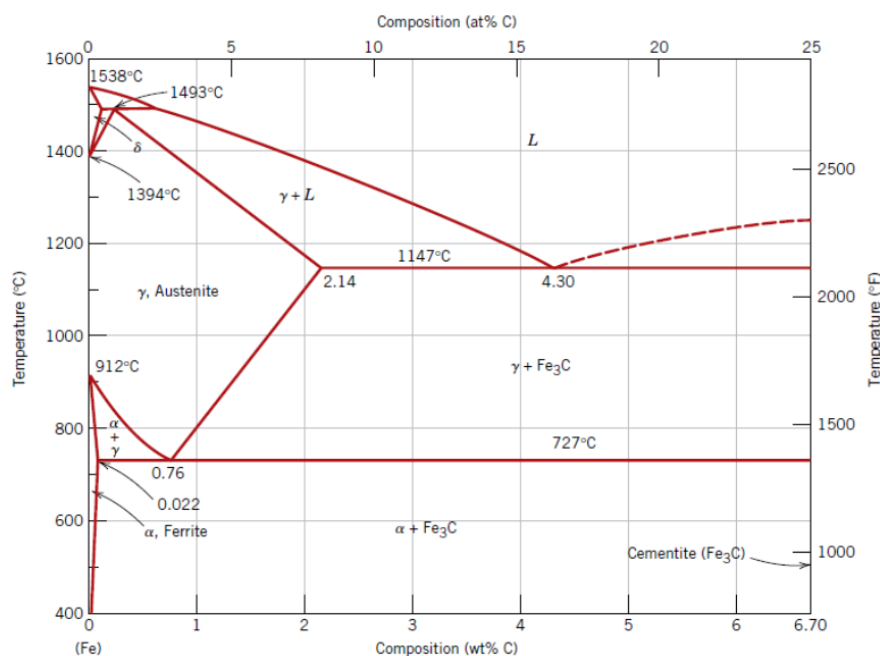


**Figure 6.1:** The Fe-C phase diagram, including the transformation temperatures [19].

In this thesis, only the hypo-eutectoid part of the diagram, where the carbon content is less than 0.80 wt. % is considered. Typical hypo-eutectoid steel at room temperature consists of a pearlite-ferrite microstructure with their volume fraction depending on the steel's carbon content. To further influence the steel properties, more alloying elements may be added, such as manganese, chromium, vanadium, aluminum, etc. [8]. The effect of each alloying element on the microstructure and properties is analyzed later in this thesis. In general, two types of alloying elements can be distinguished depending on their solubility in the iron matrix. These may be interstitially dissolved elements, like carbon and nitrogen, usually located in the octahedral voids, and substitutionally dissolved elements, like manganese, chromium, etc., located at the same lattice sites as iron atoms.

### 6.1.2. Ferrite

Ferrite ( $\alpha$ -Fe) is the body-centered cubic (BCC) allotriomorph of iron. Iron atoms are placed in the center and on the corners of the unit. Dissolved carbon atoms are located at interstitial sites, with a solubility up to 0.025 wt. % at 723 °C. The solubility of C in ferrite decreases to 0.008 wt. % at room temperature. Below the Curie temperature (771 °C), ferrite exhibits magnetic behavior and is characterized as a ferromagnetic material, while above this temperature, it becomes paramagnetic. The ferrite microstructure is the principal constituent found in carbon steels. Because of the low carbon content, the ferrite microstructure is soft and can be easily deformed. It may also contain other alloying elements such as manganese or silicon. Ferrite may be found in different forms. Polygonal ferrite appears dimensionally equal in all directions (equiaxed morphology). In cold-rolled steels, the ferrite obtains an elongated morphology. In contrast, in heat-treated carbon steels, it may have an epitaxial morphology meaning that the new ferrite phase grows epitaxially on the existing ferrite grains [20].

### 6.1.3. Austenite

Austenite is the face-centered cubic (FCC) allotriomorph of iron. Iron atoms are placed on the corners and in the centers of the faces of the unit. High solubility carbon atoms present in carbides are dissolved at the octahedral interstitial sites of austenite during heating. The FCC unit cell defines the arrangement of iron atoms in crystals of austenite. A crystal consists of a large number of atoms and its structure consists of close-packed planes of iron atoms stacked in a sequence that repeats every three layers. Three face diagonals define the orientation of each of these planes in the unit cell. The close-packed atom planes described by the {1 1 1} Miller indices are the slip planes on which the dislocations move or constitute the boundaries of annealing twins. It is possible that during some heat treatments, austenite is retained at room temperature. That austenite is considered ductile and does not undergo the ductile to brittle transition to which body-centered cubic ferritic microstructures are susceptible [4].

### 6.1.4. Martensite

At high cooling rates and in the case that the alloying of the steel is such to prevent diffusion-controlled transformation to ferrite, pearlite, or bainite, the thermodynamic driving force for the transformation of

austenite leads to the formation of body-centered crystals by a diffusionless, shear-type solid-state phase transformation and the product is called martensite. Trapped carbon atoms create a body-centered tetragonal unit cell with one axis ( $c$ ) longer than the other two axes ( $a$ ), while higher carbon content leads to greater tetragonality. Carbon atoms occupy the octahedral interstitial sites in the body-centered tetragonal unit cell of martensite. The shear martensitic transformation produces crystals with planar geometries. These geometries are lath or board-shaped in low and medium-carbon steels, while in high-carbon steels, they are plate-shaped. The formation of martensite starts at a temperature called  $M_s$ . This temperature is strongly affected by the content of carbon and other alloying elements in the steel [21], and since the transformation is diffusionless, the  $M_s$  is not affected by time.

Groups of martensite crystals may form blocks with identical or very close crystallographic orientations [22]. In each of these crystals, a high density of dislocations is expected. Small amounts of retained austenite can also be found between parallel lath martensite crystals, even in low-carbon steels.

### **6.1.5. Bainite**

Bainite is a microstructure component. Its structure consists of thin ferrite plates and cementite. It has a high dislocation density, while bainitic ferrite's dislocation density increases with decreasing transformation temperature [23]. The effect of stress and strain on bainite transformations is similar to that on martensite [24, 25]. Therefore, when the bainite transformation occurs in a plastically deformed austenite grain, the extent of transformation is reduced [24].

Bainite is distinguished into the upper and lower bainite. According to Matas & Hehemann [26], the difference between these two morphologies results from the competition between the carbide precipitation rate from supersaturated ferrite and the rate of carbon rejection from supersaturated ferrite to austenite. Upper bainite forms at higher temperatures where the carbon diffuses rapidly. The time required for the decarburization of a supersaturated ferrite plate is smaller than the time needed for carbide precipitation within the plate. The surplus carbon in the supersaturated ferrite is thus rejected into the adjacent austenite. The carbon diffusion rate decreases as the transformation temperature decreases and part of the carbon is precipitated as fine carbide particles inside the ferrite plates. This residual carbon enriches the surrounding austenite, and interplate carbides may be precipitated. Thus, the lower bainite is formed. According to Pickering [23], the carbon content of austenite undergoing the transformation affects the concentration gradient, which in turn determines the rate at which carbon diffuses from the austenite-ferrite interface.

As will be mentioned later, the bainitic ferrite grows in the form of plates adjacent to each other in groups called sheaves, Aaronson [27]. The constituent plates are also called sub-units. The sub-units within a sheaf have approximately the same crystallographic orientation, and therefore neighboring sub-units are separated by only a small angle boundary. According to Zajac et. al. [28], the misorientation angle between two bainitic ferrite laths was experimentally found to be between 48-55°, lower than the corresponding angle between two

martensite laths that is found to be between 56-65°. According to Marder et. al. [25], the ferrite sub-units' longitudinal direction is parallel to the closed packed direction  $\langle 1\ 1\ 1 \rangle_\alpha$ .

Bhadeshia [24] lists the orientation relations between ferrite and cementite in bainite, as seen below.

$$\begin{aligned} & \{0\ 0\ 1\}_\theta // \{2\ 1\ 1\}_\alpha \\ & \langle 1\ 0\ 0 \rangle_\theta // \langle 0\ \bar{1}\ 1 \rangle_\alpha \end{aligned}$$

While a major  $\alpha / \theta$  orientation relationship found in tempered martensite was:

$$\{0\ 0\ 1\}_\theta // \{2\ \bar{1}\ 5\}_\alpha$$

with  $\langle 1\ 0\ 0 \rangle_\theta$  within 2.6° from  $\langle 3\ \bar{1}\ 1 \rangle_\alpha$  and  $\langle 0\ 1\ 0 \rangle_\theta$  within 2.6° from  $\langle 1\ 3\ 1 \rangle_\alpha$ .

In upper bainite, the large number of observed  $\alpha / \theta$  orientation relationships can be explained by assuming that the cementite precipitates from the austenite according to the Pitsch variant [29, 30]:

$$\{0\ 0\ 1\}_\theta // \{2\ \bar{2}\ 5\}_\gamma$$

with  $\langle 1\ 0\ 0 \rangle_\theta$  within 2.6° from  $\langle \bar{5}\ 5\ \bar{4} \rangle_\gamma$  and  $\langle 0\ 1\ 0 \rangle_\theta$  within 2.6° from  $\langle \bar{1}\ \bar{1}\ 0 \rangle_\gamma$ .

The  $\alpha / \gamma$  ratios can be derived from the  $\gamma / \theta$  ratios as the ferrite is a variable in the  $\alpha / \gamma$  Kurdjumov - Sachs orientation ratio [31, 32].

In the lower bainite, cementite is precipitated from the carbon saturated ferrite. The  $\theta / \alpha$  orientation relation that results for the lower bainite can be expressed as follows:

$$\begin{aligned} & \{1\ 0\ 3\}_\theta // \{1\ 0\ 1\}_\alpha \\ & \langle 0\ 1\ 0 \rangle_\theta // \langle 1\ \bar{1}\ \bar{1} \rangle_\alpha \end{aligned}$$

Also, the cementite habit plane within the lower bainitic ferrite is  $(112)_\alpha$  corresponding to  $(101)_\gamma$ .

### 6.1.6. Cementite

Cementite is also referred to as  $\theta$  and is the most common precipitate found in steels [33]. It has an orthorhombic crystal structure and may precipitate from either supersaturated ferrite or austenite. In some cases [24, 34, 35], it has been found that it may precipitate at temperatures below 126 °C and in short times that do not allow any substantial diffusion of iron atoms, although the long-range diffusion of carbon atoms is mandatory. Therefore, it has been suggested that the cementite lattice is possible to be generated by the deformation of the ferrite lattice, alongside the necessary diffusion of carbon into the appropriate sites [34]. It was also shown [36] that the plane of precipitation of cementite from ferrite is the  $\{1\ 0\ 1\}_\theta // \{1\ 1\ 2\}_\alpha$ . This is consistent with the habit plane that contains the direction of reasonable fit between the  $\theta$  and  $\alpha$  lattices [34],

which is the  $\langle 0\ 1\ 0 \rangle_{\theta} // \langle 1\ 1\ 1 \rangle_{\alpha}$ . If cementite is formed during the tempering of martensite, it may assume many crystallographic variants of this habit plane in any martensite plate. In the case of lower bainite, only one such variant is usually found, with the habit plane inclined at  $60^\circ$  to the axis of the plate [37]. Cementite which precipitates from austenite exhibits the Pitsch [30] orientation relation with  $[001]_{\theta} // [2\ 2\ 5]_{\gamma}$  and  $[1\ 0\ 0]_{\theta} // [5\ 5\ 4]_{\gamma}$ .

Pearlite is a complex eutectic phase structure that is characterized morphologically by alternating ferrite and cementite lamellae. Therefore, pearlite is not a phase but a microstructure component. When eutectic steel is heated in the austenitic region and then slowly cooled, then the eutectic reaction will completely transform the austenite into pearlite. The nucleation of ferrite initiates at the boundaries of austenite grains and grows in the form of parallel ferrite plates and cementite lamellae until it is completely transformed. During the slow cooling of eutectoid steel, a percentage of austenite is transformed into ferrite as it passes through the intercritical region ( $\alpha + \gamma$ ) of the Fe-C diagram.

In contrast, the remaining austenite is continuously enriched in carbon due to the low solubility of carbon in ferrite compared to austenite. If the austenite acquires the eutectic composition (0.8% C), then the eutectic reaction transforms the austenite into pearlite until the steel is cooled to room temperature. The mechanical hardness of the pearlite structure depends on the interlamellar distance between the cementite lamellae. As pearlite contains ferrite, it can be described as ductile, although its ductility is much lower than ferrite. This decrease is attributed to the  $\alpha$ -Fe<sub>3</sub>C interfaces that may act as crack initiation sites.

## 6.2. Phase Transformations

### 6.2.1. Diffusion transformations

Diffusion is one of the most important mechanisms that control the kinetics of a metallurgical process or phase transformation. Fundamental processes in Physical Metallurgy, such as the development of a new phase, the homogenization of a cast alloy, and the carbonization of steel, are carried out by moving atoms in the crystal lattice, that is, by diffusion. Diffusion is defined as the movement of atoms at distances at least equal to the grid parameter.

Diffusion takes place so that there is always a reduction in free energy. Therefore, it is possible to observe the diffusion of an alloying element from areas with high concentration to areas with low concentration and vice versa. The diffusion of the components causes a reduction in free energy and is carried out from high to low chemical potentials. Therefore, the driving force for diffusion is better expressed as the slope of the chemical potential  $dm/dx$  of a component. The diffusion stops when the components' chemical potentials in the two solid solutions are equalized, and thermodynamic equilibrium is reached. The most common case involves diffusion from areas with high to low concentration areas to eliminate concentration differences. For this reason, and because in practice, it is easier to measure differences in concentration than differences in chemical potential, diffusion is associated with the concentration of  $dc/dx$  [38].

### 6.2.1.1. The mechanisms of diffusion

The mechanism by which atoms move within the crystal lattice depends on the type of solid solution (interstitial or substitutional). The interstitial atoms occupy the vacant interstitial sites, which for BCC and FCC are the octahedral ones. In most cases, these solids are sparse, and therefore not all interstitial sites are occupied. Thus, an interstitial atom is always surrounded by another empty interstitial site. Therefore, the interstitial atom can move to another vacant interstitial site since there is enough thermal energy to pass between two grid atoms. In steels, carbon occupies interstitial positions in the crystal lattice of iron. Thus, the carbon diffusion takes place with successive jumps from one interstitial site to another. In the case of diffusion in solid substitutional solutions, the atoms' movement can be done, as long as there is an adjacent empty lattice position, i.e., a vacancy. Thus, if the atom acquires enough oscillation energy, it can perform a successful leap and move to the next vacancy. This movement is equivalent to moving the vacancy in the position held by the atom.

For this reason, this mechanism is often called "vacancy diffusion". Two factors must be taken into account for substitutional diffusion. First of all, there must be empty lattice positions, i.e., vacancies, and atoms must acquire sufficient thermal energy so that their oscillation around their grid position can lead to a successful leap towards the vacancy. Both factors are highly dependent on temperature. This is due to the strong temperature dependence of the diffusion.

Volume diffusion occurs when the interstitial and substitutional movement of atoms in the crystal lattice takes place. The imperfections of the structure often favor the diffusion. The most common type of diffusion is boundary diffusion, in which atoms move through the grain boundaries, where the arrangement of atoms is looser. In this case, the diffusion is faster than the volume diffusion. In fact, in fine-grained metals, diffusion is faster than in coarse-grained metals because the former contains more grain boundaries. This affects metals' deformation at high temperatures, i.e., cracking, where diffusion plays an important role. Thus, coarse-grained metals are more resistant to cracking than fine-grained metals. Another error of the structure, which helps diffusion, is the linear dislocation. The space below the extra level of dislocation, that is, the nucleus of disorder, forms a tunnel or pipe through which atoms can move. This diffusion is called dislocation pipe diffusion. Both boundary and linear diffusion occur at a higher rate than volume diffusion. The grain boundaries and dislocations are high-diffusivity paths.

According to Fick's first law, the flow of an element is proportional to the concentration's degradation. It is assumed that diffusion takes place with atom leap in empty interstitial positions. For example, in austenite, the solid solution is so dilute that six empty interstitial sites surround each carbon atom. The leaps that carbon can make to these interstitial sites are completely random, meaning there is the same chance of occupying any six empty interference positions. Also, the frequency of the leaps is independent of the concentration of carbon in the austenite. Thus, Fick's first law is given by Equation 1:

$$J = -D * \left(\frac{\theta c}{\theta x}\right) \quad \text{Eq. 6.1.}$$

which correlates the flow of interstitial atoms with the inclination of the  $\theta c / \theta x$  concentration. The ratio  $D$  is called the diffusion coefficient and depends on the temperature and the composition and has units  $m^2 / s$ . According to the diffusion coefficient, carbon diffusion is faster in solids with higher carbon content because the carbon in interstitial sites deforms and "opens" the grid. This means that carbon jumps from one place to another are easier. The time change of an element's composition profile is described by Fick's 2nd law. The profile is determined by solving the diffusion equation. The flow at each point depends on the value of the diffusion coefficient  $D$  and the slope  $\theta c / \theta x$ . Thus, Fick's 2nd law is given by Equation 2:

$$\frac{\theta c}{\theta t} = \frac{\theta}{\theta x} * (D * \frac{\theta c}{\theta x}) \quad \text{Eq. 6.2.}$$

In the case that the diffusion rate does not change with the concentration of carbon atoms, then the equation is:

$$\frac{\theta c}{\theta t} = D * \frac{\theta^2 c}{\theta^2 x} \quad \text{Eq. 6.3.}$$

If the  $\theta c / \theta t$  sign is positive, then the concentration of carbon atoms increases with time, while if it is negative, then the concentration decreases with time at that point. In substitutional solid solutions, the diffusion causes macroscopic mass flow (Kirkendall effect: The macroscopic mass flow in a diffusion pair, resulting from the difference of the intrinsic diffusion coefficients) [39, 40].

#### 6.2.1.2. The role of diffusion

Diffusion has significant effects on several metallurgical processes:

- Diffusion is the main mechanism for performing diffusive phase transformations. For example, the formation of pearlite in steels during the slow cooling of austenite is carried out by diffusion of carbon and other alloying elements. If the cooling of the austenite is too fast so as not to give the necessary time for the diffusion, then martensite is formed instead of pearlite; this martensitic transformation is non-diffusive.
- Diffusion plays an important role in shaping the structure of castings. When solidifying an alloy, the alloying elements enter from the liquid to the solid phase. Most of the time, the diffusion in the solid is slow, resulting in segregation. Areas that were first solidified are poor in alloy elements, while areas that were solidified last are rich in alloys. The differentiation of castings is an undesirable phenomenon, and for this reason, after the casting, heat treatment is carried out for the homogenization of the casting. Homogenization is caused by the diffusion of alloying elements.

- Diffusion plays an important role in the deformation of metals at high temperatures, i.e., during cracking. The plastic deformation of the metals is carried out by dislocation slip. At high temperatures, the dislocations, in addition to slipping, also experience "climb". Climbing is essentially a change in the slip plane if, for some reason, the dislocation is prevented from slipping on a plane and is accomplished by diffusing atoms to or from the dislocation. By climbing, the irregularities can change the slip plane and continue to create deformation. At even higher temperatures, plastic deformation is caused exclusively by diffusion without the need for slipping of the dislocations. This deformity is called diffusional flow and is carried by diffusion of atoms in the grains, from tensile to compressive regions. Mass transfer changes the shape of the grains and causes the sliding of the grain boundaries.
- With the help of diffusion, many thermal and surface treatments of metals are carried out. For example, carbonation is carried out by diffusion of carbon to enrich the steels' surface, to increase surface hardness, and improve the anti-friction properties. Another heat treatment carried out by diffusion is the tempering of steels. The martensite, which results from the abrupt cooling of the austenite during quenching, is essentially an ultra-solid solid Fe-C solution, making it very hard but at the same time brittle. With the heating of the martensite, the carbon diffusion for the formation of cementite is activated. The crystal lattice of iron relaxes, and the hardness decreases while at the same time, the ductility is restored [38].

### 6.2.2. Alloying elements

To date, two basic principles have been used to improve the properties of steels, and in particular, to improve strength and ductility. The first is the alloying of steel with elements (e.g., nickel), which dramatically increases the cost of the material and adversely affects the raw materials' viability. Each element has a different effect on the properties and microstructure of the material. The following information is recorded:

- **Carbon (C):** It is the most important steel element, contributing significantly to their strengthening. It is necessary to form micrographic components such as pearlite, bainite, martensite, cementite, or other carbides. Microstructures consisting of one or more constituents can have a wide range of mechanical properties and construction characteristics. Increasing the carbon content increases the hardness, strength, and abrasion while reducing the ductility, brittleness, and weldability. Finally, carbon tends to diffuse to a relatively greater extent than other alloying elements [41].



**Table 6.1:** The pros and cons of the addition of carbon in the chemical composition of the steel.

Used concentrations	Positive effects	Negative effects
0.15-0.30 wt.%	<p><math>\gamma</math> stabilizer</p> <p>Determines phase distribution</p> <p>Determines retained austenite stability</p> <p>Determines the amount of second phase</p> <p>Strengthens martensite</p> <p>Strong hardenability agent</p>	<p>Decreases weldability</p> <p>Reduces toughness</p>

- **Manganese (Mn):** It is commonly found in all industrial steels with a content of more than 0.2 wt.%, which improves the processing capacity of steel. The addition of Mn also contributes to hardness and strength, but to a lesser extent than carbon. If the percentage of manganese increases, the solubility and weldability are reduced, but again not to the same degree as carbon. Manganese has a lower tendency to macro-segregation than other common elements. It is useful in surface quality for a wide range of carbon content. Finally, it binds Sulfur (S), which comes from the casting and acts negatively on the properties of steel, forming manganese sulfides (MnS) while it is considered a  $\gamma$ -stabilizer and reduces the  $A_1$  and  $M_s$  temperatures [41].

**Table 6.2:** The pros and cons of the addition of manganese in the chemical composition of the steel.

Used concentrations	Positive effects	Negative effects
1.50-2.00 wt.%	<p><math>\gamma</math> stabilizer</p> <p>Reduces carbon activity in <math>\alpha</math></p> <p>Strengthens ferrite</p> <p>Retards pearlite and bainite formation</p> <p>Increases the transformation temperatures</p> <p>Decreases C solubility in ferrite</p> <p>Regular solid solution hardening</p>	<p>Carbide formation</p>

- **Silicon (Si):** It is one of the key ingredients added to steel for deoxidization. The percentage of this element in steel, which is not always noted in the chemical composition, depends on the deoxidization technique determined for the product. In "Si killed steels" (deoxidized with Si steels), the Si ranges from 0.15-0.3%, while in "semi-killed steels", the content is lower. If other deoxidizers are used, the Si percentage may be lower. In low carbon steels, Si is usually harmful to surface quality. Si slightly increases the hardness of the ferrite without causing a large reduction in ductility, while at the same time, it has a small tendency to differentiate. High Si levels in steel lead to a reduction in the formability of the steel and create problems both during galvanizing (hot-dip galvanizing) and during the welding of steel due to creating a thin layer of oxides ( $\text{SiO}_2$ ,  $\text{MnSiO}_4$ ). Also, silicon content over 0.15 wt.% contributes to the formation of carbides and increases the residual austenite stability [41].

**Table 6.3:** The pros and cons of the addition of silicon in the chemical composition of the steel.

Used concentrations	Positive effects	Negative effects
0.10-1.50 wt.%	<ul style="list-style-type: none"> <li><math>\alpha</math> stabilizer</li> <li>Increases carbon activity in <math>\alpha</math></li> <li>Strengthens ferrite</li> <li>Prevents <math>\text{Fe}_3\text{C}</math> formation</li> <li>Solid solution strengthening</li> </ul>	Surface quality

- **Phosphorus (P):** Increases the hardness and strength of steels by significantly reducing ductility, brittleness, and impact resistance, especially in quenched and tempered steels. It increases the sensitivity of "medium carbon" steels, especially in combination with chromium (Cr), to tempered steels. P can be added intentionally to improve formability and corrosion resistance [41].

**Table 6.4:** The pros and cons of the addition of phosphorus in the chemical composition of the steel.

Used concentrations	Positive effects	Negative effects
0.01-0.30 wt.%	<ul style="list-style-type: none"> <li><math>\alpha</math> stabilizer</li> <li>Increases carbon activity in <math>\alpha</math></li> <li>Retards the <math>\text{Fe}_3\text{C}</math> precipitation</li> <li>Strengthens ferrite</li> </ul>	<ul style="list-style-type: none"> <li>Segregation</li> <li>Toughness</li> </ul>

- **Copper (Cu):** Copper has a moderate tendency to segregate. In remarkable percentages, it is harmful to heat treatment, as it causes hot cracking. It also adversely affects forging but does not affect arc welding as much. It degrades the quality of the surface and overrides the inherent defects of desulfurized steels [41].
- **Sulfur (S):** Causes a significant reduction in ductility, brittleness, impact resistance, and weldability. It also degrades formability, especially in hot rolling, while its presence increases the tendency to crack when quenching. It tends to segregate from other common elements. S is found mainly in the form of sulfate inclusions for this, and generally in steels, the tendency is the sulfur content remains below 0.05 % wt [41].
- **Aluminum (Al):** Usually used as a deoxidizer and to control grain size. When added to steels at specified rates, it controls the enlargement of the austenite grain to annealed steels and delays the precipitation of carbides. Compared to other alloying elements, aluminum is very effective in controlling grain size before quenching [41].

**Table 6.5:** The pros and cons of the addition of aluminum in the chemical composition of the steel.

Used concentrations	Positive effects	Negative effects
0.05-1.80 wt.%	<p><math>\alpha</math> stabilizer</p> <p>Strengthens ferrite</p> <p>Prevents Fe<sub>3</sub>C formation</p> <p>Refinement of Parent Austenite Grains</p>	<p>Increases M<sub>s</sub></p> <p>Castability</p>

- **Chromium (Cr):** This is a powerful carbide forming element. Chromium carbides increase the hardness and anti-friction properties of steel. Chromium also increases resistance in corrosion and oxidation and resistance to high temperatures under load and is therefore found in tool steels. The carbides form a solid solution with the austenite at a slow rate, so sufficient heating time before quenching is necessary [41].

**Table 6.6:** The pros and cons of the addition of chromium in the chemical composition of the steel.

Used concentrations	Positive effects	Negative effects
0.1-0.40 wt.%	<p><math>\alpha</math> stabilizer</p> <p>Retards ferrite and bainite transformation</p> <p>Increases the transformation temperatures</p> <p>Decreases C solubility in ferrite</p>	

- **Nickel (Ni):** When used as an alloying element in construction steels, it stabilizes the austenite phase. Because nickel does not form carbides in steel, it remains in the solid solution, giving the ferrite hardness and durability. It gives ductility and increases steels' hardenability while reducing the transition temperature from ductile to brittle fracture behavior. In combination with chromium, nickel produces steel alloys with better hardness, higher impact resistance, and better fatigue resistance than achieved in carbon steels [41].
- **Molybdenum (Mo):** Increases the hardness of steel and is particularly useful in maintaining it between specified limits. This element, especially in percentages between 0.15-0.3 wt%, minimizes steels' sensitivity to fragility after tempering. It is a powerful carbide forming element that simultaneously increases the hardenability of the steels. Molybdenum carbides form during tempering after quenching and cause secondary tempering of the steel. Mo delays the transformation of austenite to pearlite much more than the transformation of austenite to bainite. Thus, bainite can be formed by the continuous cooling of steels, which contain Mo. For low-grade steels in Si, Mo's addition lead to mechanical properties similar to high-Si steels and is therefore used to replace the latter when required [41].

**Table 6.7:** The pros and cons of the addition of molybdenum in the chemical composition of the steel.

Used concentrations	Positive effects	Negative effects
0.1-0.40 wt.%	<p><math>\alpha</math> stabilizer</p> <p>Retards pearlite/bainite transformation</p> <p>Suppression of bainitic transformation</p> <p>Ferrite forming element</p> <p>Strong solid solution hardening</p>	

- **Tungsten (W), Vanadium (V), Titanium (Ti), Niobium (Nb):** These are carbide, mainly, and nitride forming elements, which are elements of microalloying and contribute to the increase of hardness and strength with the formation of carbides (TiC) and nitrides (TiN). The formation of TiN helps to control the size of the grains at high temperatures (grain refinement). The presence of Ti appears to adversely affect the volume fraction of austenite, the stability of which is attributed to its enrichment in C because it binds C to form carbides.
- **Nitrogen (N):** Nitrogen is, along with carbon, an interstitial alloying element in steels. Nitrogen increases hardness and strength while reducing ductility. It is used to increase surface hardness. In fully deoxidized steels (deoxidation with Al), it forms a dispersion of AlN nitrides, impeding grain growth.
- **Cobalt (Co):** Cobalt is the only element that reduces the hardenability of steel, does not form carbides, and generally has little effect on steel's hardness. Its main action is to prevent the restoration of dislocations and grains' development during the annealing or tempering of steel. Thus, it contributes to the maintenance of mechanical strength at high temperatures and is used in shaping tools and refractory steels.

### 6.2.3. Crystallography of iron

Crystallographic orientation refers to how a crystallographic unit cell in a crystal structure is positioned in three dimensions of a fixed reference, usually related to the dimensions of the sample. In the case there is no texture (i.e., no preferred grain orientation) and all possible orientations may occur with equal frequency, the grains are oriented randomly, and the material has random texture, and its properties are isotropic.

Nevertheless, orientations in polycrystalline materials are rarely randomly distributed. In most materials, there are preferences for specific orientations caused by thermal stress gradients during solidification or by crystallization, followed by further thermo-mechanical processing. This occurrence is known as the preferred orientation or texture. The texture is significant as many material properties are anisotropic to the crystallographic structure and depend on it.

In order to describe the orientations of crystallites in a polycrystalline material, a coordinate system  $K_s$  needs to be defined. The selection of these fixed coordinates is arbitrary. However, in the case of a sheet, the axes conventionally coincide with the rolling direction (RD), transverse direction (TD), and normal direction (ND). For each crystallite, a second coordinate system  $K_c$ , which is fixed related to the crystal axes, is selected. These axes can be arbitrarily chosen, but they must be all the same for each crystallite. For cubic crystal symmetry the cube edge directions [100], [010] and [001] are usually chosen. The definition of the crystallographic orientation of grain is '*the position of the crystal coordinate system with respect to the reference coordinate system*'. Due to crystal symmetry, the choice of the crystal reference system  $K_c$  is not unique, and thus different solutions of the orientation matrix occur, of which the number depends on the sample and crystal symmetry. In the case of cubic crystal symmetry, there are 24 symmetry axes [42].

### 6.2.3.1. Grain boundaries and interfaces

The nature of any boundary depends on the two adjacent grains' misorientation and the orientation of the boundary plane between these grains. A **grain boundary** is a boundary between two adjacent grains with the same crystal structure but different crystal orientations. An **interphase** is a boundary between two neighboring grains of different crystallographic structures. Both of them are interfaces; nevertheless, the former is homophasic interfaces, and the latter are heterophasic interfaces. In one way, the interface is seen as a boundary between two crystallites that differ in their crystallographic orientations. Then the interface is a plane between these crystallites with several degrees of freedom. There are eight degrees of freedom, five of which are macroscopic, and three are microscopic. The three microscopic degrees of freedom refer to translations of the atoms parallel and perpendicular to the interface. These translations minimize the free energy of the interface. The local atomic array may differ at different positions of the interface. The microscopic degrees of freedom are difficult to determine because interfaces can be micrometers in length. The misorientation describes the macroscopic degrees of freedom between the grains, which take up three degrees of freedom, and the normal of the interface plane in one of the grains, which takes up two degrees of freedom. Alternatively, interfaces can be seen as lattice defects, such as strains and dislocations. These lattice defects can have different geometries, such as long-range order or compatibility between the adjacent grains. When two different phases co-exist in an alloy, heterophasic interfaces are located between these phases. These interfaces can be coherent, semi-coherent, or incoherent. A coherent interface is created when the two crystal structures adjoined in the interface plane match perfectly and are continuous across the interface. This is possible if the interfacial plane has the same atomic configuration in both phases, which requires the two crystals to have an orientation relation. Even when the atomic distance is not the same, coherency is still possible if one or both lattices are strained. These coherency strains increase the grain boundary energy. For a certain misfit, it becomes energetically favorable to replace the coherent interface with a semi-coherent interface. A dislocation periodically replaces the misfit. When there is more than one dislocation per four atom planes perpendicular to the interfacial plane, the interface cannot be determined as coherent or semi-coherent and is called incoherent. Incoherent interfaces occur when the interfacial plane has a very different atomic arrangement in the two neighboring phases, so good matching is impossible across the interface [43–45].

### 6.2.3.2. Grain boundary energy

Grain boundaries have different properties than the lattice because there are excess free volume and a lowered atomic coordination. Since grain boundaries are defects, they have an energy associated with their non-equilibrium structure. When the misorientation is small, the excess free volume is also small while the atomic coordination is relatively high, which results in relatively low grain boundary energy. Small misorientations are mostly formed by a periodic dislocation distribution and are called low angle boundaries.

Austenite can transform into martensite ( $\alpha'$ ) in many steels, which has a body-centered tetragonal crystal structure, while ferrite ( $\alpha$ ) has a body-centered cubic crystal structure. During research on the martensite formation in steels, researchers found orientation relationships between austenite ( $\gamma$ ) and martensite. Four

different orientation relationships between  $\gamma$  (FCC) and  $\alpha$  (BCC or BCT) have been found by Bain [46], Kurdjumov and Sachs [31], Nishiyama [47], and Wassermann [48], and Greninger and Troiano [49]. The latter is an intermediate between the Kurdjumov-Sachs and the Nishiyama-Wassermann relationships. These relationships are shown in **Figure 6.2**. The face-centered cubic lattice can be considered as a body-centered tetragonal lattice with an axial ratio of  $\sqrt{2}$ . According to Bain [46], the  $\gamma \rightarrow \alpha$  transformation is equivalent to a shrinkage of the long axis direction of the tetragonal lattice and a uniform expansion in the perpendicular directions until its axial ratio is 1, and thus the lattice changes from tetragonal to cubic. Kurdjumov and Sachs [31] concluded that the  $\{1\ 1\ 1\}$  and  $\{0\ 1\ 1\}$  planes lie parallel to each other. As a result, the  $[1\ 1\ 1]$  direction of martensite and the  $[1\ 0\ 1]$  direction of austenite are parallel. They agreed with Bain on the relative displacement among atoms while re-arranging from one crystal structure to the other, specifically the shear along  $(1\ 1\ 1)_\gamma$ , but not on the orientation relationship between the  $\alpha$  and  $\gamma$  phase.

Orientation relationship	Lattice correspondences	Angle/axis pair	Alt.	Variants
Bain (B)	$\{001\}_\gamma // \{001\}_\alpha$	$45^\circ / \langle 0\ 0\ 1 \rangle$	3	3
	$\langle 110 \rangle_\gamma // \langle 100 \rangle_\alpha$		1	
Kurdjumov-Sachs (K-S)	$\{111\}_\gamma // \{011\}_\alpha$	$90^\circ / \langle 1\ 1\ 2 \rangle$	4	24
	$\langle 101 \rangle_\gamma // \langle 111 \rangle_\alpha$		3	
	Twin related variants		2	
Nishiyama-Wassermann (N-W)	$\{111\}_\gamma // \{011\}_\alpha$	$95.25^\circ / \langle 3\ 6\ 2 \rangle$	4	12
	$\langle 112 \rangle_\gamma // \langle 011 \rangle_\alpha$		3	
Pitsch	$\{010\}_\gamma // \{101\}_\alpha$	$95.25^\circ / \langle 6\ 3\ 2 \rangle$	4	12
	$\langle 101 \rangle_\gamma // \langle 111 \rangle_\alpha$		3	
Greninger-Troiano (G-T)	$\{111\}_\gamma // \{011\}_\alpha$	$44.23^\circ / \langle 3\ 2\ 15 \rangle$	4	12
	$\langle 5\ 12\ 17 \rangle_\gamma // \langle 7\ 17\ 17 \rangle_\alpha$		3	
Inverse Greninger-Troiano (G-T')	$\{5\ 12\ 17\}_\gamma // \{5\ 12\ 17\}_\alpha$	$44.23^\circ / \langle 2\ 3\ 15 \rangle$	3	12
	$\langle 111 \rangle_\gamma // \langle 011 \rangle_\alpha$		4	

**Figure 6.2:** Orientation relationships between austenite and ferrite [42].

The orientation relationships have variants. Because of symmetry, the number of variants differs in each orientation relationship. The differences are due to the symmetry axes of the corresponding planes and directions.



### 6.2.4. Recrystallization of Ferrite

#### 6.2.4.1. The process of recrystallization

The heating of eutectoid steels above the  $A_{c1}$  temperature leads to ferrite recrystallization that determines the grain size and the properties of the ferrite phase. As mentioned above, austenite initially forms at cementite particles along the boundaries of ferrite grains. Nevertheless, the conversion from austenitization in a recrystallized ferrite matrix to the occurrence of parallel recrystallization and austenitization radically changes the final structure. A random spatial distribution of austenite is detected if recrystallization was completed before austenitization. In a non-recrystallized structure, austenite first forms at cementite particles lengthways the boundaries of non-recrystallized elongated ferrite grains so that it can lead to a formation of austenite aligned in the rolling direction enabling banded morphology [50].

Depending on the heating rate up to the intercritical temperature range, the level of ferrite recrystallization, and the conditions of austenite formation vary in a large way. The reheating conditions influence the microstructures. Depending on the cooling rate, martensite and bainite can be formed, austenite can be retained, and cementite and other carbides can be precipitated. If the austenitization process has not been completed, these microstructural constituents will coexist with the recrystallized ferrite that has not been transformed into austenite. Additionally, the ferrite grain size is larger in the case of slow heating rates and the amount of recrystallized ferrite increases with holding time.

Furthermore, the ferrite to austenite phase transformation happens when reaching the eutectoid temperature. These two phenomena take place with their own kinetics. For slow heating, ferrite recrystallization and austenite formation are entirely disconnected phenomena. This means that austenite formation starts after the end of the ferrite recrystallization. In fast heating, these phenomena are being overlapped. Therefore, ferrite recrystallization is strongly delayed, while austenite nucleation appears to happen more extensively. It can be assumed that deformation defects become potent nucleation sites for austenite at the expense of ferrite recrystallization. This distribution of fine austenite precipitates stabilizes the deformation structure and thus delays ferrite recrystallization. As mentioned above, the amount of austenite depends on both the reheating temperature and the heating rate.

Additionally, it has been observed that the amount of austenite decreases with the holding time in the case of fast heating. It can be assumed that these phenomena outcome from a shift in the thermodynamic conditions prevailing at the ferrite – austenite interface. Concerning fast heating, the austenite starts to form under para-equilibrium conditions. Substantial nucleation and fast growth lead to a large proportion of austenite [51]. During recrystallization, the deformed ferrite grains are being transformed into more equiaxed grains. The fraction softening of ferrite can be obtained from the hardness:

$$X = \frac{H_0 - H}{H_0 - H_{\text{Rex}}} \quad \text{Eq 6.4.}$$

$H_0$  is the initial microhardness of ferrite in the as-cold rolled steel,  $H$  is the microhardness after a given annealing condition, and  $H_{\text{Rex}}$  the microhardness corresponding to fully recrystallized steel [52].

The recovery process can be distinguished into three steps; recovery, recrystallization, and grain growth, and is a process that reduces the total energy of the system.

#### 6.2.4.2. Thermodynamics

As is the case with most processes in nature, all systems tend to decrease their internal energy. In phase transformations, the driving force is the difference in the Gibbs free energy between the initial and final state. During thermomechanical processes, such as (hot and) cold rolling, only a fraction of the total energy will be stored in the material. The major fraction of the total consumed energy will be dissipated as heat. The stored energy value depends on impurities, temperature, initial grain size, and total deformation.

As mentioned before, grain boundaries denote an increase in the internal energy as a larger number of atoms will be located in incoherent atomic positions. Elongated grains, in that way, increase the energy state of the system. Another factor contributing to the increase of the stored energy is the level of deformation and, thus, the presence of dislocations in the microstructure [53]. The formation of dislocations occurs when plastically deforming a grain in order to accommodate for the change of the grains' shape, i.e., during cold rolling. The combination of the energy increase that occurs by the higher grain boundary fraction and the increase in dislocation density are the main contributing factors to the total stored energy. This higher energy state is the driving force for recrystallization [54]. It has been observed that dislocations tend to mobilize and form sub-grains when there is enough energy to overcome the activation barrier. The energy contributed to these boundaries depends on the size and misorientation between the sub-grains.

#### 6.2.4.3. Driving force for recrystallization

A high deformation rate is introduced in the material during cold rolling, which translates to a high dislocation density that corresponds to a high free energy state. When given enough energy (through heating) to overcome an activation barrier, the material will tend to lower its free energy.

This takes place by the formation of sub-grains, recrystallization, and grain growth. During the first stage, the dislocations will mobilize and annihilate each other if they have opposite orientation, reducing the total dislocation density. The annihilation and movement of dislocations will lead to the formation of sub-grains, and this process is called recovery. Recovery is a thermally activated process, and different phenomena are more pronounced with increasing temperature, such as the annihilation of dislocations, the coalescence of sub-grains, etc. The second stage is recrystallization. The total free energy is further reduced by further reduction of dislocation density. The angles of the sub-grain boundaries increase, and grain boundaries are formed, thus creating new, strain-free grains. The process of recrystallization can be divided into nucleation of the new strain-free grains and additional growth until all deformed grains have disappeared and only strain-free grains are present in the microstructure. The grain boundaries that are now present still contribute to the increase of

the stored energy. This is encountered by the further growth of some grains at the expense of others, leading to a decrease of the total grain boundary fraction.

### 6.2.5. Austenitization

The most important step in a heat treatment process is austenitization [55]. In order to induce austenitization, the material is heated from room temperature through the intercritical region to the one-phase austenite region. The main features of austenitization are a) increase in the mobility of atoms and of the driving force with increasing temperature. With increasing overheating, the phase transition accelerates due to the increased nucleation and growth rates; b) formation of an austenitic structure with homogeneous carbon distribution from a two-phase mixture (ferrite-pearlite) [56].

#### 6.2.5.1. The formation of austenite in steels

Free energy change is defined as the difference in the free energy of the product phase (austenite) and the parent phases (pearlite or ferrite). By increasing the temperature into the austenite region, this free energy change increases as well. Hence, the rate of austenite formation increases with increasing temperature. Similarly, with increasing temperature, the atomic mobility also increases. Therefore, the rate of nucleation and the rate of growth will continuously increase with increasing temperature.

#### 6.2.5.2. The formation of austenite from pro-eutectoid ferrite and pearlite in hypoeutectoid steels

Upon heating, the pearlite regions become unstable once the eutectoid temperature is reached and transform into austenite. Nucleation takes place predominantly on the pearlite-ferrite grain boundaries [57], and the pearlite phase will be the first one to transform into austenite [58]. After the  $\theta \rightarrow \alpha$  transformation is completed, the structure consists of austenite regions, in the areas where pearlite was present, and regions of unaffected pro-eutectoid ferrite. With increasing austenitizing temperature, the austenite nuclei grow at the expense of the pro-eutectoid ferrite and disappear completely after the  $A_3$  temperature is reached [59]. Simultaneously, the austenite formed in the ferritic areas is enriched in carbon through diffusion from the austenite regions formed from pearlite colonies. Dykhuizen et al. [60] studied the austenitization in low carbon steels and found that the  $\theta \rightarrow \gamma$  and  $\alpha \rightarrow \gamma$  transformations are overlapping to some extent. According to them, ferrite cannot transform into austenite at temperatures right above the eutectoid temperature until the carbon is available from the pearlite regions. Therefore, the transformation process is impeded by the diffusion of carbon in austenite.

Schmidt et al. [61] studied the formation of austenite from a ferrite-pearlite initial microstructure. They observed that at low heating rates, the formation of austenite is controlled by the long-range diffusion of carbon. Nevertheless, at higher heating rates, the growth rate increases considerably, and the interface-controlled reaction growth mechanism is responsible for the transformation. Thus, it is suggested that a change from diffusion-controlled to interface-controlled transformation can be expected during the austenitization of steels with a pearlite-ferrite microstructure.

The  $\theta \rightarrow \gamma$  transformation proceeds faster than the  $\alpha \rightarrow \gamma$ . This reaction is shifted to higher temperatures for higher heating rates. Datta et al. [58] studied the austenitization kinetics from a pearlite/ferrite initial microstructure at different intercritical annealing temperatures in low-carbon steel. They observed that the  $\theta \rightarrow \gamma$  transformation was completed in less than one second at all tested temperatures. On the other hand, the kinetics of the  $\alpha \rightarrow \gamma$  transformation at temperatures higher than the  $A_3$  was found to be different from those tested at temperatures lower than the  $A_3$ . After the ferrite/pearlite transformation to austenite is completed, the carbon concentration gradients remain in austenite for a certain time. In the regions of the former pearlite colonies, there is an excess of carbon, whereas, in the regions of the former ferrite grains, there is a lack of carbon. These concentration gradients are determined by the heating rate and can remain for a certain time, but eventually, homogenization occurs, and the final austenitic structure will contain homogeneous carbon content.

### 6.2.6. Transformation during cooling

#### 6.2.6.1. Effect of the Cooling Rate and the Transformation Products

The cooling rate from the annealing temperature determines the product of the austenite transformation. In a steel of a given composition, the lower the heating temperature in the intercritical region, the lower the austenite fraction, and the lower the cooling rate required for the martensitic transformation. With a high cooling rate, dual-phase steels can be produced at lower carbon content and substantially reduced alloy content [62]. During rapid quenching, the amount of formed austenite and the amount of the corresponding martensite, as well as the properties of dual-phase steels, are very sensitive to heating temperature. On the other hand, with relatively slow cooling rates, ferrite formation can occur with a near-equilibrium carbon partitioning from the new ferrite to the remaining austenite. This can be less dependent on the heating temperature. An increase in the cooling rate from the intercritical region induces high residual stresses that accompany martensitic transformation and increases the density of unpinned dislocations in ferrite areas adjacent to martensite [63].

#### 6.2.6.2. Formation of ferrite from austenite

At a temperature above the  $A_{c3}$ , a carbon steel will obtain a fully austenitic microstructure. When cooled slowly until below the  $A_{c1}$  temperature, ferrite starts to form until it obtains a fully ferritic microstructure. The nucleation of ferrite starts at grain boundary faces, at grain corners, and at triple junctions, where three grain boundaries meet. Additionally, heterogeneous nucleation can occur at defects, such as dislocations. These nuclei will grow into grains until all of the austenite has transformed into ferrite.

During cooling below the  $A_3$  temperature, nucleation of ferrite in the austenite matrix takes place. According to the phase diagram (**Figure 6.1**), the BCC structure becomes favorable below the  $A_3$ -temperature. During cooling, small groups of atoms tend to arrange into the BCC structure. Some of these groups form a stable nucleus larger than a critical dimension, while smaller groups will not be stable and disappear again. In the classical nucleation theory, the Gibbs free energy change ( $\Delta G$ ) is associated with the nucleation process is expressed as:

$$\Delta G = -V(\Delta G_V - \Delta G_S) + \sum_i A_i \sigma_i - \Delta G_d \quad \text{Eq. 6.5.}$$

where  $V$  is the volume of the nucleus (in  $\text{m}^3$ ),  $\Delta G_V$  is the difference of Gibbs free energy per unit volume between austenite ( $G_V \gamma$ ) and ferrite ( $G_V \alpha$ ) and is called the driving force for nucleation;  $\Delta G_S$  is the misfit strain energy per unit volume that results from the non-perfect fit of the transformed volume into the space originally occupied by the matrix.  $A_i$  is the area of interface  $i$ ,  $\sigma_i$  the free energy per unit area of interface  $i$ , and  $\Delta G_d$  is the change in free energy associated with consumed defects in the parent phase at the nucleus's location (in J). The area  $A_i$  is positive for an interface between the nucleus and the matrix and negative for an interface between two grains of the parent phase [42].

### 6.2.6.3. Potential nucleation sites

A distinction can be made between potential nucleation sites. These can be grain faces located between two austenite grains, grain edges between three austenite grains, and grain corners found between four austenite grains. The nucleation mostly takes place on irregularities that are present in the parent phase. For example, the nucleation of ferrite on a grain boundary requires a lower  $\Delta G^*$  than a homogeneous nucleation for the same interface energies between the matrix and the nucleus. Homogeneous nucleation has the lowest nucleation rate. On the other hand, nucleation on defects reduces the change in Gibbs free energy for nucleation by  $\Delta G_d$  and favors the new phase's nucleation. Such defects can be vacancies, dislocations, stacking faults, and phase or grain boundaries. The presence of these defects favors the nucleation rate. Enomoto et al. [64] found that nucleation rates at grain faces are compared to nucleation rates at grain edges. At small undercoolings, the grain edge nucleation is preferred over grain face nucleation, while at larger undercoolings, the grain face nucleation is faster. Huang and Hillert [65] have shown that the dominance of grain corners as nucleation sites is so strong that the nucleation taking place at grain edges may have occurred at points energetically similar to grain corners.

Enomoto and Aaronson [66] studied the influence of alloying elements on the nucleation rates. They used five types of low carbon steels alloyed with molybdenum (Mo), silicon (Si), cobalt (Co), nickel (Ni), or manganese (Mn). They observed that Mn reduces the steady-state nucleation rate most effectively, followed by Ni. On the other hand, Co, Mo, and Si increase the steady-state nucleation rate to greater degrees.

Several parameters greatly influence the nucleation rates, e.g., the interface energies and the driving force for nucleation. These parameters depend differently on each type of alloying element and concentration. Segregation of alloying elements to austenite grain boundaries may reduce the  $\sigma_{\gamma\gamma}$  interfacial energy of the austenite grain boundary. Segregation to  $\alpha/\gamma$  phase boundaries will have the reverse effect [66]. Molybdenum and silicon tend to segregate easier and therefore reduce the austenite interfacial energy to a greater extent. The steady-state nucleation rate should be enhanced, but these elements also reduce the  $\alpha/\gamma$  interfacial energy, and therefore, the nucleation rate is decreasing. The observed characteristics of ferrite allotriomorph nucleation rates in the alloys studied are summarized as followed by Enomoto and Aaronson [66]:

- Mn decreases the nucleation rate of grain boundary ferrite allotriomorphs by reducing the  $\Delta G_v$  during nucleation. It further reduces the nucleation rate by decreasing the austenite grain boundary energy more than the austenite-ferrite phase boundary energy.
- Si increases the nucleation rate because the negative  $\Delta G_v$  accompanying the significant increase in the  $A_{r3}$  temperature has a stronger influence than the decrease of the nucleation rate due to reducing the austenite grain boundary energy.
- Mo increases the nucleation rates at high temperatures for the same reasons as Si.

An important factor to consider is that alloying elements change the temperature dependence of the driving force for nucleation,  $\Delta G_v$ , and also the start temperature of the nucleation process [42].

#### 6.2.6.4. The martensitic transformation

The starting temperature of martensite transformation  $M_s$  controls the substructure of martensite, probable auto-tempering throughout cooling, and the possibility of preserving some quantities of retained austenite in the final microstructure. The  $M_s$  is highly affected by alloying elements such as manganese, chromium, silicon, and carbon [34]. Carbon content in austenite fraction at the moment of its transformation in cooling from intercritical region is the main factor determining the  $M_s$  temperature and therefore the properties of martensite, the level of residual stresses, dislocation density in ferrite, etc. Depending on the carbon content of austenite in steels, the martensite transformation can differ from 0.1 to 0.6 %, which interprets to variations in  $M_s$ . The effect of alloying elements on the  $M_s$  is very noteworthy as they differ the permitted cooling rate, the amount of newly transformed ferrite and the relevant carbon enrichment of  $\gamma$ -phase. For example, aluminum affects the  $M_s$  temperature by raising it about 30 °C per 1 % of Al. In the absence of full austenitization, though, Al percentage increase leads to the formation of new ferrite, increasing the carbon content in the remaining portion of austenite and therefore, decreasing the  $M_s$  temperature [8]. On the other hand, additions of alloying elements that increase the hardenability of austenite and prevent new ferrite formation can raise the  $M_s$  temperature, compared to less alloyed steels, due to lower carbon enrichment in the remaining percentage of austenite.

#### Crystallography of Martensitic Transformations

Martensitic transformations are diffusionless, involve synchronized movements of atoms, and hence can occur at low temperatures [67], and can propagate at the speed of sound [68]. There is no composition change during its formation and growth in the parent phase. The martensite-austenite interface must be able to move without diffusion, which means that the interface must contain no more than one set of dislocations. More than one array of line vectors can lead to interference between the dislocations, and therefore, there must be at least one line fully coherent in the  $\alpha/\gamma$  interface.

#### Shape deformation

Since the arrangement of atoms in the parent crystal is specific, displacive changes occur to generate the product phase leading to a visible change in the macroscopic shape of the parent crystal during transformation



[69]. As shown in **Figure 6.3** [33], the initially flat surface normal to  $da$  tilts in respect to the line formed by the intersection of the interface plane with the surface normal to  $da$ . The straight-line  $ab$  is bent into two straight parts,  $ae$  and  $eb$ . It is also shown that the martensitic transformation is diffusionless as labeled rows of atoms in the parent crystal are expected to remain in the correct arrangement in the martensite lattice. This means that a particular atom in the martensite has originated from a corresponding particular atom in the parent crystal. Concerning the reconstructive transformation illustrated in **Fig. 6.3**, the product phase can have a different composition from the parent. Also, there has been a rearrangement of atoms during transformation, and the order of atoms in the product lattice is different from that in the parent lattice. As the reconstruction of the parent lattice is involved during the transformation, the atoms are able to diffuse around without any crystal shape deformation. The  $ab$  line is unaffected by the transformation.

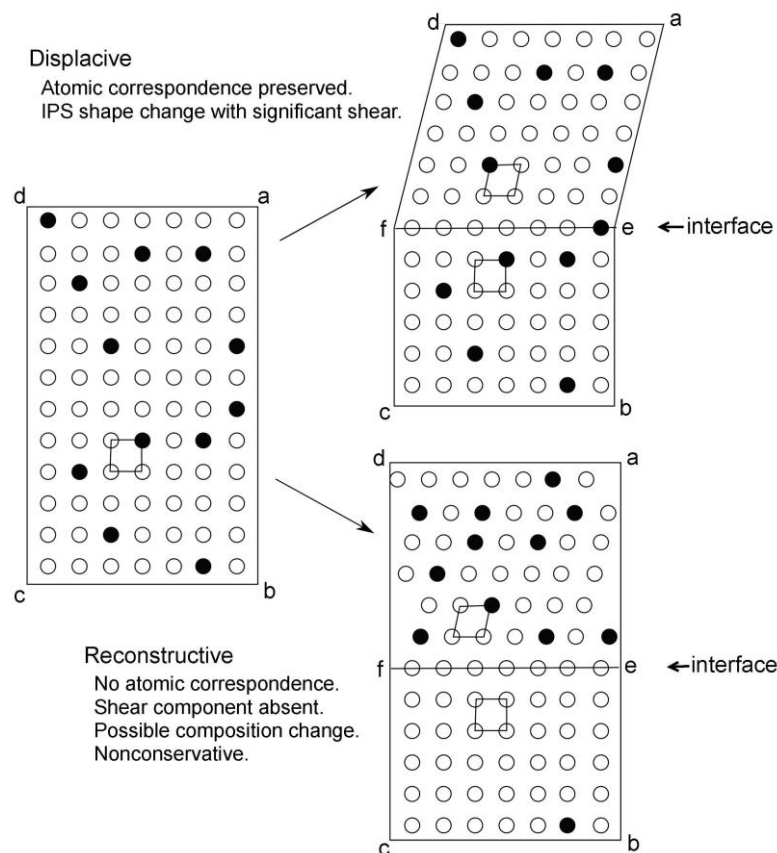


**Figure 6.3:** Schematic illustration of the mechanisms of diffusional and shear transformations [33].

#### 6.2.6.5. The bainitic transformation

Bainite forms at temperatures between the pearlite and martensite transformation temperatures, and in some cases, they may overlap. That is why bainite exhibits characteristic features of both pearlite and martensite transformation. According to Bain, it can be defined as a ‘*non-lamellar aggregate of lath- or plate-shaped ferrite and carbide*’ [24, 70]. The microstructure of bainite may vary with the composition and the temperature of its transformation. Thus, it is distinguished into two types, the upper bainite, and the lower bainite. The suppression of the carbide component of bainite is possible in steels that contain a sufficient concentration of alloying elements such as Si or Al. This

bainite consists of ferrite plates and untransformed austenite. This bainitic morphology has also been reported in very low carbon steels [71].

The bainitic ferrite nucleates at austenite grain boundaries and grows in the form of plates adjacent to each other. These groups of plates are called sheaves [72]. These sheaves and the constituent plates (sub-units) within them do not cross the austenite grain boundaries. The thickness of the sub-units decreases with decreasing transformation temperature, but the length is unaffected [23]. The sub-units in a sheaf have almost identical crystallographic orientations and are separated by small-angle grain boundaries. Other phases such as cementite, untransformed austenite, or martensite may occupy the regions between the sub-units. In the case of lower bainite, carbides are present within the sub-units, aligned at an angle of about 55–60° to the long axis of the ferrite plate. The transition from upper bainite to lower bainite usually occurs at around 350°C [73], but it is not sharp, as both upper and lower bainite can form at intermediate temperatures. In many steels, the transformation to bainitic ferrite may occur without any interference from other reactions such as carbide precipitation. In such steels, the transformation to bainitic ferrite ceases earlier, before austenite gains the expected para-equilibrium composition. The reaction is then incomplete, and the phenomenon is called the ‘*incomplete reaction phenomenon*’ [74].

### **Solute drag effect**

During the transformation of bainite, substitutional solute elements do not partition between austenite and ferrite. However, they may segregate to their interface, given necessary negative interaction energy with the interfaces, thus applying a drag force on the interface's migration of disordered areas. This drag force decreases the mobility of the interfaces. The extent of segregation, and thus the drag force, increases with decreasing temperature. The ferrite growth kinetics slow down when the drag force becomes stronger, compared to the chemical driving force for ferrite growth. Eventually, a saturation point for segregation is reached, but the driving force still increases as the temperature is reduced. Once it overcomes the drag force, the mobility of the interface is restored, and the transformation continues. These alloying elements also reduce the nucleation rate of ferrite [75] and contribute to the incomplete reaction phenomenon. Strong carbide forming elements, such as Mo, favor this effect and the efficiency of an alloying element depends on its effect on the activity of carbon in austenite.

In upper bainite, cementite precipitates from austenite. On the other hand, in lower bainite, carbide precipitates from austenite at the austenite-ferrite interface and is eventually incorporated into the ferrite plate [76], based on the observation that the carbide particles are aligned in the ferrite plate.

The bainitic ferrite plates initially grow along the length, with the diffusion of carbon into the parent austenite, and hence, the initial plates do not contain any carbides. Next, the plates thicken perpendicular to their length by the growth of the ferrite and the carbides after their nucleation, which initiates the thickening. It was, therefore, suggested that lower bainite be regarded as a eutectoid mixture. According to [74], bainite forms by a displacive, shear mechanism, including the coordinated movement of several atoms across a glissile interface. The growth of bainite takes place alongside an invariant plane strain shape deformation with a large shear component. Even though carbon diffusion takes place during para-equilibrium nucleation, the growth is considered diffusionless [74]. Finally, bainite nucleation occurs at the parent austenite grain boundaries, but the plates do not exceed these boundaries or twin boundaries.

Compared with martensite, bainite grows at higher temperatures, in which the austenite is weak and cannot accommodate the shape deformation elastically. So, it undergoes plastic deformation in the area next to the bainite plate in order to relieve the large shape strain. This leads to an increase in the local dislocation density, which impedes the glissile transformation interface's motion. The accumulation of dislocations eventually impedes the plate's growth, and thus, the plate has a smaller length than the austenite grain diameter. The reaction keeps progressing by the nucleation of new sub-units next to the existing ones [24]. Also, [77] studied the growth rate of sheaves and showed that the lengthening rate is greater than expected from carbon diffusion-controlled growth. According to Takahashi [78], the driving force for the transformation of bainite is smaller than that for martensite. Due to the plastic deformation caused by the shape change, the bainite plates will grow much slower than martensite plates. According to the aforementioned, the rate of the sheaf growth as a whole is much lower than that of an individual sub-unit growth rate and is contingent on the time taken by the sub-unit to reach its limiting size. This slows down the overall kinetics of the bainitic transformation.

In the case of a complete transformation, the composition of the bainite will be the same as that of the parent austenite. It is supersaturated with carbon at the beginning of the transformation, as the growth of the bainitic ferrite is diffusionless. However, the parent austenite grain does not transform instantly in its entirety. As the bainite transformation takes place at high temperatures, the plate of bainitic ferrite that is formed first will reject its excess carbon into the residual austenite during the transformation because there is sufficient time. The next plate of bainite will then grow from austenite that is enriched in the carbon rejected from the first plate with a lower driving force. This process continues until the driving force for diffusionless shear transformation drops to zero, and the reaction stops.

### 6.3. State of the Art: Ultra-fast Heating as a thermal treatment method

#### 6.3.1. The introduction of Ultra-fast heating

The application of high heating rates has been used over the years as a surface hardening technique [79]. It was recently introduced as a thermal treatment method for bulk specimens by Lolla [16–18] and Cola [15]. In their work, they used a special experimental setup to ‘flash process’ steel samples. They concluded that high heating rates affect the transformation mechanisms that occur during conventional thermal treatment. Thus, the final products of the microstructure may differ. The need to reduce the production time of steel grades has been supported in [80]. Until now, it has been found that the application of high heating rates can affect various metallurgical phenomena that occur during the thermal treatments of steel.

#### 6.3.2. The effect of heating rate in an annealing treatment

In cold-rolled steels, increasing the heating rate leads to an increase of the required heat needed for the nucleation of austenite grains at the ferrite grain boundaries. The application of high heating rates translates into short heating time, and thus the nucleation of austenite at ferrite grain boundaries is impeded. The lack of heating time means that the diffusion distances are shortened, which creates carbon-rich and carbon-depleted areas in the microstructure. The nucleation of austenite occurs preferentially in the carbon-rich areas. Therefore, austenite growth occurs along the rolling direction, where the distance between the existing nuclei of austenite is smaller.

The growth of austenite fraction,  $V$ , with time,  $t$ , can be described by the Avrami equation:

$$X = 1 - \exp(-bt^n) \quad \text{Eq. 6.6.}$$

Where  $X$  is the recrystallized volume fraction of ferrite as a function of annealing time,  $n$  is a constant, and  $b$  is reflective of the temperature dependence of the nucleation and the growth rates.

Significant acceleration of austenite growth during the isothermal holding of both low-carbon C–Mn–Mo DP and C–Mn–Si TRIP steels at given temperatures reached at higher heating rates were observed by Huang et al. [52]. Another study [50] used 0.17C–0.74Mn steel and heating rates ranging from 1 to 900 °C/s and found that higher heating rates affected the austenite transformation during continuous heating of only initially hot-rolled microstructure. In contrast, in the case of cold-rolled steels, the austenite fractions were relatively independent of heating rates. The authors explained these results by the differences in the initial microstructure prior to austenite formation. In the hot-rolled microstructure, the increase in the heating rate required superheating until a network of austenite grains was formed at ferrite grain boundaries. The chemical composition of steels can substantially affect both the recrystallization and the  $A_{c1}$  temperature, as well as the propensity to spheroidization of  $(\text{FeMn})_3\text{C}$ . This could explain significant inconsistencies in the results of studies of heating rate effects using different steels.

### 6.3.3. *The effect of the initial microstructure*

It has been reported [81] that minimal heating times impede the dissolution of cementite inside the pearlitic zones of the initial material. In this case, the initial microstructure plays a vital role. In the case of conventional treatments, where slow heating rates are applied, the dissolution of cementite occurs, followed by diffusion of carbon and other elements that enrich the microstructure's ferrite. This will favor the  $\alpha \rightarrow \gamma$  transformation, as will be mentioned later in this thesis. In the case of an initial ferrite-pearlite microstructure, the nucleation of austenite occurs at the boundaries between the pearlitic colonies and the ferrite grains and on the interfaces between the cementite lamellae and the interspatial ferrite. If the steel contains spheroidized carbides in the ferrite matrix, then the austenite nucleates primarily at carbide particles located at ferrite grain boundaries. The spheroidization of cementite is usually achieved by thermo-mechanical processing. The spherical carbides are more stable than the lamellae and more difficult to dissolve [82]. Also, they offer a more abundant and more evenly distributed nucleation site for the formation of austenite. According to Garcia and Deardo [83], carbides located within ferrite grains do not contribute to austenite nucleation. Instead, they dissolve later in the ferrite matrix with carbon diffusing to the growing  $\gamma$ -phase. When heating a preliminary-quenched steel with martensite microstructure into the intercritical region or in the case of Q&P steels, austenite first nucleates at the parent austenite grain boundary triple junctions, then at the surfaces of prior austenite grains, and finally, at martensite plate boundaries. As a result, a microstructure similar to Widmanstätten is produced with an acicular shape of austenite that may have been transformed to martensite upon cooling, retaining acicular fiber-type morphology. Tempering of the preliminary martensite may also take place during the heating stage. The initial microstructure controls the austenitization kinetics and the morphology of austenite-ferrite mixture, which will be a defining factor for the steel's final microstructure after cooling. The effect of the initial microstructure corresponds to a shift in the critical temperatures of phase transformations and in the rate of austenite growth at increasing holding temperature or time. Deformed initial microstructures (after cold rolling) lead to an increased number of nucleation sites and favor the diffusion of atoms through the dislocations (pipe diffusion) and thus increase the number of austenite nuclei resulting in acceleration of the initial stages of austenitization. However, the overall effect of cold working on the austenitization kinetics depends not only on the microstructure before cold deformation but also on the heating rate, holding time, and carbon content in steel [8]. Concerning the effect of the initial microstructure in UFH treatments, Cerda et al. [84] studied the effect of UFH on different microstructures. Specifically, they used a ferrite-pearlite (F+P) initial microstructure compared to a ferrite-martensite (F+M) initial microstructure in a 1 to 1 ratio. They found that the steels with F+P microstructure displayed higher ductility and lower strength than steels F+M initial microstructure after all thermal cycles. Also, the pearlite colonies in the F+P samples were not fully dissolved. This means that a large fraction of the carbon content has not been diffused into ferrite, which will also affect the nucleated austenite composition. Also, Papaefthymiou et al. [85] studied the effect of UFH on thermo-mechanically processed steels consisting of ferrite and spheroidized cementite. They found that the spherical carbides were not dissolved due to high heating rates. It was also found that partial diffusion took place as they found a gradient in the carbon content around the spheroidized cementite. Based on the modified fault migration theory [82], the model for the mechanism of pearlite spheroidization is explained as follows. Various

lamellar faults occur in a pearlitic lamellar structure, and even new faults may occur during the spheroidization. The spheroidization will initiate and develop from these lamellar faults, with the driving force being the chemical potential gradient between the highly curved faults and the neighboring flat interfaces. The morphological changes will appear as local increases in the lamellar thickness and reduction of the lamellar length. The lamellae will also show holes and fissures. This morphological change is anisotropic and is related to the anisotropy of the  $\alpha/\text{Fe}_3\text{C}$  interfacial energy. The most frequently observed preferred orientations along which the faults grow are the [0 1 0] and [2 1 0] directions. The holes and fissures grow, leading to the connection of their profiles and the break-up of large cementite platelets into small particles. Due to Ostwald ripening [86, 87], large cementite particles become larger at the expense of smaller ones, and all the cementite particles will gradually evolve into spheroids. The partial dissolution of cementite of the initial microstructure, in addition to the short time available for diffusion means that there is no enrichment of ferrite grains in carbon before austenitization. Therefore, and due to the short diffusion distances, carbon-rich areas are found in close proximity to undissolved cementite particles and as the distance from them increases, the carbon content decreases. In another study, Papaefthymiou et al. [88] concluded that ultra-fast heating rates impede the motion of the carbon atoms through an interface due to intense segregation of substitutional atoms near cementite/austenite. This led to partial carbide dissolution which in turn leads to chemical heterogeneity in the austenite matrix. In the case that the initial microstructure consists of coarser carbides complete carbide dissolution cannot be achieved compared to other microstructures containing finer carbides [89].

Cryderman et al. [90] reported that martensitic initial microstructures lead to a decrease in the hardness, compared to a ferrite-pearlite initial microstructure attributed to an increased volume fraction of retained austenite. This increase in retained austenite (RA) is rationalized by a drop in the  $M_s$  temperature due to a more complete dissolution of carbides in the initial martensitic microstructure.

#### **6.3.4. Nucleation of austenite**

The austenite nucleation at the carbon-rich areas can be rationalized from the work of Savran [56]. As she explained, when the temperature is raised into the austenite region, the difference in the free energy of the product phase (austenite) and the parent phases (pearlite or ferrite) increases. Hence, the formation rate of austenite should increase with increasing temperature. In addition, with increasing temperature mobility of atoms also increases. Therefore, both the thermodynamic driving force for the formation of austenite and the atomic mobility increases at higher temperatures. Thus, the nucleation rate and growth rate will continuously increase with increasing temperature. Upon heating, the pearlite regions, which contain almost the entire carbon content, become unstable above the eutectoid temperature, and transform to austenite. This nucleation takes place predominantly on the pearlite-ferrite grain boundaries [57]. The pearlite will transform to austenite first [58]. After the pearlite fully transforms to austenite, the microstructure consists of austenite regions that have replaced the original pearlite colonies and unaffected pro-eutectoid ferrite regions. The pro-eutectoid ferrite is being reduced with increasing austenitizing temperature and will disappear completely after the  $A_3$  temperature is reached [59]. Simultaneously, the carbon in the austenite regions formed from pearlite colonies diffuses to the austenite formed from the ferrite regions. The transformation of the pro-eutectoid ferrite to

austenite is a diffusion-controlled process in which carbon diffusion in austenite is the rate-controlling factor. [9]. However, at higher heating rates, the growth rate increases drastically, and the interface-controlled reaction growth mechanism is responsible for the transformation.

Kaluba [91–93] introduced the massive  $\alpha \rightarrow \gamma$  transformation mechanism when high heating rates are applied. Specifically, if the driving force is high enough, the transformation starts in a displacive manner before the nucleation process of a reconstructive transformation is completed. For this to be achieved, an increase of the carbon concentration at the grain boundaries due to an easy carbon diffusion path occurs, thus ensuring favorable thermodynamic conditions. Such conditions can also be produced at  $\alpha/\theta$  interfaces. At this stage of reaction, the volume of the product phase is very small. Therefore, the carbon supply to the reaction zone can be achieved without any visible dissolution of cementite. According to [94, 95], the carbon concentration can increase in the interior of a boundary and possibly, in its close vicinity.

The observation of pro-eutectoid ferrite grains in the work of Cerda [96] indicates that the diffusion of carbon controls the advance of the  $\gamma/\alpha$  interface. These grains have similar morphology to those of the initial microstructure. However, the morphology and grain size of this ferrite is differentiated. These changes indicate that the mechanism of austenite formation is no longer diffusion-controlled but instead interface-controlled. Therefore, the ensuing transformation of ferrite during cooling, which starts as an interface-controlled process, proceeds as a diffusion-controlled process. Papaefthymiou and Bouzouni [97–99] studied the dissolution of carbides and austenite formation under rapid heating processes. With the aid of simulation, they have showed that when high heating rates are applied, although the time for diffusion is limited, short-range diffusion occurs alongside partial dissolution of carbides. The refinement of the parent austenite grains at peak temperature was rationalized from the existence of these undissolved carbides that prevent the growth. Also, the dissolution rate of the carbides depends on the segregation of substitutional elements such as Cr, Mn, and Mo. Enrichment in such elements was observed on the carbide interfaces. This creates a solute drag effect in carbide/austenite interfaces, which delays the carbide dissolution. Therefore, the segregation of substitutional atoms impedes austenite formation and results in carbon-depleted austenite grains, leading to chemical heterogeneity at the peak temperature [100].

### 6.3.5. Growth of austenite

As mentioned before, austenite grows into both pearlite and pro-eutectoid ferrite. When this austenite is nucleated at the  $\alpha/\theta$  interface, it starts to grow, and the newly formed  $\gamma/\alpha$  interface moves towards both pearlite and pro-eutectoid ferrite. When the heating rate is low, then austenite forms via carbon diffusion. Though, with increasing heating rate, the resulting austenite fractions deviate from the equilibrium values expected in slow heating rates. At high heating rates, the rate of austenite formation is partly controlled by carbon diffusion. Eventually, the system will reach some temperature in which the austenite is more stable than the ferrite in equilibrium with cementite.

Cerda [96] also found that austenite nucleation occurs preferentially at the  $\alpha/\theta$  boundaries. Ultra-fast heating leads to a substantial increase in the driving force for nucleation, and thus increases the probability of austenite



to form at the  $\alpha/\theta$  interfaces. This newly formed austenite grows in all directions. Nevertheless, its growth rate into pearlite is higher than the growth rate into pro-eutectoid ferrite. During the first stages of the austenite formation and growth, the governing mechanism is diffusion-controlled, evident at conventional heating rates. Though, at later stages of the austenite growth, the massive transformation mechanism occurs when thermodynamically possible. The velocity of the moving boundaries is affected by the local chemical composition at the  $\gamma/\alpha$  interface and by the heating rate.

#### 6.3.5.1. Austenite growth into pearlite

It was also found that a cold-rolled ferrite-pearlite initial microstructure favors the spheroidization of cementite, which affects the formation of austenite. On the other hand, when even higher heating rates are applied, pearlite's lamellar structure can be retained, depending on the treatment. The spheroidization process of cementite is related to the austenite distribution in the matrix. When cementite is still lamellar, the formation of austenite takes place in the pearlitic areas [101]. Then, a banded mixture of ferrite and austenite is observed in the microstructure. In the case that cementite is partially spheroidized, the growth of austenite will be radial and slower, as the distances between cementite spheres are larger than the interlamellar spacing. Therefore, the cementite spheres located at the  $\alpha/\alpha$  boundaries will be the preferred places for austenite nucleation, while not all of the spheres will act as nucleation sites.

#### 6.3.5.2. Austenite growth into pro-eutectoid ferrite

The growth of austenite into pearlite and in pro-eutectoid ferrite take place simultaneously. Nevertheless, there is a kinetic difference between these two processes [102]. The kinetics of austenite's growth into the pro-eutectoid ferrite is slower than its growth into pearlite since the carbon diffusion distances are longer than the interlamellar spacing of pearlite. When the temperature is increased slightly above the eutectoid, the  $\alpha/\gamma$  equilibrium will be defined by the Gibbs free energy curves of ferrite and austenite. With increasing temperature, the  $\alpha/\gamma$  equilibrium will be defined by the Gibbs free energy of ferrite and austenite until they become equal. According to these, Cerda [96] concluded that the growth of austenite does not occur preferentially into recrystallized or deformed ferrite because the diffusion of carbon in austenite is the main factor controlling the reaction.

In **Figure 6.4** [103], the formation of austenite during traditional and fast heating is depicted. As mentioned before, during traditional heating, spheroidization and dissolution of pearlite take place, and the austenite nucleates on the interfaces between ferrite with cementite, ferrite with pearlite, and intergranularly of the ferrite grains. In the case of fast heating, the dislocations in ferrite are retained, and the dissolution of pearlite is impeded. All these act as nucleation sites for austenite to form and grow, leading to a more refined microstructure in the annealing temperature.

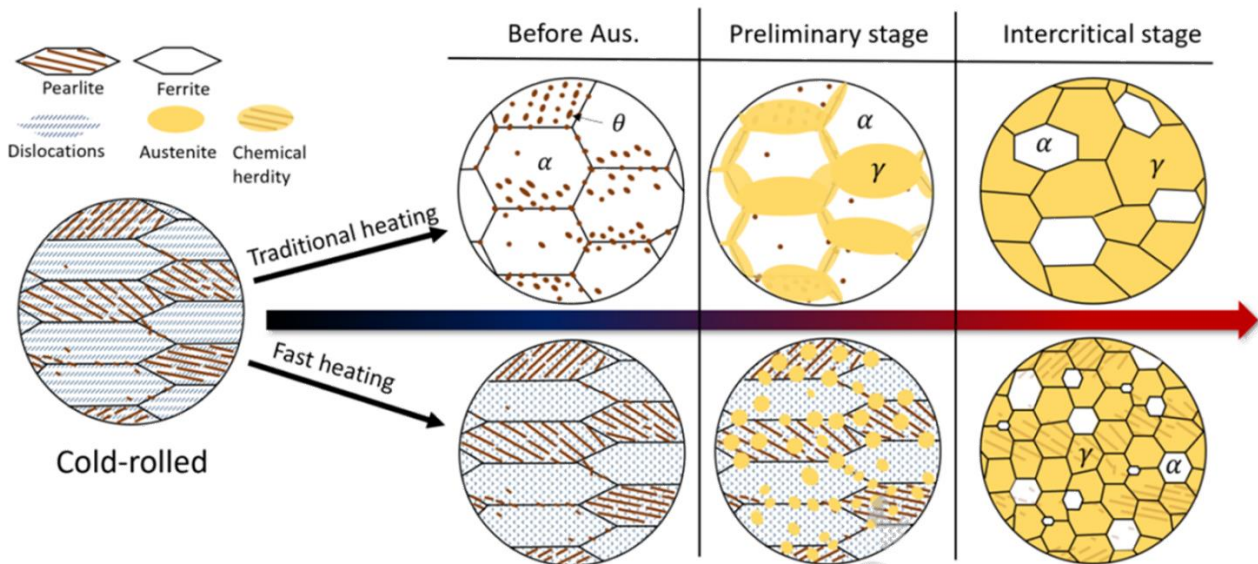


**Figure 6.4:** Schematic representation of the austenite nucleation and growth under traditional and fast heating conditions [103].

### 6.3.6. Effect of Ultra-Fast Heating on Recovery and Recrystallization

It has been reported [104] that the time required to complete recrystallization decreases with increasing heating rate. At the same time, its initiation is shifted to higher temperatures compared to those of conventional heating treatments. Muljono et al. [105, 106] claimed that UFH increases the initiation temperature of recrystallization. Atkinson [107] attributed the impeding of the recrystallization process to interstitial solute atoms that may act as barriers to the movement of the dislocations in the deformed ferrite matrix and thus hinder the nucleation of new grains. On the other hand, high heating rates may lead to significant changes in the recovery characteristics, which may result in an increased recrystallization rate [108]. Another study [109] revealed that interstitial atoms have a much greater influence on the kinetics of recrystallization at low heating rates compared to higher heating rates.

It has been found [110–115] that recrystallization and phase transformation are processes that occur rather independently. However, they are expected to overlap at high heating rates due to the impediment of ferrite recrystallization. In this case, austenite grows into both deformed or partially recovered ferrite and fully recrystallized ferrite. The fragmentation of pearlite that occurs during cold rolling affects both ferrite recrystallization and austenite formation. Specifically, small fragmented cementite has a pinning effect on the grain boundaries of the new ferrite grains, while it offers a higher amount of potential nucleation sites for austenite [111].

Bandi et al. [116] also concluded that the recrystallization kinetics increase when increasing the isothermal holding temperature and cold-rolling reduction. Higher cold-rolling reduction leads to a higher driving force for the recrystallization, which leads to an increase of the recrystallization fraction that occurs before the austenite formation. On the other hand, and confirming the claims mentioned above by Cerda et al. [96], increasing heating rates lead to a decrease in the fraction of recrystallization before austenite formation, even

though these two processes overlap. Bandi [116] also claimed that for the recrystallization process and the austenite formation to overlap completely, a heating rate over 500 °C/s must be applied.

In addition, Li et al. [117] found that the overlapping of the two processes affects the spatial distribution and morphology of the austenite. They observed that the morphology of martensite shifted from a network structure to a chain shape. This was observed for heating at lower annealing temperatures (<800 °C). Reis et al. [118] observed a texture memory effect after the  $\alpha$ - $\gamma$ - $\alpha$  transformation. This means that the initial material's texture will be retained in the final microstructure after the thermal treatment. The memory effect may affect the properties of the material, as according to [119], a strong ND fiber in cold-rolled materials will be retained after UFH. This leads to better isotropy in the material's properties. Such findings were also reported by [84, 120], who found that the application of high heating rates intensifies the RD fiber at the expense of the ND fiber.

It was also found that in a DP980 steel sheet [121], the morphology of austenite changes from a random to a fibrous distribution as the heating rate increase, which is attributed to the overlapping of the recrystallization and austenitization processes. In the same study, it was also found that high heating rates affect the transformation temperatures. This was also confirmed by [106, 122, 123], who have shown that increasing the heating rate does not only impede the initiation of the recrystallization, but it also shifts the transformation temperatures to higher values. This leads to a lower fraction of austenite than that resulting from a conventional annealing at the same temperature.

### **6.3.7. Effect of Ultra-Fast Heating on Grain Refinement**

Grain refinement means a reduction of the size of the grains that consist in a steel grade. Many studies have shown that yield and tensile strength are increased due to grain refinement, whereas uniform and total elongation are less affected. With a decrease in the grain size, the strain hardening rate is being increased. In contrast to other methods that aim to increase the strength of the steel, grain refinement also improves the material's toughness and capability to absorb energy under impact conditions. The most distinct mechanical properties of the DP steels are the low elastic limit, the high initial strain hardening and the overall continuous yielding in the quenched state. These features have been attributed to residual stresses and dislocation heterogeneities present in the ferrite due to the austenite-to-martensite transformation. This transformation involves a volume expansion of 2-4 %, depending on the chemical composition, causing an elastically and plastically deformed zone in the ferrite adjacent to martensite. The elastic stresses enable plastic flow during the early phases of yielding. Interaction between dislocations and their concentration at ferrite - martensite interfaces and the corresponding long-range elastic back stresses contribute to rapid strain hardening. In DP steels, uniform and total elongation are slightly affected by a decreasing ferrite grain size. Grain refinement increases strain hardening rate at low strains; at higher strains, it levels off and equals the rate of the coarse-grained reference material. This leads to an almost unaffected uniform elongation with the decreasing ferrite size. The reason for this occurrence is because of the higher fraction of grain boundaries and heterophase

interfaces that increase the number of dislocation sources and increase the dislocation density, and therefore, the strength [124].

It was found [118] that when high heating rates are applied, refinement of the microstructure takes place. As mentioned before, the recrystallization and austenitization processes overlap when high heating rates are applied. In the case of intercritical annealing, this means that as the recrystallization process is not complete, the ferrite grain size will be finer, as there is no time for the formation of new, coarser ferrite grains. On the other hand, there is no time for austenite growth as it depends on carbon diffusion, which requires a longer time.

### 6.3.8. Production of AHSS via Ultra-Fast Heating

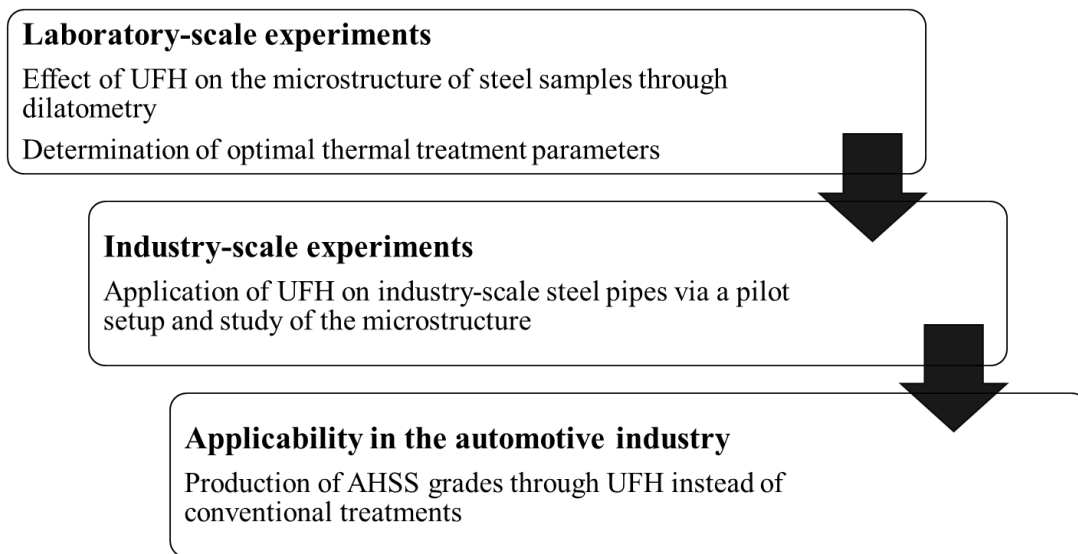
Dai et al. [125] claimed that UFH could provide a feasible way to produce high-performance DP steels by taking advantage of austenite decomposition. When the used cold-rolled DP980 sheet was fully heated above the  $A_{c3}$  temperature, at a heating rate of 300 °C/s, it was found that very fine martensite surrounded by interconnected network ferrite can be obtained with a holding time of 100 s at 800 °C. The total elongation of the produced steel sheet was improved to 16.7% with a UTS of about 1200 MPa. Concerning the mechanical properties, [126] found that the grain refinement that is achieved after ultra-fast heating has a minor effect on the YS and UTS, compared to the microstructural constituents. According to Massardier et al. [127], this grain refinement is controlled by the distribution of the initial undissolved carbides. Cerda et al. [84] also claimed that an increase in the heating rate improves both strength and ductility at heating rates up to 800 °C/s while heating rates up to 1200 °C/s lead to a decrease in the ultimate tensile strength (UTS) and total elongation (TE). They attributed this behavior to the carbon gradients that are formed in austenite during UFH experiments.

Hernandez-Duran et al. [128] and Vercruysse et al. [129] recently studied the effect of UFH on the production of Q&P steels. They concluded that the grain refinement is not as pronounced above a certain heating rate as it is for lower heating rates. They also found extended heterogeneity in the chemical composition of the microstructural constituents of their UFH samples, though the work hardening behavior depends on the TRIP effect. They also found that the uniform elongation of the UFH samples is improved due to the refinement of the transformation products and the better distribution of the retained austenite. An improvement in the properties of Q&P steels that have been subjected to UFH was also found by De Knijf et al. [123]. This improvement was also confirmed by Dai et. al. [125], who attributed the increase in elongation to low-carbon parent austenite and the bainite formation during the partitioning stage. The heterogeneity of the parent austenite in carbon and manganese is thoroughly studied by Muljono et. al. [103]. They found that the gradient in the Mn content in the initial pearlite-ferrite microstructure is inherited to the parent austenite during flash heating, affecting the austenite decomposition and carbon partitioning upon the subsequent Q&P process. In the UFH samples, they claimed that the grain refinement and Mn heterogeneity in the parent austenite grains could accelerate ferrite formation and promote carbon partitioning into austenite, a major factor for its stabilization.

## 7. Experimental Implementation

### 7.1. Thermal Treatments

The experiments were designed to explain the impact of high heating rates on the microstructure of automotive steels. To that end, three sets of experiments were conducted. In the first two approaches, the scope was to find the optimal parameters for the heating treatment in laboratory-scale and industry scale samples respectively. In the third set, the possibility to use the UFH treatment to replace existing steel production methods is examined. To that end, high heating rates are applied in a commercial steel to produce grades similar to those currently used in the automotive industry.



Different heating setups were used in each approach. The dilatometer was used in the laboratory-scale experiments, described in Chapter 8.1. In this chapter, the parameters of UFH treatments were studied. Due to the setup and the small size of the samples, the heating and cooling parameters can be easily controlled in the dilatometer. Once the optimal parameters are obtained, large-scale samples were treated in a pilot setup, described in Chapter 8.2. The application of UFH in larger samples through this setup aims to simulate whether such a treatment can be applied in large scale industrially. Also, the aim is to confirm the formation of bainite and retained austenite that is indicated by the microstructure characterization on the dilatometry samples, as shown in Chapter 8.1. Finally, the Gleeble simulator is used for the experiments of Chapter 8.3. This setup is used because it can reach higher heating rates than the aforementioned setups. Also, sheet samples are used and the mechanical properties can be studied more easily.

#### 7.1.1. Dilatometry

Phase transformations are one of the factors that most influence steel properties, especially the  $\gamma \rightarrow \alpha$  transformation. Dilatometry is a classic technique, along with differential thermal analysis and quantitative analysis of microstructures, most commonly used to determine the start and end of phase transformations in steels.

## *7. Experimental Implementation*

---

The DIL805A of Bähr Co. is a special dilatometer used to determine the deformation parameter and the creation of time-temperature-transformation (TTT) and dilatation-transformation-temperature (DTT) diagrams. The distinctive features of the DIL805A are the high heating rates of up to 4000 °C/s and cooling rates of 2500 °C/s. Though, the accuracy of the results decreases with increasing heating rates. It was found that when the heating rate surpasses 200 °C/s, the results can be precarious. The dilatometer was used for the experiments in Chapters 8.1 and 8.3.



**Figure 7.1:** *The setup of the used dilatometer. The sample is positioned inside the coil and anchored between two metallic rods.*

The specimens are inductively heated in the vacuumed testing chamber by a double coiled induction coil driven by a high-frequency energy generator. Through the outer coil, a water supply is conducted to control sensible heat generated as a result of coil resistance. The inner coil's function is to circulate the cooling gas through the bores located on its inner surface. To measure the temperature, two K-type thermocouples of 0.1 mm diameter are spot welded to a central position on the specimen surface. According to the cooling capacity, argon gas is applied, and the gas pressure is regulated by means of different valves depending on the aimed cooling rate. The samples used in Chapter 8.1 are cylindrical with a length of 10 mm and a diameter of 4 mm. On the contrary, the samples used in Chapter 8.3 are sheets with a length of 10 mm, a width of 2 mm, and a thickness of 1 mm and were cut from the cross-sections of hot-rolled bars.

### **7.1.2. Pilot-scale induction heating machine**

A pilot setup was used in order to perform the heat treatments in larger-scale samples. In this setup, a hollow seamless steel tube is placed inside a large copper coil. Electrical current is applied on the coil, and the sample is heated via induction through the Joule effect. The equipment is designed to heat tube samples with an outer diameter of 30-50 mm and a wall thickness of 1.5 – 2.5 mm, reaching a maximum peak heating rate of 200 °C/s.

The temperature is measured at the sample's surface with a very high response thermocouple, and the measurement is used by the software to control the power. After the thermal cycle, the sample can automatically be released in a quenching tank, filled with water for rapid cooling. This setup was used for the experiments in Chapter 8.2.

### **7.1.3. *Gleeble Thermo-Mechanical Simulator***

Controlled-heating experiments were performed using a Gleeble 3800 Thermo-Mechanical Simulator (Dynamic Systems Inc., Poestenkill, NY, USA) for the experiments in Chapter 8.3. Gleeble systems are based on resistance heating. An alternating electrical current is passed directly through the specimen resulting in its heating via the Joule effect. Extremely rapid and precise temperature control enables to create detailed thermal profiles needed to conduct accurate simulations. The Gleeble varies both the peak current and power angle in order to follow the programmed thermal cycle. It can reach high heating rates up to 10000 °C/s, depending on the sample geometry. Quenching took place either with argon or helium gas, and the treatments were performed. An additional step in the programming of the heat treatment was included to avoid overshooting due to the fast-heating rates.

The sample dimensions were 100 mm × 14 mm, while the rolled sheets' thickness was 1 mm. The temperature was controlled by a 0.1 mm diameter K-type thermocouple, which was spot-welded to each processed sample's midsection. The heat treatment data were recorded with a frequency of 100 Hz. The heating/cooling rate was calculated as the slope of the experimental temperature-time plots.





**Figure 7.2:** The setup of the Gleeble 3800. The sample is anchored between the copper holders and heated by the two coils in the middle of the setup.

## 7.2. Material Characterization

### 7.2.1. Sample preparation

In order to be able to observe the microstructure, special sample preparation needs to be performed. For the Light Optical Microscope (LOM) and Scanning Electron Microscope (SEM), the preparation of the sample consists of the following steps:

The first step is grinding the sample at 180, 220, 400, 800, 1200, and 2000 grit (SiC grains/inch<sup>2</sup>) papers. Through this step, any deformed surface layers are removed from the material. The grinding step was performed manually, and water was used to cool the rotating grinding disk and remove any detached particles from the surface. After each grit, the samples were cleaned with water and ethanol and dried with warm air.

The second step was polishing with 6  $\mu\text{m}$  and 1  $\mu\text{m}$  diamond pastes until a mirror-like surface is achieved. For some samples, even a 9  $\mu\text{m}$  diamond paste was used. The polishing was performed manually on DP-Mol or DP-Nap soft cloths, and the appropriate lubricant was used for each paste. Each sample was polished for 15-20 minutes at each paste. After each polishing step, the samples were cleaned the same way as in the grinding process.

This process is followed by chemical etching with 2 % v/v HNO<sub>3</sub> in ethanol (Nital 2%) for 5-10 sec at room temperature to reveal the microstructure. The Nital etches first constituents of the microstructure with higher energy, such as grain boundaries. Consequently, the etching allows easy observation of the boundaries and the crystallographic orientation of the grains, phases, and precipitates of the microstructure.

The grinding and polishing steps that were used for the SEM are also used for the sample preparation for the Electron Backscatter Diffraction (EBSD) analysis. Though, two polishing steps are added using 0.3  $\mu\text{m}$  aluminum oxide and 0.1  $\mu\text{m}$  colloidal silica (OPU) while no etching is done. This leads to an even more flat surface, which is necessary for EBSD, as the electron beam is scattered on the sample's surface under a specific

angle. Both steps were performed manually. The polishing with aluminum oxide was performed for 15-20 minutes, while the polishing with OPU was performed for 45-60 minutes.

Finally, the Transmission Electron Microscope (TEM) samples were ground to 100  $\mu\text{m}$  thickness and then cut into discs with a diameter of 3 mm. For the grinding, SiC papers were used at 220, 400, and 800 grit, as lower grit papers may induce dislocations in the sample. Once the sample has reached the desired thickness, it is cut into discs into the TEM disc punch cutter. The disc is then mounted on a specific sample holder and is ground to a final thickness of 40  $\mu\text{m}$ . Finally, the Precision Ion Polishing System (PIPS) was used. The argon ions beam hits the center of the sample at an angle to reduce the thickness of the sample until a hole is created in the middle. Once the hole is created, the surrounding area of the sample is expected to have a thickness from a few nm up to 150 nm. This process was also applied in the samples that were studied with the TKD method.

### **7.2.2. Scanning Electron Microscope (SEM)**

The SEM was used in order to study the microstructures of the initial materials and the materials after the heat treatments. The constituents and phases of the microstructures were analyzed, as long as their grain sizes and the sizes of the parent austenite grains. An approximation of the fraction of each constituent was also made.

For the experiments performed at the National Technical University of Athens, a JEOL6380LV SEM was used with an accelerating current of 20kV and a working distance of 10mm in secondary electron imaging mode.

For SEM analysis in the University of Ghent, an FEI Quanta TM 450-FEG-SEM (FEI Company, Hillsboro, OR, USA) operating at 20 kV and spot size 5 in SE (BSE) mode was used.

### **7.2.3. Electron Back-Scatter Diffraction (EBSD)**

Electron backscatter diffraction (EBSD) patterns are obtained in the SEM by focusing a stationary electron beam on a crystalline sample. Electron Backscatter Diffraction Patterns (EBSPs) are observed when a fixed, focused electron beam is positioned on a tilted specimen. Tilting is used to reduce the path length of the backscattered electrons, and in order to obtain sufficient backscattered electrons, the specimen is tilted between 55-75°, where 70° is considered ideal. The backscattered electrons escape from 30-40 up to 100 nm underneath the surface; hence there is a diffracting volume. The image is then captured using a low-light CCD camera. The bands in the pattern represent reflecting planes in the diffracting crystal volume. Thus, the geometrical arrangement of the bands is a function of the orientation of the diffracting crystal lattice.

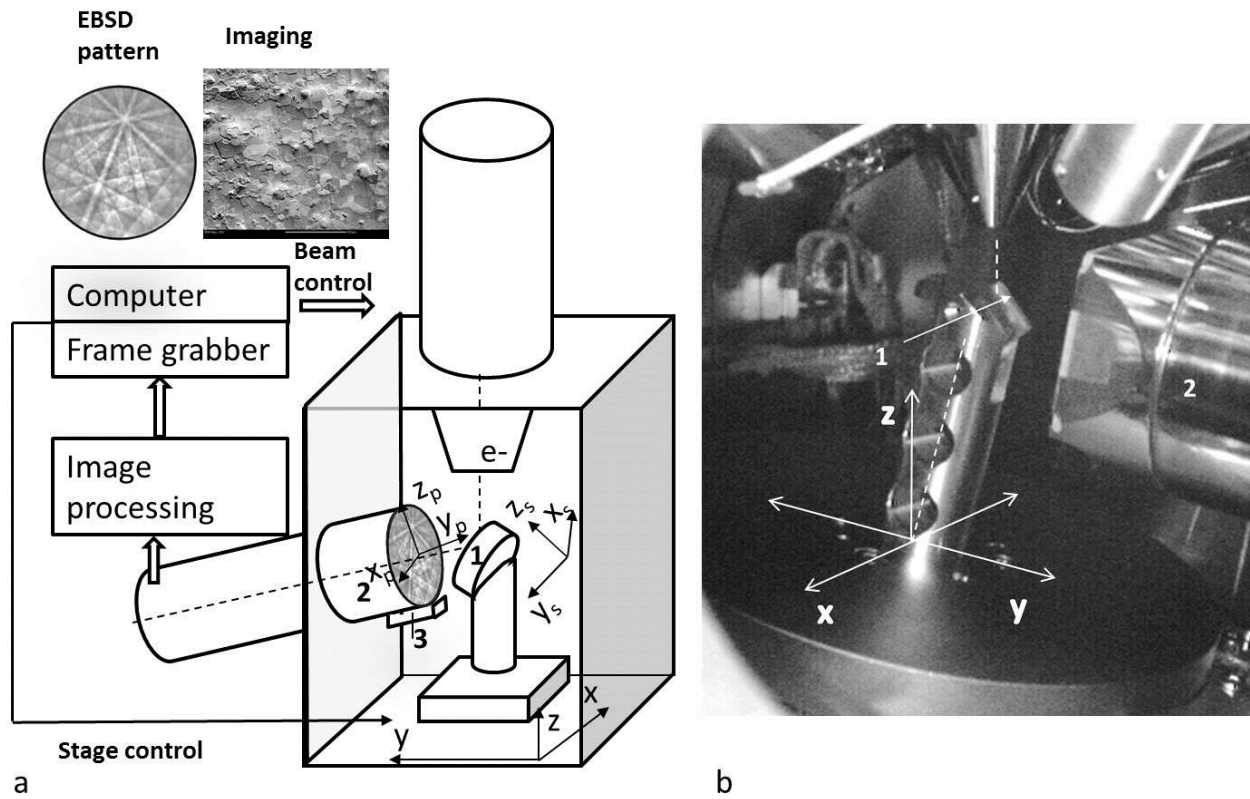


**Figure 7.3:** The setup of the EBSD. The sample is placed on the holder in position 1 and tilted  $70^\circ$  to the phosphorous screen in position 2.

EBSD patterns, consisting of Kikuchi bands, are formed when a stationary electron beam interacts with a crystalline lattice in a highly tilted sample in the SEM

- The geometrical relationships of the bands hold information about the crystal lattice in the diffracting volume
- The width and intensity of a band is directly related to the spacing of atoms in the corresponding crystal plane
- The symmetry of the crystal lattice is reflected in the pattern
- The orientation of the crystal lattice with respect to a laboratory reference frame can be determined from a pattern assuming the material is of a known crystal structure.

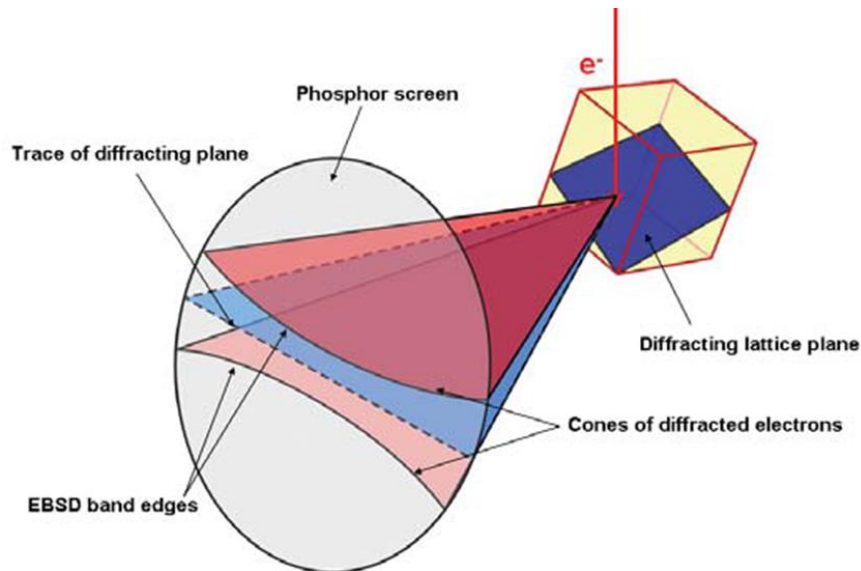


**Figure 7.4:** Formation of Kikuchi bands on the phosphor screen

In the Hough Transform, bands in the pattern are transformed to peaks, reducing the band detection problem to identify the peaks' positions. The key to the Hough Transformation is the following equation:

$$\rho = x * \cos\theta + y * \sin\theta \quad \text{Eq 7.1}$$

Where  $x$  and  $y$  are the coordinates (column and row) of a pixel in the EBSD pattern image,  $\rho$  and  $\theta$  are the coordinates of lines that pass through the pixel. Thus, a pixel in the image space becomes a sinusoidal curve in the transform space, as shown below. If the equation is applied to every pixel in the image, then the Hough Transform becomes a large set of sinusoidal curves.

The image quality parameter, IQ, describes the quality of an electron backscatter diffraction pattern and equals with the sum of detected peaks in the Hough transform. It is dependent on the material, its condition (strained or not), and sample preparation.

EBSD can measure orientations directly. Grain boundaries are determined by quantified orientation changes (misorientations), and therefore grains are determined by grouping together similar orientations. When grouping pixels as grains, it is possible to specify the minimum number of pixels required. This helps improve confidence in grain determination, and it is important relative to grain size distribution and step size.

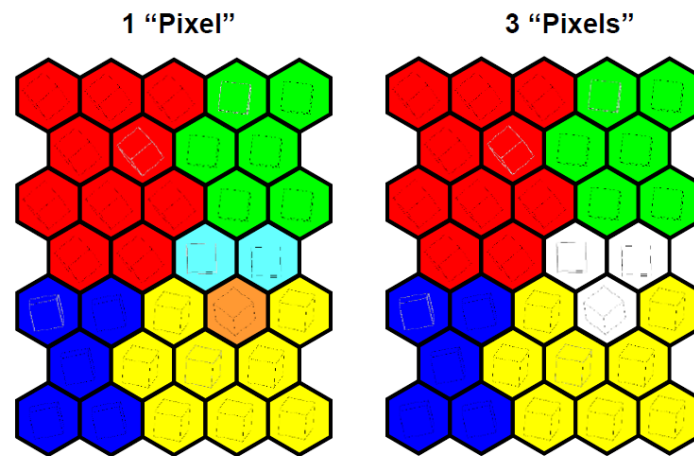


**Figure 7.5:** In the EBSD processing software, the definition of grains differs with different settings parameters.

Therefore, the grain boundaries can be classified as Low Angle  $5^{\circ}$ - $15^{\circ}$  (LAGB) and High Angle  $15^{\circ}$ - $65^{\circ}$  (HAGB). The associated grain boundary energy is dependent on the grain boundary type and increases with increasing misorientation angle. The type of boundary also influences etching behavior for traditional visualization. Therefore, a LAGB can be described as an array of dislocations that cause sub-grain dislocation cell structures. On the other hand, with larger misorientations in HAGBs, the interface can no longer be described by dislocations, and the disorder at the transition zone influences boundary properties such as diffusion and segregation.

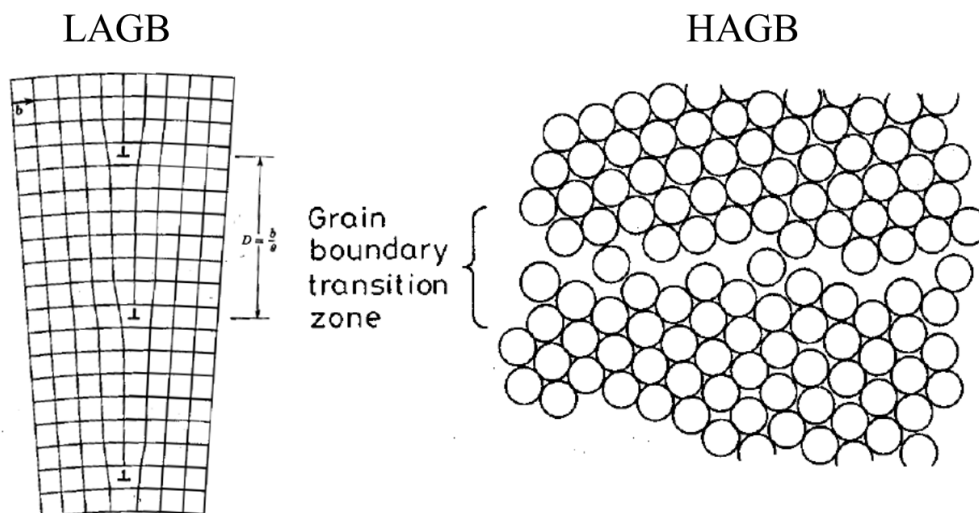


**Figure 7.6:** The definition of LAGBs (left) and HAGBs (right).

EBSD was used to study multiple aspects of the samples. The fractions of constituents as ferrite and martensite were estimated as long as the existence of bainite. The grain sizes were also measured. Through EBSD maps, the recovery and recrystallization stages were also studied during UFH.

An accelerating current of 20kV is used for the Quanta TM 450-FEG-SEM EBSD in the University of Ghent and a working distance of 8 mm. The resulting patterns were acquired on a hexagonal scan grid by a Hikari

detector operated with EDAX TSL–OIM-Data Collection version 6 software. The EBSD scans were performed at a step size of 50 nm. The corresponding orientation data were post-processed with EDAX-TSL-OIM-Data Analysis version 7 software using the following grain definition: Misorientation with neighboring grains higher than 5°, a minimum number of points per grain was 2, and confidence index (CI) higher than 0.1. The raw EBSD data were post-processed (cleaned) to re-assign the dubiously indexed points using the grain confidence index standardization and neighbor CI correlation procedure.

The transmission Kikuchi diffraction (TKD) was performed using the same equipment. The working distance was set to 5 mm and the step size to 20 nm. A TEM disk sample was placed on a special sample holder and was set so that the electron beam went through the sample and to the detector at an angle of 70°.

#### 7.2.4. *Transmission Electron Microscopy (TEM)*

TEM was used to prove the existence of different phases and constituents expected from simulation and EBSD. The morphologies of each constituent were studied, their composition via EDS, and indexing of the selected areas diffraction was performed for the characterization.

In the NTUA, the Jeol 2100 HR TEM was running at 200kV and was mounted with an EDS detector, while in Ghent University, a Jeol JEM-2200FS, 200 kV field emission TEM (JEOL Ltd., Tokyo, Japan) was used for the analysis. The electron source is a LaB<sub>6</sub> wire. The Digital Micrograph Software by Gatan© was used to index the patterns received from TEM and measure the size of the constituents. For the indexing, the planar distance  $\vec{g}$  of the spots was measured in nm<sup>-1</sup>. Then the d spacing is calculated from the equation:

$$d = \frac{1}{|\vec{g}|} \quad \text{Eq. 7.2.}$$

Then, d is compared with the data derived from X-Ray Diffraction analysis and corresponded to specific hkl indexes of family planes. This process is repeated for at least three spots.

The next step is to calculate the angle between these spots using the equation:

$$\cos\varphi = \frac{h_1h_2 + k_1k_2 + l_1l_3}{\sqrt{(h_1^2 + k_1^2 + l_1^2)(h_2^2 + k_2^2 + l_2^2)}} \quad \text{Eq. 7.3.}$$

where  $\varphi$  is compared with the angle calculated by the contractor. Finally, the crystal zone axis for the indexed diffraction spots needs to be defined. To do so, the following formulas need to be followed:

$$\langle uvw \rangle = \{h_1k_1l_1\} \times \{h_2k_2l_2\} \quad \text{Eq. 7.4.}$$

$$\begin{bmatrix} i & j & k \\ h_1 & k_1 & l_1 \\ h_2 & k_2 & l_2 \end{bmatrix} = i(k_1l_2 - l_1k_2) - j(h_1l_2 - l_1h_2) + k(h_1k_2 - k_1h_2) \quad \text{Eq. 7.5.}$$

### 7.2.5. X-Ray Diffraction (XRD)

The XRD was also used to identify the phases present in the commercial steel that was studied in Chapter 8.3. The samples were prepared by grinding in 240, 500, 800, 1200 grit SiC papers. Between each step, Nital 2% was applied on the surface in order to reduce the deformation of the material, which may affect the diffraction of X-rays.

The XRD used had a Mo source (Mo K-alpha: 17.45 keV,  $\lambda = 0.7107 \text{ \AA}$ ) and the sample was rotated at angles between 20-45°. The detector remained at each degree for 12 minutes and each scan's duration was 5 hours.

## 7.3. Simulation software

### 7.3.1. Parent austenite reconstruction software ARPGE

ARPGE [130] is a software written in Python and uses theoretical results to reconstruct parent grains from EBSD data automatically. The misorientations between the scanned grains are identified with operators, the daughter grains are identified with indexed variants, the orientations of the parent grains are determined, and some statistics on the variants and operators are established.

With this program, the scanned grains are identified alongside the misorientations between them. It then uses either the Kurdjumov-Sachs (K-S) or the Nishiyama–Wassermann (N-W) orientation relationships between ferrite and austenite in order to determine the orientations of the parent austenite grains.

In order to verify the accuracy of this software, the following experiment was done. The IPF map of a martensitic steel was made via EBSD, seen in **Figure 7.7a**. This steel consisted of 96 % BCC and 4 % FCC (retained austenite) phases, as shown in **Figure 7.7b**. Thus, the IPF map of the FCC phase only was made (**Figure 7.7c**) and compared with the IPF made by the software (**Figure 7.7d**). To make the comparison easier, the boundaries of the parent austenite grains are integrated into the IPF map of austenite in white color. As can be observed, the orientations of the retained austenite match almost perfectly the orientation of the parent austenite grains.



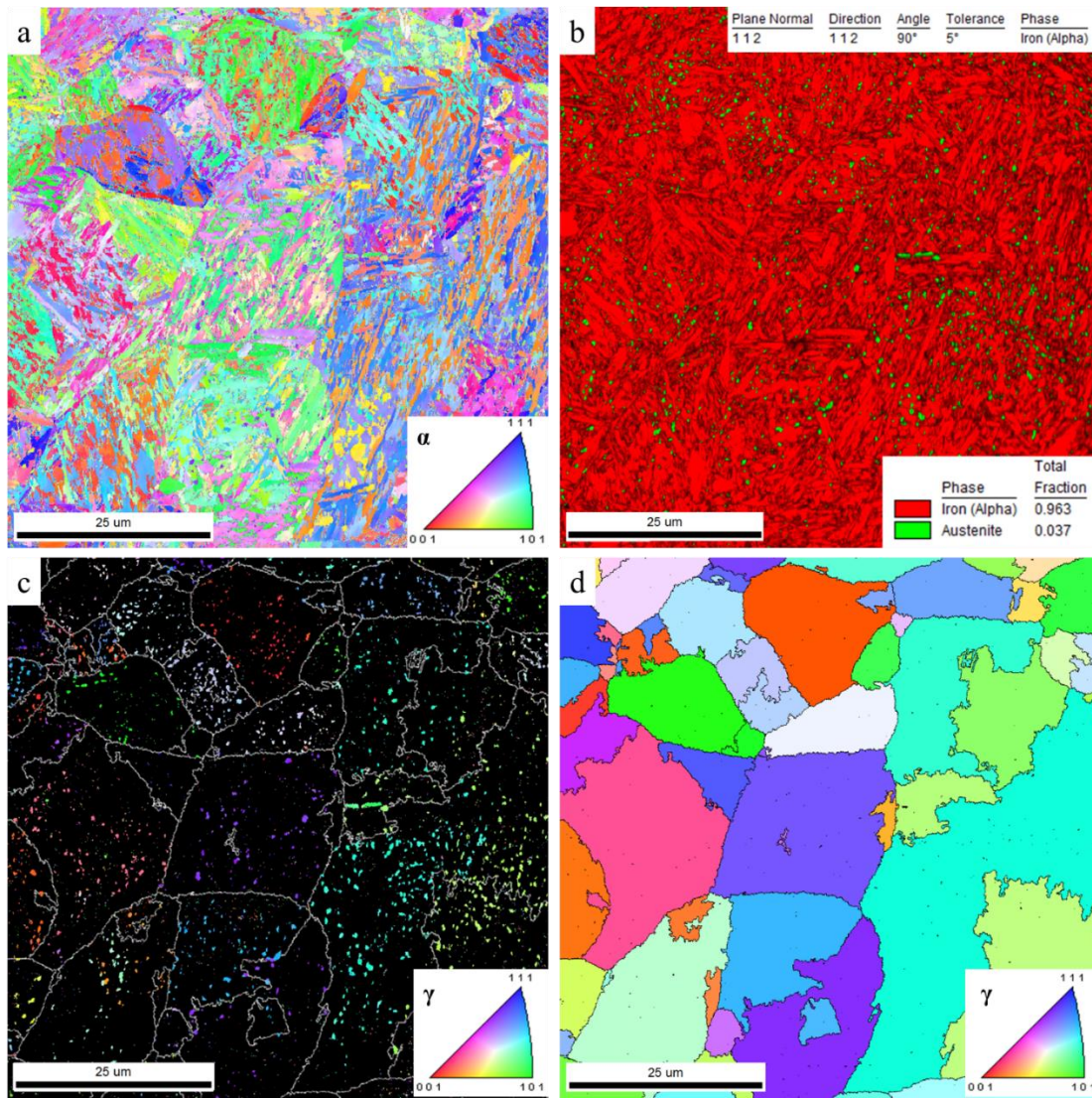


**Figure 7.7:** (a) IPF map of the ferrite phase of a UFH steel sample. (b) Phase map of the same area indicating the presence of RA (green). (c) IPF map of the austenite phase only. (d) IPF map of the reconstructed PAGs created by the ARPGE software. The orientations of the PAGs match perfectly the orientations of the RA. Step size: 50 nm.

## 7.4. Mechanical properties

### 7.4.1. Tensile tests

An Instron 5000 tensile testing equipment with a 50 kN load cell and crosshead of 2.4 mm/min (strain rate 0.007) was used to evaluate the tensile properties. **Figure 7.8** shows the sub-size dog-bone geometry designed according to [28]. The tensile sample's shoulders and gauge length are inside the homogeneously heated zone that was obtained after the heat treatments. Three tensile tests were performed per condition. The yield strength was determined by the conventional 0.2% offset method. The strain obtained during the tensile test was measured by 2D-digital image correlation (2D-DIC), and the acquired data was post-processed with the MatchID software.



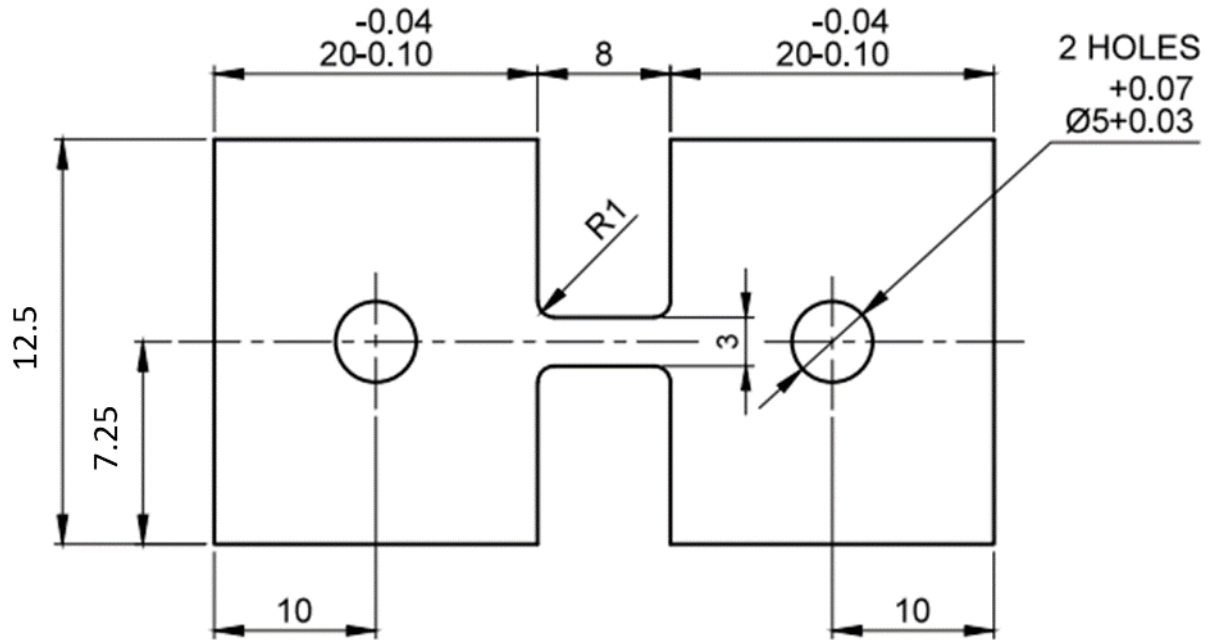


**Figure 7.8:** Schematic of the dog-bone sample that was cut for the tensile tests.

**Digital image correlation** (DIC) is a non-contacting optical full-field deformation measurement approach that addresses the complex behavior of TRC materials. Developed by Sutton et al. [131] and Bruck et al. [132], this method has been widely applied for composites and reinforced concrete. In order to perform DIC, an area of interest is manually specified and divided into an evenly spaced virtual grid. The displacements are computed at each point of the virtual grids to obtain full-field deformation. In the current experiments, the gauge length of the tensile samples was painted white. Then, black paint was applied from a specific distance through spraying so that a random distribution of black dots is achieved. The first image (**Figure 7.9a**) is taken before any load is applied and is used as a reference. As the tensile test is performed, the elongation is measured by the change in the gauge length and the distance between the black dots. **Figure 7.9b** is taken a moment before the sample cracks, while **Figure 7.9c** is taken right after the sample's failure.

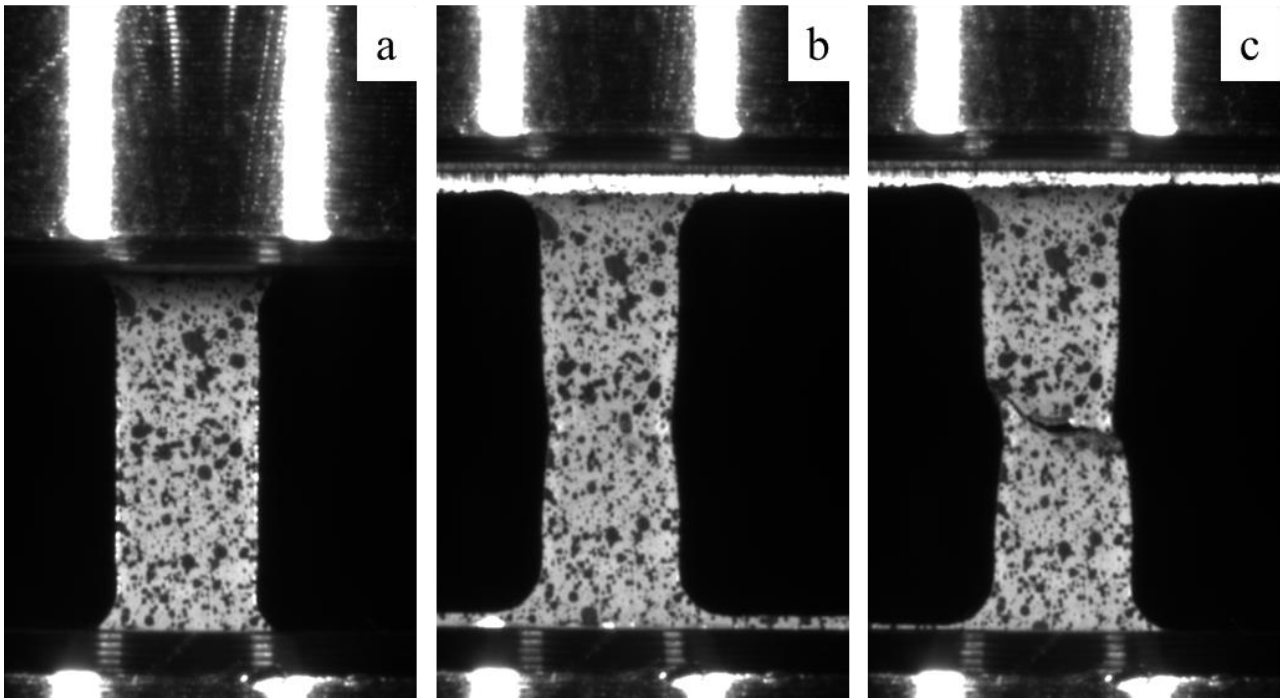


**Figure 7.9:** The samples were painted white and black dots were added with black spray paint. The DIC camera tracked the change in the dots and their distance along with the tensile test. (a) initial position, (b) necking (c) fracture.

With the use of DIC, the R-value was also calculated. The plastic strain ratio R is a parameter that indicates a sheet metal's ability to resist thinning or thickening when subjected to either tensile or compressive forces in the plane of the sheet. It is a plastic anisotropy measure and is related to the preferred crystallographic orientations within a polycrystalline metal. This resistance to thinning or thickening contributes to forming shapes, such as cylindrical flat-bottom cups, by the deep-drawing process. The value of R, therefore, is considered a measure of sheet-metal drawability. It is particularly useful for evaluating materials intended for parts where a substantial portion of the blank is drawn from beneath the blank holder into the die opening. To calculate the R-value, measure the axial strain (the strain along with the thickness of the specimen, yy) and transverse (xx) strain were calculated. For instance, the calculated strain on the yy axis is shown in **Figure 7.10**. Similarly, the strain in the x-axis and the strain parallel to the thickness of the sample (zz) is calculated.

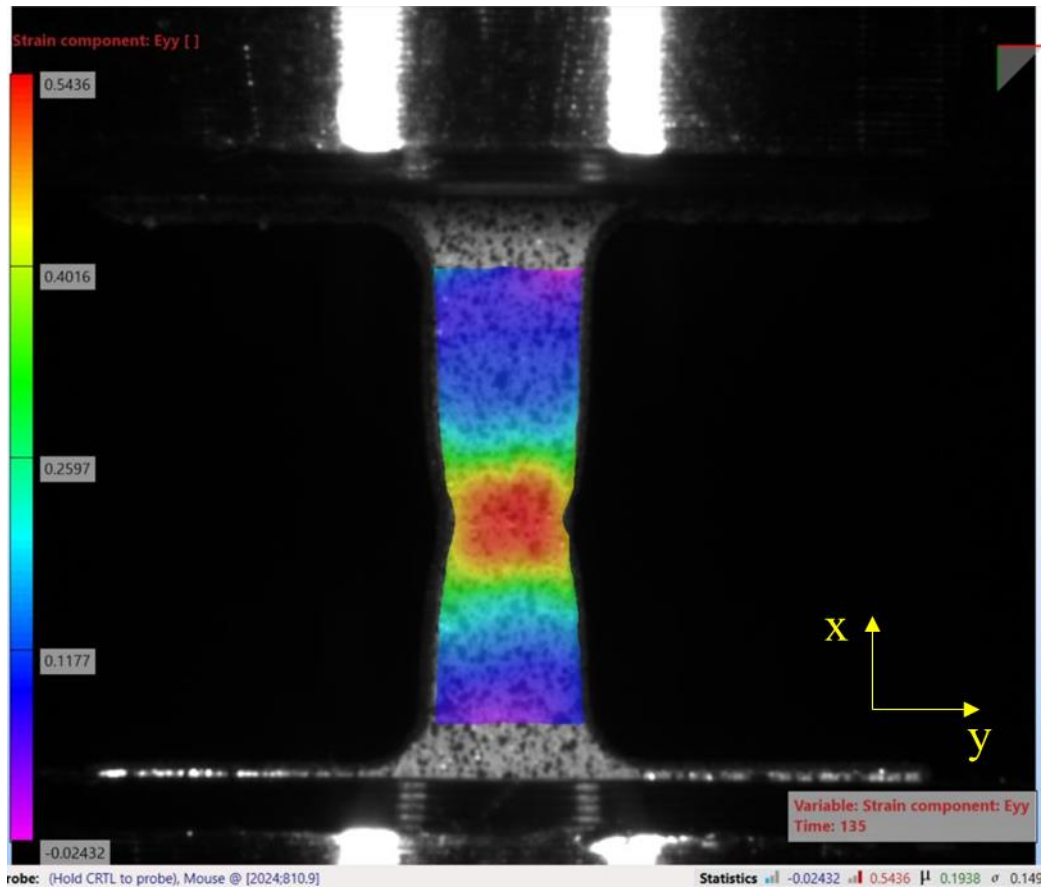


**Figure 7.10:** Schematic of the strain accumulation in the sample at the point before the fracture.

Then the R-value is given from the equation:

$$R = \frac{e_y}{e_z} \quad \text{Eq. 7.6}$$

In order to measure the average normal R-value, the tensile tests were performed at 0°, 45°, and 90° angle to the rolling direction. Then the normal R-value is calculated from the equation:

$$R = \frac{1}{4} (R_0 + 2R_{45} + R_{90}) \quad \text{Eq. 7.7}$$

The planar anisotropy ( $\Delta R$ ) can also be calculated as follows:

$$\Delta R = \frac{1}{2} (R_0 - 2R_{45} + R_{90}) \quad \text{Eq. 7.8}$$

The R-value is an indicator of a material's ability to demonstrate a non-earing behavior (lower is better), while  $\Delta R$  is an excellent indicator of the ability of a material to be deep drawn (higher is better). A combination of high R and  $\Delta R$  provides optimum drawability. For better understanding, the normal and planar anisotropies are shown in **Figure 7.11**.

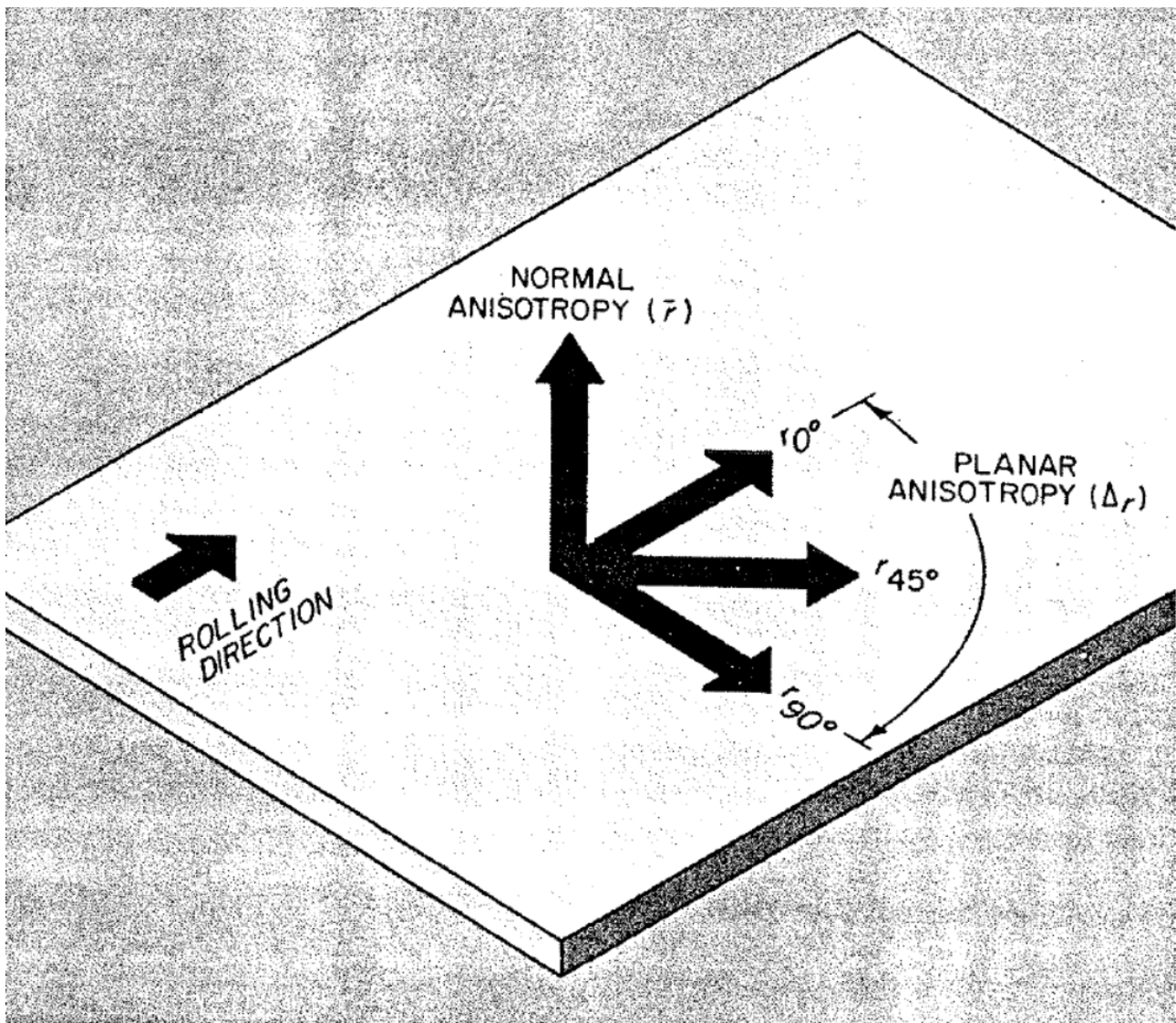


**Figure 7.11:** Schematic that shows the normal ( $R$ ) and planar ( $\Delta R$ ) anisotropies on a rolled sheet [133].

#### 7.4.2. Hardness test

During the Vickers hardness (HV) test, the indent is a very small diamond pyramid with a peak angle  $\alpha = 136^\circ$ , which is pressed onto the specimen's surface with a force of 198 N. The resulting imprint is observed under a microscope, and the diagonals are measured. Then the measurement is converted to hardness through specific tables. In each sample, 10-12 measurements were taken in order to obtain a better statistical result, and the average was calculated. Before the hardness test, the samples were ground up to a 1200 grit paper.

## 8. Experimental Results

### 8.1. The effect of the thermal treatment's parameters

#### 8.1.1. Introduction

The application of high heating rates was firstly studied at small-size samples with the use of a dilatometer. Therefore, it is possible to study the effect of different heating and sample parameters easier. Some of the studied parameters described in this thesis are the effect of the chemical composition, the heating rate, the peak temperature, and the soaking time at the peak temperature. This will give a better insight into the thermal treatment that should be applied in large-scale samples to achieve optimal results.

#### 8.1.2. Implementation

Three different experiments were conducted in this set, the implementation of which follows. Controlled-heating experiments were performed in a Bähr 805A quench dilatometer. The samples had a length of 10 mm, width 2 mm, and a thickness of 1 mm and were cut from the cross-sections of hot-rolled bars. An S-type thermocouple controlled the temperature, spot welded to the midsection of each test sample. The heat treatments were performed using induction heating. For the microstructure characterization, electron microscopy techniques were combined. Specifically, SEM and TEM were utilized to observe the micro-constituents and STEM/EDS for their chemical analysis. In contrast, EBSD was utilized to further study the microstructural constituents, their size, crystallographic orientation, and the prior (parent) austenite [130] orientation and morphology. ThermoCalc® and DICTRA [134] were employed to study the diffusion of alloying elements and the carbide dissolution during ultra-fast heating and isothermal holding at peak temperature. The sample preparation followed is the one mentioned in the previous chapter. For Scanning Electron Microscopy (SEM) analysis, a JEOL6380LV SEM operating at 20 kV in SE (BSE) mode was used. For Electron Back-Scatter Diffraction (EBSD) analysis, an FEI Quanta TM 450-FEG-SEM was operated under the following settings: The accelerating voltage was 20 kV with a beam current corresponding to an FEI spot size of 5, aperture size of 30  $\mu\text{m}$ , and a working distance of 11 mm. The sample was tilted by 70° toward the EBSD detector. The resulting patterns were acquired on a hexagonal scan grid by a Hikari detector operated with EDAX TSL—OIM-Data Collection version 6 software. The EBSD scans were performed at a step size of 0.5  $\mu\text{m}$  and 0.05  $\mu\text{m}$ . The corresponding orientation data were post-processed with EDAX-TSL-OIM-Data Analysis version 7 software using the following grain definition: Misorientation with neighboring grains higher than 5°, the minimum number of points per grain was 2 and confident index (CI) higher than 0.1. Based on the EBSD data, prior austenite grains were reconstructed using the ARPGE software developed by C. Cayron [130]. A Jeol 2100 HR, 200 kV Transmission Electron Microscope (TEM) was used for the TEM analysis in bright field imaging mode. For the calculation of the CCT diagrams, the models of Kirkaldy [135] and Bhadeshia [136, 137] were used, taking into account the chemical composition of the steel and the grain size of the parent austenite. During the calculations, the composition's homogeneity and grain sizes are assumed, while the conditions are considered near-equilibrium.

### 8.1.3. Effect of the Chemical Composition

#### 8.1.3.1. Materials and methods

The first experiment was designed so that the effect of alloying elements such as Mn, Cr, and Mo is studied. Thus, two steel grades were chosen to undergo the same UFH treatment. The chemical compositions can be seen in **Table 8.1.1**.

**Table 8.1.1:** The chemical compositions in wt. % for the two samples that were used in this experiment.

	C	Mn	Si	Cr	Mo	P	S
42CrMo4	0.43	1-1.43	0.3-0.4	1.1-1.23	0.1-0.25	<0.04	<0.04
C45	0.42-0.45	0.5-0.8	<0.4	<0.4	<0.03	<0.035	<0.035

The initial microstructure of both grades consists of ferrite and pearlite, and the samples were hot-rolled before the thermal treatment. As these two grades have the same carbon content, the pearlite fraction in the initial microstructure is expected to be the same. The ratio of ferrite to pearlite was calculated with the grid method at approximately 1/1. The images from the LOM for the initial microstructure of the two steels are shown in **Figures 8.1.1a, b**.

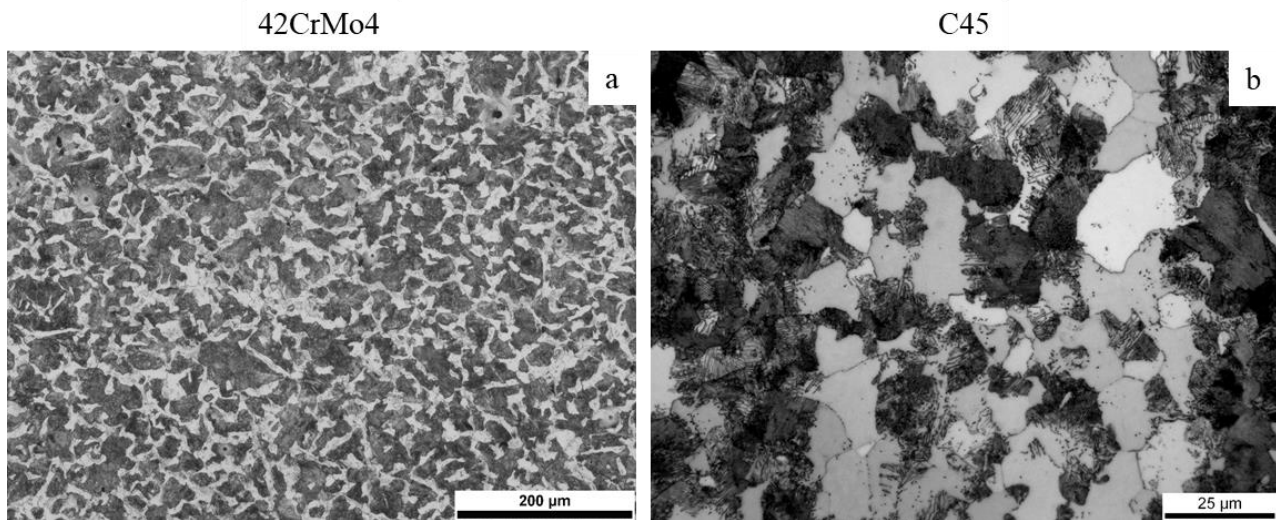


**Figure 8.1.1:** LOM images of the initial microstructures of the (a) 42CrMo4 and (b) C45 samples.

For this experiment, the two samples were submitted to the same thermal treatment. A high heating rate of 100 °C/s was applied until the peak temperature of 1080 °C was reached. This temperature was chosen high inside the austenitic region of the phase diagram in order to avoid incomplete austenitization. As mentioned before, higher heating rates lead to an increase in the transformation temperatures, and thus, lower peak temperatures may lead to remnants of ferrite in the microstructure. The soaking time at this temperature was short, specifically 3 s, and was followed by quenching with helium gas. The heat treatment is better shown in the diagram of **Figure 8.1.2**.

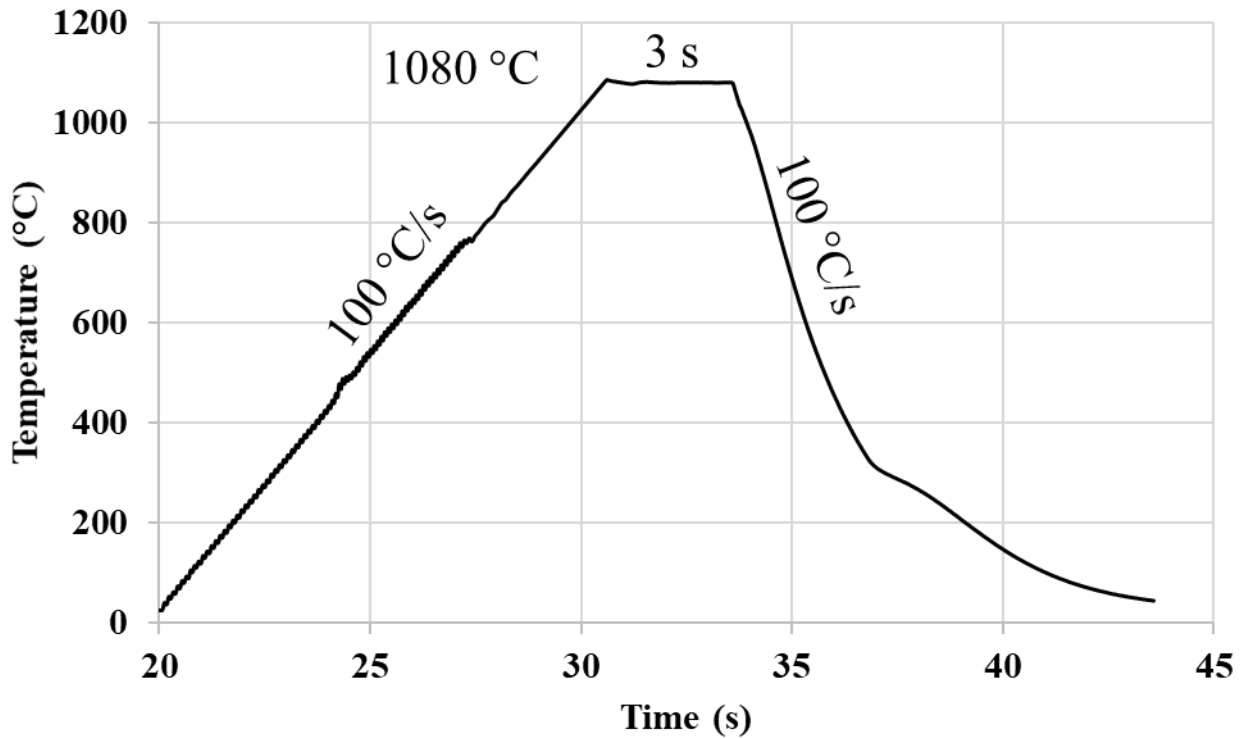


**Figure 8.1.2:** The heat treatment that was applied in both samples.

### 8.1.3.2. Results

From the dilatometer's thermal treatments, the change in the sample's length due to dilation is measured as a fraction of temperature. From this change, the diagrams shown in **Figures 8.1.3a,b** are plotted for the 42CrMo4 and C45 samples, respectively. It can be observed for both samples that a decrease in the samples' length occurs during heating. This is due to the transformation from the BCC microstructure to the FCC. As the former has an APF of 0.68 and the latter 0.74, the iron atoms in the FCC lattice are more closely packed than the BCC lattice. Thus, a decrease in the length of the sample is observed. Therefore, the beginning of the slope is associated with the  $A_{c1}$  temperature while the end of the slope with the  $A_{c3}$ . As complete austenitization is achieved, the samples continue to increase in length due to dilation. The same applies to the observed slope during cooling and is associated with the  $M_S$  temperature. It has been calculated that the  $A_{c1}$  temperature for the 42CrMo4 sample is 810 °C while for the C45 is 30 °C lower, at 780 °C. Respectively, the  $A_{c3}$  temperature for the 42CrMo4 sample is 850 °C while for the C45 is only 10 °C lower, at 840 °C. Finally, the  $M_S$  temperatures were measured to be almost the same.

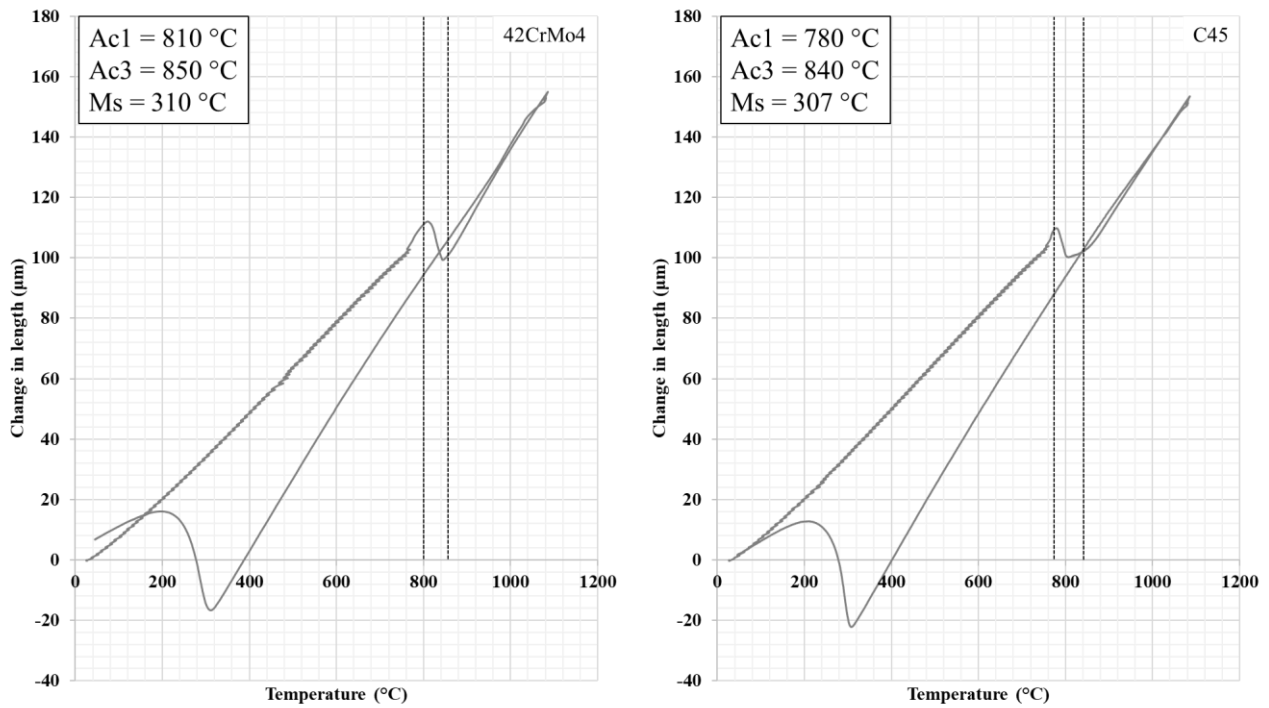


**Figure 8.1.3:** Temperature-dilatation diagrams that were plotted from the dilatometry data for the 42CrMo4 (left) and C45 (right) samples. The transformation temperatures  $A_{c1}$ ,  $A_{c3}$ , and  $M_s$  were calculated from this diagram.

Both samples were studied in the SEM. In **Figures 8.1.4 a, c, e**, the microstructure of the 42CrMo4 sample is shown at different magnifications. Accordingly, the microstructure of the C45 sample is shown in **Figures 8.1.4b, d, f**. It appears that both samples consist mainly of martensite laths. No cementite is observed, which means that the dissolution process is completed. In the 42CrMo4 sample, some PAGs are indicated with a dashed yellow line (**Figures 8.1.4c, e**), while in the C45 sample, they are not so easily distinguished, except for **Figure 8.1.4d**. From the SEM, the PAGs of the two samples appear to be similar in size, though a more thorough analysis is described later in the EBSD comparison. In the 42CrMo4 sample some indications for lower bainite (designated with a yellow arrow) and some films between laths that may correspond to retained austenite films or cementite (designated with green arrows) were also observed. The TEM analysis of such films is shown in Chapter 8.2 of this thesis. In sample C45, it is difficult to observe such morphologies. Finally, in the 42CrMo4 sample, some large martensite laths are observed, up to 10  $\mu\text{m}$  in length, while the martensite laths in the C45 sample appear finer.



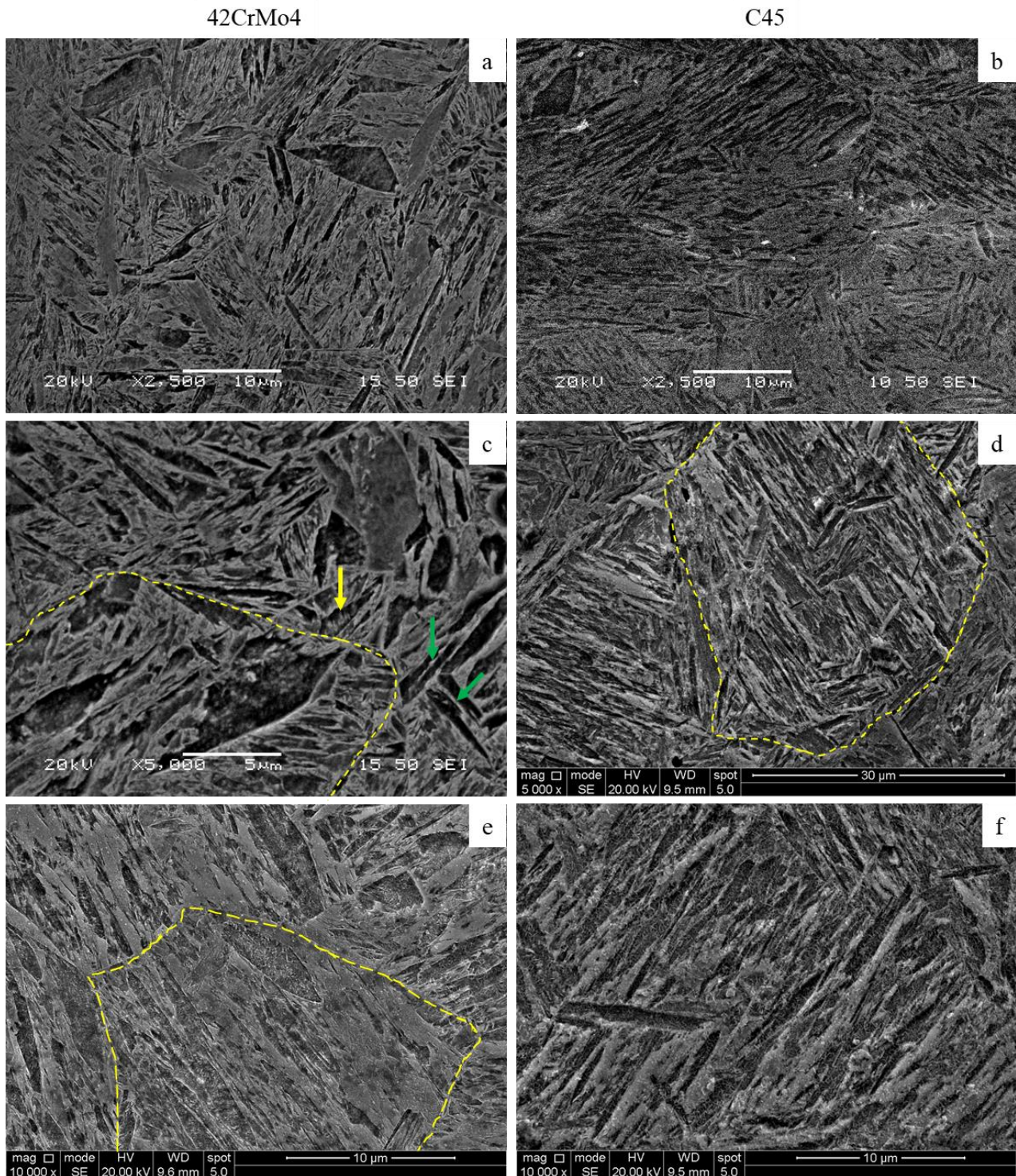


**Figure 8.1.4:** SE SEM images at different magnifications for the 42CrMo4 (a, c, e) and C45 (b, d, f) samples. Yellow arrows indicate possible bainitic laths, and green arrows possible austenite films. PAGs are indicated by yellow dashed lines.

EBSD analysis was also performed in the two samples. From the IQ maps (**Figures 8.1.5a, b**), not many differences are observed between the microstructures of the two samples. They both appear to consist of martensite laths, which agrees with the LOM and SEM images. Nevertheless, in the GAIQ maps (**Figures 8.1.5c, d**), where the rotation angles are included, indications for the existence of bainite are found. According to Zajac [28], high rotation angles between  $56^\circ$  and  $65^\circ$  correspond to high angle grain boundaries between



martensite laths and are shown in blue color. In the case of bainite, the transformation of which takes place at higher temperatures and is less disruptive, the rotation angles are lower, and specifically between  $48^\circ$  and  $55^\circ$ . They are shown in red color. Finally, the rotation angles between two ferrite grains are even lower, between  $17^\circ$  and  $47^\circ$ , and correspond to the angles between the PAGs. The charts shown in the same figure (Figures 8.6e, f) show that the fraction of rotation angles that correspond to bainite is slightly higher in the 42CrMo4 sample. In these charts, the misorientation angles are correlated to a random distribution of misorientation (MacKenzie type), and the rectangles indicate the delineated areas of PAGs (black), bainite (red), and martensite (blue) on the GAIQ map.

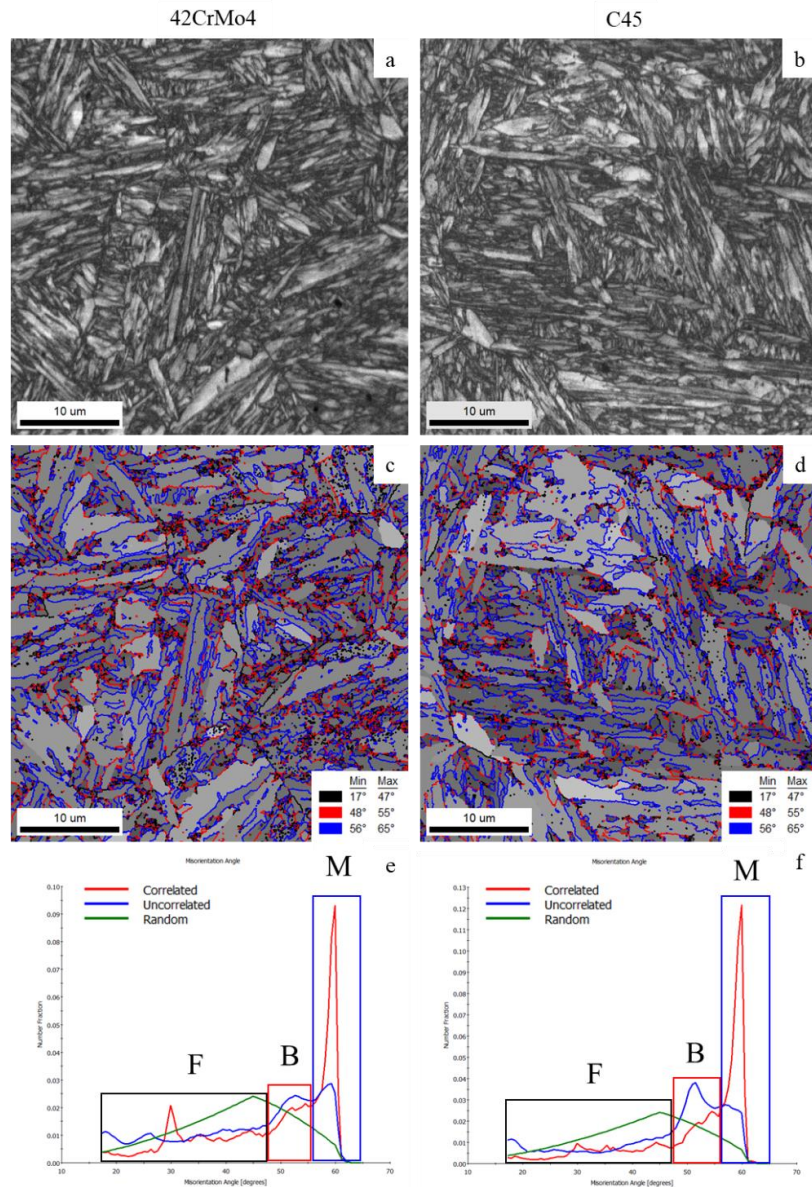


**Figure 8.1.5:** (a, b) EBSD IQ maps of the studied area. (c, d) GAIQ maps of the same area with rotation angles included. Black lines correspond to  $17^\circ$  -  $47^\circ$ , red lines to  $48^\circ$  -  $55^\circ$ , and blue lines to  $56^\circ$  -  $65^\circ$ . (e, f) Charts that show the number fraction of the different rotation angles. An uncorrelated and a random (McKenzie) distribution are added for reference. Step size: 70 nm.

From EBSD analysis, the GAM (**Figures 8.1.6a, b**) and KAM (**Figures 8.1.6c, d**) maps were plotted. As the samples are mainly martensitic, it is expected that they have high dislocation densities. In the GAM maps, the average grain deformation is indicated while the LAGBs are shown in white lines. In comparison to the KAM maps, it can be observed that the dislocation density is quite high in both samples. This is expected as the as-quenched martensite has high dislocation density due to the nature of its shear transformation.

From the IPF maps (**Figures 8.1.7a, b**), some martensite blocks can be observed. These blocks can be distinguished by laths with the same color, which means they have the same orientation. It can be observed that the martensite blocks in the 42CrMo4 sample are somewhat finer than in the C45 sample. This is an indication of the size of the parent austenite grains, which will be discussed later. In **Figures 8.1.7c, d**, the phase maps are plotted. In these maps, ferrite is shown in red color, austenite in green, and for better correspondence, the K-S relationship for  $\alpha$ - $\gamma$ :  $\langle 112 \rangle 90^\circ$  is drawn in white. Very small fractions of retained austenite are found in both samples, specifically, 2.2 % for the 42CrMo4 sample and 1.3% for the C45 sample, which is a minor difference. It is though observed that this austenite is mainly retained in the boundaries of smaller martensite laths. This makes sense, considering the transformation of martensite. As the first laths are formed, piercing through the entire length of the PAG, the rest of the austenite is enriched in carbon. As this process is repeated and smaller martensite laths are formed, at some point, the austenite that has not transformed yet will have a very high C content. Thus, the  $M_s$  temperature will be decreased to the point that the austenite can be retained.



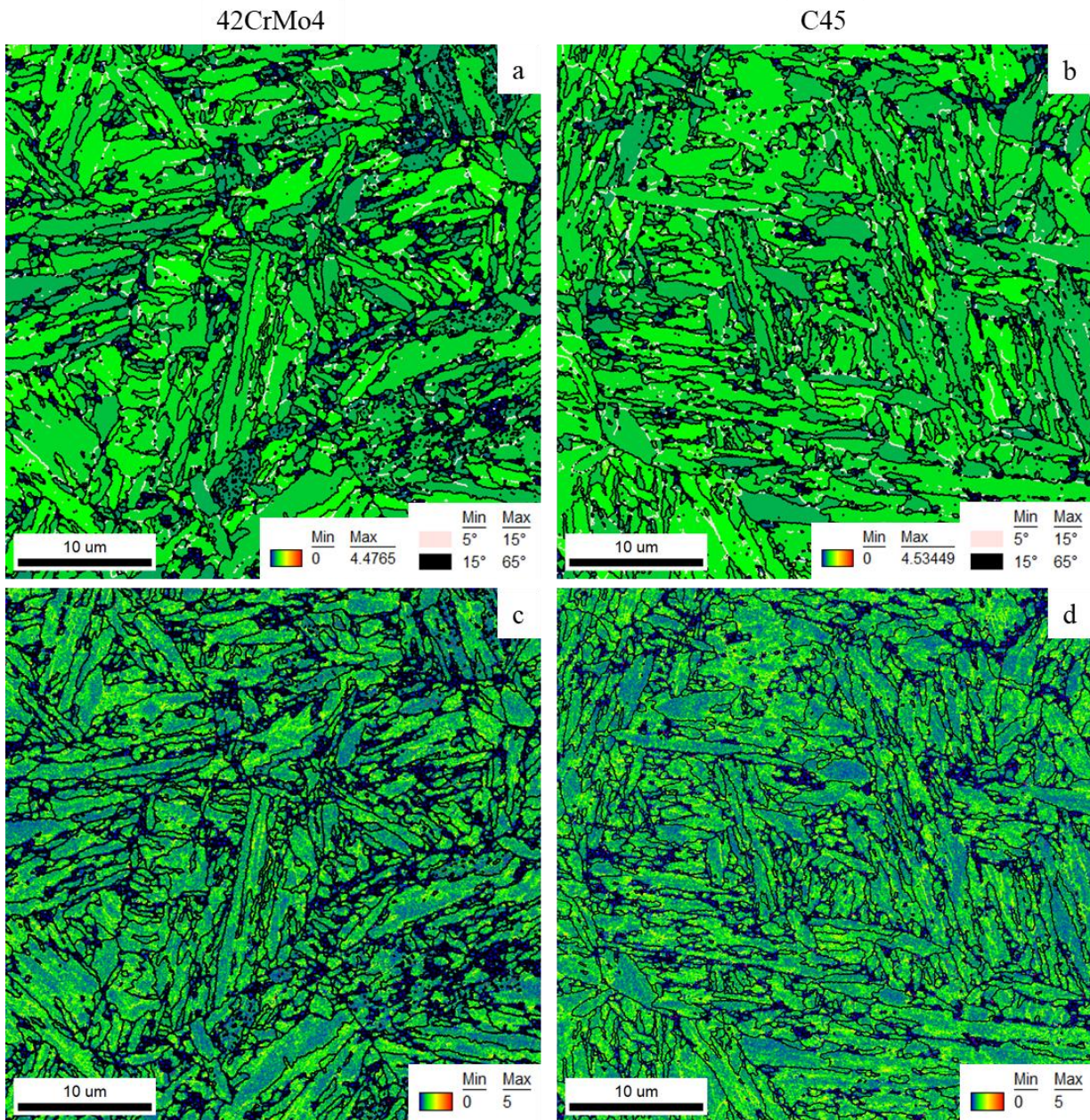


**Figure 8.1.6:** (a, b) GAM maps of both samples that indicate highly deformed grains in both samples, (c, d) 2<sup>nd</sup> neighbor KAM maps that show the dislocation density. Step size: 70 nm.



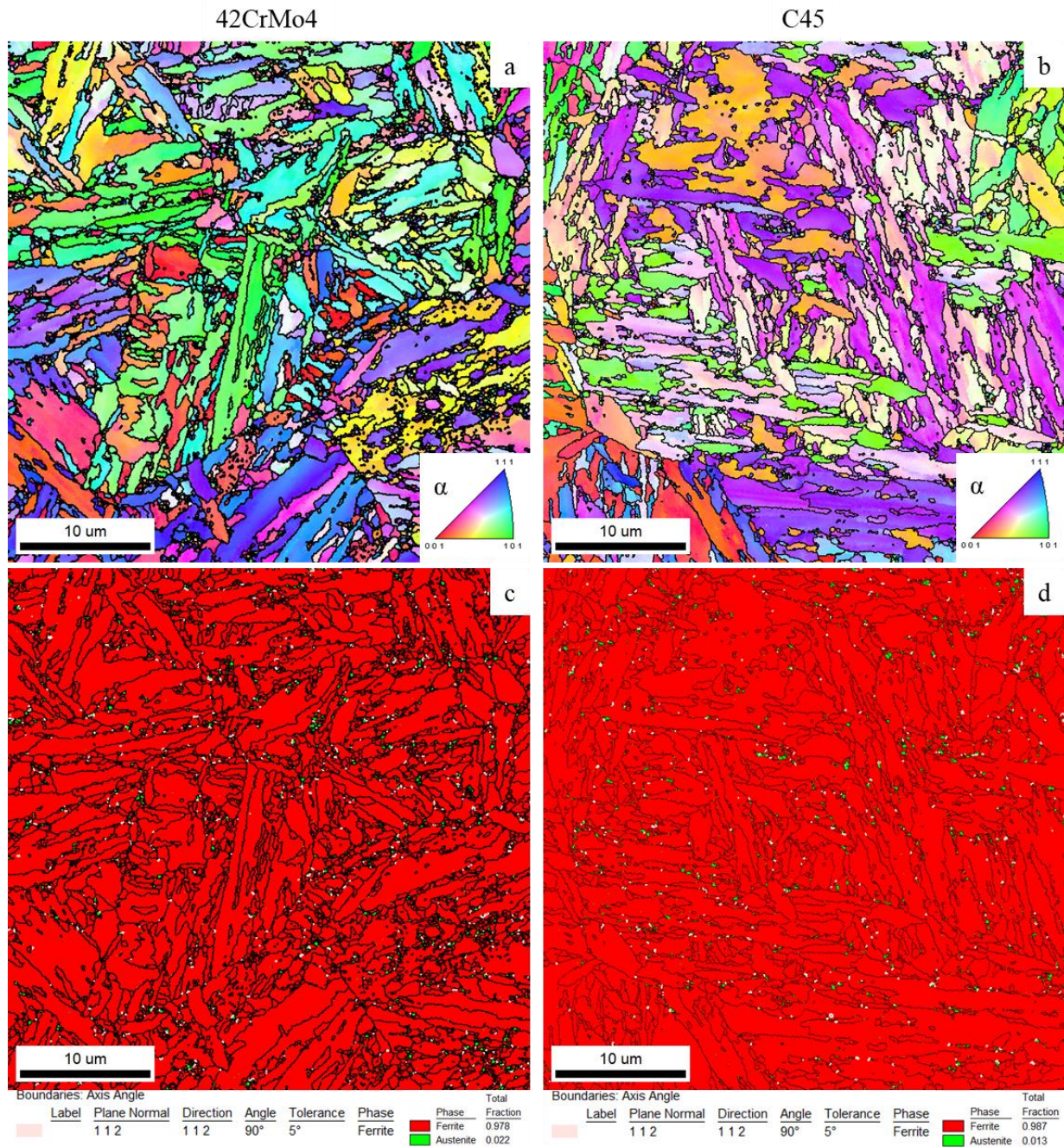


**Figure 8.1.7:** (a, b) IPF maps of the two samples that show the orientations of the martensitic laths. (c, d) Phase maps of the two samples that indicate the presence of retained austenite (green) and ferrite (red). With white color, the K-S relationships have been drawn. Step size: 70 nm.

Finally, from the EBSD analysis, the average grain size in area ( $\mu\text{m}^2$ ) was calculated. As seen in **Figure 8.1.8a**, the average martensite lath size for the 42CrMo4 sample is calculated at  $5.87 \mu\text{m}^2$ . On the other hand, and as can be seen in **Figure 8.1.8b**, the average martensite lath size for the C45 sample is  $13.37 \mu\text{m}^2$ . As both samples went through the same treatment, in order to explain this difference, the PAG size was calculated. To achieve this, the ARPGE software [130] was used. From its results, the average PAG size for the 42CrMo4 sample was calculated at  $126.48 \mu\text{m}^2$  (**Figure 8.1.8c**), while for the C45 sample, it was much larger, at  $1083.15 \mu\text{m}^2$  (**Figure 8.1.8d**). It has been reported [97, 99] that alloying elements such as Cr, Mn, and Mo tend to segregate on the  $\alpha/\alpha$  and  $\alpha/\theta$  interfaces during heating. In the current experiments, it is possible that during the



spheroidization and dissolution of the cementite lamellae, these elements that are mostly present in the 42CrMo4 sample segregate on the  $\alpha/\theta$  interfaces, impeding their dissolution by the process of solute drag effect. As the dissolution of cementite is impeded and above the  $A_{c1}$  temperature, these cementite particles can impose a pinning effect on the movement of the austenite boundaries, thus impeding its growth. Therefore, the PAGs in this sample are expected finer due to the retarding of the cementite dissolution compared to the C45 sample, in which the fraction of these elements is quite lower.

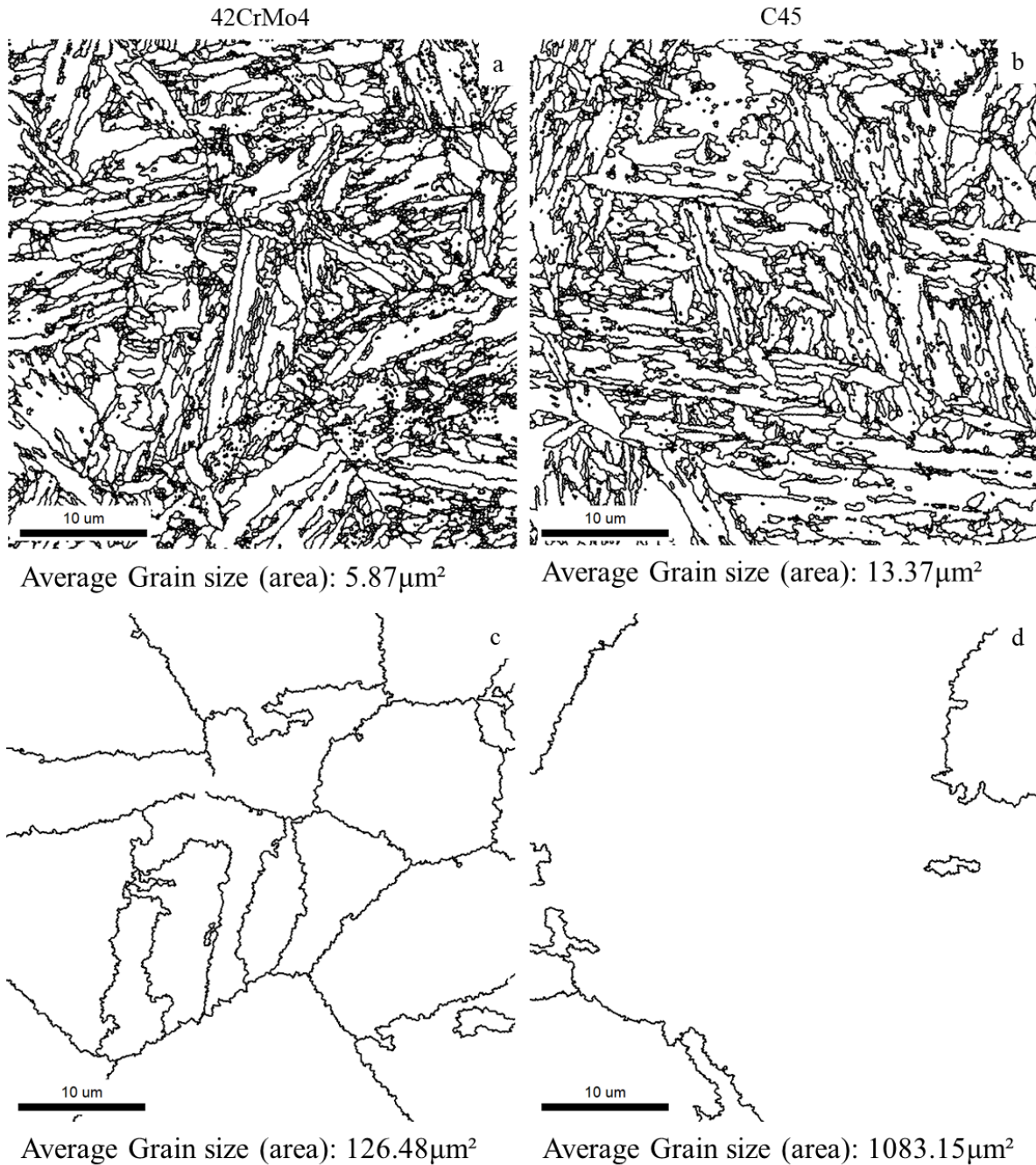


**Figure 8.1.8:** (a, b) Grain Boundaries maps for the two studied samples and the calculated average grain size. (c, d) Grain Boundaries maps for the reconstructed PAGs of both samples with the calculated average grain size. Step size: 70 nm.

To summarize, an ultra-fast heat treatment was applied on two different steel grades. In both grades, the initial microstructure consisted of ferrite and pearlite on a 1/1 ratio, and the content of Cr, Mn, and Mo was different. After the treatment, both samples had a mainly martensitic microstructure, with a small fraction of RA and indications of bainite. Both samples had a high dislocation density due to the high carbon content in martensite, while the retainment of austenite takes place in between the finer martensite laths. The main difference in these samples is the average grain size of the PAGs and, consequently, the final microstructure's martensite laths. The refinement of the microstructure of the 42CrMo4 sample is attributed to the solute drag effect that takes place due to the segregation of its alloying elements that are not found in the C45 sample. This probably retards the dissolution of cementite, which has a pinning effect on the movement of the boundaries of the austenite nuclei, impeding their growth.

### 8.1.4. *Effect of the heating time*

#### 8.1.4.1. **Materials and methods**

The second experiment was designed so that the effect of the soaking time is studied. Thus, one steel grade was chosen to undergo two UFH treatments. The chemical composition of the grade can be seen in **Table 8.1.2**.

*Table 8.1.2: The common chemical composition in wt. % of the samples used in this experiment.*

C	Mn	Si	Cr	Mo	P	S
0.43	1.43	0.4	1.23	0.1	<0.04	<0.04

The grade's initial microstructure consists of ferrite and spheroidized cementite from thermo-mechanical processing before the thermal treatment. The metallography from the LOM for the initial microstructure of the grade is shown in **Figure 8.1.9a**. The spheroidized cementite is better observed in the TEM BF image of **Figure 8.1.9b**.

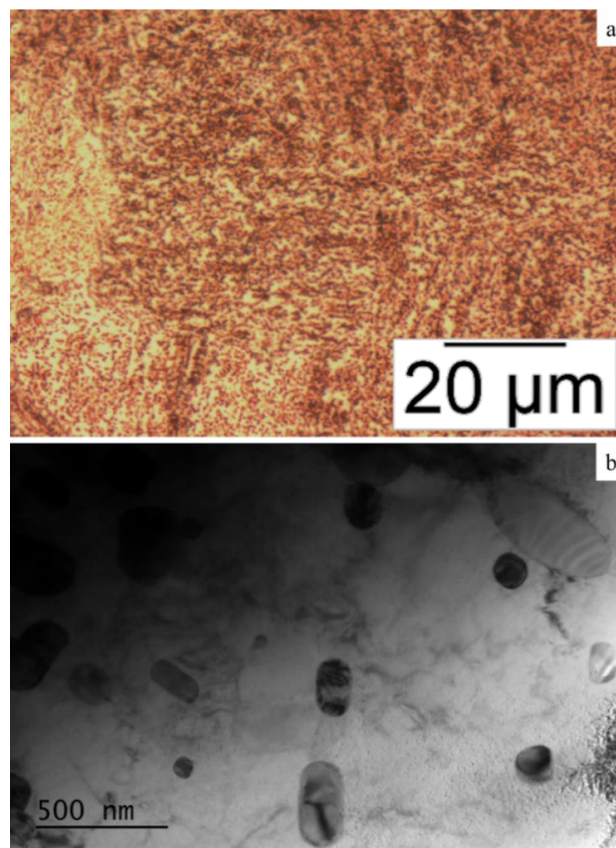


**Figure 8.1.9:** (a) LOM image of the initial microstructure consists of ferrite and spheroidized cementite, (b) BF TEM image of the initial microstructure that shows the cementite spheres.



For this experiment, two samples were submitted to two different thermal treatments. A high heating rate of 300 °C/s was applied until the peak temperature of 900 °C was reached. This temperature was chosen inside the austenitic region of the phase diagram in order to avoid incomplete austenitization. For the first sample (UF&Q), the soaking time at this temperature was short, specifically 2 s, followed by quenching with helium gas. For the second sample (UF&S&Q), the soaking time was 300 s. The heat treatments are better shown in the diagram of **Figure 8.1.10**.

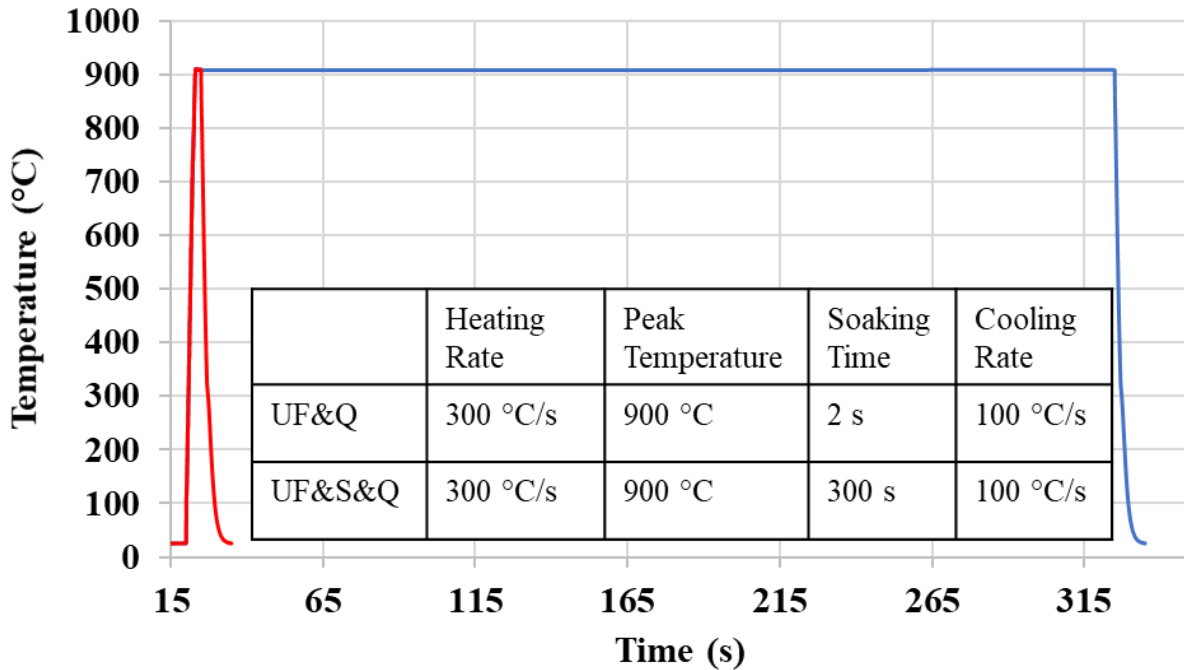


**Figure 8.1.10:** Time-Temperature diagram with the heat treatments that were applied in the two samples.

**8.1.4.2. Results**

From the dilatometry tests, the  $A_{c1}$  and  $A_{c3}$  temperatures can be extrapolated. As the samples' chemical composition and the heating rate were the same, the transformation temperatures are not expected to change. Thus, only the temperature-change in length diagram for the UF&Q sample is shown (**Figures 8.1.11**). It was calculated from this diagram that the  $A_{c1}$  temperature is 837 °C, the  $A_{c3}$  temperature 895 °C, and the  $M_s$  is 355 °C. These temperatures have higher values than the transformation temperatures calculated in the previous experiments (**Figures 8.1.3 a, b**) due to the higher heating rates and the different content of the  $\gamma$ -phase stabilizing alloying elements (Mn).

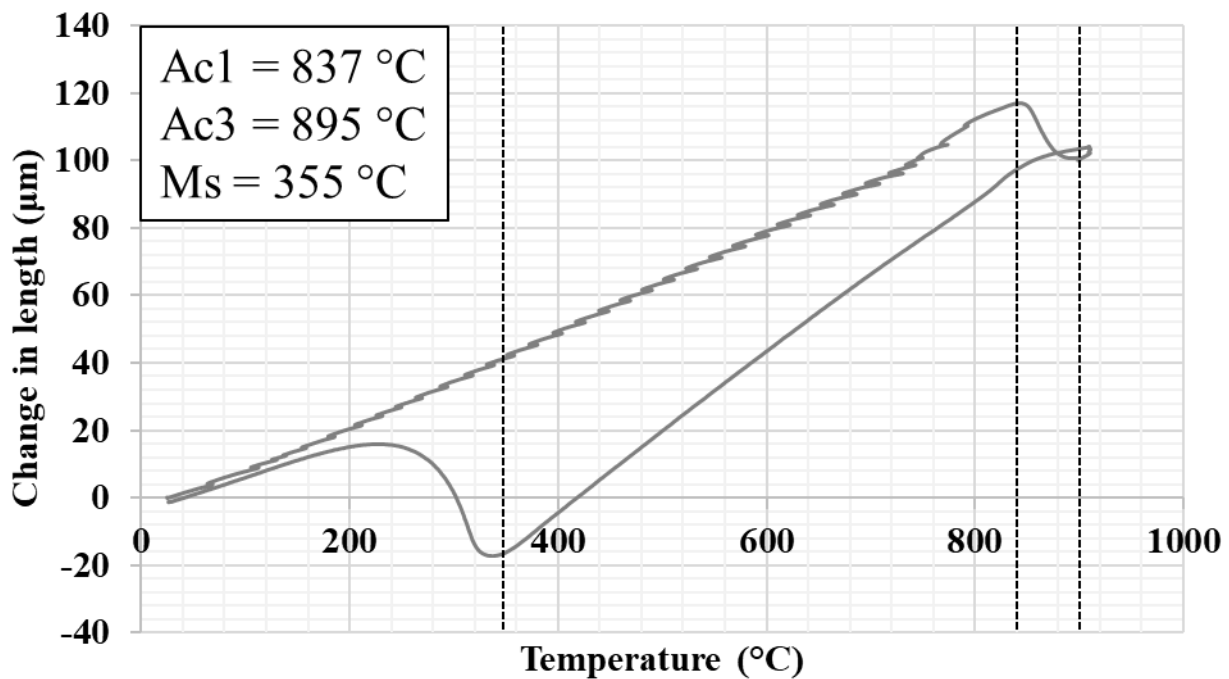
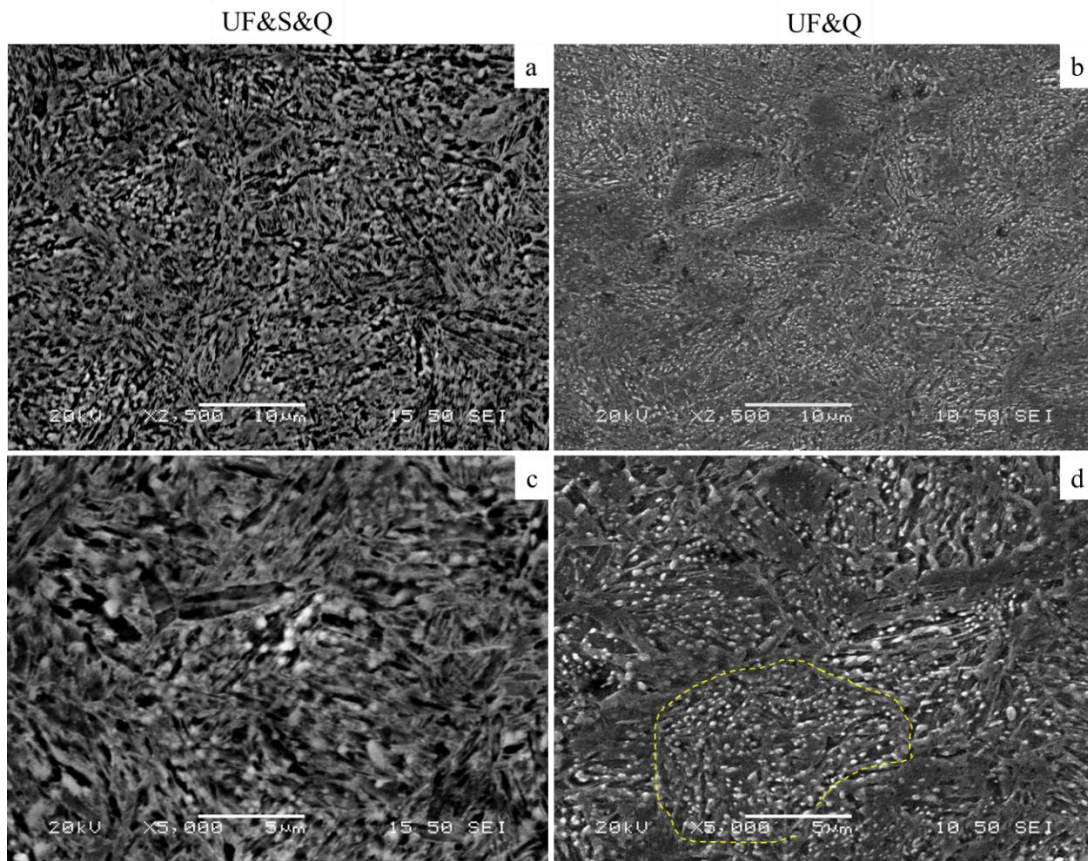
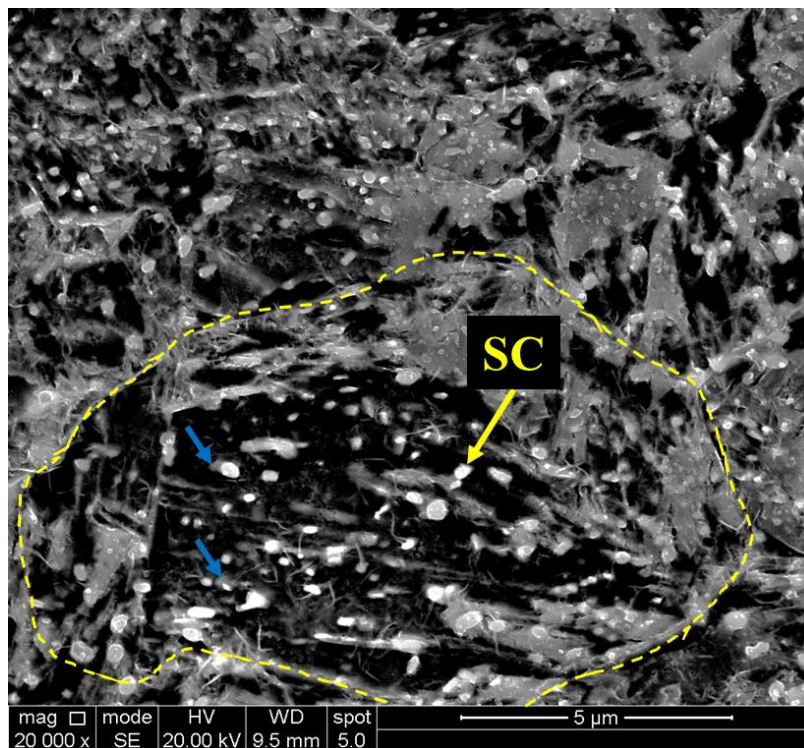


Figure 8.1.11: Temperature-dilatation diagram of the UF&Q sample with the calculated transformation temperatures.

From the SEM (Figures 8.1.12a, b), it can be observed that the spheroidized cementite from the initial microstructure has not been dissolved. Thus, both microstructures (Figures 8.1.12c, d) appear to consist of martensite and cementite in spherical form. According to [81, 89], partial dissolution of cementite takes place when high heating rates are applied. Therefore, the size of the spheroidized cementite is expected lower than that of the initial microstructure. It is also observed that the fraction of cementite in the UF&Q sample is higher as the lack of soaking time is preventing the dissolution of cementite. With a closer observation in the SEM, in Figure 8.1.13 for the UF&Q sample, a PAG boundary is shown with the yellow dashed line. Two types of martensite are observed in this grain. The first one ( $M_1$ ) is found near the PAG boundary as the nucleation of the martensite laths begins preferentially on such interfaces [42]. The other type of martensite ( $M_2$ ) is found in the grain's inner areas and between the SCs. This is attributed to the heterogeneous nucleation of austenite on the  $\alpha/\theta$  interfaces of the SCs. It is possible, though, that due to the high carbon content that is found around the partially dissolved carbides [81], that some of this heterogeneously nucleated austenite is retained and not transformed into martensite. The blue arrows indicate such possible RA, but TEM is required to confirm this. Finally, ferrite is observed in the inner areas of this grain, surrounding the SCs. The undissolved spheroidized cementite (SC) will be intergranular as the austenite forms during heating. In Figure 8.1.13, the PAG boundary is indicated with the yellow dashed line. The intergranular SCs can be observed. As martensite forms upon quenching, the grain will consist of martensite, spheroidized cementite and austenite. As the diffusion of carbon takes place in short range, due to the lack of time, increased carbon content is expected on the interfaces between cementite and austenite, which might lead to the retainment of the latter. This is indicated in the figure with blue arrows.



**Figure 8.1.12:** SE SEM images of the (a, c) UF&S&Q and (b, d) UF&Q samples. In both cases, the dissolution of spheroidized cementite is not completed.



**Figure 8.1.13:** SE SEM image of the UF&Q sample shows that dissolution of cementite is not complete. The blue arrows indicate possible RA attached to the spheroidized cementite (SC). The yellow dashed line indicates the PAG boundary.

EBSD analysis was performed in the two samples as well. From the IQ maps (**Figures 8.1.14a, b**), not many differences are observed between the microstructures of the two samples. The main difference is the observed size of the martensite laths. In the UF&S&Q sample, the laths appear to be both thicker and longer than in the UF&Q sample. Both samples appear to consist of martensite laths, as the SCs are too small for the EBSD scan to recognize.

Nevertheless, in the GAIQ maps (**Figures 8.1.14c, d**), the rotation angles are included, and indications for the existence of bainite [28] are found as well. Again, high rotation angles between  $56^\circ$  and  $65^\circ$  that correspond to high angle grain boundaries between martensite laths are shown in blue. The rotation angles for bainite are between  $48^\circ$  and  $55^\circ$  and are shown in red, while the rotation angles between two ferrite grains are between  $17^\circ$  and  $47^\circ$  and are shown in black color. The charts presented in the same figure (**Figures 8.1.14e, f**) show that the fraction of rotation angles that correspond to bainite is similar in both samples. In these charts, the misorientation angles are correlated to a random distribution of misorientation (MacKenzie type), and the rectangles indicate the delineated areas of PAGs (black), bainite (red), and martensite (blue) on the GAIQ map. It has to be noted that this method is not decisive on the existence of bainite, and TEM must be employed. The TEM analysis for the existence of bainite is described in the next chapter.



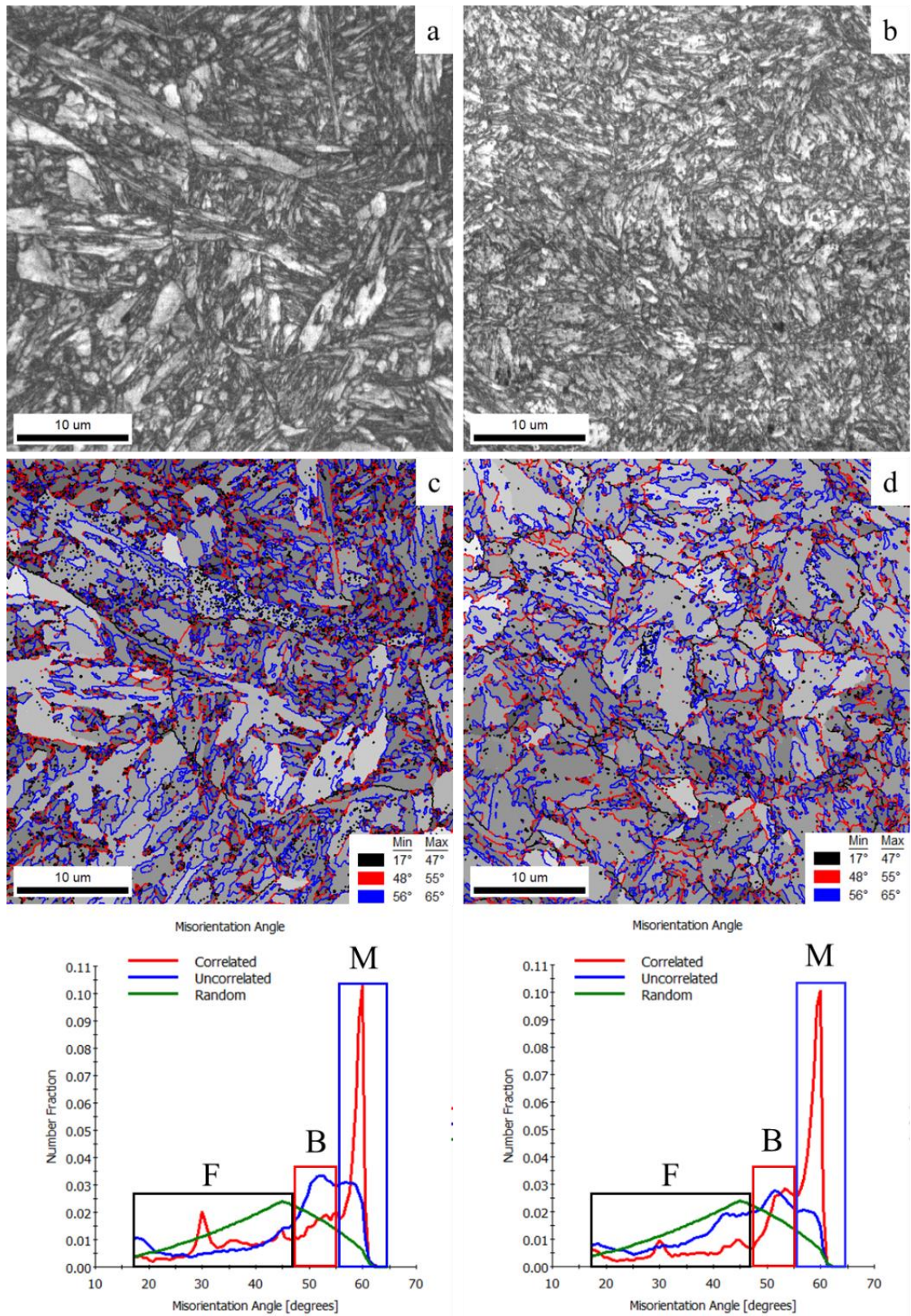


**Figure 8.1.14:** (a, b) EBSD IQ maps of the studied area. (c, d) GAIQ maps of the same area with rotation angles included. Black lines correspond to 17° - 47°, red lines to 48° - 55°, and blue lines to 56° - 65°. Step size: 70 nm. (e, f) Charts that show the number fraction of the different rotation angles. An uncorrelated and a random (McKenzie) distribution are added for reference.

The GAM (**Figures 8.1.15a, b**) and KAM (**Figures 8.1.15c, d**) maps were plotted. As the samples are mainly martensitic, it is expected that they have high dislocation densities. In the GAM maps, the average grain deformation is indicated while the LAGBs are shown in white lines. Due to thermal treatment, no LAGBs are expected. With dark blue color, some areas with a high fraction of SCs are observed in both samples. In comparison to the KAM maps, the dislocation density can be determined to be quite high. This is expected due to the martensitic microstructure and from the presence of SCs.

From the IPF maps (**Figures 8.1.16a, b**), some martensite blocks can be observed in these samples as well, with the  $\langle 101 \rangle$  and  $\langle 111 \rangle$  orientations being the most dominant. In **Figures 8.1.16 c, d**, the phase maps are plotted. In these maps, ferrite is shown in red color, austenite in green, and for better correspondence, the K-S relationship for  $\alpha$ - $\gamma$ :  $\langle 112 \rangle 90^\circ$  is drawn in white. Very small fractions of retained austenite are found in both samples, specifically, 2.3 % for the UF&S&Q sample and 0.8 % for the UF&Q sample. As seen from the phase maps, the RA is mostly found in the areas where the SCs are denser and specifically the areas with dark blue color in the GAM maps (**Figures 8.1.15a, b**). As reported from [81], due to the partial dissolution of SCs, a gradient of the carbon concentration is created. Thus, regions with a high number of SCs are expected to contain a larger carbon content. This favors the retainment of austenite.



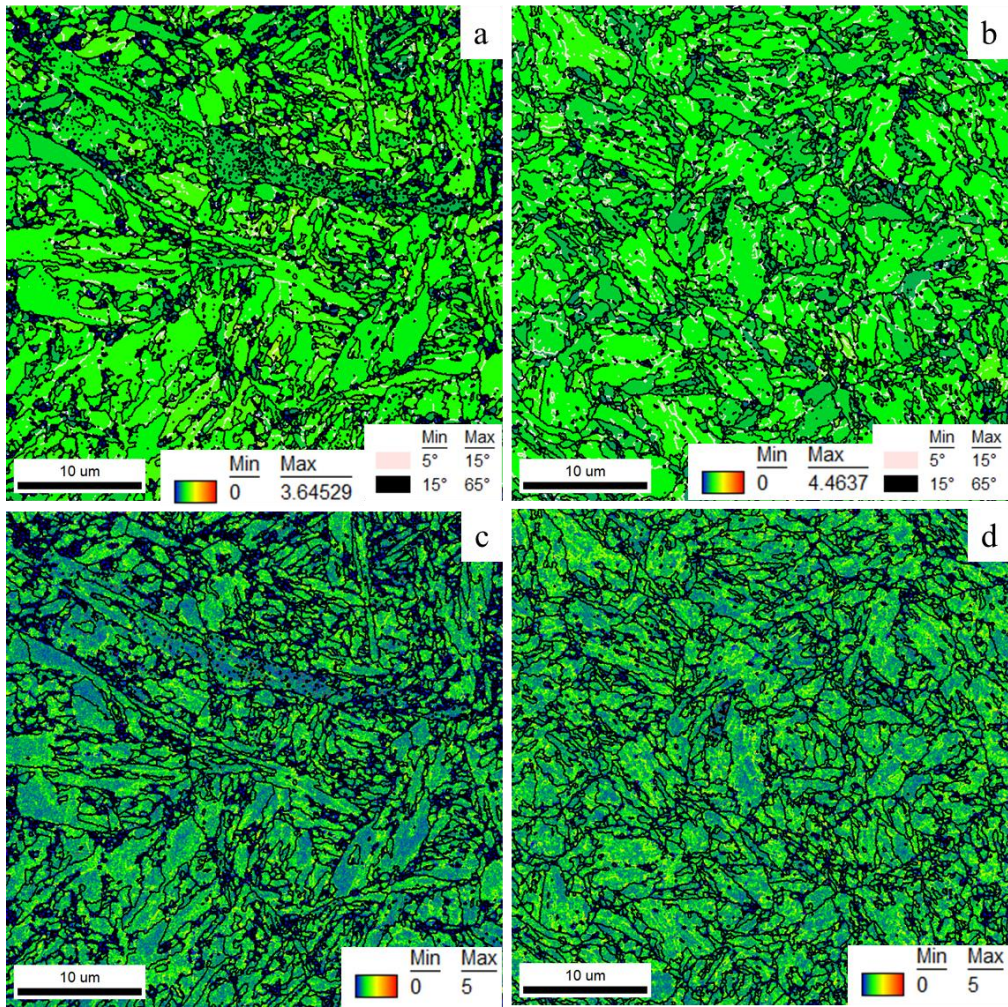


**Figure 8.1.15:** (a, b) GAM maps of both samples that indicate highly deformed grains in both samples, (c, d) 2nd neighbor KAM maps that show the dislocation density. Step size: 70 nm.



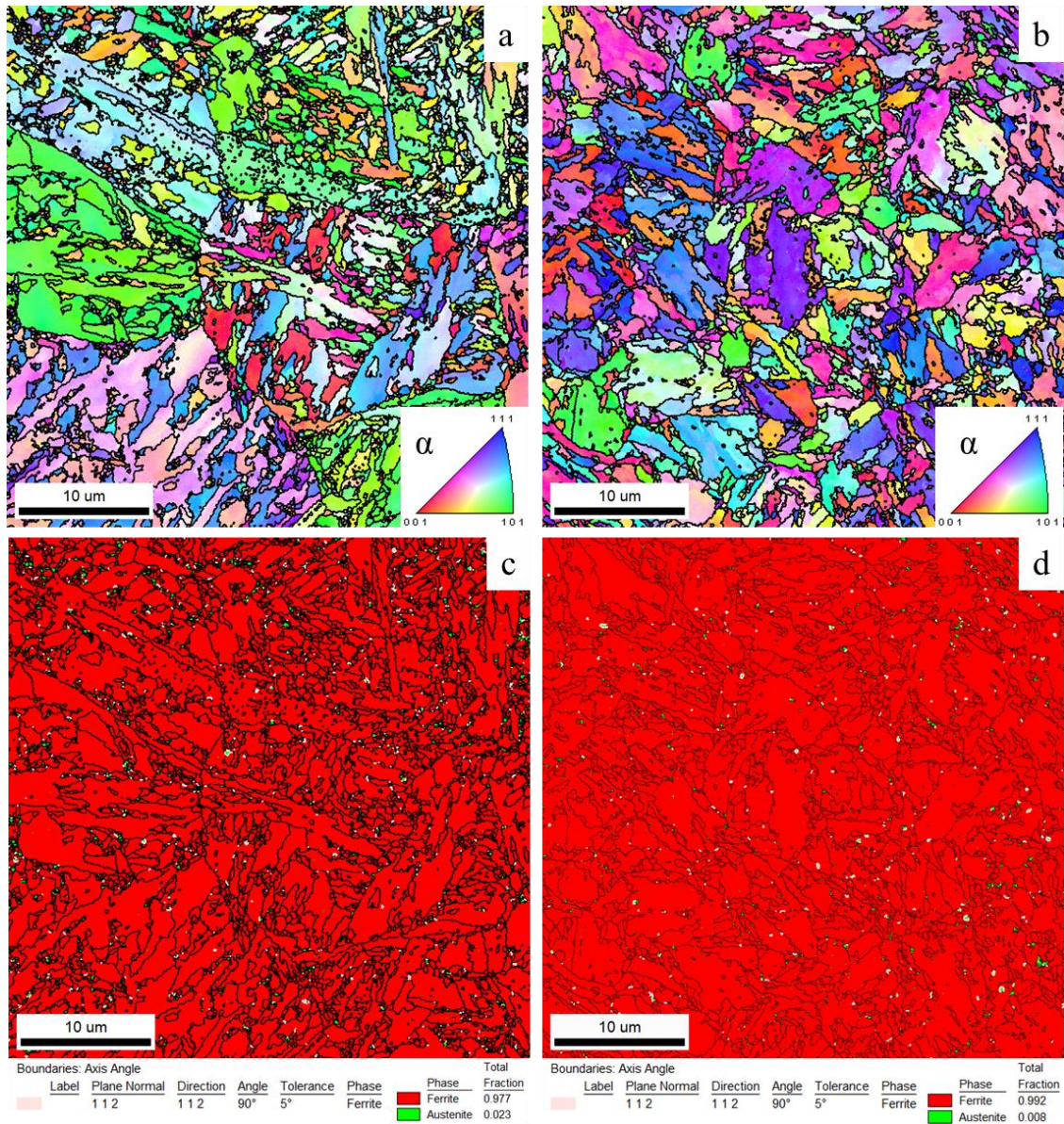


**Figure 8.1.16:** (a, b) IPF maps of the two samples that show the orientations of the martensitic laths. (c, d) Phase maps of the two samples that indicate the presence of retained austenite (green) and ferrite (red). With white color, the K-S relationships have been drawn. Step size: 70 nm.

Finally, from the EBSD analysis, the grain size was studied in area. As observed from **Figures 8.1.17a, b**, both samples have similar martensite lath size in area. For the UF&S&Q sample, the average lath size is calculated at almost  $8 \mu\text{m}^2$ , while for the UF&Q sample, it was calculated at  $6.4 \mu\text{m}^2$ . The larger average grain size is expected in the former sample due to the higher heating time, which favors the parent austenite grains' growth. Concerning the PAGs (**Figures 8.1.17c, d**), the difference observed in the grain size is quite larger. Specifically, the PAG average size for the UF&S&Q sample is  $252.5 \mu\text{m}^2$  while for the UF&Q sample,  $53.5 \mu\text{m}^2$ . This difference is attributed to two main factors. First, the lack of heating time in the UF&Q sample prevents the growth of the parent austenite grains. The second factor has to do with the SCs. They might have a pinning effect on the movement of the PAG boundaries and thus impede its growth.



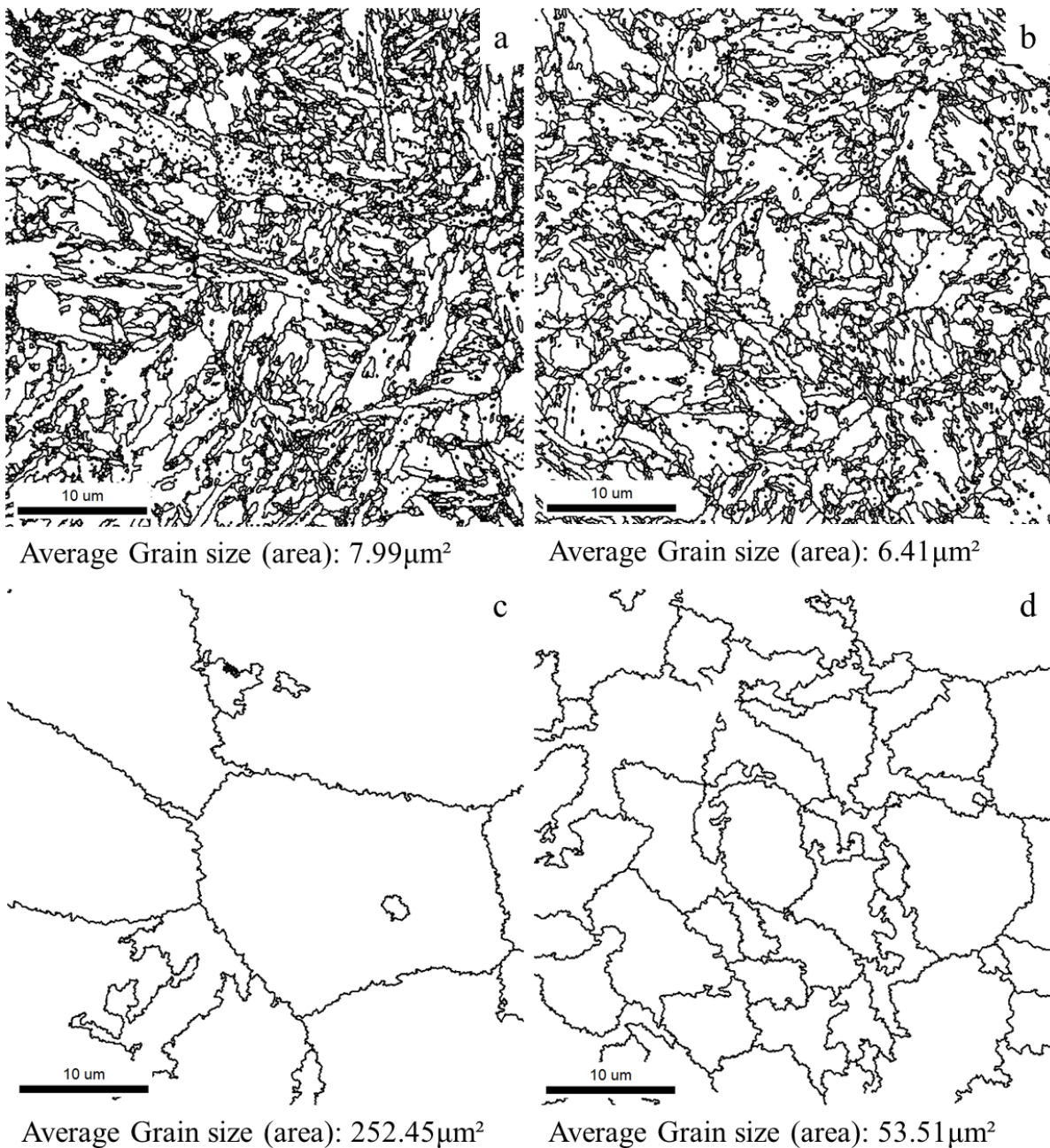


**Figure 8.1.17:** (a, b) Grain Boundaries maps for the two studied samples and the calculated average grain size. (c, d) Grain Boundaries maps for the reconstructed PAGs [XX] of both samples with the calculated average grain size. Step size: 70 nm.

In summary, both samples consisted of spheroidized cementite and martensite, while indications for bainite and retained austenite were found. Ferrite is also found in the UF&Q sample, as the austenitization process may not be complete. The presence of SCs in both microstructures has a great effect on the microstructure. As reported elsewhere [81], gradients of carbon are created around these SCs that favor the retainment of austenite in close proximity. Also, they impede the growth of the parent austenite grains by a pinning effect leading to a refined microstructure. Between the two samples, the amount of SCs is expected to be lower in the UF&S&Q sample as the longer heating time leads to further dissolution.

### 8.1.5. Comparison of an ultra-fast heating cycle with a conventional heating cycle

#### 8.1.5.1. Materials and treatments

The purpose of this experiment is to compare qualitatively and quantitatively, where possible, the microstructures of a hot-rolled chromium molybdenum medium carbon steel formed after conventional heating, isothermal soaking and quenching (CHT) with a UFHT steel with heating rate 300 °C/s and soaking for a maximum of 2 s at the austenitization peak temperature. The chemical composition of the grades is the same as the previous set of experiments and can be seen in **Table 8.1.2**.

The experiments were performed in a Bähr 805A quench dilatometer. The heat treatments for the conventional (CHT) and the ultrafast (UFHT) heat-treated samples are summarized in **Figure 8.1.18**. The  $T_{\text{peak}}$  is significantly increased in the ultrafast heat-treated sample to avoid the intercritical region because the increased heating rate shifts the  $A_{c3}$  temperature to higher values [44,45]. Both samples' initial microstructure is also similar to the previous experiments and consists of ferrite and spheroidized cementite, as shown in **Figure 8.1.9**.

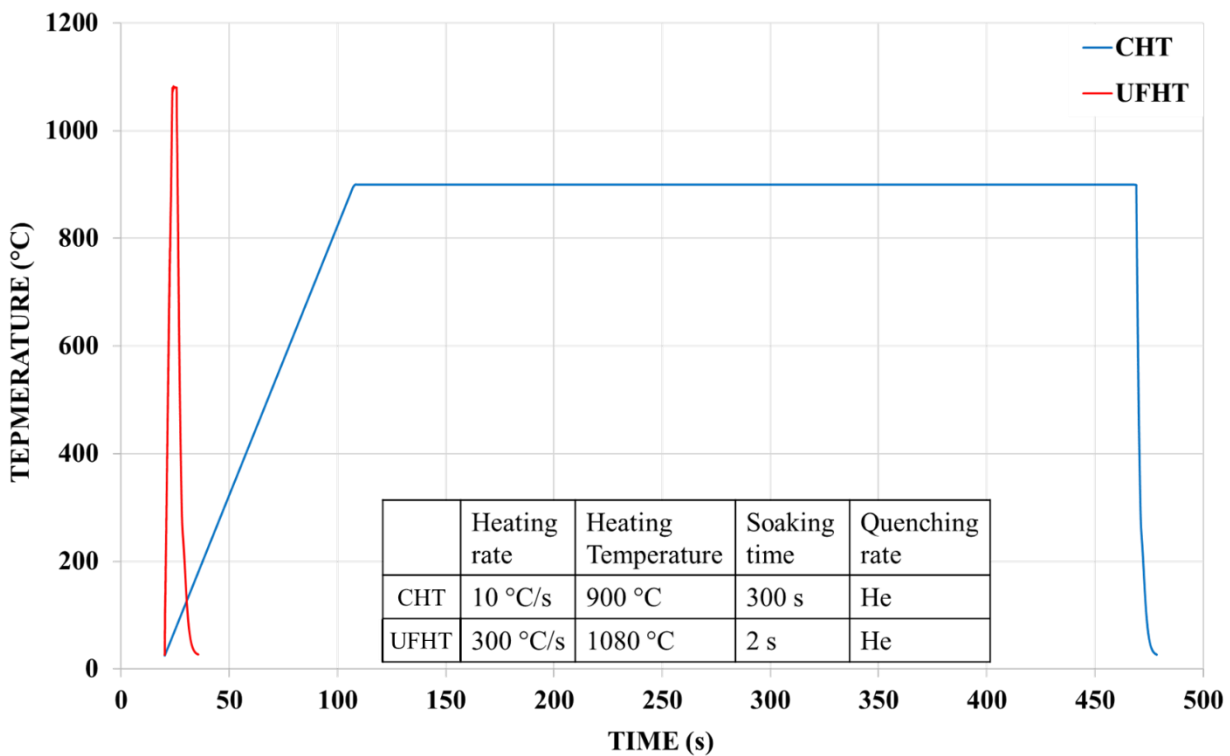


**Figure 8.1.18:** Time-temperature diagram with the heat treatments that were applied to the sample for this experiment.

The transformation temperatures of the UFHT sample calculated from the dilatometer are the same as those of the previous experiments, as the chemical composition and heating rates are the same. Specifically, those were found to be the following:  $A_{c1}$  temperature = 837 °C,  $A_{c3}$  = 895 °C and  $M_s$  = 355 °C. For the CHT sample, the transformation temperatures are closer to the ones determined from the Fe-C diagram. According to the

diagram that was plotted in **Figure 8.1.19** [85], the  $A_{c1}$  and  $A_{c3}$  transformation temperatures were calculated to be 710 °C and 770 °C, respectively, in equilibrium conditions.

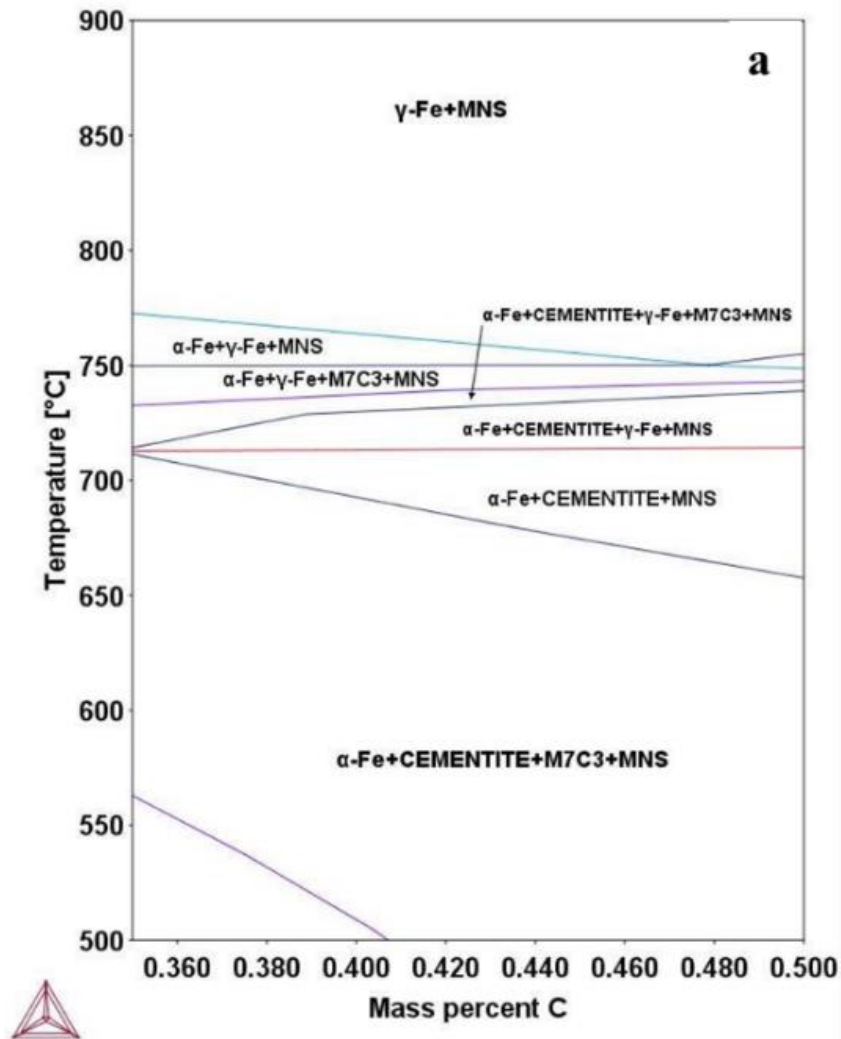


**Figure 8.1.19:** Isoleth of the phase diagram of CrMo steel calculated using Thermocalc®. [85]

### 8.1.5.2. Results

The microstructure of the conventional sample is shown in **Figure 8.1.20a, c**. The volume fraction of martensite appears to be 100%, while there is no evidence for the presence of cementite or undissolved carbides. The size of martensite laths is very similar, while it is larger than the average lath size of the UFHT sample, as shown in **Figure 8.1.20b, d**. According to this figure, the microstructure of the UFHT sample demonstrates a mixed microstructure with coarse and fine martensite laths and SCs.



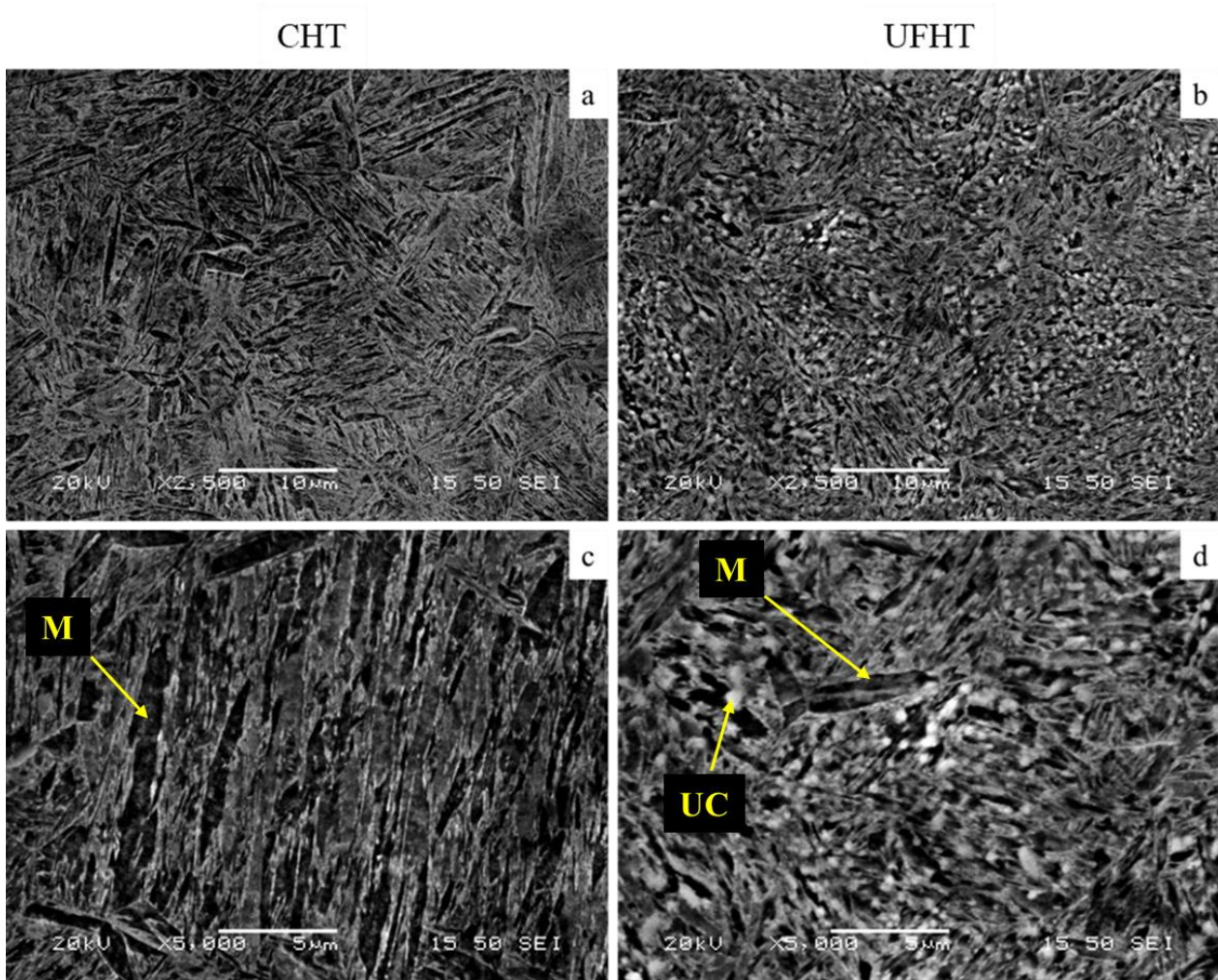


**Figure 8.1.20:** SEM images of the CHT (a) and the UFHT sample (b). The CH consists of a martensitic (M) matrix, while the UFH sample consists of a martensitic (M) matrix and undissolved cementite (UC).

From the EBSD analysis of the grain size (diameter), the coarser plate in the CHT sample (**Figure 8.1.21d**) was measured at an average of 3.77  $\mu\text{m}$ . In contrast, finer plates were measured at an average of 1.93  $\mu\text{m}$  in UFHT (**Figure 8.1.21e**), indicating that the martensitic laths are significantly refined compared to the CHT sample. Using the ARPGE software [46], the prior austenite grains were reconstructed, and the normal direction inverse pole figure (ND IPF) maps are shown in **Figures 8.1.21a, b**. For the UFHT (**Figure 8.1.21b**), these PAGs are significantly smaller in size than in the CHT sample, while the deviation between the PAGs in the UFH is quite large. In particular, the average calculated grain size for the PAGs is 11.12  $\mu\text{m}$  for the CHT sample and 7  $\mu\text{m}$  for the UFHT sample. As seen in **Figure 8.1.21c**, for the conventional heat-treatment, almost 40 % of the PAGs have a diameter of 20  $\mu\text{m}$ . After quenching, the martensitic laths in the final microstructure vary in size between 1.6 and 3.6  $\mu\text{m}$  (**Figure 8.1.21d**). Concerning the UFHT sample, the PAG size has greater variation. Specifically, most of the PAGs have a diameter between 8 and 14  $\mu\text{m}$  (**Figure 8.1.21c**). The reason for these smaller austenite grains, except for the shorter heating time, is that the undissolved cementite spheres act as nucleation sites and austenite nucleates at the  $\alpha/\theta$  interfaces and at  $\alpha/\alpha$  interfaces [56]. This means that there is a higher amount of austenite nuclei whose growth is impeded by the lack of heating time.

Moreover, undissolved carbides have a pinning effect, thus, further impeding the growth of austenite grains. After quenching, the microstructural constituents mostly have sizes between 0.2 and 1.8  $\mu\text{m}$  resulting in a very fine microstructure. The undissolved carbides (UC) can be seen in **Figures 8.1.22a, b**, which are bright-field TEM images of the UFHT sample.

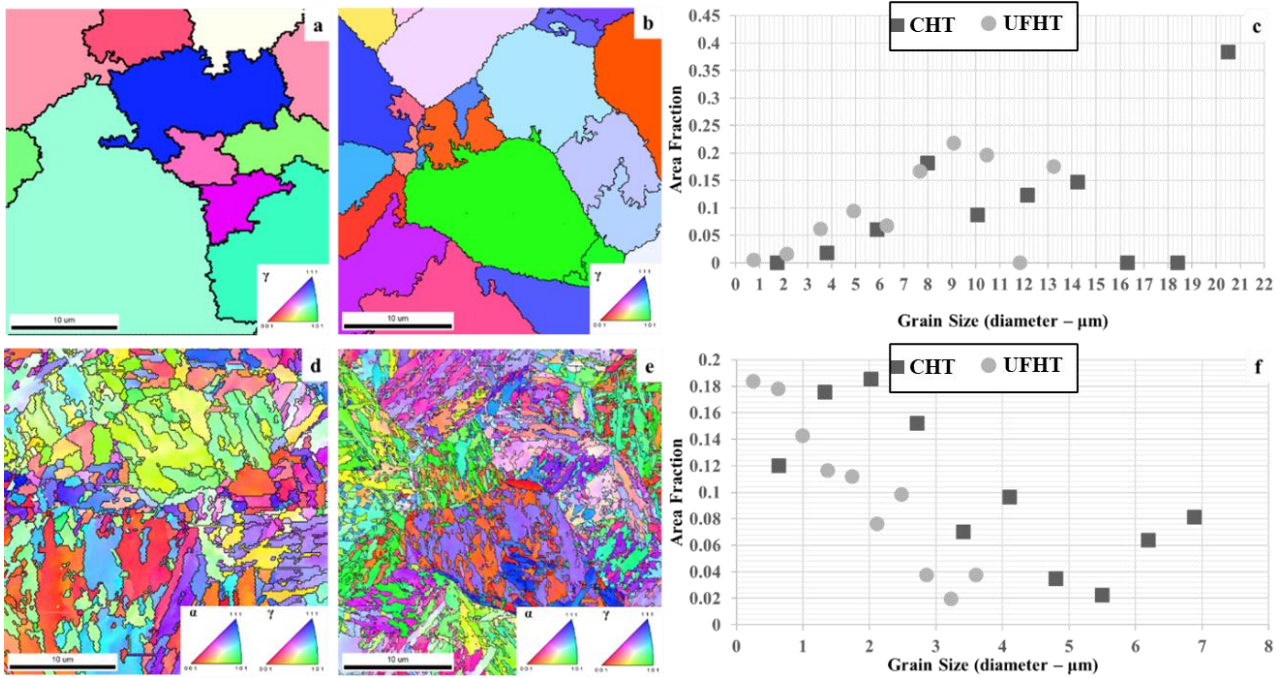


**Figure 8.1.21:** (a) IPF map of the reconstructed PAGs of the CHT sample with the use of the ARPGE [46] software, (b) IPF map of the reconstructed PAGs of the UFHT sample with the use of the ARPGE [46] software, (c) grain size chart for the PAGs of both samples indicating the refinement of austenite in UFHT, (d) IPF map of the final microstructure of the CHT sample, (e) IPF map of the final microstructure of the UFHT sample, (f) grain size chart for the final microstructure of both samples indicating the refinement of grains and laths in the UFHT. Step size: 70 nm.



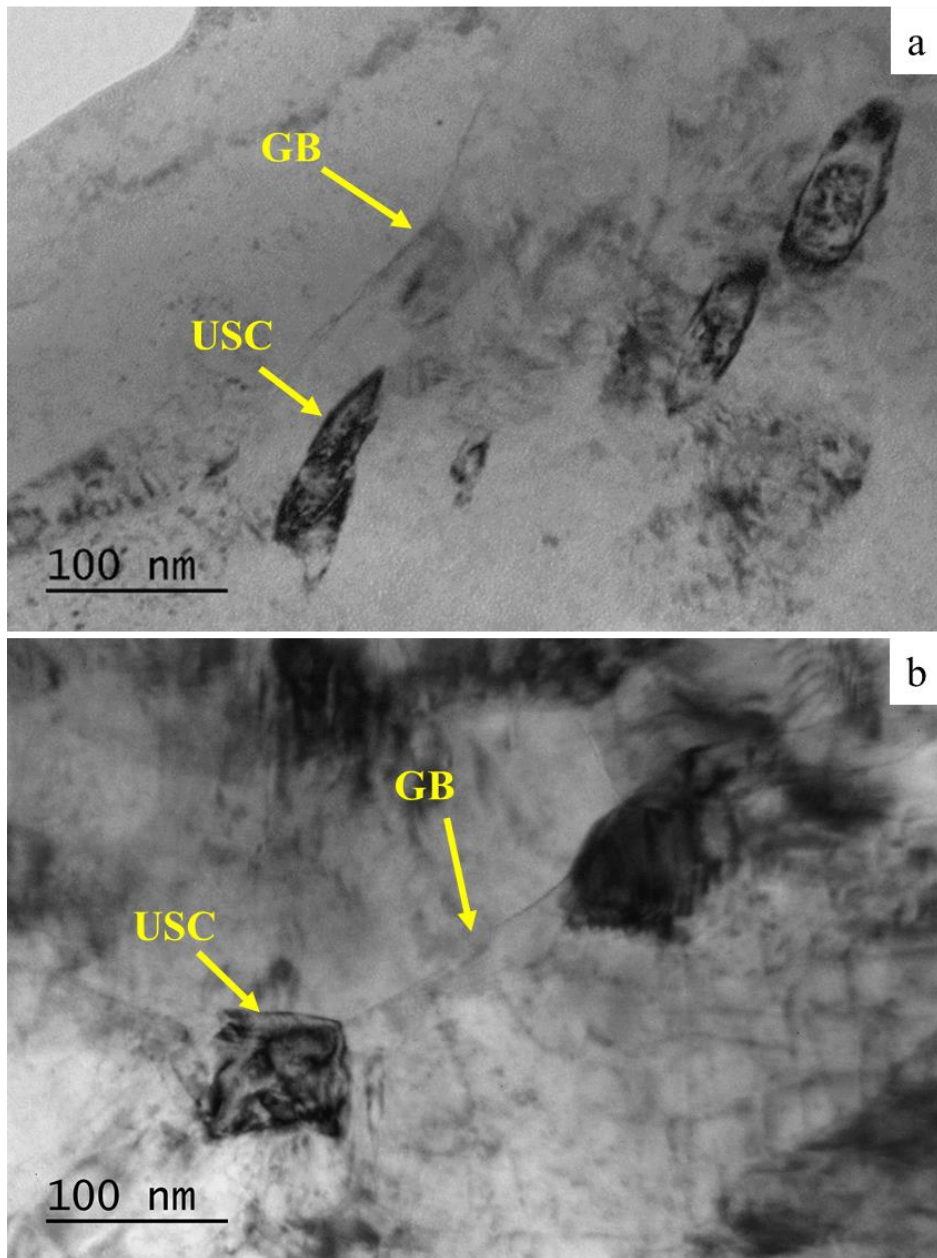


**Figure 8.1.22:** (a) undissolved spheroidized cementite (USC) is present in the final microstructure of the UFHT sample, (b) some of these USCs are also found on grain boundaries (GB), which is an indication of the pinning effect they impose on the movement of the boundaries.

Further investigation on the UFHT sample based on grain average Image Quality (GAIQ) confirmed the presence of ferrite. At the same time, there are strong indications for bainitic laths or martensite laths with low C content. This technique depends on the distortion of the lattice of each constituent and the diffraction pattern it produces. Depending on the diffraction pattern's quality, the IQ will differentiate for each constituent during the analysis of the EBSD data. This technique has been used before to distinguish ferrite from martensite and bainite [97, 138]. In this case, the selected cut off ranges have to be defined very carefully as the dislocation density, and corresponding lattice distortions in bainite and martensite are very close. Therefore, green areas denote grains with low grain average image quality with possibly high dislocation density regions that most probably correspond to martensitic grains, blue areas denote the grains with the highest GAIQ and possibly

with the lowest dislocation density and correspond to ferritic areas, whereas the red areas can be bainitic laths or martensitic laths with low C wt.% (**Figure 8.1.23a**). According to Pinard et al. [139], higher lattice distortion in martensite leads to a lower quality of its diffraction patterns. According to the GAIQ, the percentage of martensite (green) is 54.2 %, that of ferrite is 1.3 %, and the percentage of low carbon martensite or bainite is 40.3%. The presence of ferrite in the microstructure is also confirmed from the TEM, as shown in **Figure 8.1.24**. The reason ferrite is retained in the microstructure lies on the fact that increasing heating rates shift the transformation temperatures to higher values [122]. Thus, the austenitization process is not complete in the UFHT sample.

A grayscale GAIQ map (**Figure 8.1.23b**) was used to make a closer approximation of the bainite fraction, including the misorientation angles. According to [39], misorientation angles between  $17^{\circ}$ - $47^{\circ}$  (indicated in black) correspond to PAGBs, angles between  $48^{\circ}$ - $55^{\circ}$  (red) correspond to bainite, while those between  $57^{\circ}$ - $65^{\circ}$  (blue) correspond to martensite. From this map and the chart provided, it appears that only a small fraction of misorientation angles corresponds to bainite. This chart depicts the misorientation angle (red line) correlated to a random distribution of misorientation (MacKenzie type), while the rectangles indicate the delineated areas of PAGs, bainite, and martensite on the GAIQ map. When combining these two maps, it can be said that only a small part of the red-colored laths corresponds to bainite while the rest corresponds to low-carbon martensite. Bainitic morphologies are observed in the SEM (**Figures 7.25 c, d**) and are shown inside the yellow dashed circles. The presence of bainite in the microstructure of ultra-fast heat-treated steels is also supported in the work of Cerda et al. [126] on 0.2 % and 0.44 % carbon steels where they observed bainitic morphologies in OM and SEM. Its presence is further analyzed in the next chapter.

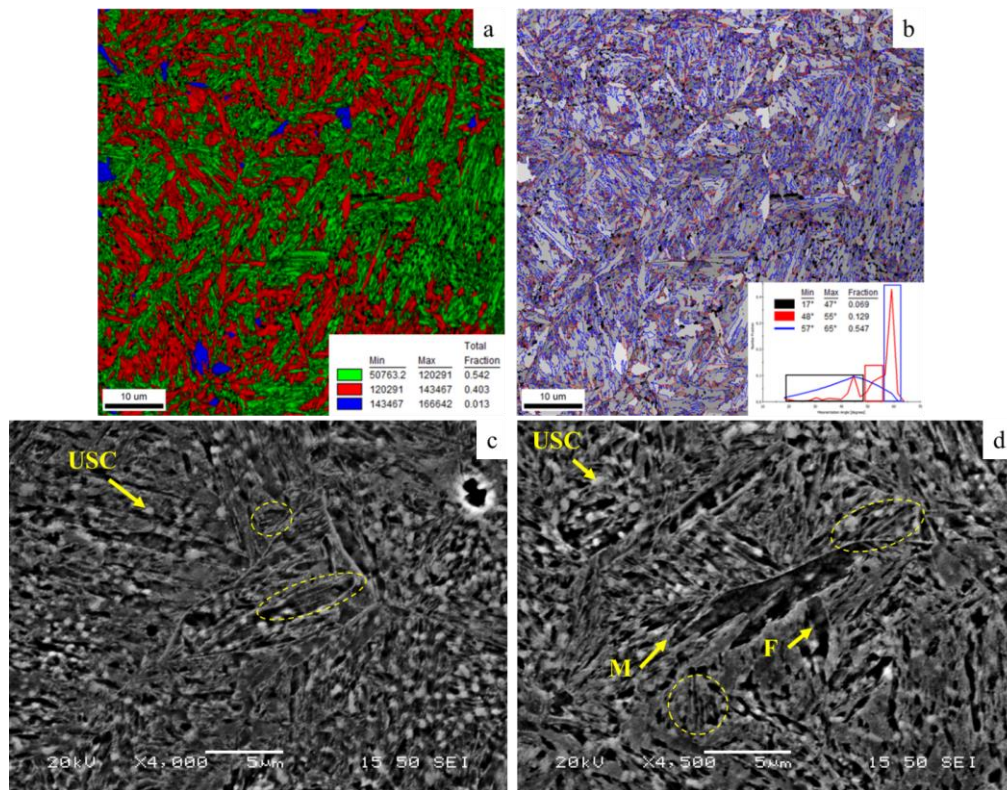


**Figure 8.1.23:** (a) colored GAIQ map for the UFHT sample. Martensite is indicated in green, ferrite in blue while low-carbon martensite and bainite in red, (b) gray-scale GAIQ map of the same area with misorientation angles indicating the boundaries between ferrite (black), bainite (red) and martensite (blue). Step size: 70 nm. (c) the presence of bainite has been observed in TEM and (d) in SEM. The two SEM micrographs indicate the presence of bainitic areas in the microstructure.

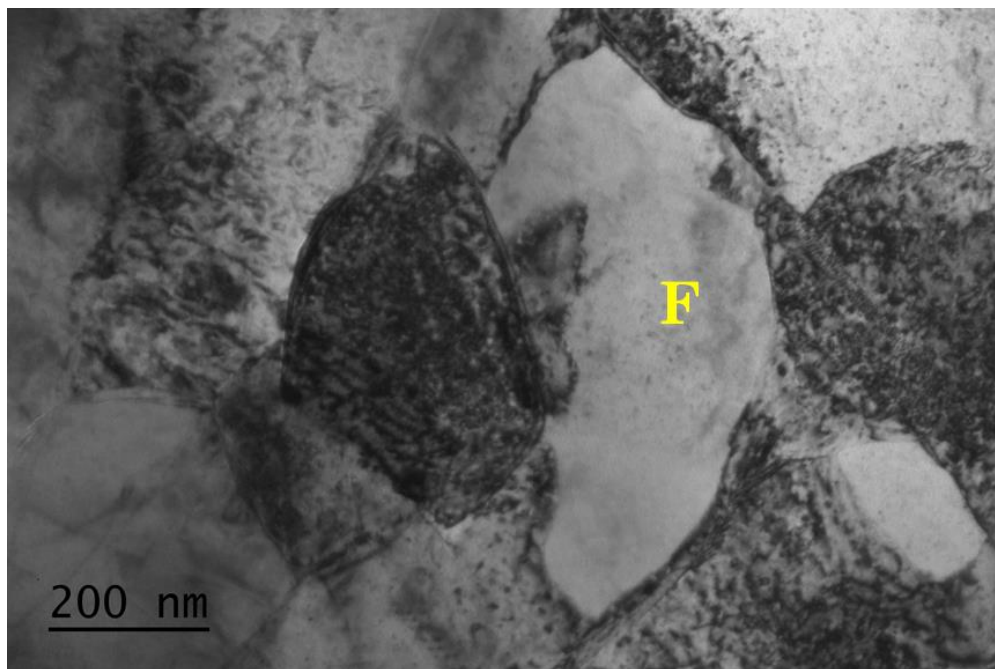


**Figure 8.1.24:** BF TEM image showing ferrite grains (F) found in the UFHT.



Austenite was also found in the microstructure of both samples. **Figures 8.1.25a,b** show the phase maps for the CHT and UFHT samples, respectively, which indicate the existence of retained austenite. In the CHT sample, only a very small amount (0.2 %) of austenite was detected, while in the UFH sample, the identified amount of austenite is 4.2 %. To obtain the austenite amount, other constituents with FCC structure (such as MnS) had to be excluded, and, thus, the K-S relationship for  $\alpha$ - $\gamma$ :  $\langle 112 \rangle 90^\circ$  was used.

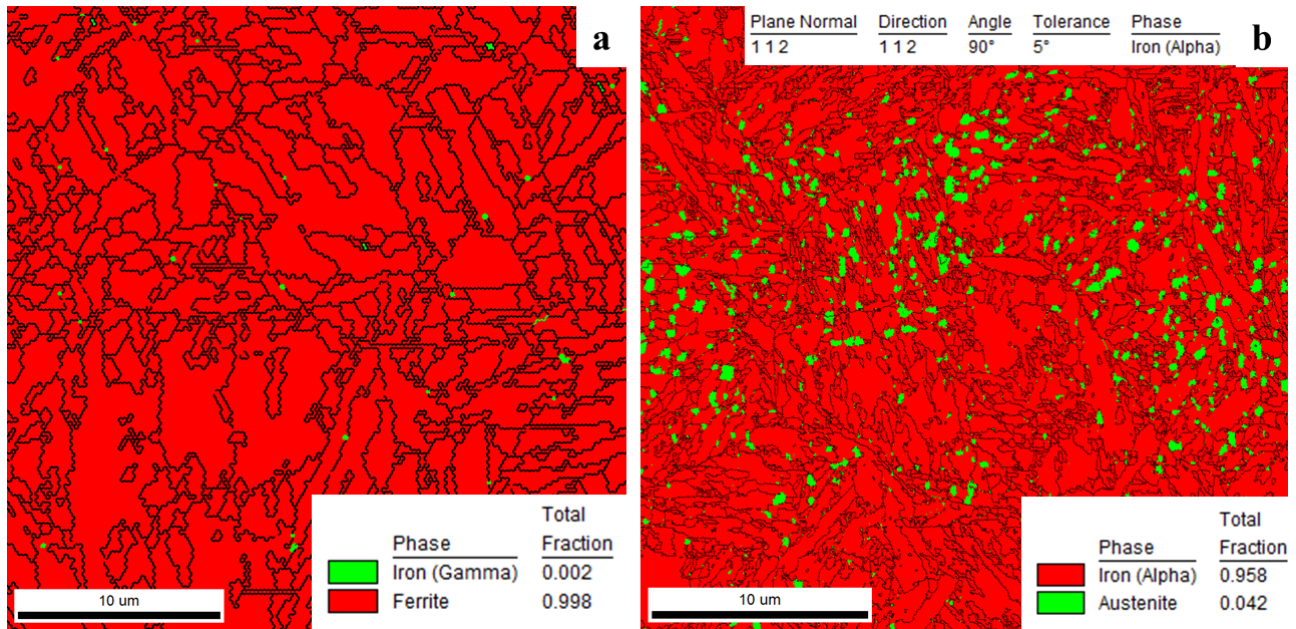


**Figure 8.1.25:** (a) Phase map of the CH sample, which consists of 0.2% austenite, (b) phase map of the UFH sample in which the amount of austenite is considerably higher (4.2%). Step size: 70 nm.

content. The same phenomenon is expected even more pronounced when the initial microstructure consists of ferrite and spheroidized cementite. As has been observed, the spheroidized cementite particles do not dissolve when high heating rates are applied. This means that the carbon content is concentrated in these particles. As has been observed, only partial dissolution of cementite takes place, which creates a gradient of carbon content in close proximity to the cementite spheres. The austenite formed on the  $\alpha/\theta$  interfaces or near them will be enriched in carbon, while the austenite formed at ferrite grains will have a lower carbon content. In both cases, though, austenite enriched in carbon and austenite poor in carbon is expected at peak temperature.

Nevertheless, austenite nucleation initiates preferentially on the  $\alpha/\theta$  interfaces due to better thermodynamical conditions (higher difference in carbon content). Then, austenite will also nucleate on  $\alpha/\alpha$  interfaces due to possible segregation of carbon and other elements on the boundaries, as found by [97]. In the CHT sample, the aforementioned mechanisms are not expected as there is enough soaking time for dissolution of cementite and homogenization of the chemical composition. The rest of the samples consisted mainly of martensite, while traces of bainite and retained austenite were found. The existence of retained austenite and bainite in the microstructure is thoroughly explained in the next chapter. The former is mainly attributed to the high carbon content found in very close proximity to the cementite particles. In contrast, the latter is attributed to the lower carbon content of the austenite formed in ferritic areas.

## 8.2. The formation of bainite and retainment of austenite in industry-scale samples

### 8.2.1. Introduction

Although using high heating rates is a familiar technique for surface hardening processes, it has not been used yet as a bulk heat-treatment process. The greatest challenge in this method is the ability to control the heating rate and peak temperature in the volume of the sample. Efforts have been made to apply ultra-fast heating in flat samples using the Gleeble machine and small cylindrical samples using dilatometers. Those efforts have been quite successful, as a homogeneously heated zone has been created on these samples. In these zones, studies have shown that ultra-fast heating leads to the formation of refined complex microstructures that may consist of fine martensite, undissolved cementite, lower bainite, and traces of retained austenite (and ferrite in some cases), as is indicated. In this research, high heating rates are applied on a medium-carbon steel, and the evolution of the microstructure is studied. Simulation software is used to calculate the composition of the different phases at peak temperature and after quenching to predict the phase transformations that occur during this process. Finally, characterization techniques are used to study the constituents of the microstructure and confirm the results that were predicted from the simulation. For this research, a medium-carbon steel is used with ferrite and pearlite as initial microstructure formed as a hollow seamless tube. The whole tube is then heated rapidly, and once the peak temperature is reached; it is quenched with water. As predicted by the simulations and shown by the microscopy results, heterogeneity is achieved in the composition and size of the parent austenite grains. This heterogeneity is responsible for the formation of different constituents during quenching, such as ferrite, martensite, and bainite, and can explain the retainment of austenite that is found.

### 8.2.2. Materials and methods

The material used in this research is a medium-carbon, low-manganese steel, and the exact composition can be seen in **Table 8.2.1**.

**Table 8.2.1:** The chemical composition in wt. % of the steel used for rapid treatments.

C	Mn	Si	P	S	Cr	Mo	Fe
0.43	1.0	0.35	0.035	0.04	1.10	0.25	Balance

The initial microstructure is shown in **Figure 8.2.1**; it consists of ferrite and pearlite in a 3/1 ratio. The ferrite grains are not elongated and free of deformation as no cold-rolling has taken place.

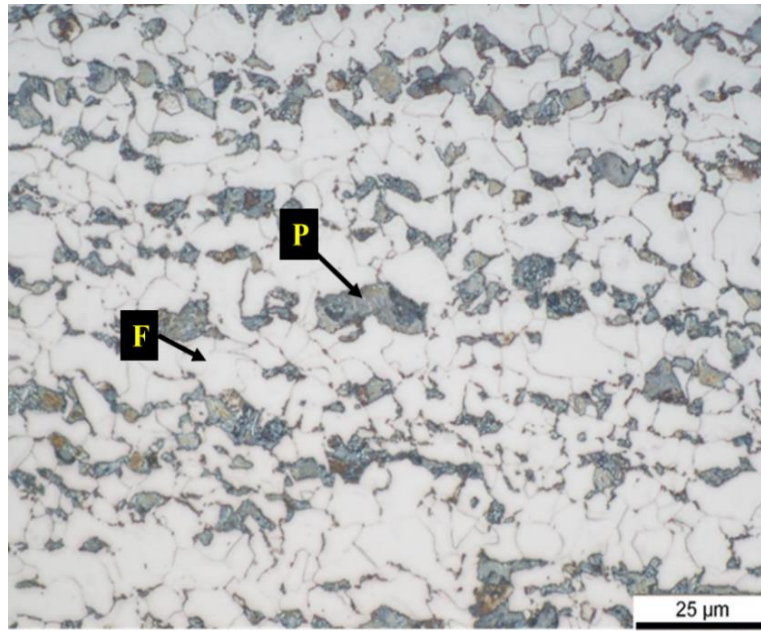


Figure 8.2.1: The initial microstructure of the steel consisted of ferrite and pearlite in a 3/1 ratio.

The TCFE8 database was used in Thermo-calc to plot the Fe-C diagram (Figure 8.2.2) for the composition of the material given in Table 8.2.1 in equilibrium conditions. From this diagram, the  $A_{c1}$  and  $A_{c3}$  temperatures are measured at 710 ° and 760 °C, respectively.

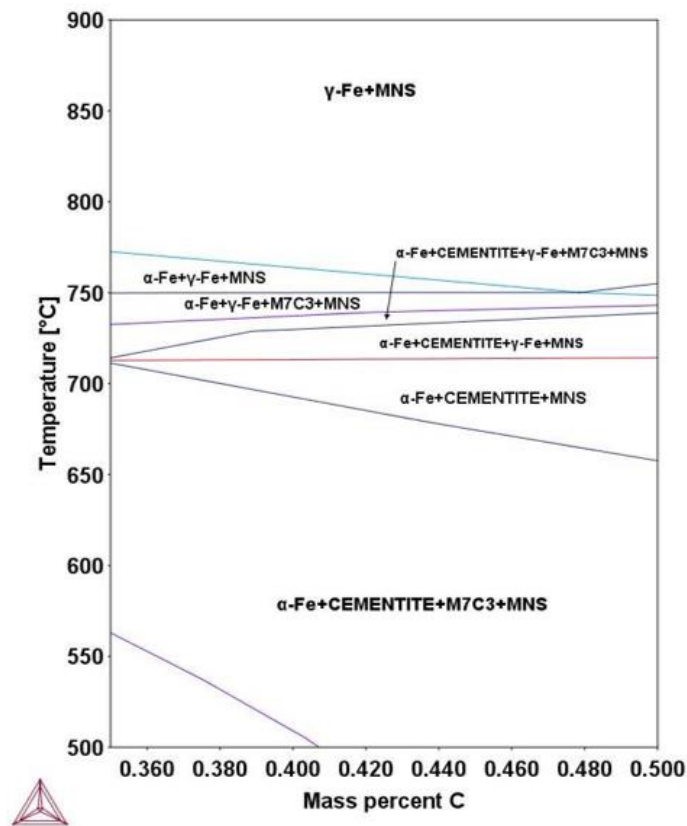


Figure 8.2.2: The Fe-C diagram as was calculated from Thermo-calc for the given composition and in equilibrium [85].



According to the phase diagram, the following heat treatment was selected, shown in **Table 8.2.2**. The high heating rates were applied through a coil via induction heating. A pre-heating stage was included that did not affect the microstructure, but its purpose was to aid the heating machine to achieve the heating rate of 100 °C/s. Keeping in mind that the transformation temperatures increase with high heating rates [116], the peak temperature was chosen high in the  $\gamma$  region. The soaking time at peak temperature was minimal, and the sample was quenched in water. For comparison reasons, another sample was studied in the OM, which underwent a conventional heating treatment, and was used as a reference. The parameters of the treatment for this reference sample are also shown in **Table 8.2.2**.

**Table 8.2.2:** The parameters used for the ultra-fast thermal treatment.

Samples	Annealing stage			Cooling stage
	Annealing rate (°C/s)	Peak Temperature (°C)	Soaking Time (s)	Quenching medium (°C/s)
UFH sample	100	930	-	Water
Reference sample	10	930	1800	Water

During ultra-fast heating, the homogenization of the composition in the microstructure is limited as there is not enough time for the dissolution of cementite and diffusion of carbon. In a previous work [97] using DICTRA in the same material, it was shown that two possible types of parent austenite exist in the microstructure at the peak Temperature. The parameters used for this simulation approach are in detail described in [123, 126]. The C-rich austenite is estimated to have a higher concentration of carbon (C), manganese (Mn), and chromium (Cr). It is expected to be in small proximity to the pearlitic colonies of the initial microstructure. The second parent austenite composition is depleted in carbon, and the reason is that it is expected in areas relatively further from the pearlitic areas. Due to the short heating time, the diffusion distance of carbon from the dissolving cementite is limited. Thus, ferrite grains located away from the pearlitic colonies will transform into austenite without profound enrichment in carbon. The two types of austenite composition are shown in **Table 8.2.3**.

**Table 8.2.3:** *The composition of the parent carbon-rich and carbon-depleted austenite, as calculated from DICTRA simulation [97].*

Parent Austenite	Cr (wt. %)	Mn (wt. %)	Mo (wt. %)	C (wt. %)
C-depleted	0.5	0.4	0.1	0.2
C-rich	0.6	0.8	0.1	0.7

For the characterization of the microstructure, different microscopy techniques have been used. In order to be able to observe the microstructure, special sample preparation is required. For the Light Optical Microscopy (LOM) and Secondary Electron Microscopy (SEM), the sample preparation consists of the following steps: grinding up to 2000 grid SiC paper and then polishing with 6  $\mu\text{m}$  and 1  $\mu\text{m}$  diamond paste until a mirror-like surface is achieved and followed by chemical etching with 2 % v/v  $\text{HNO}_3$  in ethanol (Nital 2%) for 8-10 s at room temperature to reveal the microstructure. A JEOL6380LV SEM was used; an accelerating current of 20 kV and a working distance of 10 mm in secondary electron imaging mode was selected.

The grinding and polishing steps are also used for the sample preparation for the EBSD analysis. Though an additional polishing step is added using a 0.1  $\mu\text{m}$  colloidal silica (OPU), no etching is applied. An accelerating current of 20kV is selected for the Quanta TM 450-SEM EBSD and a working distance of 8 mm. The resulting patterns were acquired on a hexagonal scan grid by a Hikari detector operated with EDAX TSL–OIM-Data Collection version 6 software. The EBSD scans were performed at a step size of 50 nm. The corresponding orientation data were post-processed with EDAX-TSL-OIM-Data Analysis version 7 software using the following grain definition: Misorientation with neighboring grains higher than  $5^\circ$ , a minimum number of points per grain was 2, and confidence index (CI) higher than 0.1. The raw EBSD data were post-processed (cleaned) to re-assign the dubiously indexed points using the grain confidence index standardization and neighbor CI correlation procedure.

Finally, the TEM samples were ground to 100  $\mu\text{m}$  thickness and then cut into disks with a diameter of 3 mm. They were then ground again to a thickness of 40  $\mu\text{m}$  and in the end ion milled with the PIPS. The Jeol 2100 HR TEM was running at 200kV and was mounted with an EDS detector.

### 8.2.3. *Results*

The heating cycle applied in the reference sample was that of a conventional treatment for the production of a martensitic steel. Thus, the microstructure is expected to be fully martensitic. This can be confirmed by the LOM metallography of **Figure 8.2.4a**. It can be observed that the microstructure consists of martensitic laths that may reach up to 50  $\mu\text{m}$  in length. Martensite laths may form martensite blocks with similar orientations

along the parent austenite grains. The boundaries of some PAGs are indicated with yellow dashed lines. Their increased size is expected from the extended heating time that allows austenite to grow.

From the LOM (**Figure 8.2.4b**) and SEM (**Figures 8.2.5 a, b**), it is observed that the microstructure is mainly martensitic, and the size of the parent austenite grains (PAGs) varies between 10-30  $\mu\text{m}$ . According to the PAG size, the length of the martensite blocks also varies between 5-20  $\mu\text{m}$ . It is also observed that variation exists in the martensite lath width even inside of the same block. The martensite laths are closer observed via TEM in **Figures 8.2.6a,b**. The formation of martensite is expected during quenching and due to the high carbon content in the steel. It is shown that some martensite laths are separated from another phase that appears darker on the TEM. Two possible explanations can be given to describe this. The first one is that the angle of the lath boundaries appears darker from the transmission of the electron beam. The other possible explanation is that once the laths are formed with shear transformation during quenching, carbon is accumulated on the boundaries, leading to the retainment of austenite. Finally, from these figures, it is observed that martensite is formed in blocks with their size depending on the parent austenite grain size. The advance of the block will end once it meets the boundary of the parent austenite or once it meets another martensite block. The laths inside the same block are expected to have the same orientation, and this can be seen in the IPF map of **Figure 8.2.7a**. Finally, martensite is expected to be surrounded by HAGBs due to its shear transformation mechanism. To verify this, the rotation angles for the same EBSD scan are shown in **Figure 8.2.7b**, where blue color indicates boundary misorientation angles between  $56^\circ$  and  $65^\circ$ . According to Zajac [28], these angles

correspond to misorientations between martensite laths. As the formation of martensite is a shear transformation, the high angle grain boundaries are expected.

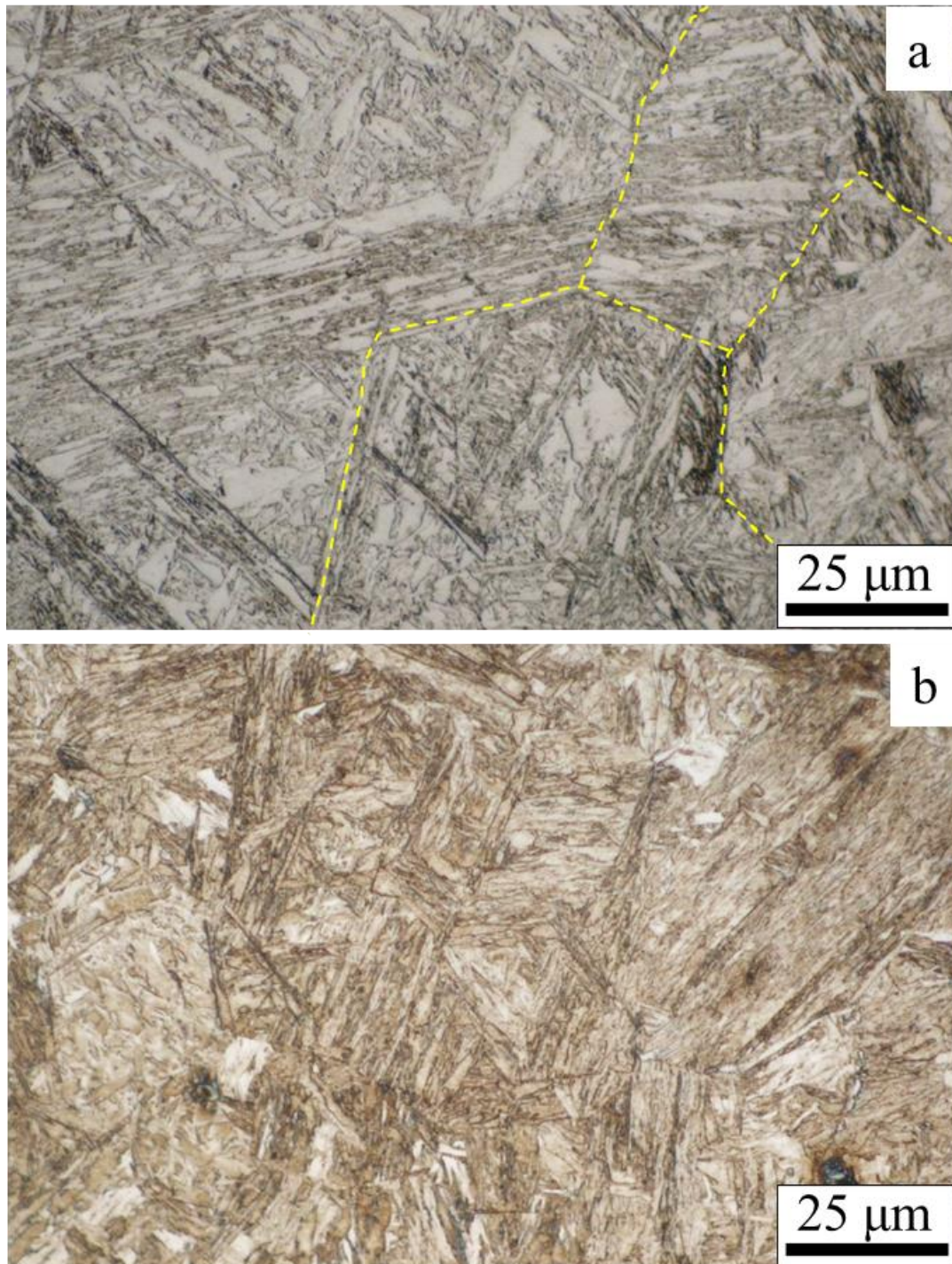


**Figure 8.2.4:** (a) OM metallography of the reference sample showing a fully martensitic microstructure. Some PAGBs are shown with yellow dashed lines. (b) OM metallography of the UFH sample, the microstructure of which appears more complicated.



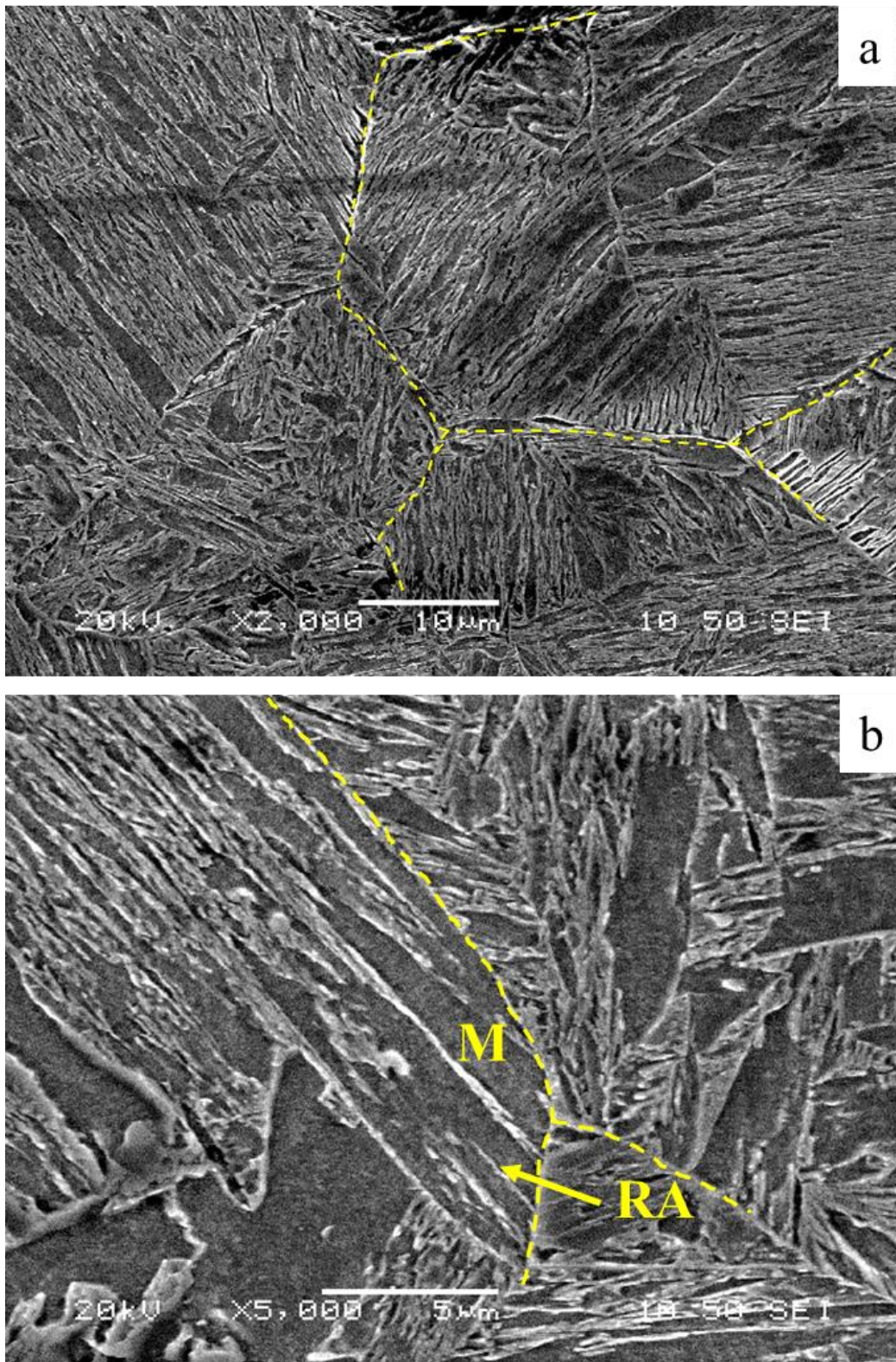


*Figure 8.2.5: SE SEM images showing the martensite laths at (a) 2000x and (b) 5000x magnification.*

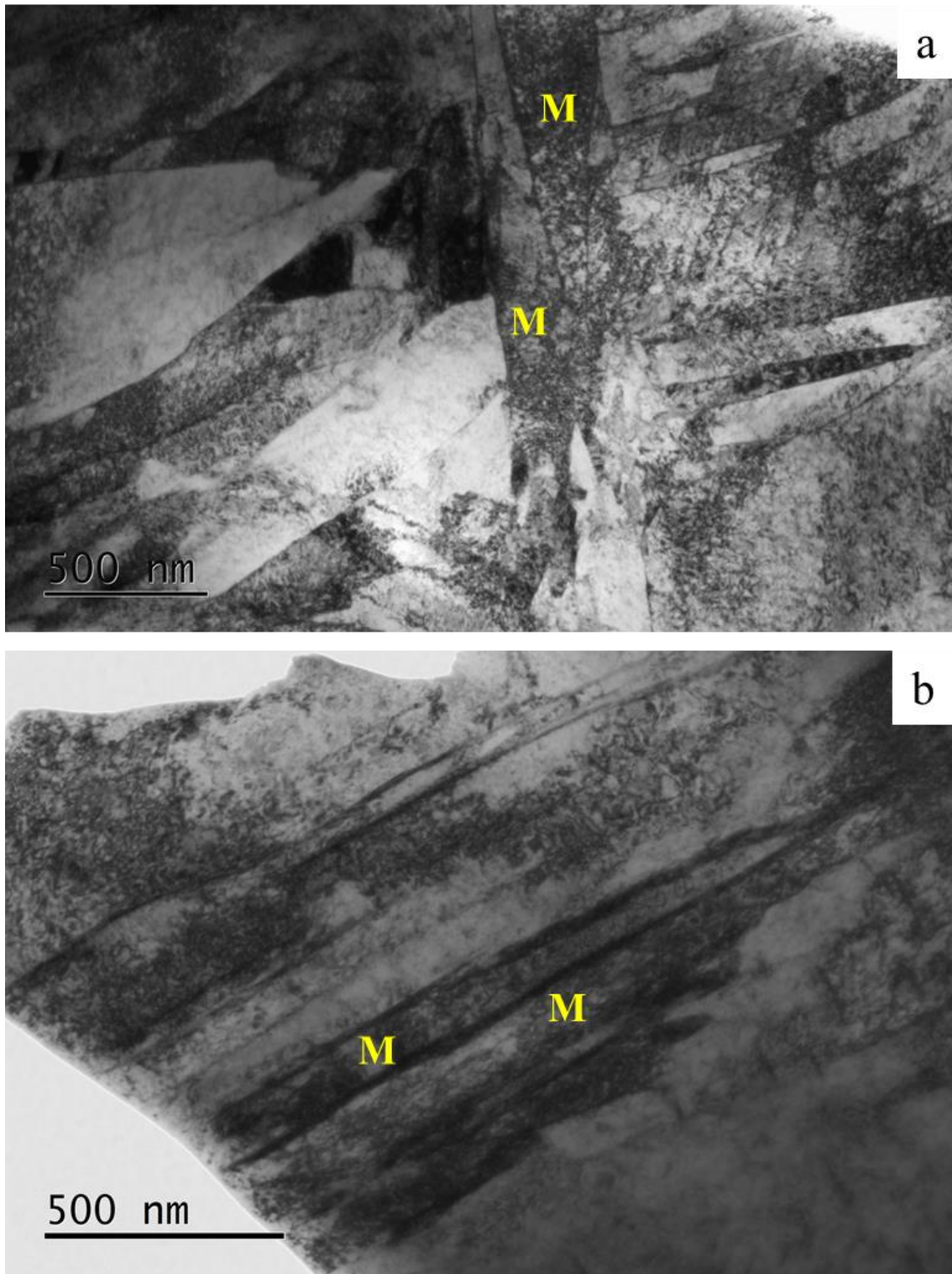


**Figure 8.2.6:** (a, b) BF TEM images showing the martensite laths. They are distinguished from their lath shape, the high deformation from the shear transformation, and the lack of cementite precipitates inside the lath.



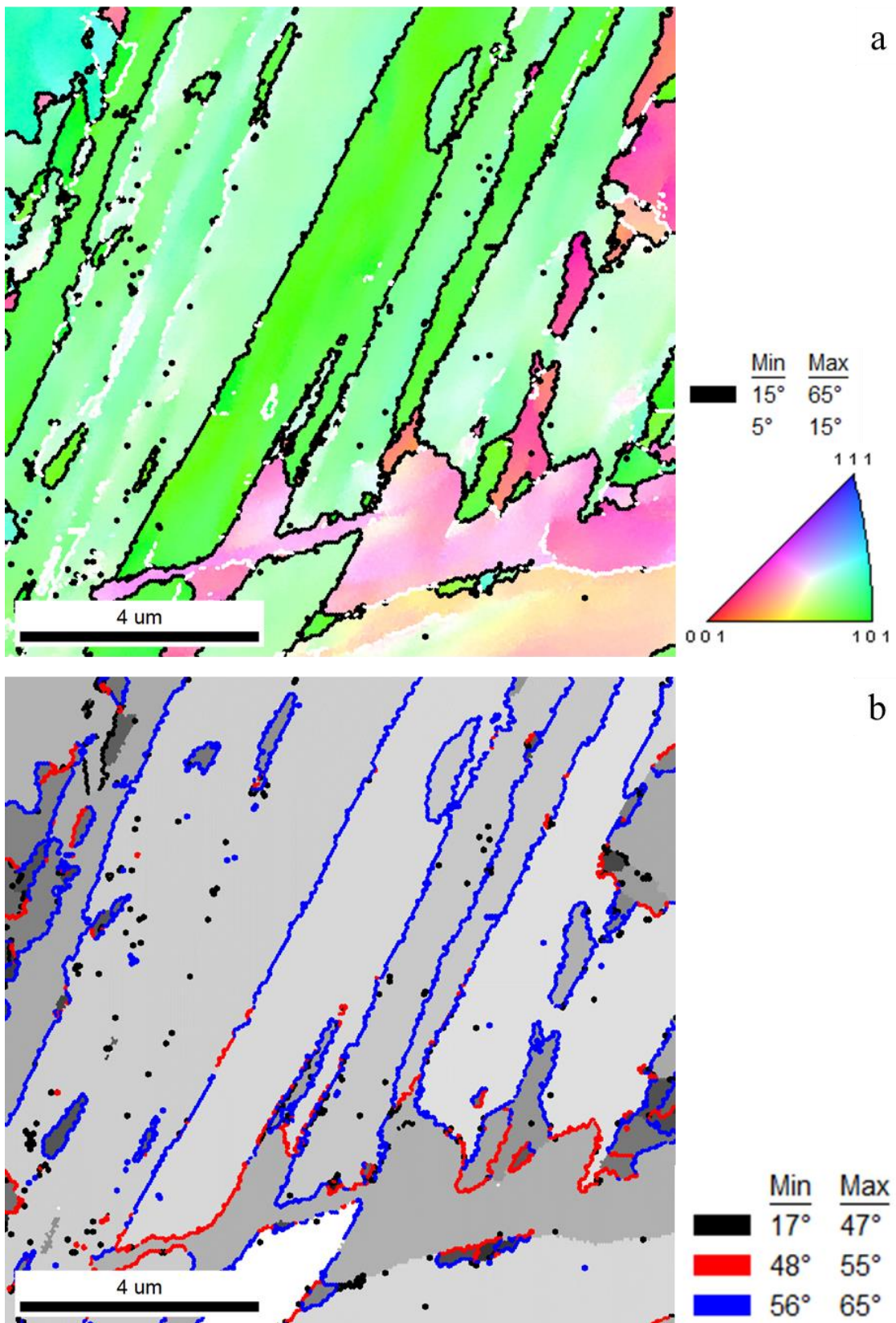


**Figure 8.2.7:** (a) IPF map indicating that the martensite laths inside the same block have the same orientation. (b) High rotation angles ( $56^{\circ}$ - $65^{\circ}$ ) shown in blue color indicate the martensitic laths. Step size: 50 nm.

8. Experimental Results

In order to analyze the grain size of the martensite laths, five EBSD scans were performed with a sum of 789 identified grains taken into account. From these scans (**Figure 8.2.8a-e**), the average grain size (area) was calculated at  $21.75 \mu\text{m}^2$ . The refinement of the microstructure depends on the size of the parent austenite grains. Due to short heating times during UFH, the PAGs are not expected to have time to grow. From the OM and SEM images (**Figure 8.2.5**), it is calculated that they have a diameter of  $15 \mu\text{m}$  on average. If they are considered circular, the area is calculated to be equal to  $176.7 \mu\text{m}^2$ . From the same OM and SEM Figures, it is also observed that there is heterogeneity in the sample concerning the PAG size. As reported [35], martensite nucleation starts on the PAG boundaries, and therefore, smaller PAGs translate to smaller martensite laths.

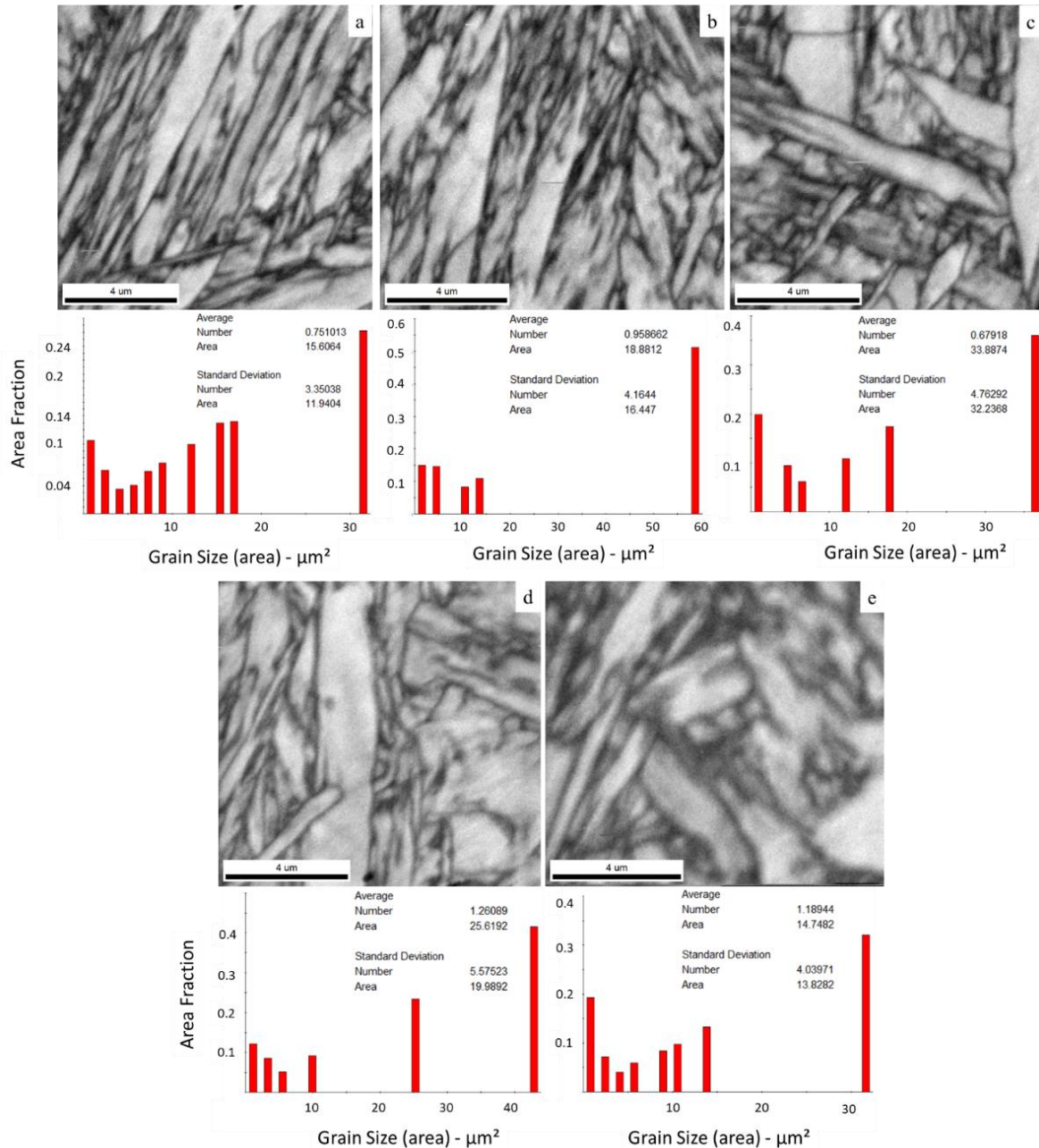


**Figure 8.2.8:** (a-e) IQ maps in different areas of the sample. The grain size (area) of each scan was taken into account, and the average grain size was calculated. Step size: 50 nm.

Further PAG refinement could be expected if there was no cementite dissolution due to a pinning effect [85]. Instead, in the current sample, no cementite from the initial microstructure is found, which means that complete dissolution has been achieved at this heating rate. Nevertheless, complete homogenization of the chemical composition is not achieved.

From the EBSD analysis (**Figure 8.2.9**), traces of retained austenite (yellow) are found in the microstructure. To verify this, the K-S relationship  $\langle 112 \rangle 90^\circ$  misorientations between ferrite and austenite are shown in blue color in the Image Quality (IQ) map. The presence of film-like retained austenite is also shown from TEM analysis, as shown in **Figures 8.2.10a, 8.2.11a, and 8.2.12a**. The average thickness of the RA films is calculated at 25 nm. Morito et al. [140] thoroughly studied the retainment of austenite in films. The diffraction pattern of the selected area (saed) shown in the green circle is shown in **Figures 8.2.10b, 8.2.11b, and 8.2.12b** indicating the existence of retained austenite. In both TEM images, the RA is found in films.

The main reason for the retainment of austenite in the microstructure is higher carbon concentration locally, which would drop the  $M_s$  to lower temperatures. During ultra-fast heating, the homogenization of the composition in the microstructure is limited as not enough time exists due to rapid treatment for the dissolution of cementite and carbon diffusion. No pearlite remnants were observed in the current work, so it is assumed that the dissolution of cementite is completed. However, a gradient in the carbon content is expected due to a lack of heating time above the  $A_{c3}$  temperature, and therefore homogenization cannot complete. Thus, the areas near the dissolved pearlite colonies will be enriched in carbon, and the retainment of austenite is more plausible in the proximity. From [88,99], DICTRA software has shown that there are two possible types of parent austenite in the microstructure at peak temperature. The first one has a high carbon concentration and is expected to be in small proximity to the initial microstructure's pearlitic islands. The other one is depleted in carbon, and the reason is that it is expected in areas relatively further from the pearlitic areas. Specifically, the nucleation of austenite during UFH can occur with two different mechanisms. The first one takes place near or inside the pearlitic colonies where the carbon content is higher, and ferrite enrichment can occur in short distances. Then the nucleation of austenite is controlled by the difference in the carbon content and, therefore, the difference in the Gibbs energy between cementite and ferrite, as would take place in a conventional heat treatment. In the case of austenite nucleation between ferrite grains, where there no pearlite is present and therefore the maximum carbon content is defined by its solubility in ferrite, the mechanism is different. Kaluba et al. [91-93] reported that when high heating rates are applied, homogenization of the microstructure and enrichment of ferrite in carbon is averted as the diffusion distances are shortened. Then, in the C-depleted areas, the nucleation of austenite is not driven by the carbon diffusion but by the mobilization of the interfaces and the transformation of the FCC structure from the previous BCC. The distinction of the parent austenite in C-rich and C-depleted through DICTRA was shown earlier in **Table 8.2.3**. From this table, it is also shown that the C-rich austenite is also enriched in manganese alongside the carbon enrichment. This alloying element is considered a  $\gamma$ -phase stabilizer and thus favors austenite ( $\gamma$ ) retainment in these areas during quenching.



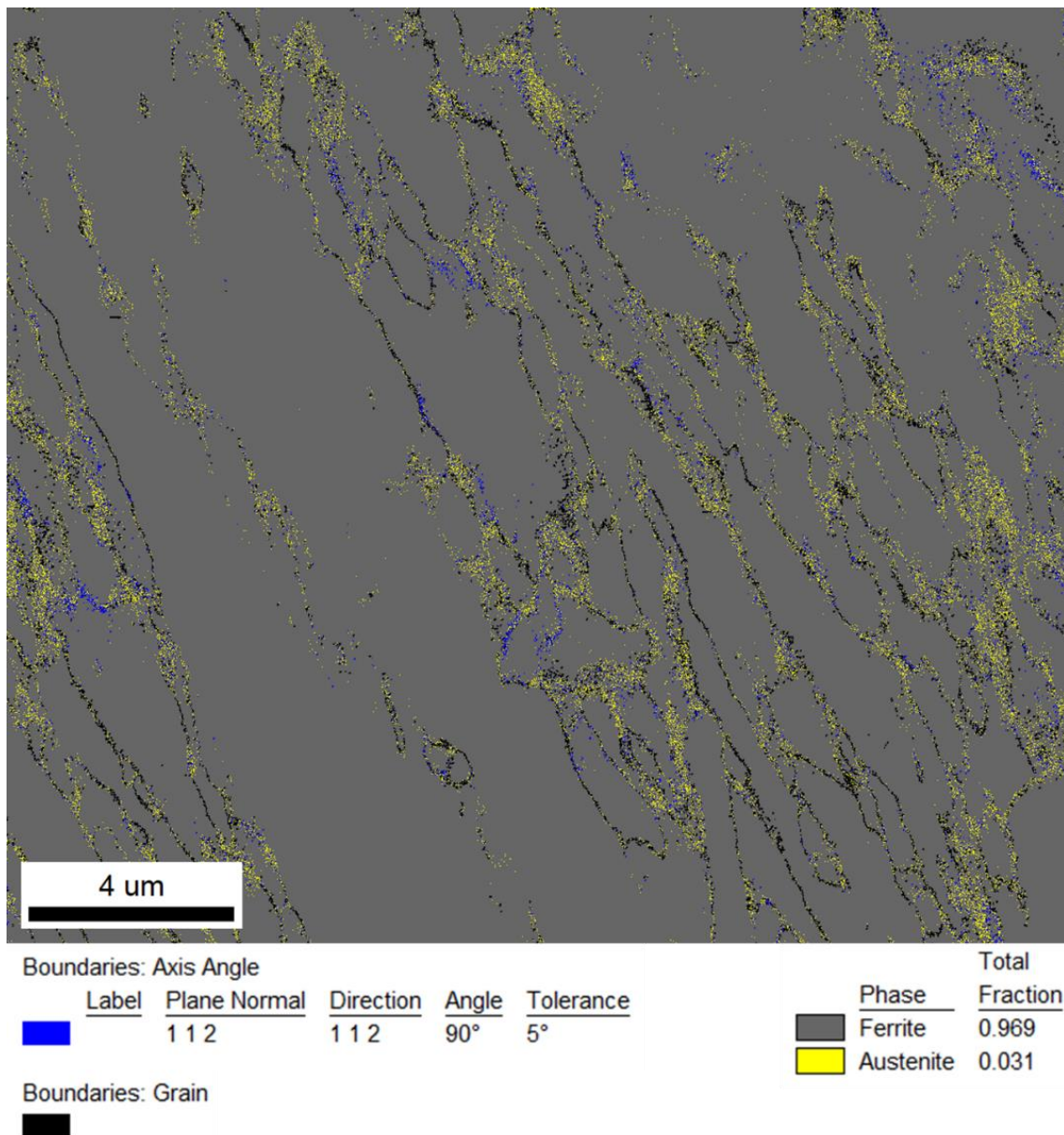


**Figure 8.2.9:** Phase map of the sample with the  $\langle 112 \rangle 90^\circ$  K-S relationship misorientation between ferrite and austenite. Due to the small thickness of the RA films and the limitation to the minimum step size, the depiction of RA is not corresponding to the TEM images. Step size: 15 nm.

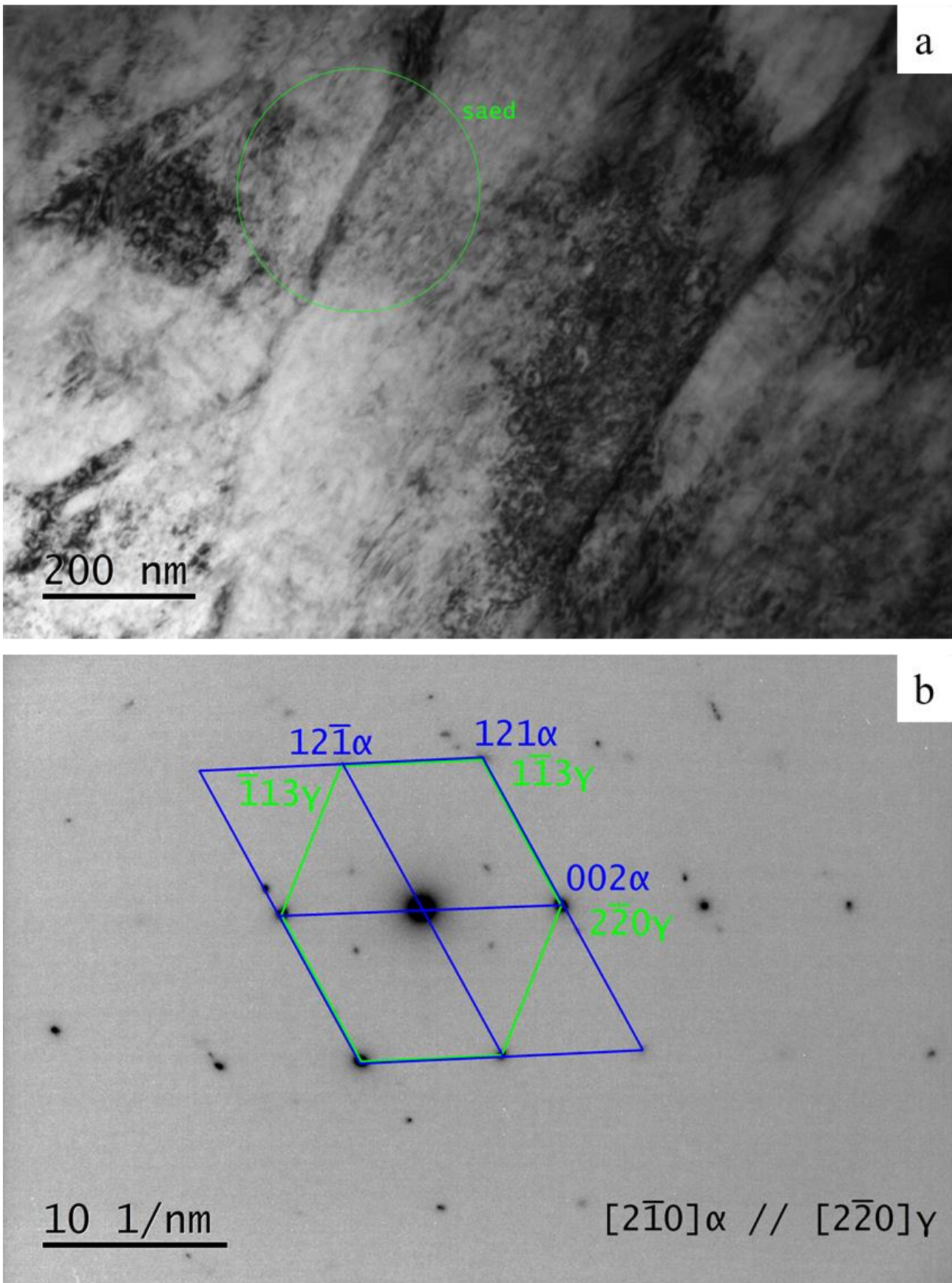


**Figure 8.2.10:** (a) Bright-field TEM showing an RA film on the edge of a lath. (b) The diffraction pattern of the saed indicated inside the green circle is indexed.

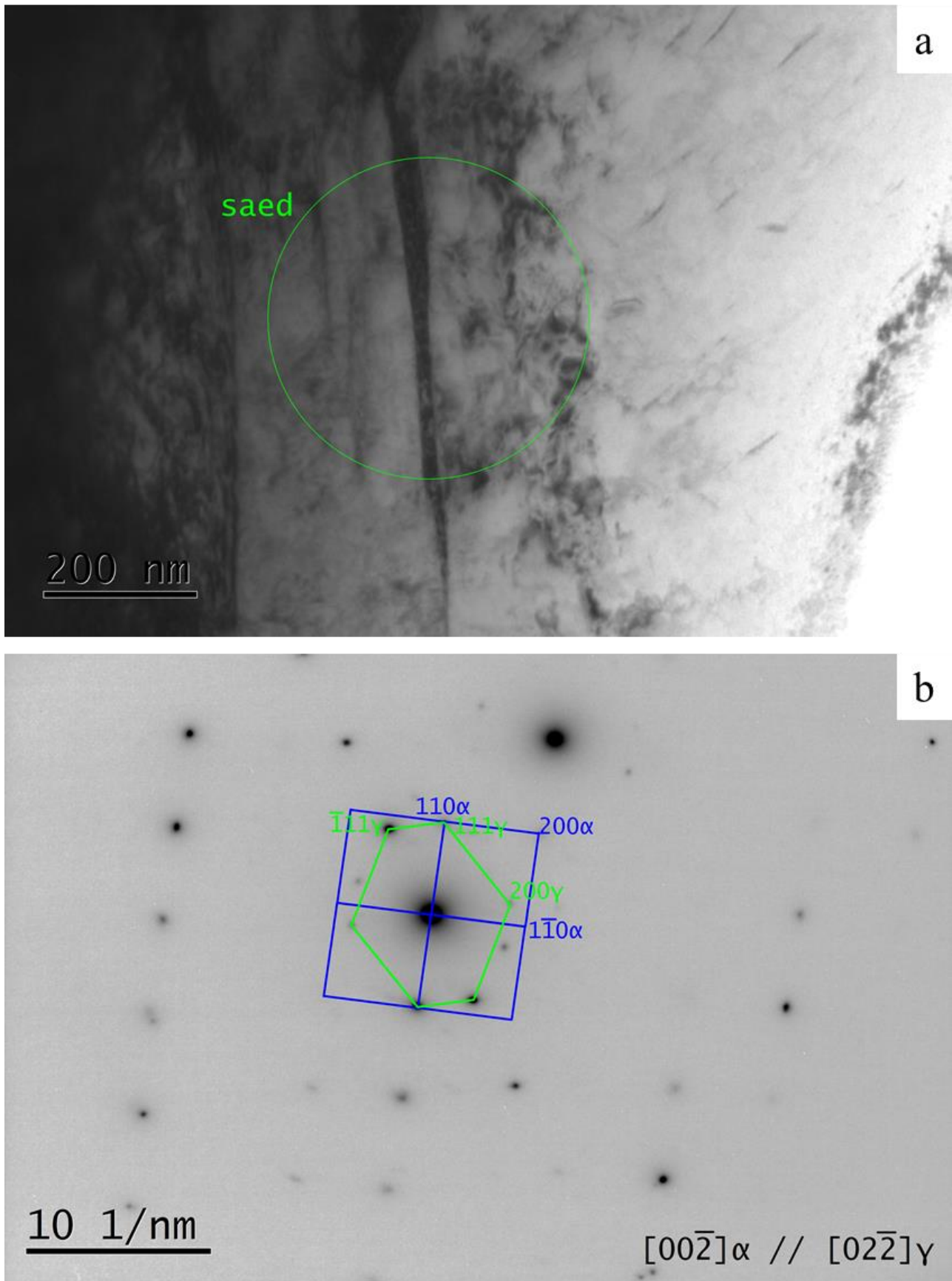


**Figure 8.2.11:** (a) Bright-field TEM showing an RA film on the edge of a lath. (b) The diffraction pattern of the saed indicated inside the green circle is indexed.



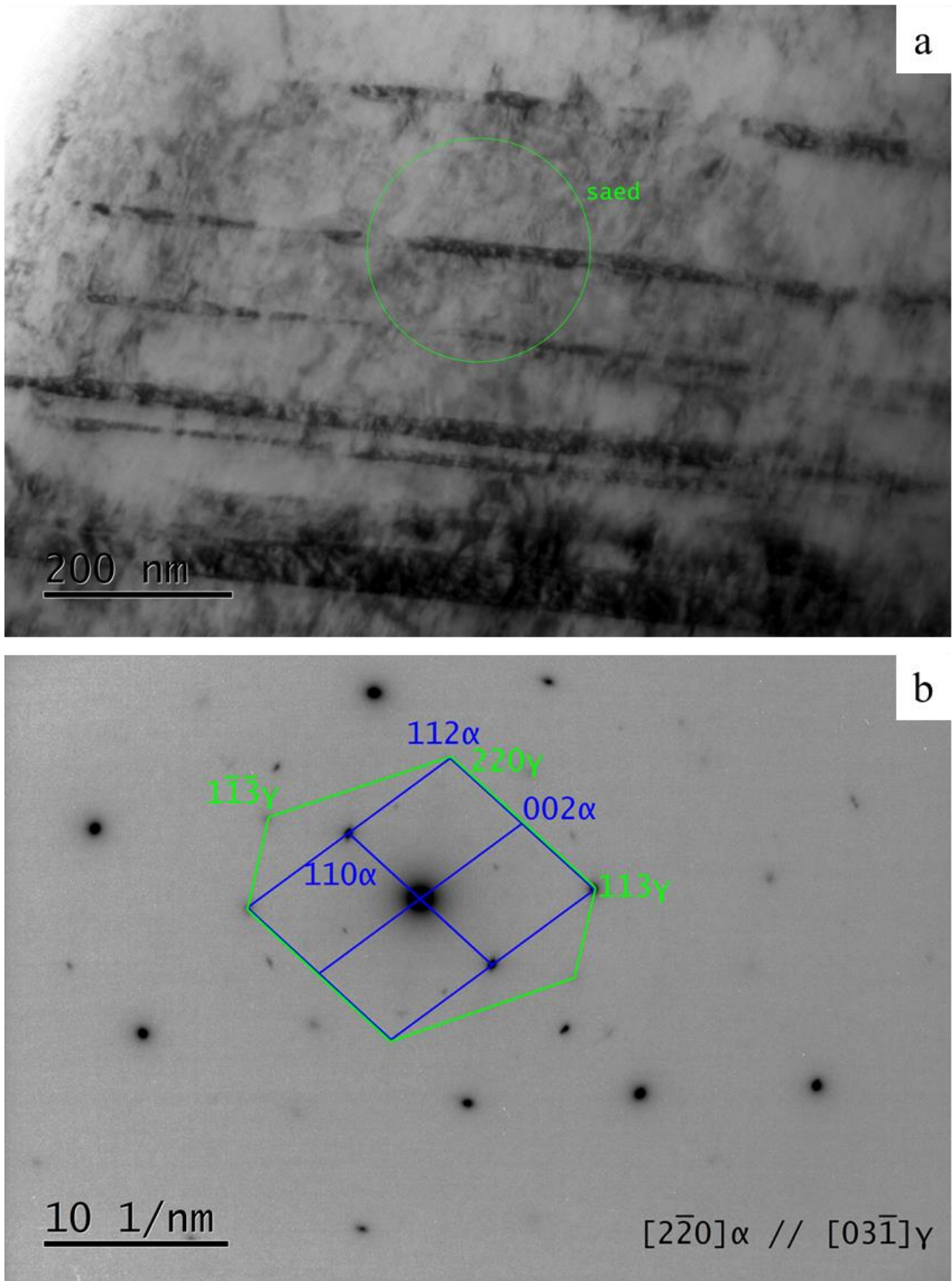


**Figure 8.2.12:** (a) Bright-field TEM showing an RA film on the edge of a lath. (b) The diffraction pattern of the saed indicated inside the green circle is indexed.

Using the two compositions of **Table 8.2.3** and with the models of Kirkaldy [29, 30] and Bhadeshia [31], the continuous cooling transformation (CCT) diagrams are plotted (**Figure 8.2.13a**). It is observed that in the C-rich areas, the  $M_s$  temperature decreases at almost 200 °C in comparison to that of the C-depleted areas. In addition to the aforementioned increase in Mn in the C-rich parent austenite, the retainment of austenite is possible in these areas alongside the martensite transformation. On the other hand, the decrease of carbon content in the C-depleted areas leads to a shift of the  $B_s$  curve to the left-hand side of the CCT diagram. This means that at high cooling rates (higher than 100 °C/s), bainite formation is possible in these areas. As the sample was quenched in water at room temperature, it is expected that the cooling rate exceeds 100 °C/s. Even at a cooling rate of 100 °C/s, the C-depleted parent austenite grains may transform into bainite or martensite as the specific cooling rate curve intersects the  $B_s$  and  $M_s$  curves but not the  $B_f$  curve.

On the other hand, according to the CCT diagram, the C-rich grains can transform only into martensite, as the  $B_s$  curve does not intersect the curve of the specific cooling rate. According to the literature, in this sample, indications from EBSD are found (**Figure 8.2.13b**) from misorientation angles between 48° and 55° that are shown in red and correspond to bainite [28]. In order to validate these indications, TEM was used. From this analysis, large laths were found in the microstructure with elongated parallel cementite particles inside (**Figures 8.2.14a, b, 8.2.15a, b, 8.2.16**). According to the work of Bhadeshia [34], these morphologies correspond to lower bainite with the precipitation of cementite during quenching. The formation of lower bainite occurs at the lower part of the CCT diagram and by the shear transformation. Thus, the carbon is trapped inside the bainitic laths forming fine parallel cementite particles. To confirm this cementite inside the bainitic laths, the diffraction pattern (**Figure 8.2.17b**) was taken from the selected area in **Figure 8.2.17a**. From the TEM analysis (**Figures 8.2.18a, b and 8.2.19a, b**), it is also observed that parallel laths are found to a great extent with cementite or austenite films in between. According to the work of Takahashi [78], this morphology corresponds to lower bainite, as well. During its formation, carbon is displaced from the formed ferritic plate due to its low solubility in carbon. This excess of carbon is then segregated on the space between the plates and may lead to the parent austenite retainment in films [140]. In addition, due to the short cooling time given, the carbon located in the middle of the plate is trapped, as there is not enough time for diffusion.

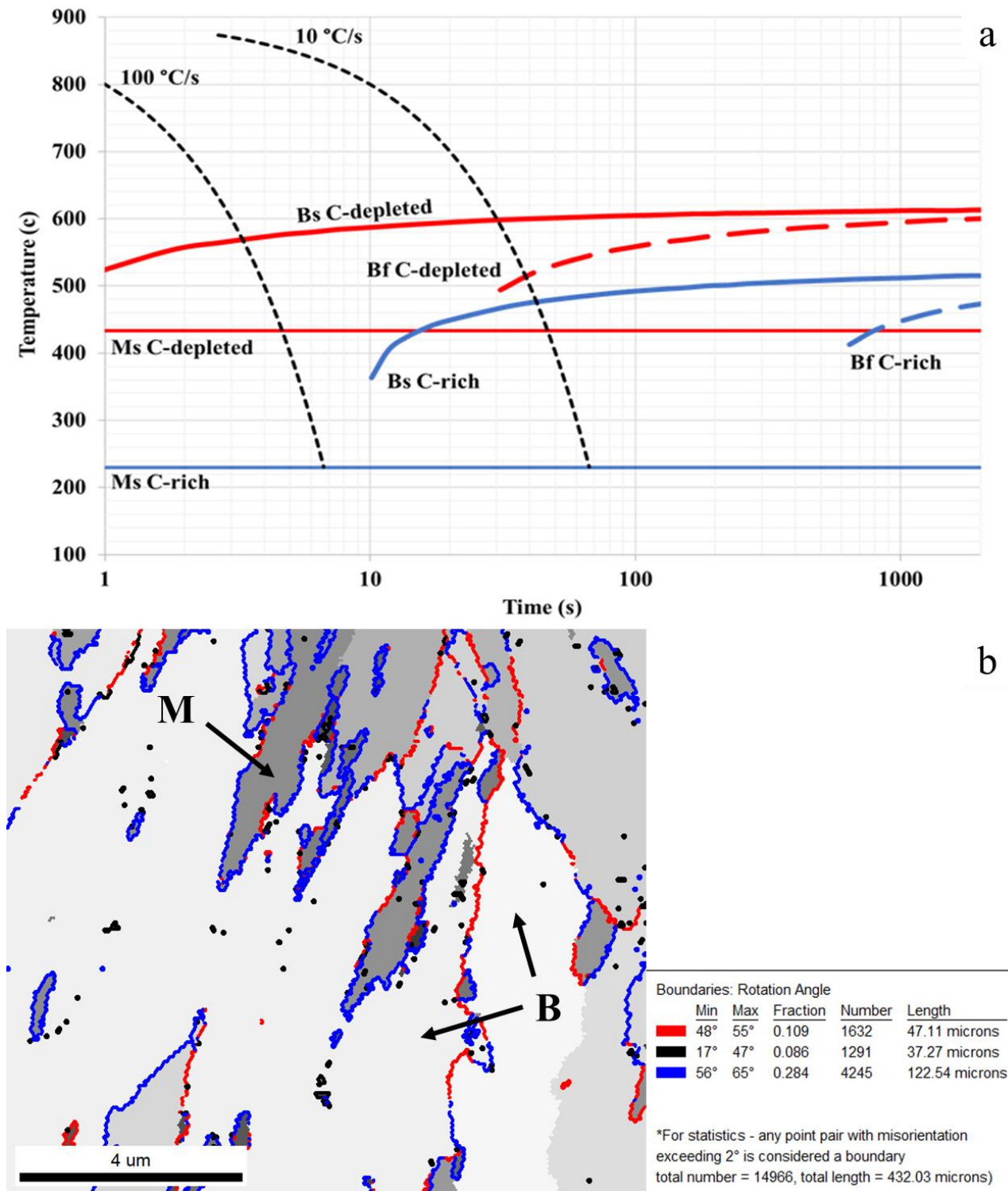


**Figure 8.2.13:** (a) CCT diagram plotted using the models that shows the Bs and Bf curves for the C-rich and C-depleted parent austenite compositions. (b) EBSD GAIQ with the rotation angles. According to [28], bainite laths (B) have low misorientation and rotation angle between 48°-55°. Due to the nature of the martensitic transformation, martensite laths (M) show bigger misorientations with an angle between 56°-65°.



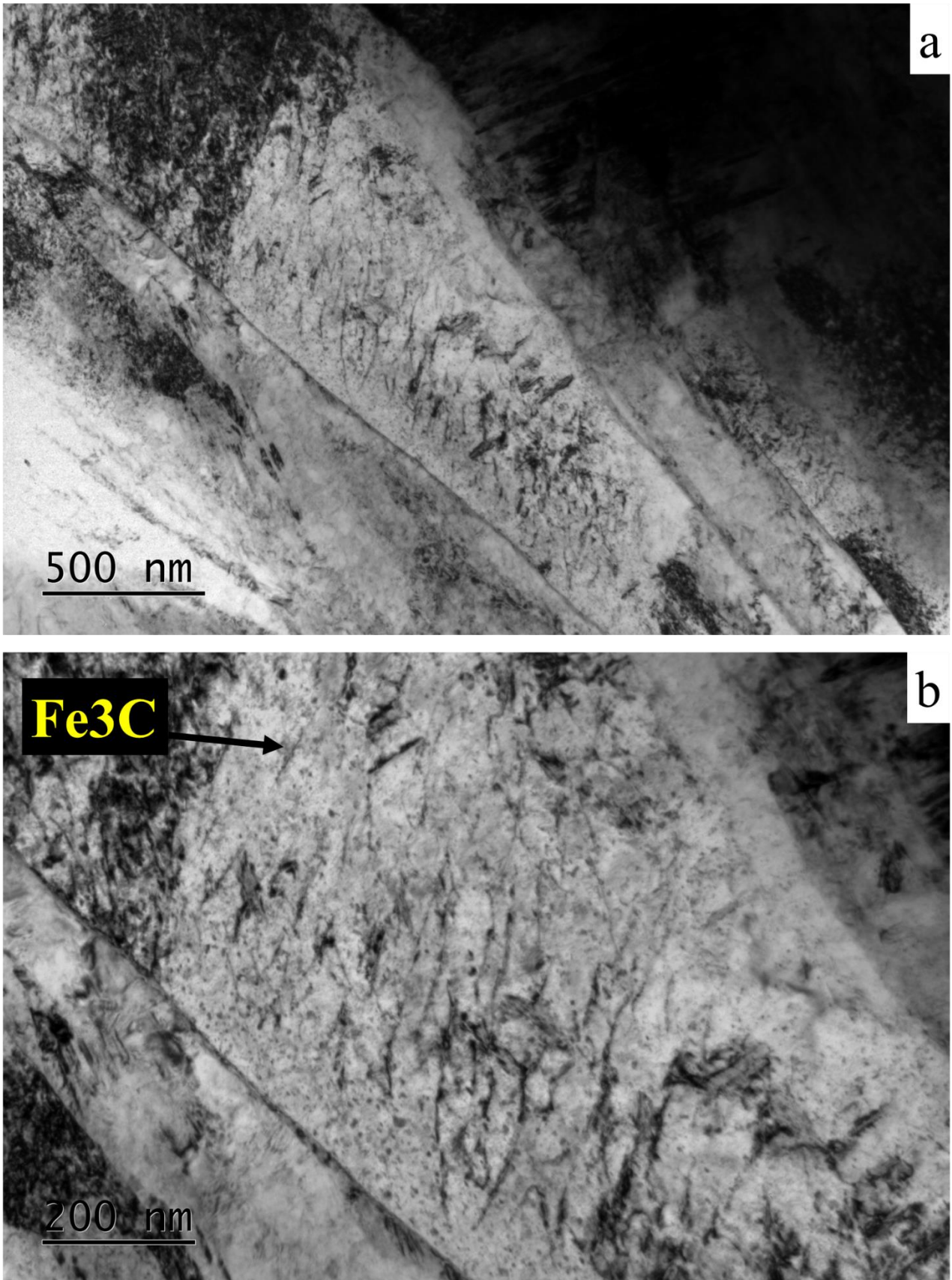


**Figure 8.2.14:** (a) BF TEM showing large laths with parallel cementite particles inside, indicating the existence of lower bainite in the microstructure. (b) Magnification of the first image where the parallel cementite ( $Fe_3C$ ) particles are better observed.

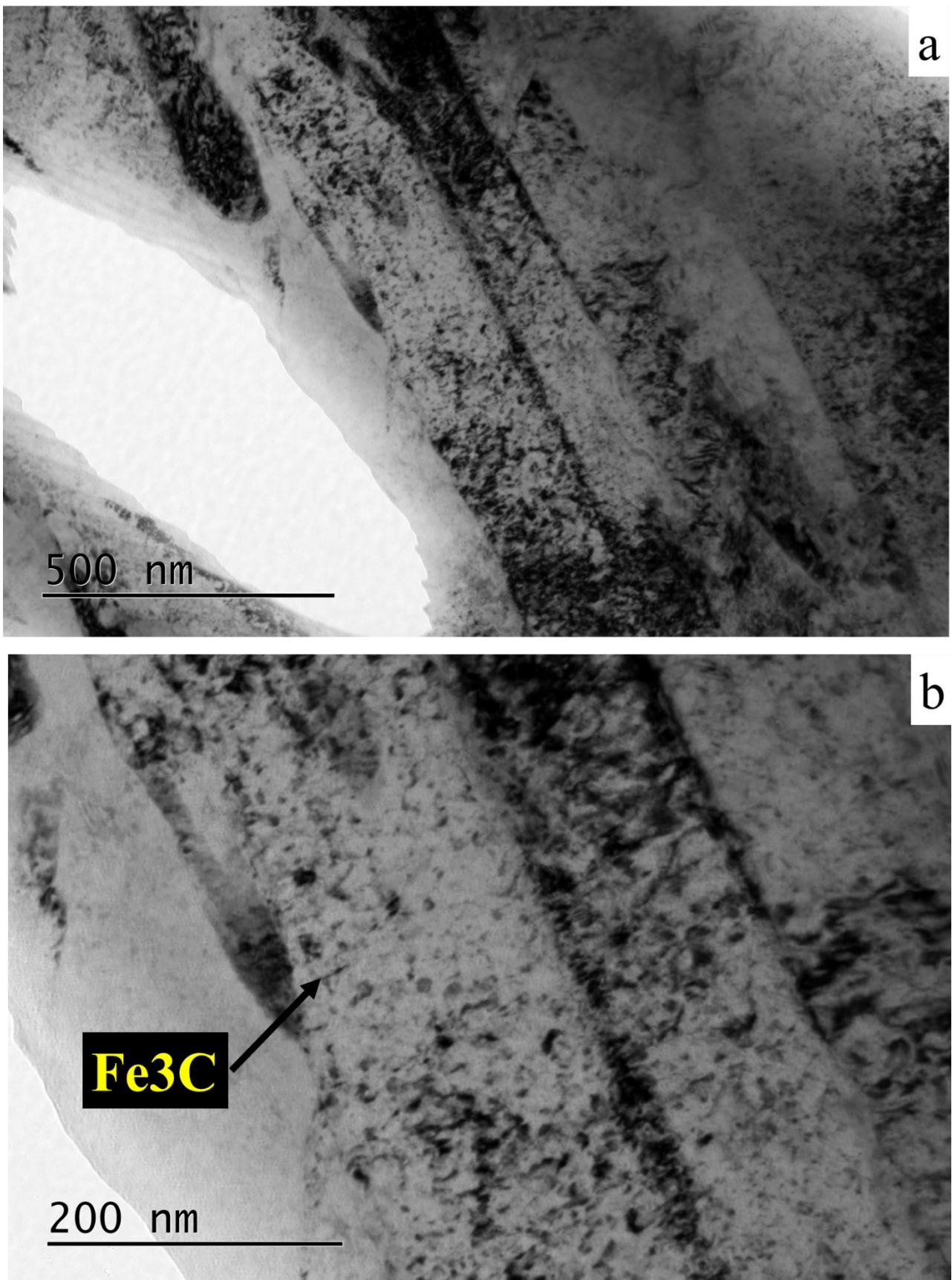


**Figure 8.2.15:** (a) BF TEM showing large laths with parallel cementite particles inside, indicating the existence of lower bainite in the microstructure. (b) Magnification of the first image where the parallel cementite ( $\text{Fe}_3\text{C}$ ) particles are better observed.



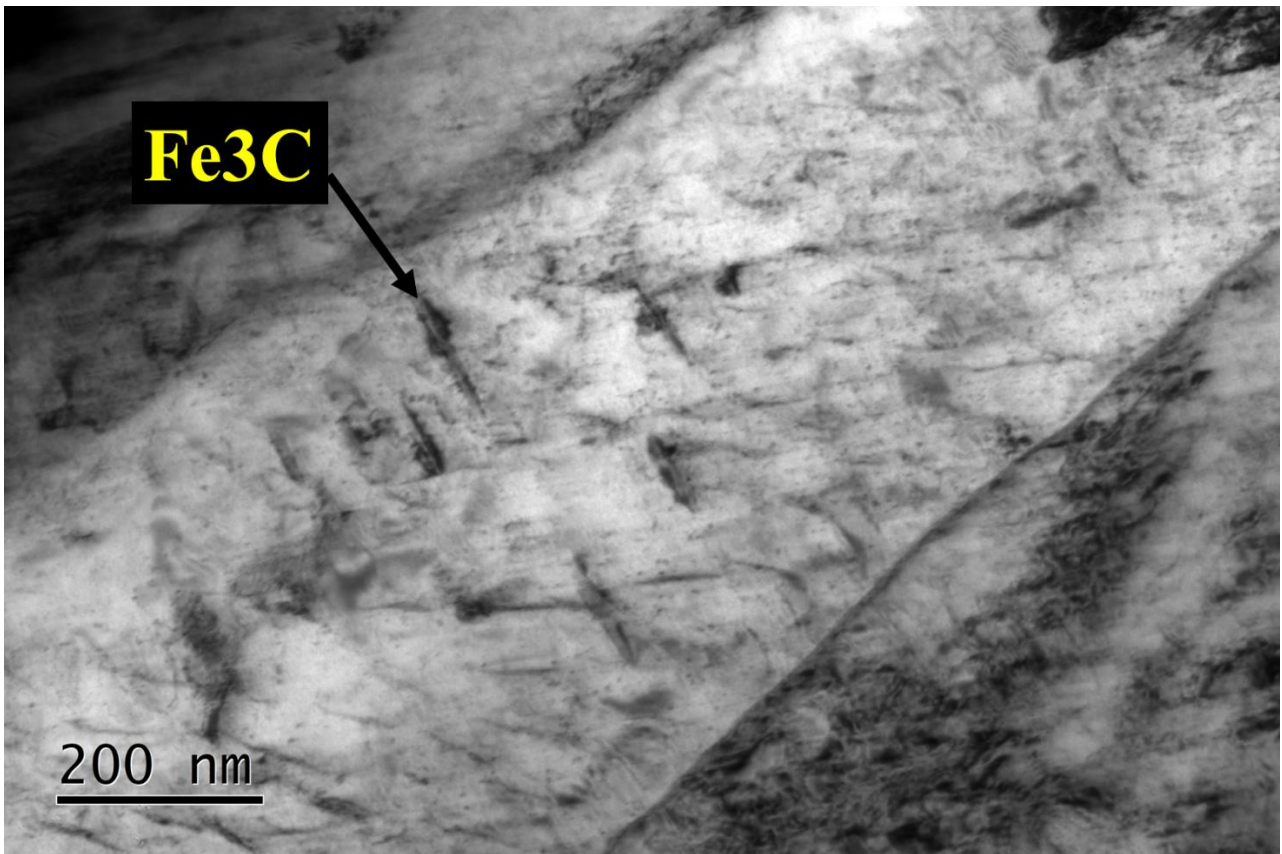


*Figure 8.2.16: (a) BF TEM showing a bainitic ferrite lath with parallel cementite particles ( $Fe_3C$ ) inside, indicating the existence of lower bainite in the microstructure.*



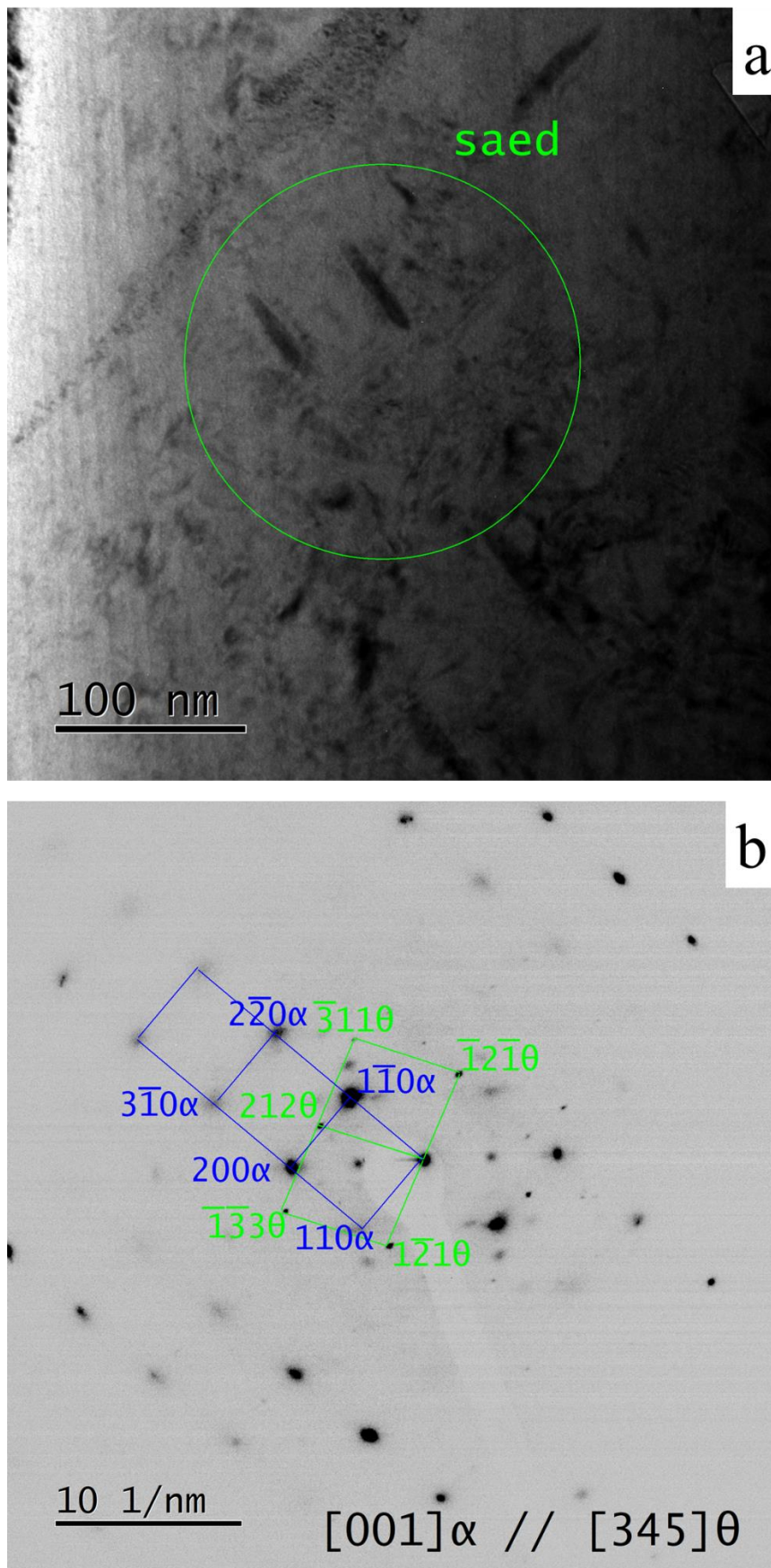


**Figure 8.2.17:** (a) The parallel cementite particles found inside a bainitic ferrite lath. (b) saed diffraction pattern from the area shown inside the yellow circle indicating the correlation between the cementite ( $\theta$ ) and ferrite ( $\alpha$ ) lattices.

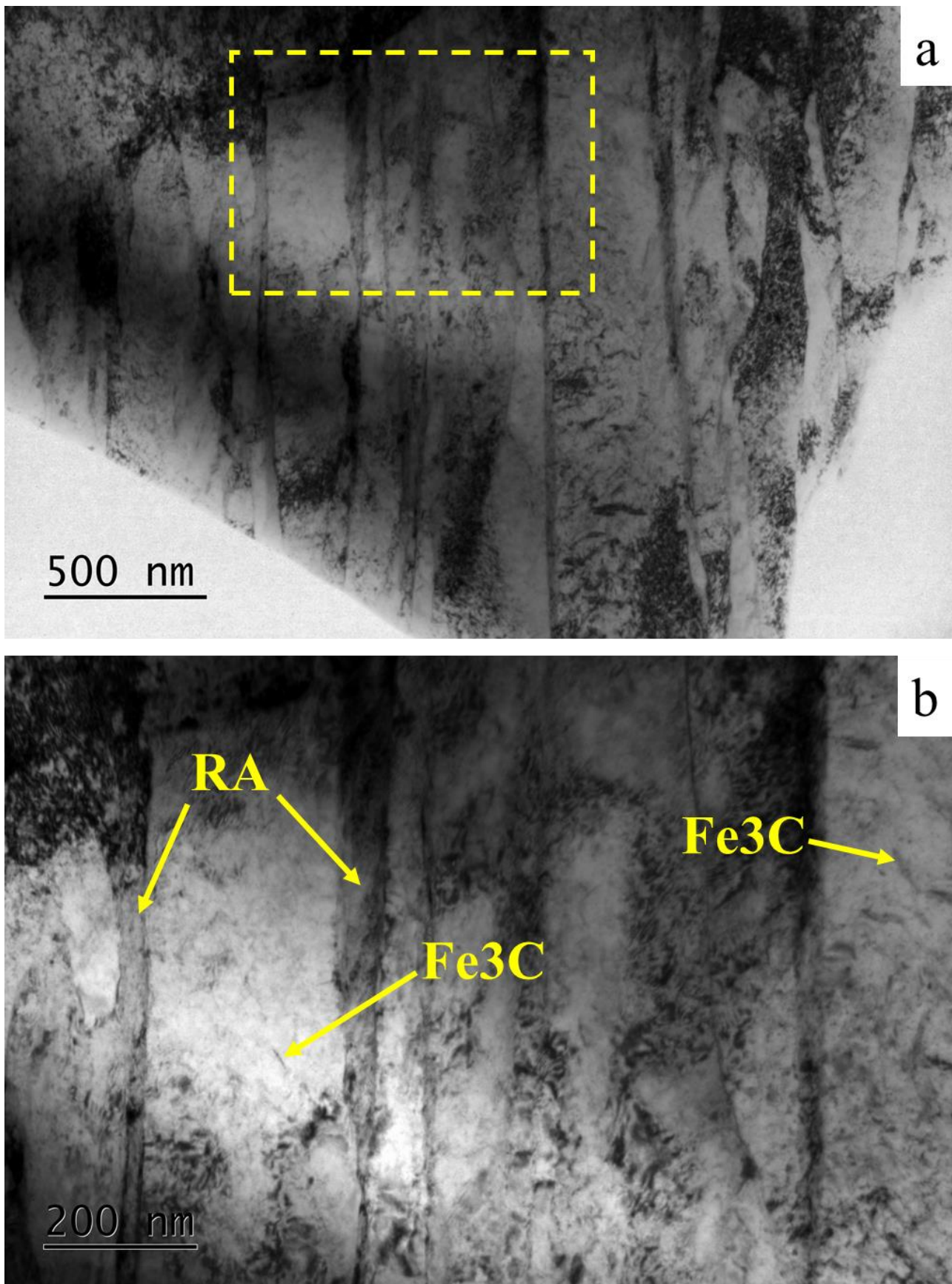


**Figure 8.2.18:** (a) BF TEM images of lower bainite. It is shown that parallel bainitic ferrite plates exist in the microstructure with RA formed in between (b) It can be observed that inside these plates, there are cementite particles that have precipitated upon cooling ( $Fe_3C$ ),



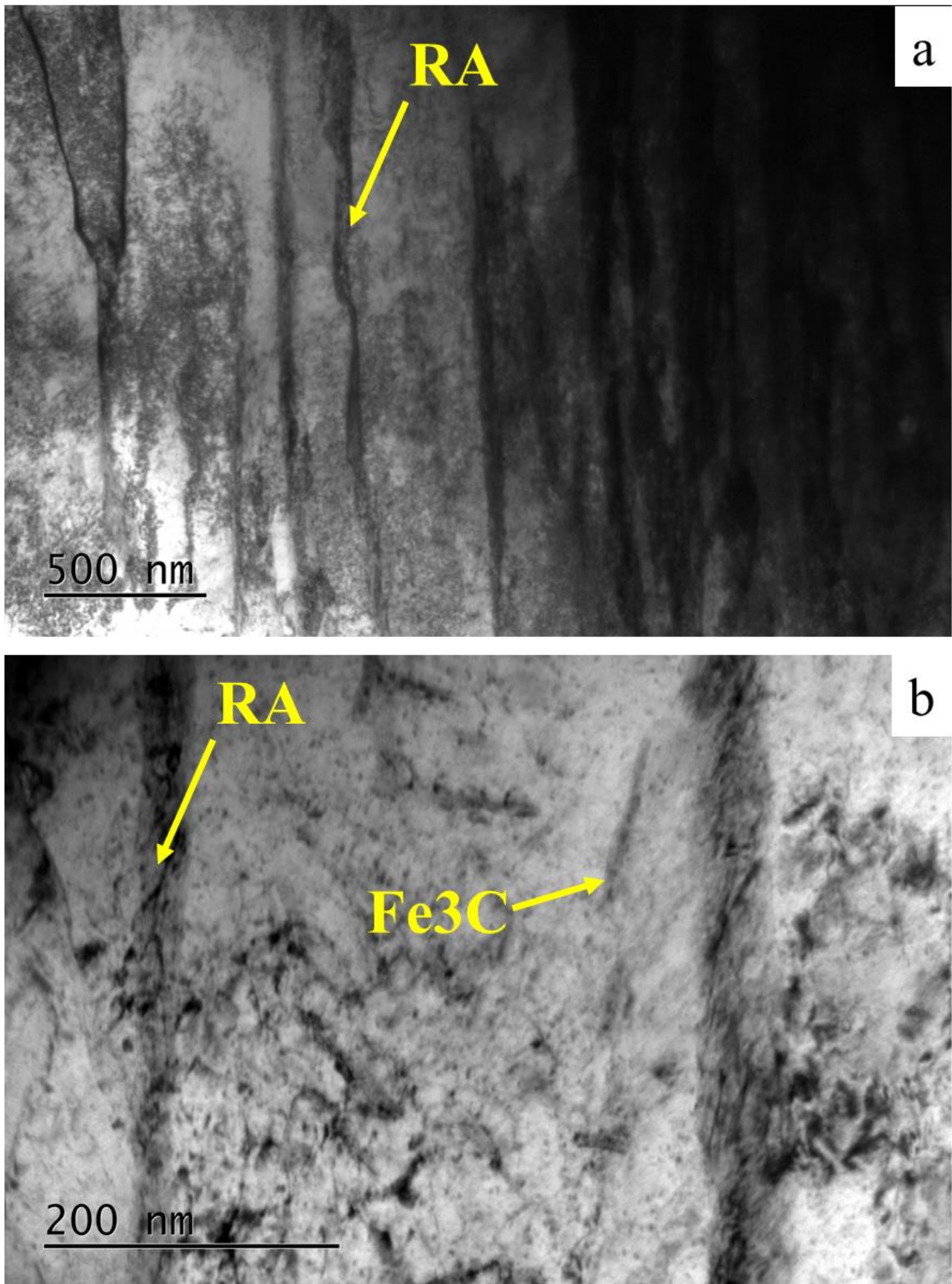


**Figure 8.2.19:** (a, b) BF TEM images of the lower bainite. Again, parallel bainitic ferrite plates exist in the microstructure with RA formed between and Fe<sub>3</sub>C precipitated inside.

The measured micro-hardness of the two samples is shown in **Table 8.2.4**. It appears that the hardness of the UFH sample is higher than that of the reference sample by approximately 50 HV. As the microstructure of the reference sample is fully martensitic, it is expected to have increased hardness, compared to the UFH sample, as the presence of bainite should decrease the overall hardness. Though, the grain refinement that is observed in the UFH sample can contribute to the increase of the overall hardness of the sample, as is the case with these samples.

**Table 8.2.4:** *The average Vickers hardness for the UFH and reference samples*

---

<b>Samples</b>	<b>Average HV</b>	<b>Average Deviation</b>
Reference sample	413	36
UFH sample	465	10

---

### 8.3. The Ultra-Fast Heat Treatment as a method to produce commercial DP Steels

#### 8.3.1. Introduction

In order to fully comprehend the viability of UFH, experiments were performed in commercial grades that are already in use in the industry. DP steels have been thoroughly used in the automotive industry due to their respectively easy production. They consist of martensite islands on a ferritic matrix, and their strength depends on the martensite fraction and hardness, while their good elongation is attributed to the fraction of the ferritic matrix. In this chapter, the purpose was to produce such a grade using ultra-fast heating. Using a commercial grade as initial material, a typical DP cycle was applied and then compared to the UFH cycle. The phenomena that may occur or be impeded during the heating stages when high heating rates are applied are studied. Such phenomena are the dissolution of cementite in the pearlitic colonies, recovery and recrystallization of ferrite, enrichment of ferrite in carbon, and nucleation and growth of austenite. These phenomena occur during conventional heat treatments as time is necessary, but during UFH, in which case the heating time is limited, they are either impeded or even averted. Whether these phenomena take place or not and their impact on the microstructure and properties of the material is studied in this chapter.

#### 8.3.2. Materials and methods

Until now, the study of UFH cycles has focused on the explanation and understanding the phenomena that take place using special steel grades. Nevertheless, to connect this method with the automotive industry, commercial steel grades were selected for this study that is already applied in the industry. Hence, a low-carbon, low-manganese steel was selected that was cold-rolled to a 1 mm thickness (60 %) thickness and consisted of ferrite and pearlite/martensite in an 87 %-13 % fraction. The composition of the material is shown in **Table 8.3.1**, and the initial microstructure in **Figure 8.3.1**.

**Table 8.3.1:** The chemical composition in wt. % of the commercial steel used for the experiments.

C	Si	Mn	Cr	Mo	S	P	Nb+Ti	Fe
0.14	0.24	1.7	0.25	0.25	0.004	0.014	0.05	rest



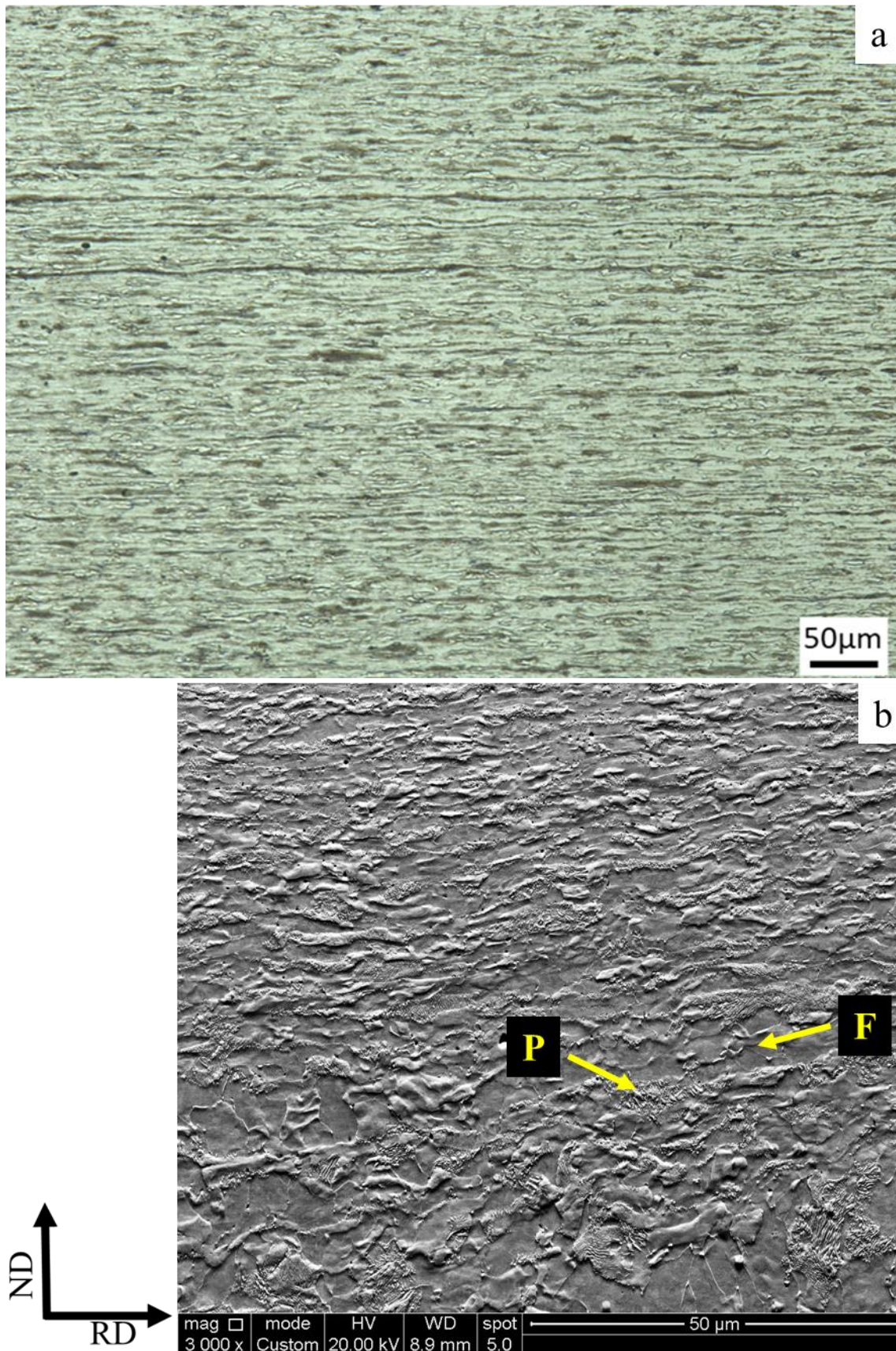


**Figure 8.3.1:** (a) OM metallography of the Initial Material that consists of ferrite (bright areas) and pearlite/martensite (dark areas). (b) SEM image of the initial material showing the ferrite and pearlite in the microstructure.

The heat treatments were performed in a Gleeble machine and consisted of three different experiments. An ultra-fast heating (**UFH**) cycle was performed at a very rapid heating rate until the peak temperature is reached inside the intercritical range with subsequent quenching. This cycle was compared with a conventional heating (**CH**) with a slow heating rate to the same temperature and subsequent quenching and finally with a cycle intended to simulate the continuous annealing line heating (**CALH**) cycles used in the industry right now. This cycle consists of slow heating to the peak temperature, soaking time, and then quenching. All previous cycles had a preheating (**PH**) stage intended to make the leap to the peak temperature smaller and make the heating easier for the machine [141]. Nevertheless, the PH cycle's microstructure was also studied to confirm no change in the microstructure. The parameters of the heating cycles are shown below in **Table 8.3.2** and **Figure 8.3.2**.

**Table 8.3.2:** The heat treatments that were performed in the Gleeble.

	Pre-heating stage			Annealing stage			Cooling stage
	Heating rate (°C/s)	Heating temperature (°C)	Heating time (s)	Annealing rate (°C/s)	Peak Temperature (°C)	Soaking Time (s)	Quenching rate (°C/s)
PH	10	300	30	-	-	-	-
CALH	10	300	30	10	760	240	65
CH	10	300	30	10	760	0.2	65
UFH	10	300	30	780	760	0.2	65

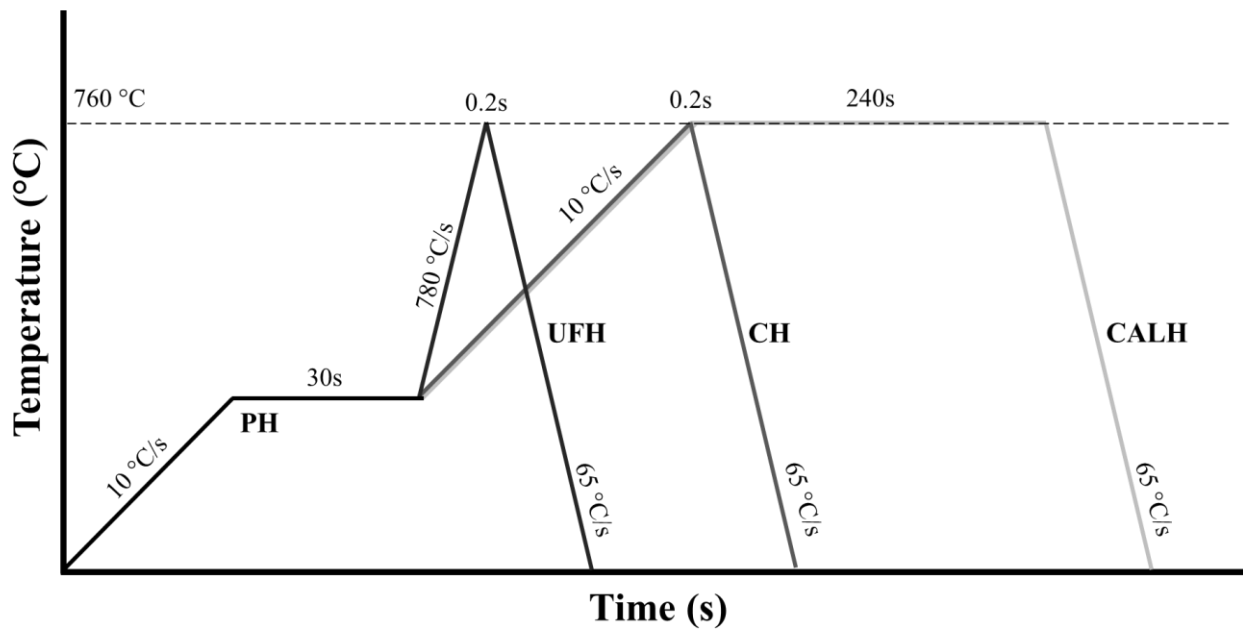


*Figure 8.3.2: Time – Temperature diagram with the treatments that were performed in the Gleeble.*

With the use of Thermocalc, the phase diagram was calculated in equilibrium and plotted in **Figure 8.3.3a**. From this diagram, the  $A_{c1}$  and  $A_{c3}$  temperatures were found at 670 °C and 840 °C, respectively. It has been reported by Valdes-Tabernero et al. [122] that when high heating rates are applied, these temperatures tend to shift at higher values. This was confirmed for the studied material using the models developed by Kirkaldy and Bhadeshia [135–137] and by dilatometry experiments. The results can be observed in **Figure 8.3.3b**. For the dilatometry experiments, heating cycles were performed on flat samples with dimensions 10x4x1 mm at constant temperatures above the  $A_{c3}$  with different heating rates ranging from 1 to 200 °C/s. It is well observed that the  $A_{c1}$  temperature is shifting to higher values with increasing heating rates, but the curve for the  $A_{c3}$  temperature tends to normalize after a critical heating rate.

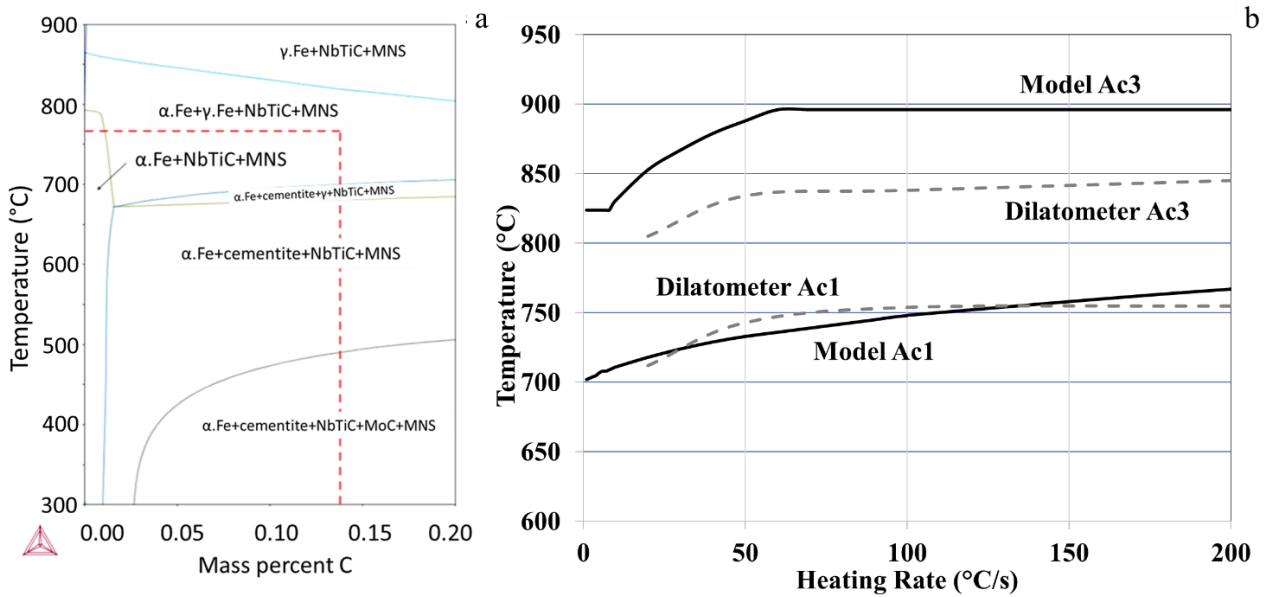


**Figure 8.3.3:** (a) Phase diagram of the used material calculated by Thermocalc for the given composition. (b) Heating rate – Temperature diagram comparing the resulting  $A_{c1}$  and  $A_{c3}$  temperatures (full lines) and dilatometry (dashed lines).

The samples for the microstructure characterization were cut from the homogeneously heat-treated zone of the Gleeble specimens. Then they were ground and polished to a mirror-like finish using 6  $\mu\text{m}$  and 1  $\mu\text{m}$  diamond pastes and etched in a chemical solution of 2% v/v  $\text{HNO}_3$  in ethanol (Nital 2%) for 5–8 s at 20 °C to reveal the microstructure. For TEM and transmission Kikuchi diffraction (TKD) analysis, disk samples were cut from the Gleeble specimens. Then they were manually ground to a thickness of 100  $\mu\text{m}$  and ion milled using a PIPS. SEM analysis, an FEI Quanta TM 450-FEG-SEM operating at 20 kV and spot size 5 in SE (BSE) mode, was used. The same microscope was used for EBSD analysis operating under the following settings: The accelerating voltage was 20 kV with a beam current corresponding to a spot size of 5, aperture size of 30  $\mu\text{m}$ , and a working distance of 7 mm. The resulting patterns were acquired on a hexagonal scan grid by a Hikari detector operated with EDAX TSL–OIM-Data Collection version 6 software. The EBSD scans were performed at a step size of 50 nm. The corresponding orientation data were post-processed with EDAX-TSL-OIM-Data Analysis version 7 software using the following grain definition: Misorientation with neighboring grains higher than 5, the minimum number of points per grain was 2, and confidence index (CI) higher than 0.1. The raw EBSD data were post-processed (cleaned) to re-assign the dubiously indexed points using the grain confidence index standardization and neighbor CI correlation procedure. Based on the EBSD data, the prior austenite grains were reconstructed using the ARPGE software developed by C. Cayron [29]. The transmission Kikuchi diffraction (TKD) was performed using the same equipment. The working distance was set to 5 mm and the step size to 20 nm. A Jeol JEM-2200FS, 200 kV field emission transmission electron microscope was used for the TEM analysis. The continuous cooling transformation (CCT) diagrams were plotted using the models of Kirkaldy and Bhadeshia [136–138] and were calculated considering the chemical composition of the steel and the grain size of the parent austenite.

### 8.3.3. *Results*

#### 8.3.3.1. **Microstructure comparison**

The microstructures of the different heat treatments were compared through the SEM. The microstructure of the PH (**Figures 8.3.4a-c**) stage appears to be very similar to that of the IM and has not been affected by the low-temperature heating. It consists of ferrite and pearlite, and the cold-rolled microstructure is maintained with bands of pearlite/martensite between the elongated and deformed ferrite grains. The purpose of this step is not to change the microstructure and avoid any recovery from the initial material [141]. Despite, it facilitates the Gleeble to achieve the high heating rates required as the leap from the 300 °C to 760 °C is easier to reach than the leap from 25 °C to 760 °C. On the other hand, the microstructure of the CALH sample (**Figures 8.3.5a-c**) is a typical DP microstructure that consists of martensite islands on a ferritic matrix. The martensite islands are intergranular and surround the large ferritic grains. Most ferritic grains are still elongated in parallel to the rolling direction and appear to be clear of any deformation, and one can suppose that the recrystallization process is complete. The diameter of the ferrite grains along the ND axis appears to be similar to that of the IM, indicating that the cold rolling bands have been partly retained. Concerning the CH sample (**Figures 8.3.6a-c**) though, the microstructure appears different from the CALH, even though the slow heating rate is the same. The martensite fraction appears smaller in the CH sample, while pearlite colonies remain in the microstructure and have not been fully dissolved. The cementite in these undissolved colonies appears in both lamellar and spheroidized forms. Both deformed and non-deformed ferrite grains exist in the microstructure, and the cold-rolling bands are more profound than they are in the CALH sample. Finally, in the UFH sample (**Figures 8.3.7a-c**), the overall microstructure is more similar to the IM and PH samples than the annealed samples. The cold-rolling bands have been retained; most ferrite grains remain deformed from the rolling and elongated parallel to the rolling direction. Their diameter in the ND axis appears smaller than in the CH and CALH samples. The martensite islands appear to be more refined than in the CALH and CH samples, and the pearlitic colonies have been retained to a greater extent than in the CH sample. Both spheroidized and lamellar cementite appear in the microstructure, with the latter form being more pronounced.



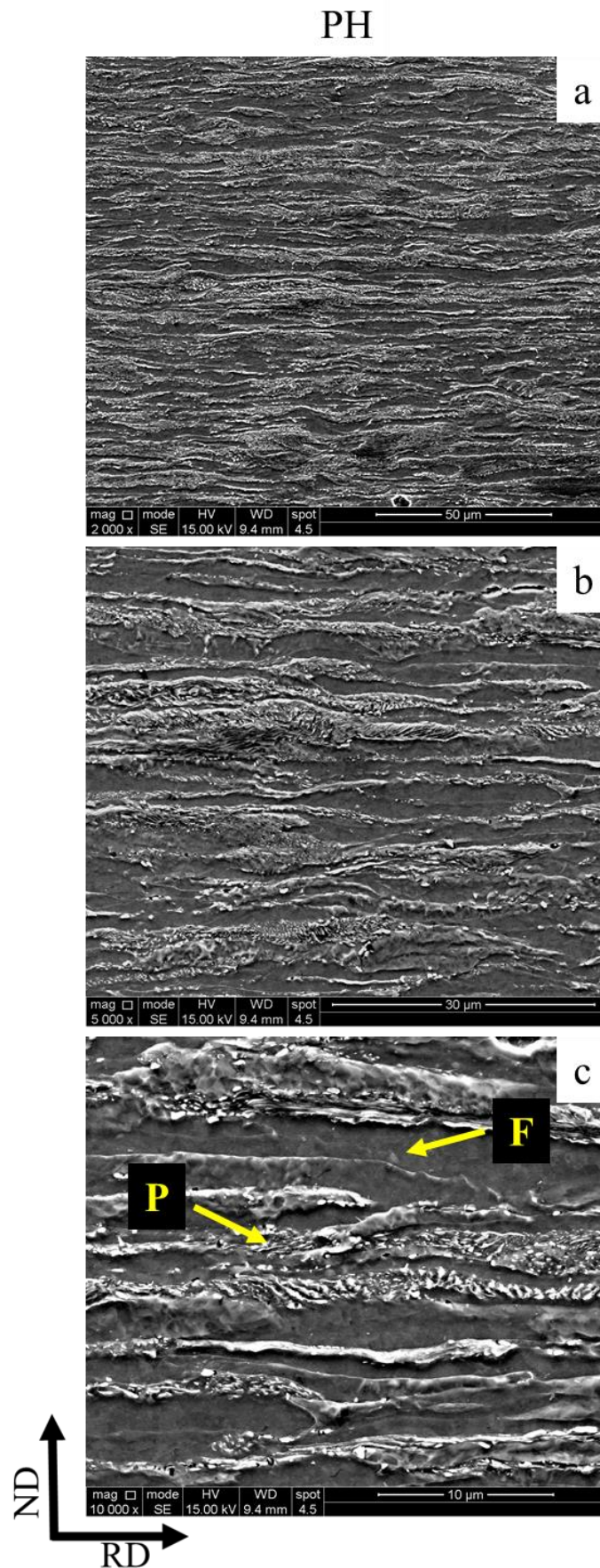


**Figure 8.3.4:** SE SEM image of the PH sample at (a) 2000x magnification, (b) 5000x and (c) 10000x. The microstructure consists of ferrite (F) and pearlite (P).

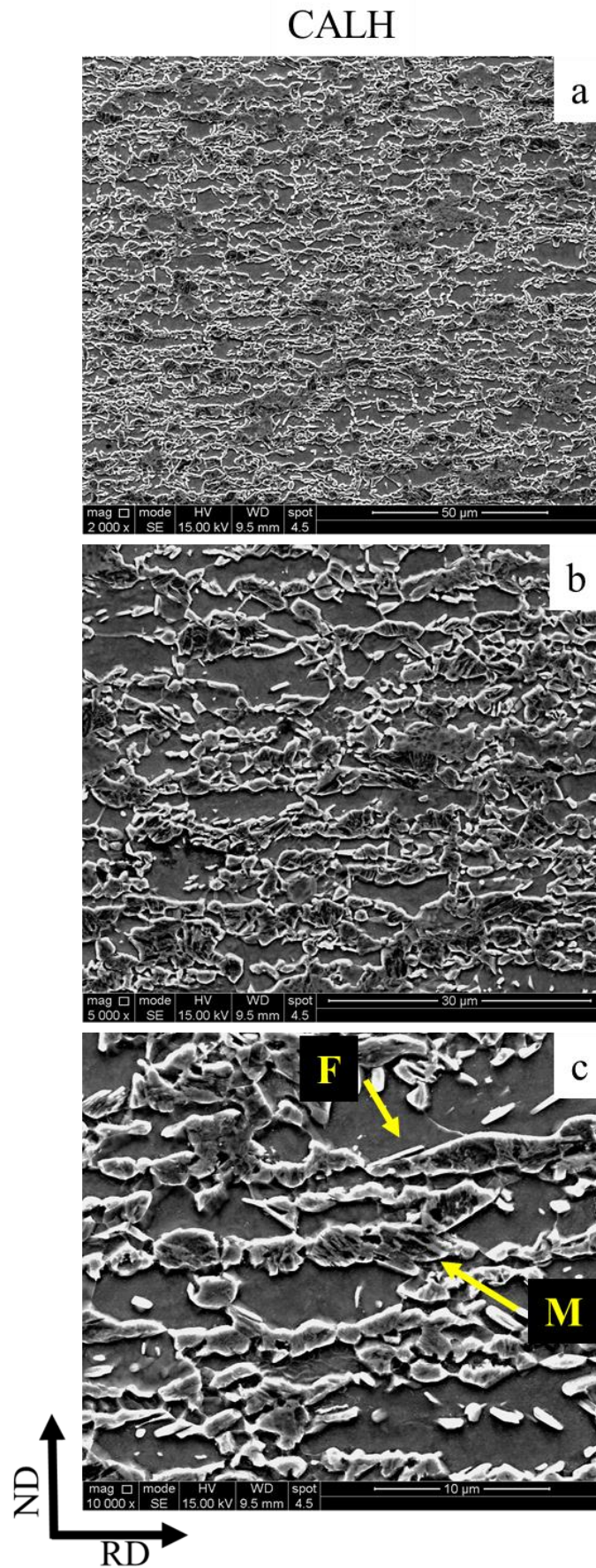


**Figure 8.3.5:** SE SEM image of the CALH sample at (a) 2000x magnification, (b) 5000x and (c)10000x. The microstructure consists of ferrite (F) and martensite (M).



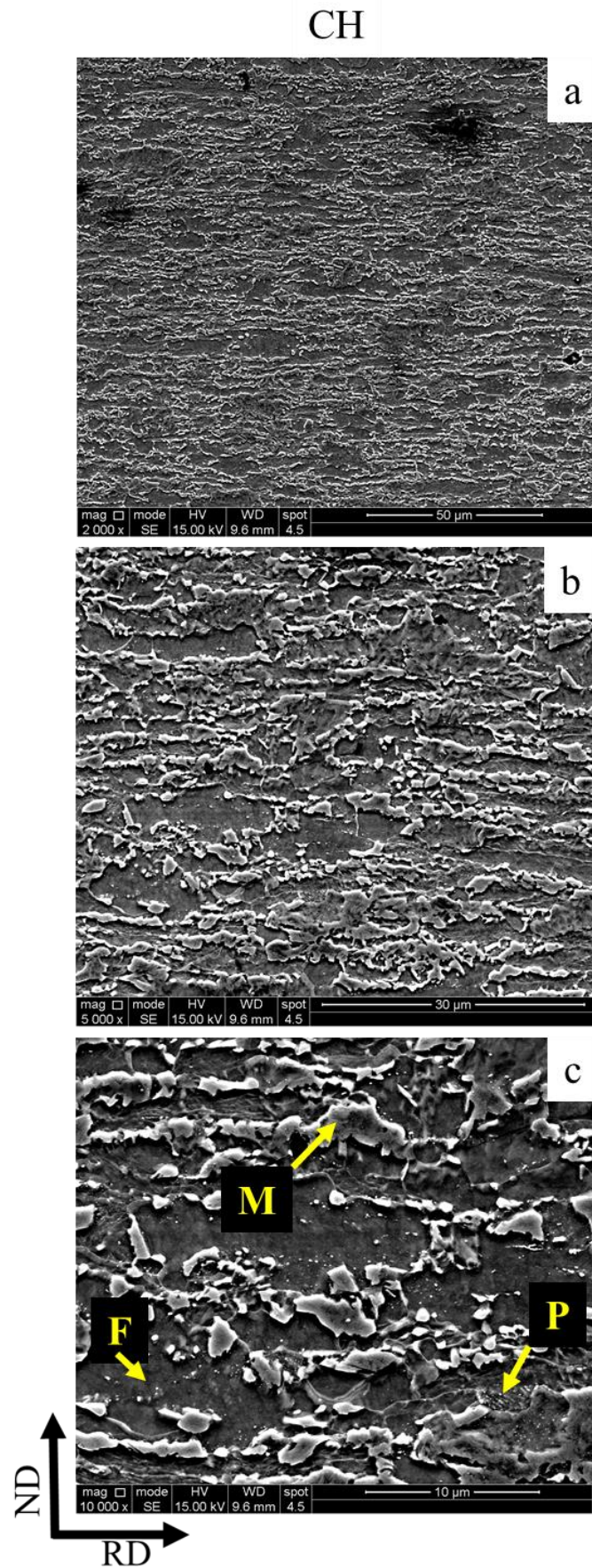


**Figure 8.3.6:** SE SEM image of the CH sample at (a) 2000x magnification, (b) 5000x and (c) 10000x. The microstructure consists of ferrite (F), martensite (M), and pearlite (P).

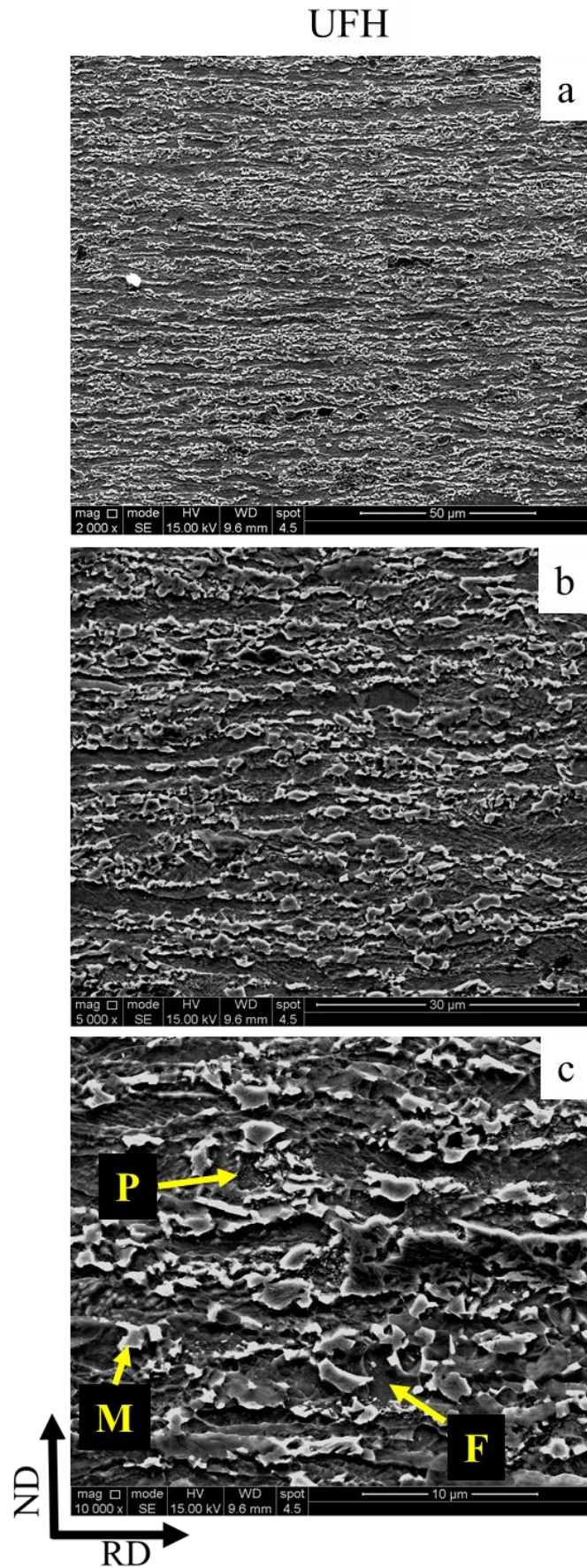


**Figure 8.3.7:** SE SEM image of the UFH sample at (a) 2000x magnification, (b) 5000x and (c) 10000x. The microstructure consists of ferrite (F), martensite (M), and pearlite (P).

### 8.3.3.2. Austenite nucleation

With a closer look at the CH and UFH samples in SEM, two different types of martensite were observed, depending on their position inside the pearlitic colonies or on ferrite grains' interfaces. The position of these martensite islands gives an insight into the  $\alpha \rightarrow \gamma$  transformation mechanism when the heating time is not enough. According to Kaluba [91-93], when the heating rates are high, the transformation that occurs is not controlled by the diffusion of carbon but by the mobility of the interfaces. This applies in UFH, where the high heating rates impede the full dissolution of cementite and thus the carbon diffusion and homogenization of the composition. This creates gradients in the microstructure with areas rich in carbon in close proximity to the pearlitic colonies and areas depleted in carbon when there is no carbon source nearby. According to these, the nucleation of austenite inside the pearlitic colonies (**Figures 8.3.8a, c**) is expected due to the high carbon content. This excess in carbon favors the kinetics of the transformation due to the difference of the Gibbs free energy, as was explained by Savran [56]. Nevertheless, this cannot explain austenite's nucleation between two ferrite grains (**Figures 8.3.8a, d**), where no difference in carbon content is expected. In this case, the driving force for this nucleation derives from the segregation of carbon and other elements on the grain boundaries. As has been reported by Bouzouni et al. [98, 99] and Papaefthymiou et al. [97] via simulation software, segregation of alloying elements on the grain boundaries take place even during UFH, which creates the difference in carbon content to make the austenite nucleation possible according to the Gibbs free energy. Savran [56] also showed that during heating in the temperature range between the  $A_{c1}$  and  $A_{c3}$  temperatures, the maximum carbon content of ferrite is decreasing according to the Fe3C diagram. This rejected carbon also contributes to the local chemical heterogeneity being a driving force for austenite nucleation. As this phenomenon is happening for both slow and ultra-fast heating rates, it can be assumed that it is not affected by the heating rate, although the diffusion and segregation of alloying elements depend on it.



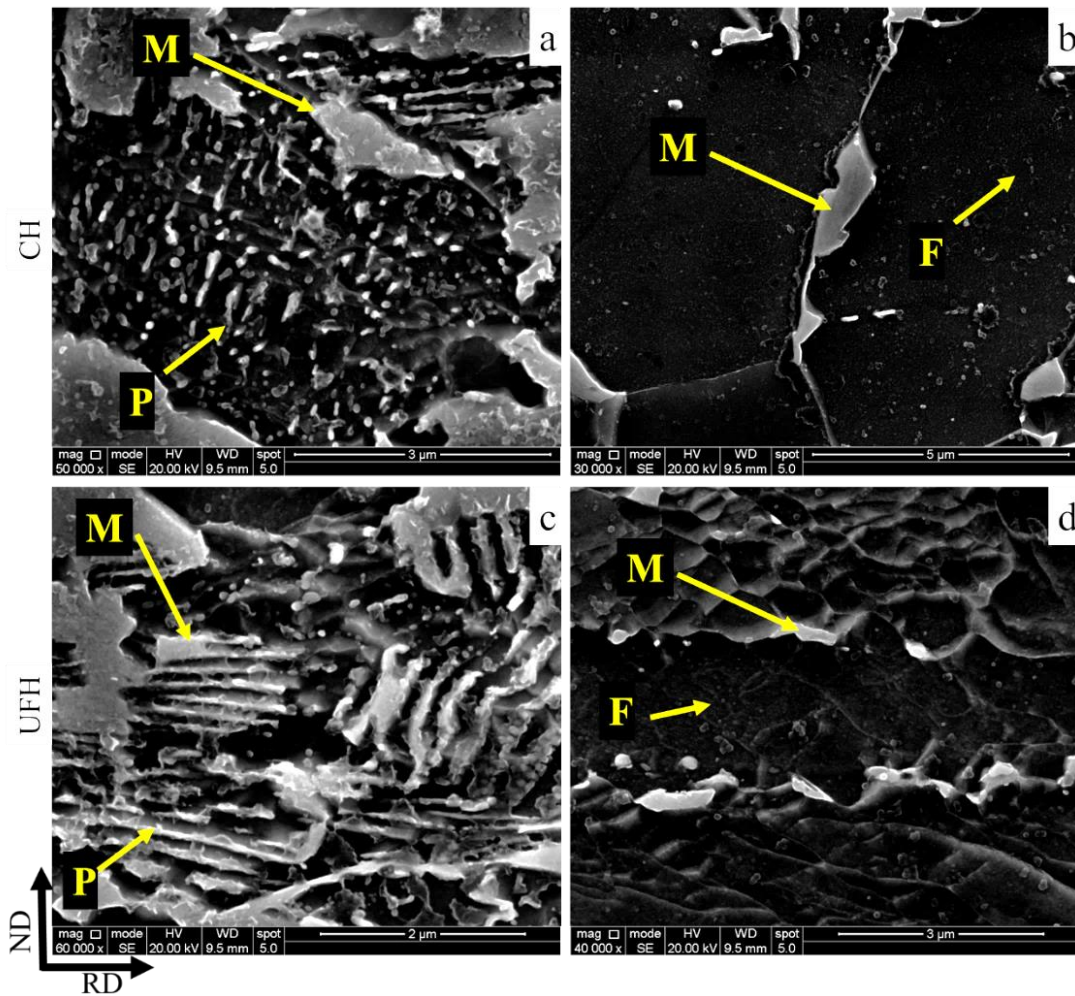


**Figure 8.3.8:** SE SEM images indicating the nucleation sites of austenite from the positions of martensite inside the pearlitic colonies for the CH (a) and UFH (c) samples and also between ferrite grains (b, d) with no apparent carbon source.

### 8.3.3.3. Dissolution of pearlite

The pearlite was also studied under TEM for both samples. Similar to the outcomes of the SEM analysis, undecomposed pearlite is observed in both samples. In the CH sample (**Figures 8.3.9a-c**), pearlite is found in both lamellar and spheroidized morphologies, with the latter prevailing. In the UFH sample (**Figures 8.3.10a-c**), the lamellar form of pearlite is found in a larger fraction than the spheroidized one. This observation can be rationalized based on a shorter heating time during UFH treatment. According to different theories of spheroidization [82], a potential chemical gradient leads to a curvature in the lamellar interface. Atoms move from the curvature of a lamella through diffusion to the flat interfaces of neighboring or the same plates and eventually lead to the lamellar plate's break. The curvature of the plates can be seen in (**Figures 8.3.5b**) for the CH sample. Undissolved cementite is also found in the CH sample, which means that the dissolution needs more time than that given in this treatment. This also means that in the CALH treatment, the dissolution initiates during the soaking stage and not during the heating. Even though the heating time is minimal in the UFH treatment, spheroidization of the lamellas takes place due to the very high energy induced in the system during heating.

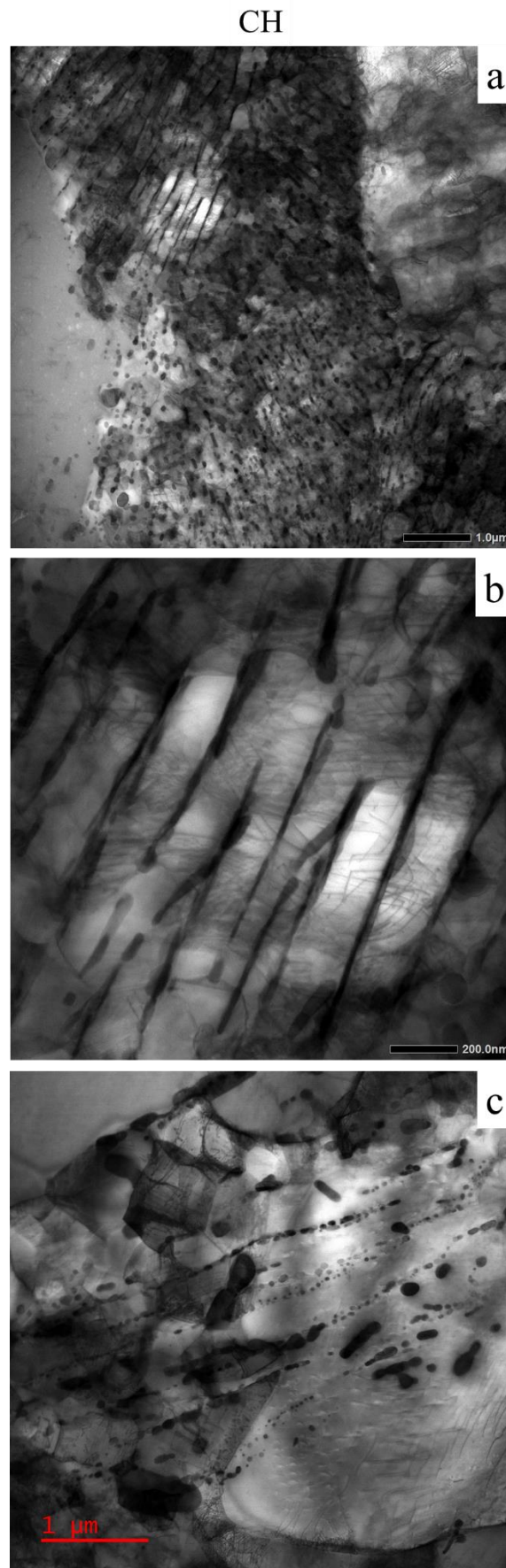


**Figure 8.3.9:** BF TEM images for the CH (a-c) sample indicating the incomplete process of spheroidization of cementite during heating.

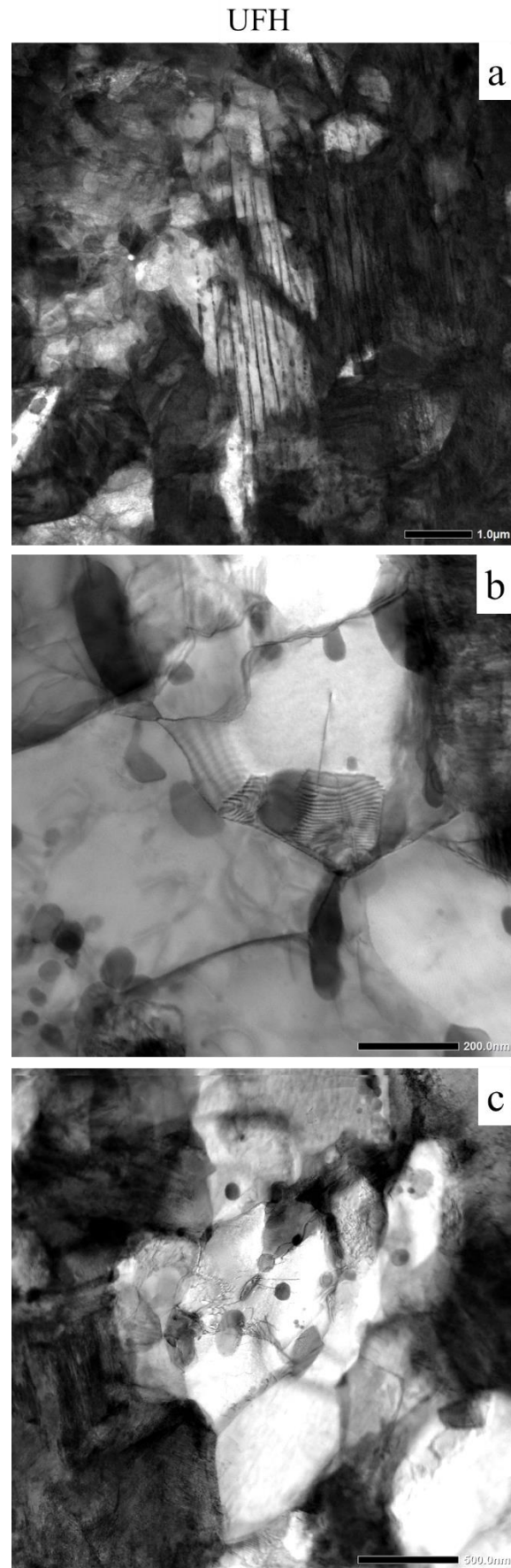


**Figure 8.3.10:** BF TEM images for the UFH (a-c) sample indicating the incomplete process of spheroidization of cementite during heating.

From the EDXS analysis, it is seen that alloying elements such as manganese and chromium are concentrated in the cementite of the microstructure. This is in accordance with the results of Papaefthymiou et al. [85], who predicted the accumulation of these elements in cementite by simulation using Thermocalc and DICTRA software. It is seen from the EDX line scans in **Figures 8.3.12a, b** that the calculated mass % intensity for Cr and Mn is higher in the cementite lamellae and spheres compared to that of the adjacent ferritic matrix. The same was observed for the CH sample in **Figures 8.3.11a, b**. From those figures, it can also be seen that the spheroidization process was more pronounced in the CH samples compared to the UFH sample. **Figure 8.3.12c** shows that the mass % intensity of Cr and Mn was increasing near the grain boundaries of three ferrite grains. The segregation of these elements favor nucleation of austenite as mentioned earlier and, after quenching, martensite. Nevertheless, concerning the slow heating, a homogenization of the topical chemical composition occurs due to the longer heating time, as shown from the EDXS analysis results (**Figures 8.3.11c**) of the CH sample.



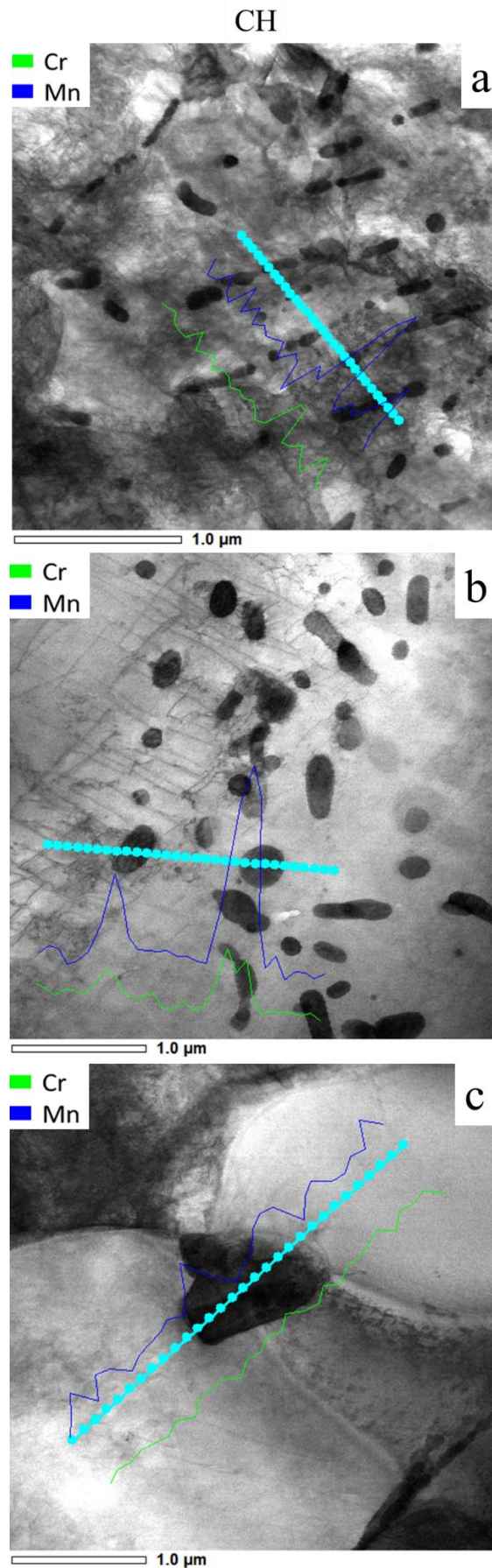


**Figure 8.3.11:** STEM images for the CH sample, including EDS line scans for Cr and Mn along (a) lamellar cementite, (b) spheroidized cementite, and (c) martensite.



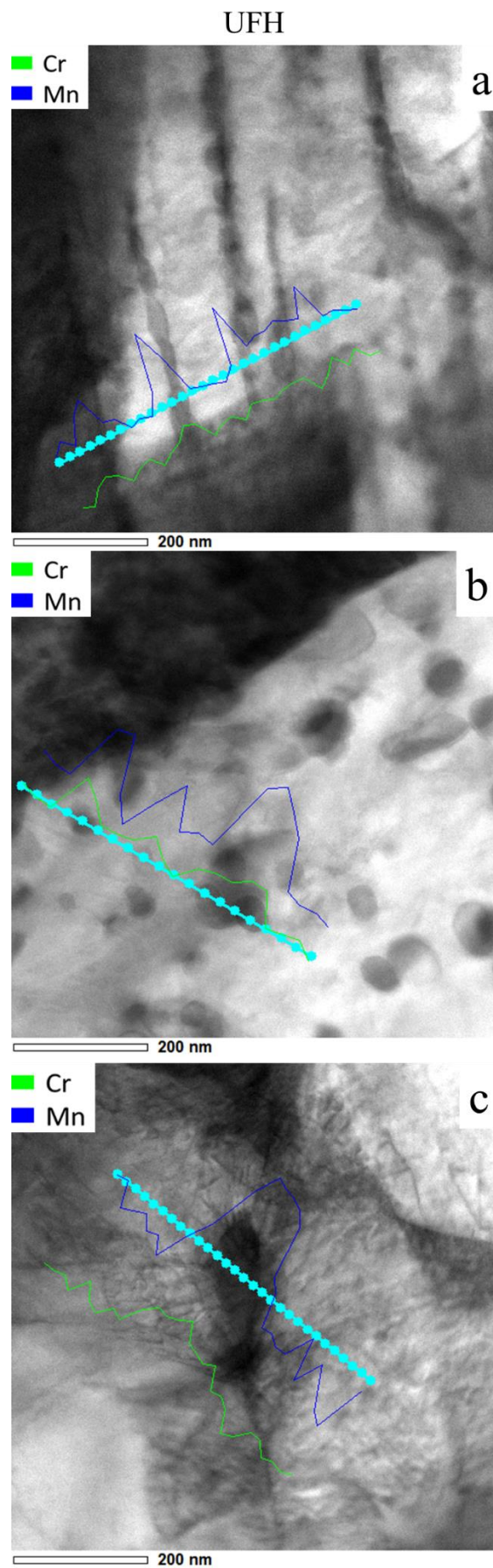


**Figure 8.3.12:** STEM images for the UFH sample, including EDS line scans for Cr and Mn along (a) lamellar cementite, (b) spheroidized cementite, and (c) martensite.

#### 8.3.3.4. Grain size analysis

EBSD was used for the grain size analysis. Three scans for each condition (CALH, CH, and UFH) were obtained with a scan size of  $40\ \mu\text{m} \times 40\ \mu\text{m}$ . For the CALH treatment, the scans included an average of 3305 grains, for the CH treatment, an average of 7059 grains, while the scans for the UFH treatment included an average of 9818 grains. The difference in the recognized grain number is due to the different average size of the grains in each condition. The ARPGE 2.4 software, developed by C. Cayron [130] and was used in automatic mode to plot the grain boundary (GB) maps of the reconstructed prior austenite grains (PAGs) for the three samples and are shown in **Figures 8.3.13a, c, e**. For the UFH (**Figure 8.3.13e**), these PAGs combined with the pro-eutectoid ferrite have a significantly smaller size than the CALH and CH samples. In particular, the average calculated grain area for the PAGs was  $79.14\ \mu\text{m}^2$  for the CALH,  $71.87\ \mu\text{m}^2$  for the CH, and  $64.43\ \mu\text{m}^2$  for the UFH. The difference in the PAG grain sizes is attributed to the different heating times used in each treatment. In CALH, where there is soaking, the PAGs have more time to grow.

Nevertheless, an error should be considered in these calculations as the ferrite's size is also measured. After quenching, the final microstructure had an average grain area of  $32.79\ \mu\text{m}^2$  for the CALH,  $17.27\ \mu\text{m}^2$  for the CH, and  $12.61\ \mu\text{m}^2$  for the UFH (**Figures 8.3.13b, d, f**). The reason for these smaller austenite grains is most likely that austenite nucleates at the interface of undissolved cementite with ferrite and at ferrite/ferrite interfaces, therefore smaller PAGs lead to an increase in the grain boundaries and hence, more martensite nucleation sites and finer microstructure.

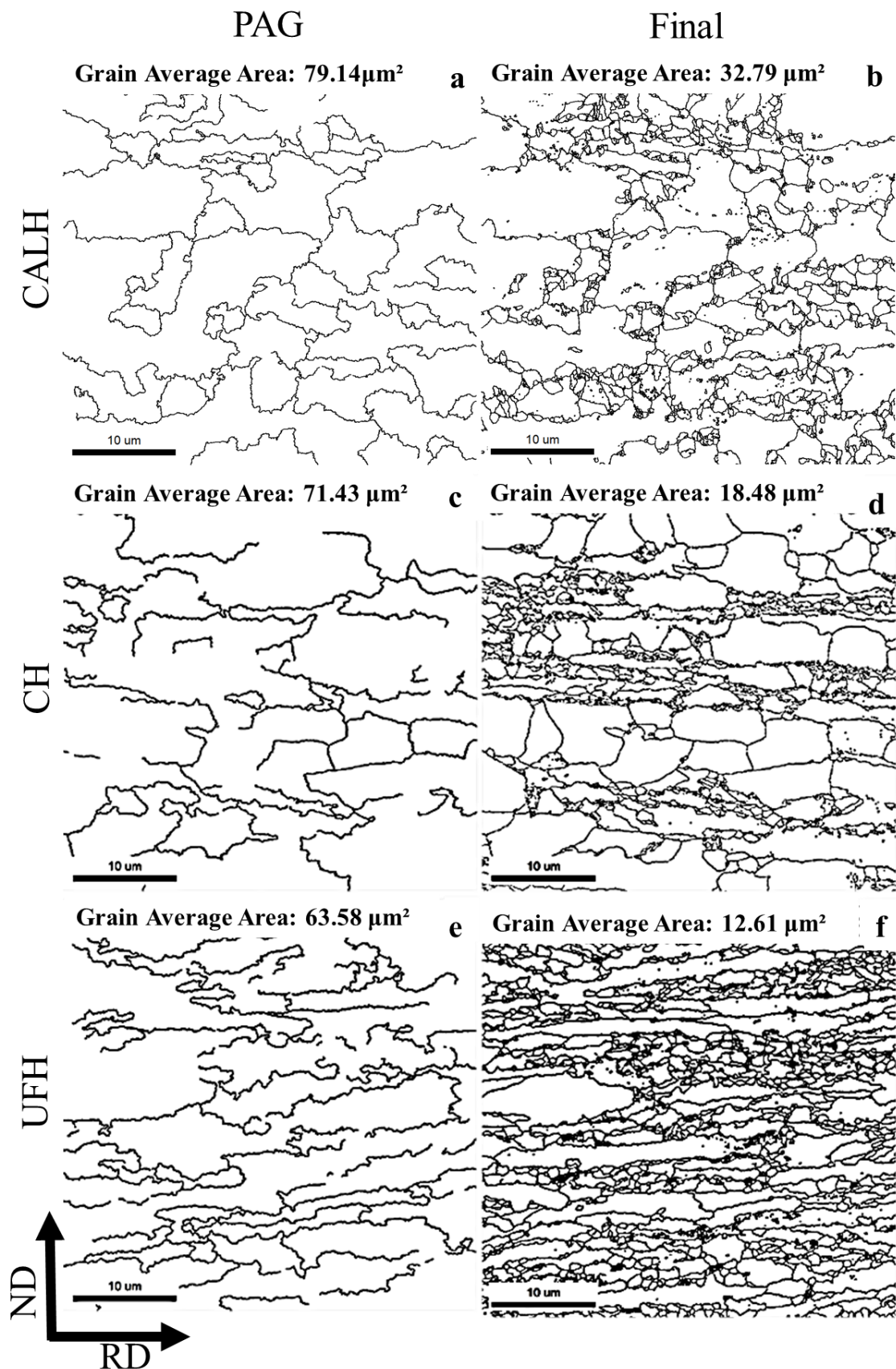


**Figure 8.3.13:** EBSD Grain boundaries maps for the PAGs and final microstructure respectively of the CALH (a,b), CH (c,d), and UFH (e,f) samples. Step size: 50 nm.

Moreover, undissolved pearlite–spheroidized cementite has a pinning effect, thus, impeding further the growth of austenite grains by impeding the movement of austenite interfaces. This does not take place in the CALH sample, where the cementite has been fully dissolved. Thus, due to the absence of undissolved cementite and higher heating and soaking times, the parent austenite grains can grow larger in this sample. On the other hand, in the CH and UFH samples, spheroidized or lamellar cementite in the microstructure impedes the movement of the PAG boundaries and hinders its growth. This effect can be seen in **Figure 8.3.14a** for the CH sample and **Figure 8.3.14b** for the UFH sample. In the former, the disintegration and spheroidization of pearlite are visible with very fine ferrite grains in between. The dissolution of pearlite is even less pronounced in the latter, and cementite partly maintains its lamellar form. After quenching, the microstructural constituents mostly had an average grain area of  $17.3 \mu\text{m}^2$  for the CH and  $12.6 \mu\text{m}^2$  for the UFH sample.

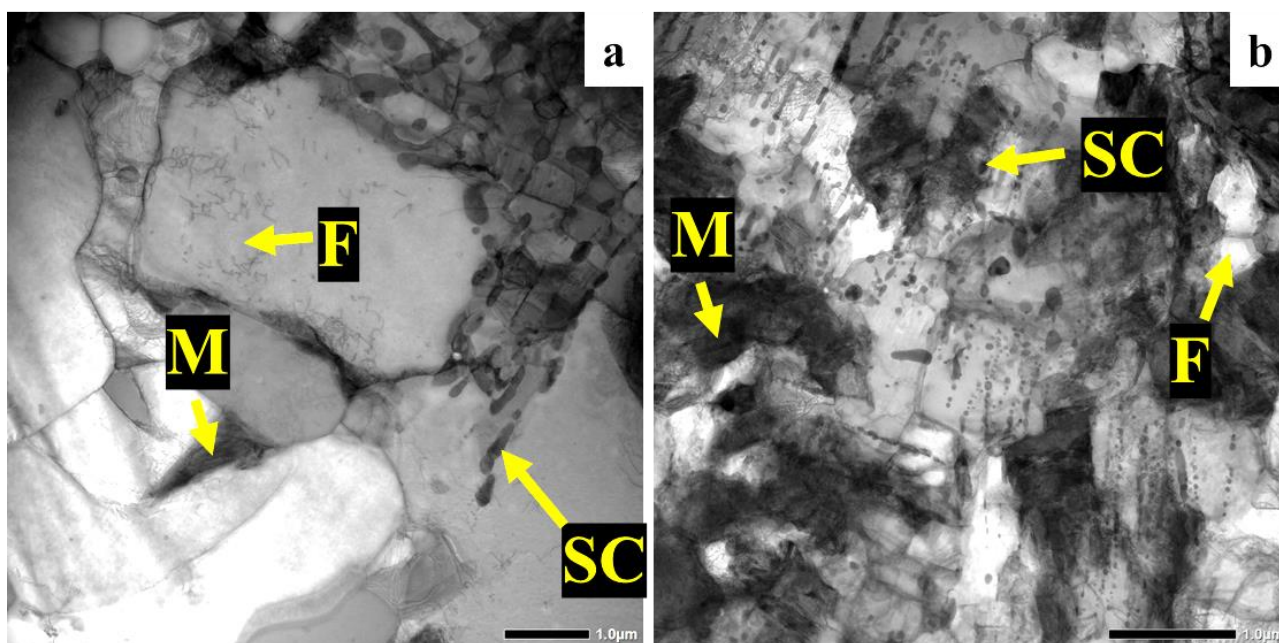


**Figure 8.14:** BF TEM images of the CH (a) and UFH (b) samples indicating the pinning effect of undissolved cementite on the movement of grain boundaries and thus the growth of austenite.

### 8.3.3.5. Retainment of austenite

From XRD (**Figures 8.3.15a-c**) and EBSD analysis, small fractions (<1 %) of retained austenite were also observed in the CH and UFH samples. This retainment of austenite is possible due to the heterogeneity in the topical chemical composition. Specifically, as mentioned before, due to the short heating times, the dissolution of cementite is not completed, and the diffusion of carbon is limited throughout the microstructure. Therefore, areas near or inside the undissolved pearlite colonies are expected to have higher carbon contents than ferritic areas far from any carbon source. This higher carbon content decreases the  $M_s$  temperature locally and can make the retainment of austenite possible. This is confirmed from the EBSD phase maps (**Figure 8.3.16a,b**), where the retained austenite (green) appears inside martensitic or pearlitic areas.

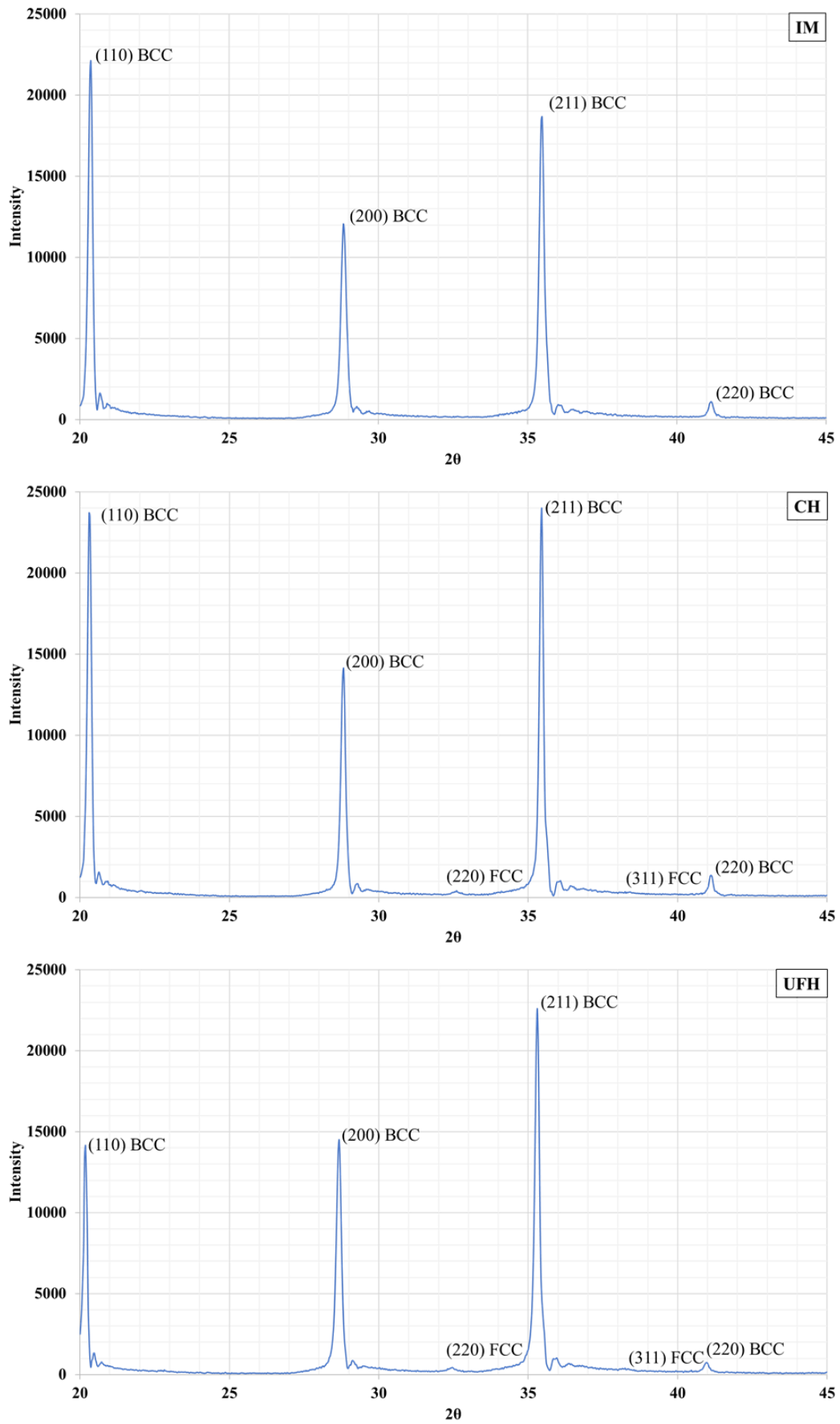


**Figure 8.3.15:** XRD analysis of the (a) Initial Material, (b) Conventional Heating sample, and (c) Ultra-Fast Heating sample. In the CH and UFH samples, a small fraction of retained austenite (FCC) is found.



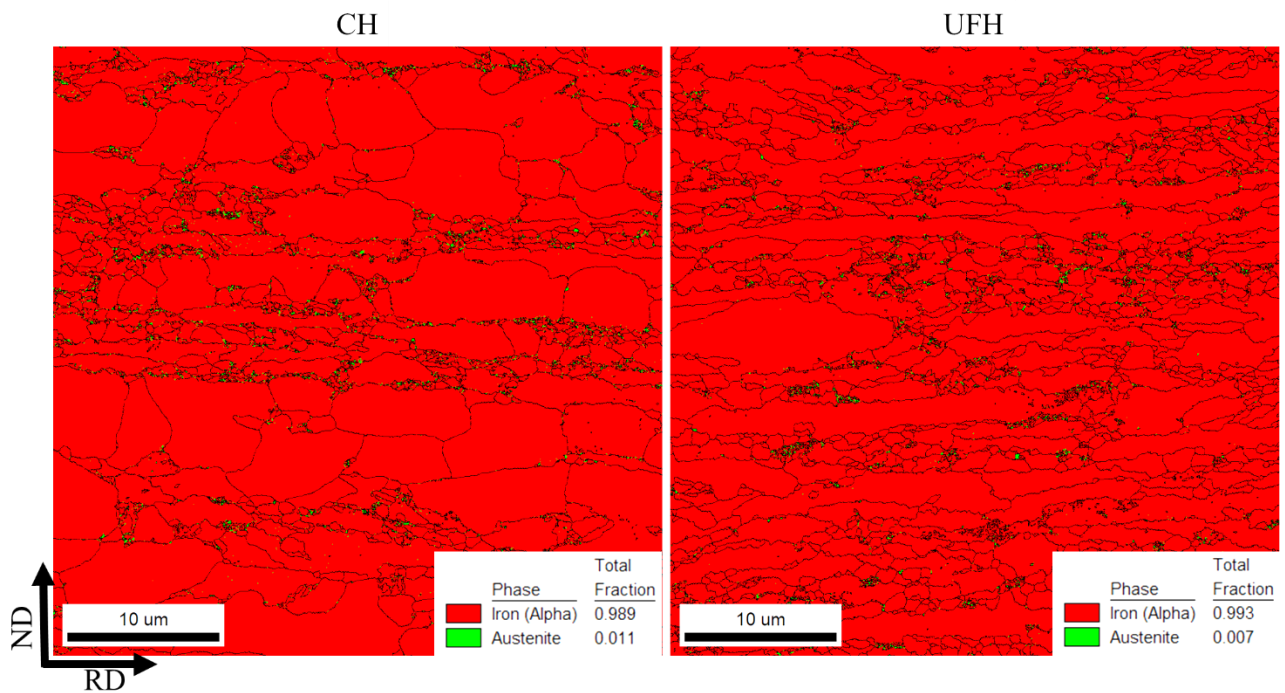


**Figure 8.3.16:** EBSD phase maps of the CH (a) and UFH (b) samples showing small fractions of retained austenite in both samples. Step size: 50 nm.

To further analyze this, simulations were performed in DICTRA [142] (**Figures 8.3.17a-d**). A spheroidized cementite was assumed in these simulations with size 5 nm and 6.67 % of carbon content. In the simulations, the content of different alloying elements was calculated according to the distance from the cementite. As it seems, the contents of C and Mn drop with increasing distance from the cementite (**Figures 8.3.17a, c**). On the other hand, elements such as Cr and Mo (**Figures 8.3.17b, d**) tend to segregate on the interface between  $\theta$  and  $\alpha$ . This is explained as the solute drag effect and the accumulation of these elements on the interfaces, further impeding cementite dissolution. In the case that there is no apparent carbon source (cementite), the results are shown in **Figures 8.3.18a-d**. According to these results, the carbon content (**Figure 8.3.18a**) in austenite is above the average carbon content of the material, which is explained by the higher solubility of carbon in austenite as the transformation is not completed. The manganese content is higher in austenite than ferrite as manganese is an austenite stabilizer alloying element (**Figure 8.3.18b**). Chromium content in austenite tends to accumulate near the  $\gamma/\alpha$  interface and decrease slightly near the  $\gamma/\alpha$  in ferrite (**Figure 8.3.18c**), dictating that chromium content in ferrite must decrease in order to satisfy the local equilibrium condition meaning that chromium diffuses from ferrite to austenite. Molybdenum, similarly to chromium, is a ferrite stabilizer. Therefore, it has a higher solubility in ferrite compared to austenite. Molybdenum content near the  $\gamma/\alpha$  tends to decrease, showing that the diffusion is achieved from austenite to ferrite. The results of the simulations are proven by EDS on TEM, as seen in **Figure 8.3.19a**. In this figure, a line scan was taken from the center of a spheroidized cementite. It appears that the mass% intensity of Mn (purple line) is decreasing with increasing distance from the cementite. Additionally, as shown from the yellow line for Cr, the mass% intensity has a peak on the interface between the cementite and the ferritic matrix, as was predicted from the simulations. Due to its small fraction, retained austenite could not be found in TEM, but its presence

is shown in the EBSD phase map **Figure 8.3.18b** with green color whereas the axis angle  $\langle 112 \rangle 90^\circ$ , which is characteristic between  $\alpha$  and  $\gamma$  is shown in blue color. The IQ map is also given to predict the location of the retained austenite, which is inside the expected pearlitic areas. This is expected as these areas are enriched in carbon due to the short diffusion distance, which leads to a decrease in the  $M_s$  temperature.

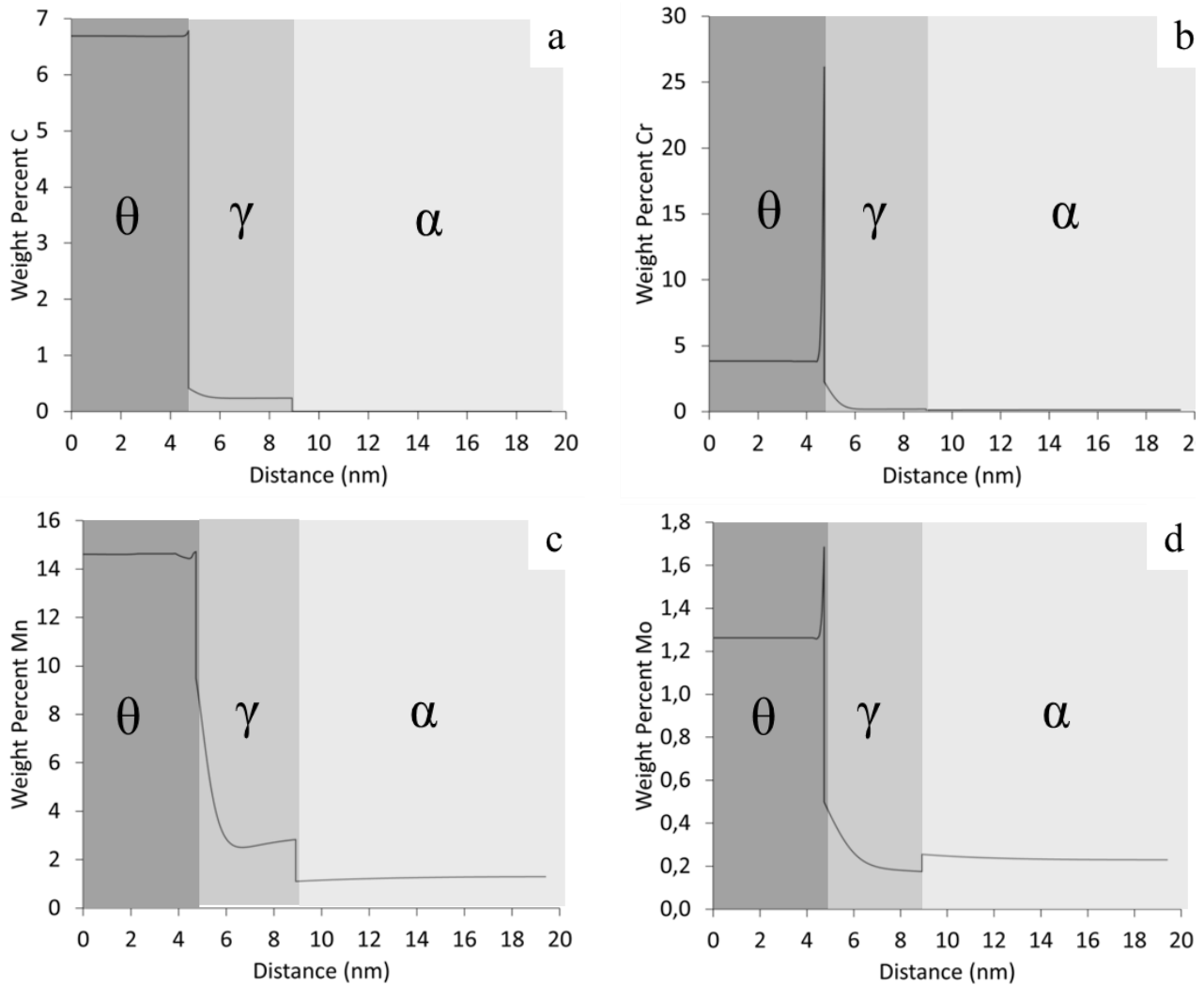


**Figure 8.3.17:** Composition profiles for (a) C, (b) Cr, (c) Mn, (d) Mo during ultra-fast heat treatment in cementite – ferrite system at  $T_{peak}$  temperature [142]. The phase between cementite ( $\theta$ ) and ferrite ( $\alpha$ ) is the newly formed austenite ( $\gamma$ ).

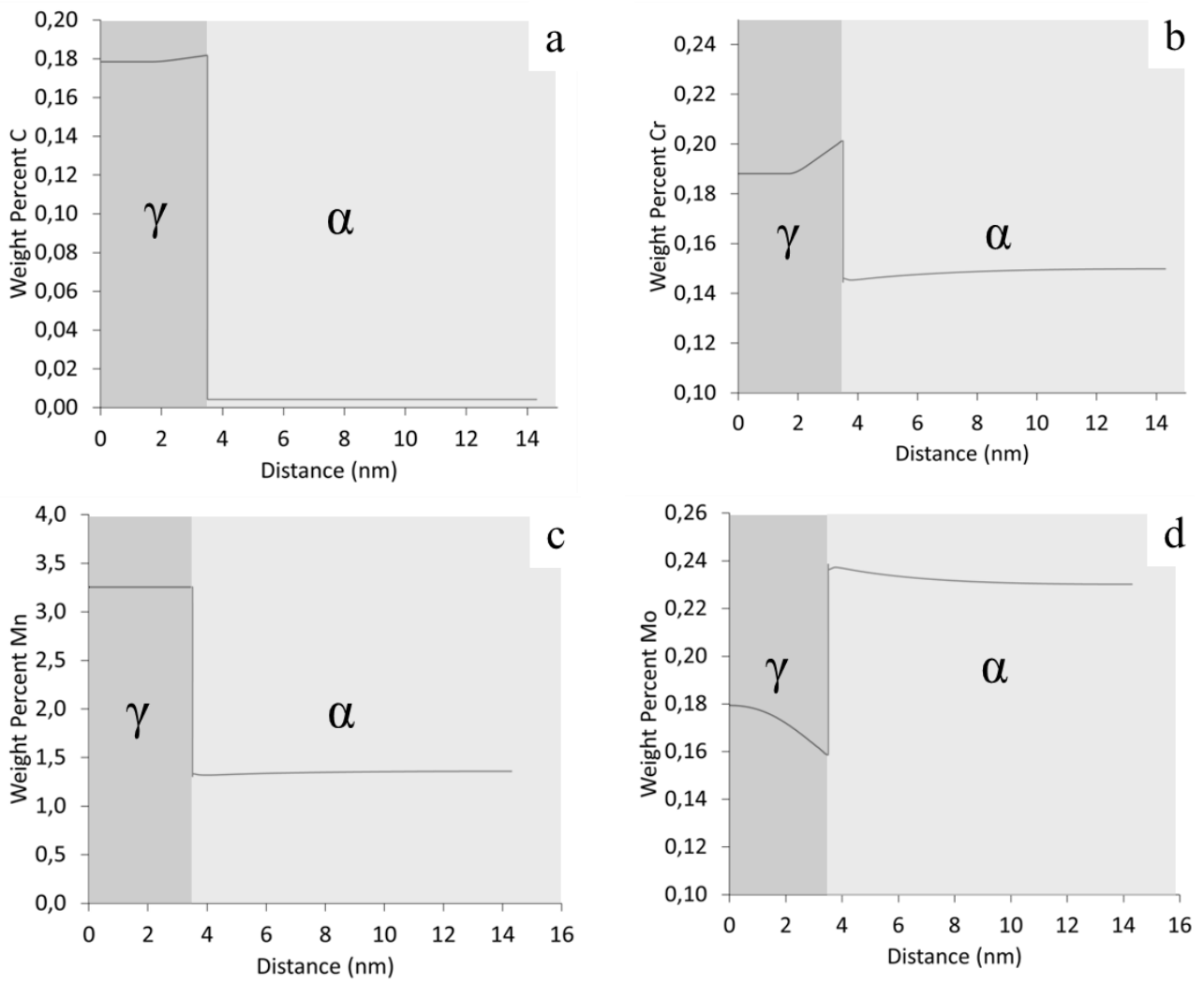


**Figure 8.3.18:** Composition profiles for (a) C, (b) Cr, (c) Mn, (d) Mo during ultra-fast heat treatment in ferrite/ferrite ( $\alpha/\alpha$ ) system at  $T_{peak}$  temperature [142]. The second phase formed is austenite ( $\gamma$ ).

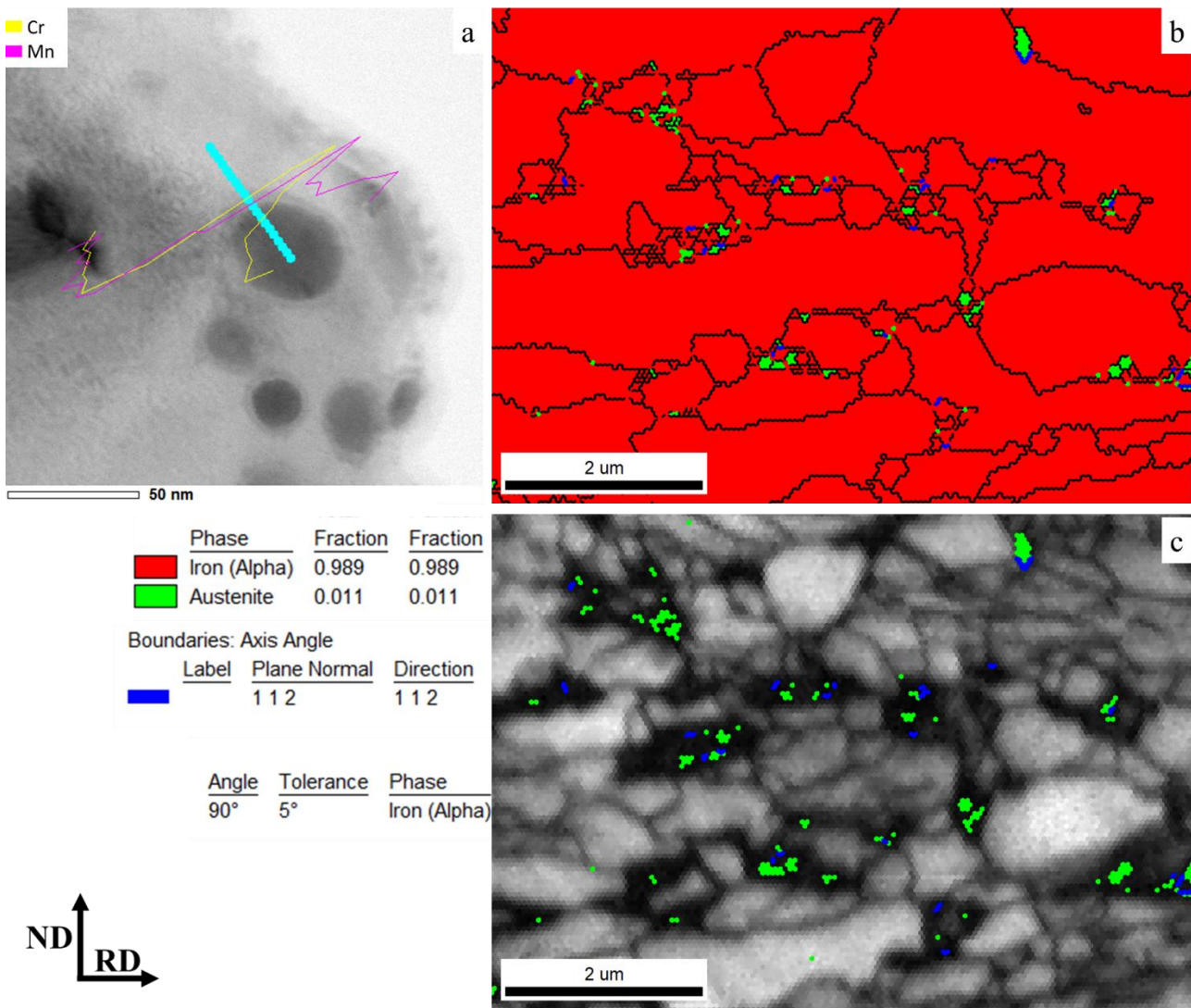


**Figure 8.3.19:** (a) EDS on TEM confirms the DICTRA results on the segregation of Cr and Mn on the interfaces between  $\theta$ - $\gamma$ - $\alpha$ . (b) Phase Map (PM) of the scanned area where the retained austenite is shown with green color. For further certainty, the KS relationships for  $\langle 112 \rangle 90^\circ$  between ferrite and austenite are shown in blue. (c) Image Quality (IQ) map of the same area where the retained austenite is highlighted. The location of the retained austenite is shown to be inside low image quality areas that correspond to martensite or pearlite. Step size: 50 nm.

### 8.3.3.6. Recovery, recrystallization, and texture analysis

From the SEM analysis in the CH and UFH samples, deformed ferrite grains were observed in both samples (**Figures 8.3.20a, b**). This means that the recrystallization process has not been completed in any of the treatments. Nevertheless, the fraction of recrystallized ferrite (RexF) grains in the microstructure differs in the two samples, with the UFH sample consisting of a much smaller fraction of RexF. From the SEM, it is also observed that in the UFH sample, the dislocations maintain the rolling direction, indicating that the recrystallization process is at a very early stage.

Further analysis was conducted with EBSD. The grain average misorientation (GAM) map (**Figures 8.3.20c**) as well as the kernel average misorientation (KAM) [37] map (**Figures 8.3.20d**) were plotted. The former shows the fraction of misorientations inside each grain, while the latter shows the local orientation gradient

due to dislocations present in the scanned area. Recrystallized ferrite grains should have low average misorientation and appear in blue, while the recovered ferrite and martensite appear in green. Local misorientation can be characterized using a misorientation Kernel approach. For a given point, the average misorientation of that point with all of its neighbors is calculated with the provision that misorientations exceeding some tolerance value (maximum misorientation) are excluded from the averaging calculation. Therefore, the KAM map can offer a qualitative distribution of the material's strain based on the local misorientations that occur due to strain. During recrystallization, these dislocations mobilize, forming new grains, and thus the recrystallized ferrite appears free of dislocations. Before the completion of this process, these grains can be located from the dislocations that surround them before they turn into grain boundaries. According to Peranio et al. [143], the most important driving force for recovery and recrystallization is the reduction of strain energy within the ferrite grains, which occurs through a reduction of dislocation density. In addition, the low angle grain boundaries (LAGB) that are expected in recovered ferrite were included in the GAM map with red color to further distinguish the two types of ferrite. Concerning the CALH treatment (**Figures 8.3.21a, b**), 100 % completion of the recrystallization process is expected due to the high heating time. From the KAM map (**Figure 8.3.21b**), it is seen that the dislocation density is high at the martensitic areas and on the boundaries with ferrite. This is why the average misorientation appears higher in this sample's GAM map (**Figures 8.3.21a**). In this sample, the fraction of martensite is 44 %. It was also calculated that the recrystallization of ferrite was much more pronounced in the CH sample than in the UFH sample. In specific, it was calculated from the IQ and GAM maps that the area fraction of recrystallized ferrite for the CH sample was 77.4 %, while the fraction of recovered ferrite was 8.6% (**Figures 8.3.21c, d**). The remaining fraction (14%) was considered to be martensite and pearlite (cementite). In the case of UFH, the fraction of recrystallized ferrite was calculated as 23.7%, of recovered ferrite as 54.5 % (**Figures 8.3.21e, f**), and of martensite plus pearlite as 21.8%. These fractions are summarized in **Table 8.3.3**. From these calculations, it is seen that the fraction of martensite in the UFH sample was somewhat higher than that in the CH sample. This result contradicts previous research [97, 122, 123], where it was supported that the increase of the heating rate leads to an increase in the  $A_{c1}$  temperature, and thus, less martensite is expected in the microstructure of the UFH sample than in the CH sample. Though, the difference can be explained by the lack of recrystallization of ferrite in the UFH sample. According to [141], the phase transformation in deformed ferrite is faster than in recrystallized ferrite as it provides an increased number of nucleation sites for austenite formation. The deformation also reduced the nucleation energy barrier between  $\alpha/\gamma$  interfaces by increasing the strain energy. This strain energy is the driving force for both recrystallization and phase transformation [144]. Finally, the deformed ferrite contains a larger number of dislocations and grain boundaries. These lead to a dislocation pipe diffusion of carbon, which favors the phase transformation of austenite thermodynamically [145]. Cerda [96] and Meshkov [100] related this phenomenon to the spheroidization of cementite that takes place in CH. Thus, the higher fraction of martensite in the UFH sample's microstructure can be explained even though the transformation temperatures have shifted to higher levels than those expected in equilibrium conditions.



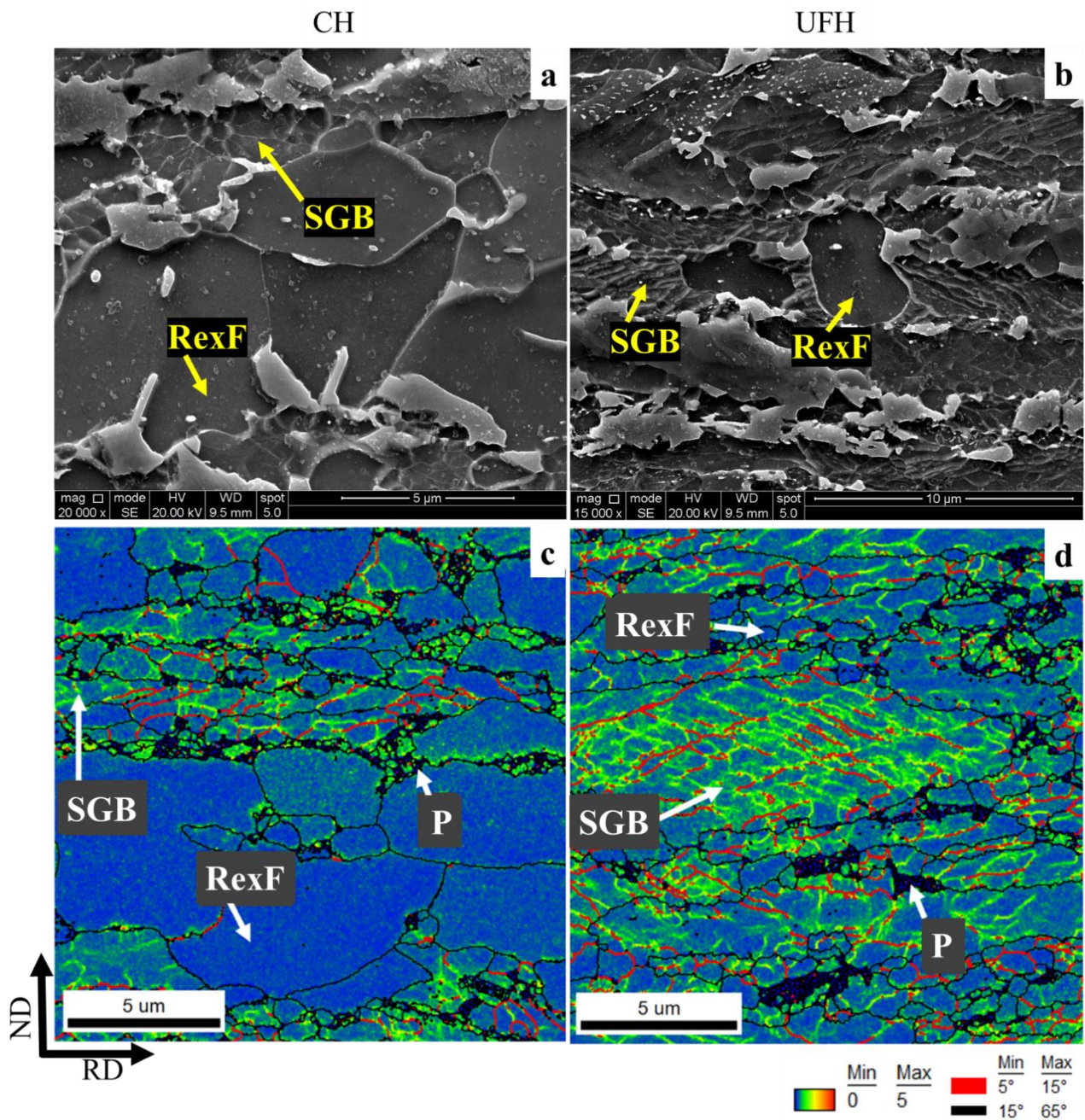


**Figure 8.3.20:** (a) SE SEM image of the CH sample indicating the existence of large recrystallized ferrite (RexF) grains alongside deformed ferrite grains that contain sub-grain boundaries (SGBs). (b) SE SEM image showing that the fraction of deformed ferrite is much larger in the UFH sample. (c) KAM EBSD maps for the CH and (d) UFH samples showing the result of the dislocations on the microstructure (green) and the formation of low angle grain boundaries (red). Step size: 50 nm.



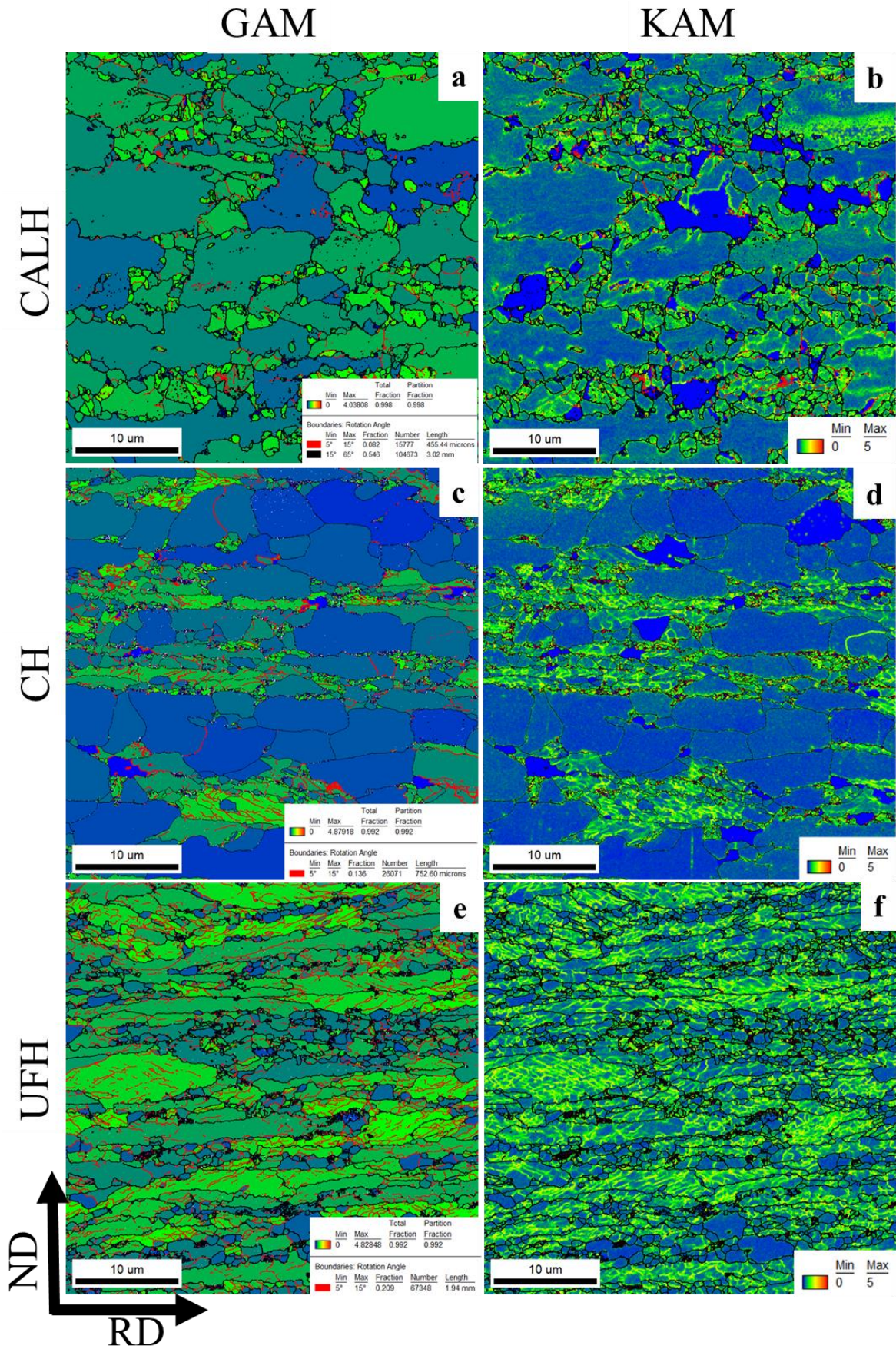


Figure 8.3.21: GAM and KAM EBSD maps for the (a,b) CALH, (c,d) CH and (e,f) UFH samples. These maps indicate the density of dislocations and thus the level of deformation in ferrite and martensite. Recrystallized ferrite grains are virtually free of dislocations and thus appear in blue. Step size: 50 nm.

**Table 8.3.3:** The fractions of recrystallized ferrite, non-recrystallized ferrite, and martensite/cementite, as calculated from the GAM and KAM maps.

Area fraction%	CH	UFH	CALH
Recrystallized ferrite	77.4 %	23.7 %	56 %
Non-recrystallized ferrite	8.6 %	54.5 %	0 %
Martensite/Cementite	14 %	21.8 %	44 %

Further analysis of the recovery and recrystallization of ferrite was performed using the TKD method. From the maps in **Figure 8.3.22c**, it appears that during the heating of the CH sample, the dislocations move and start to accumulate, forming Low Angle Grain Boundaries (LAGBs) shown in red lines. With increased heating time (i.e., slower heating rate), the recovery and recrystallization phenomena can take place, and these boundaries are expected to become High Angle Grain Boundaries (HAGBs) (black lines) in order to form new grains with lower strain internal energy and free of dislocations. From the Inverse Pole Figure (IPF) map of **Figure 8.3.22e**, it appears that these dislocation ‘walls’ are responsible for orientation gradients within a single grain. This phenomenon is called polygonization. The case is not the same for the UFH sample. In these maps, martensite was removed as it reached an image quality lower than 0.1 and appeared as black areas in **Figures 8.3.22b, d, f**. In this case, the dislocation density was high in the ferritic grains neighboring to martensite grains. This is expected due to the difference in the hardness between martensite and ferrite [124]. The ‘walls’ that appear in the CH sample were also not observed in the UFH sample. This means that, after heating with very high rates, the dislocations were not affected, indicating that recovery and recrystallization of ferrite were impeded locally in some areas.



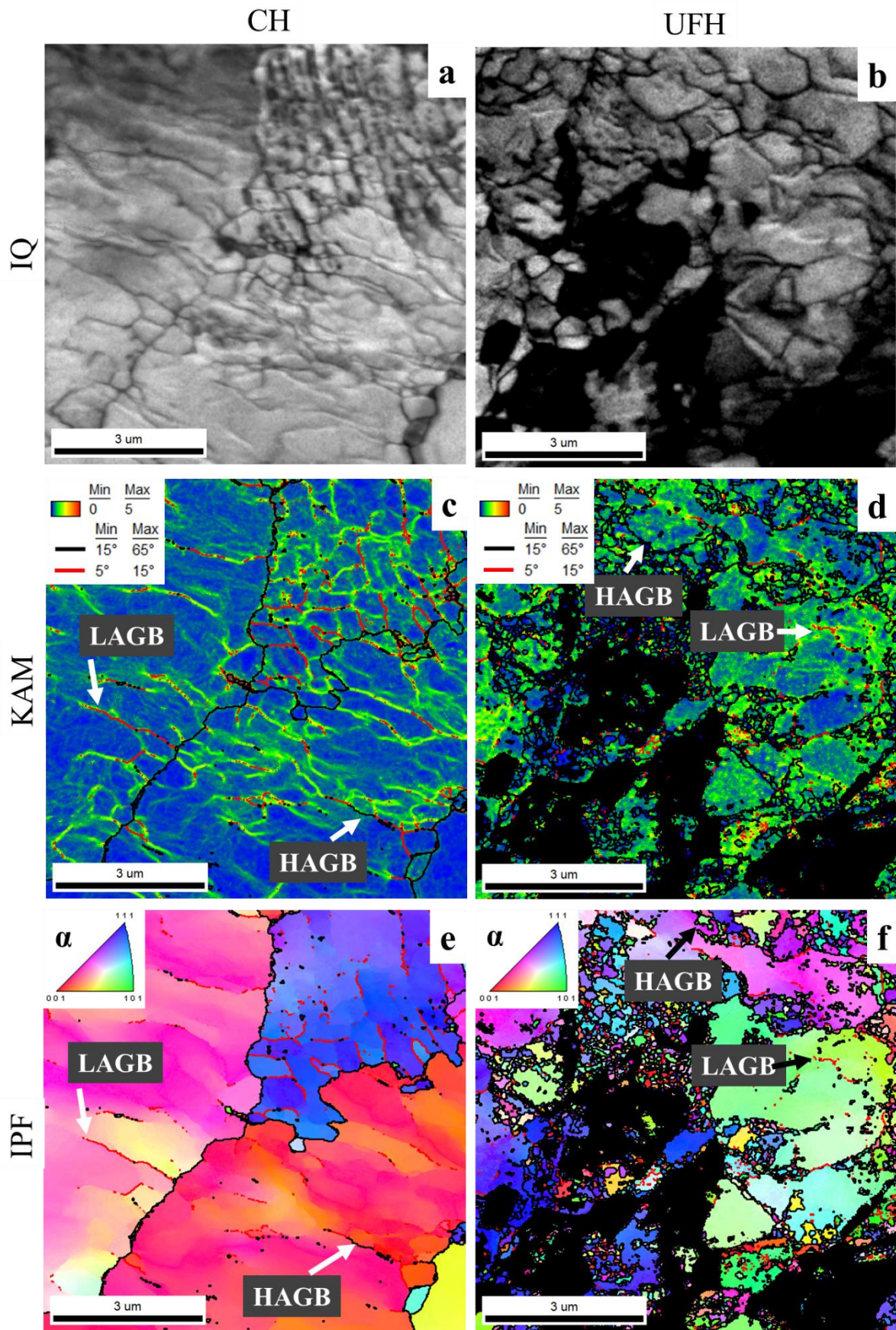


**Figure 8.3.22:** TKD IQ maps for the (a) CH and (b) UFH samples. (c,d) KAM maps of the same areas indicating the density of dislocations (green) and the formation of LAGBs (red). (e,f) IPF maps of the same areas indicating misorientations inside the grains due to the formation of dislocation walls. Step size: 20 nm.

EBSD analysis was also performed to study the effect of UFH treatment on the texture and recrystallization of the steel. In **Figure 8.3.23**, the most important body-centered cubic (BCC) texture components in the  $\varphi_2 = 45^\circ$  section of Euler space are shown next to the Orientation Distribution Function (ODF) maps of the cold-rolled initial material (IM), the CALH, CH, and UFH samples. As it appears, the ODF map of the UFH sample is slightly different from that of the initial material (IM). The components of the cold-rolled material have remained unaffected during UFH. On the other hand, the ODF map of the CH appears quite different than those of the IM and the UFH sample. The main reason for this is the recrystallization of ferrite that takes place on a much larger scale during conventional heating. As it was mentioned by Cerda [96], during UFH, the recrystallization of ferrite takes place simultaneously (overlaps) with the phase transformation. Therefore, the main fraction of ferrite maintains its cold-rolled texture. For the CALH sample, the RD and ND fibers are still visible, but the overall texture is more similar to that of the CH sample due to the high fraction of RexF. Main components, such as the  $(0\ 0\ 1)[1\ 1\ \bar{0}]$  and the  $(0\ 0\ 1)[1\ \bar{1}\ \bar{0}]$ , remain unaffected during UFH as they are frequently present and show a maximum frequency in the texture of both the IM and the UFH sample. The story is similar for components on the ND fiber such as the  $(5\ 5\ 4)[2\ 2\ 5]$ ,  $(1\ 1\ 1)[1\ 2\ \bar{1}]$  and  $(1\ 1\ 1)[1\ \bar{1}\ \bar{2}]$  that appeared in high frequency in the texture of all three samples.

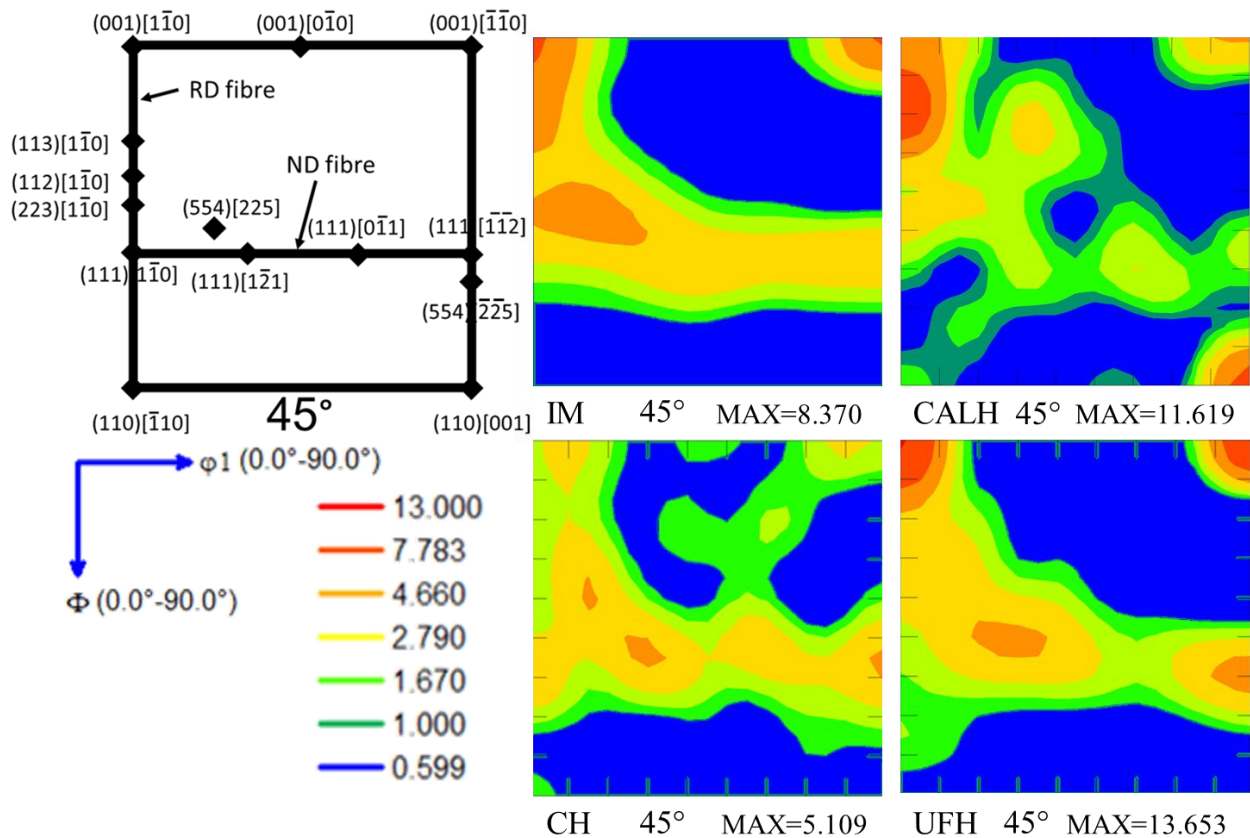


**Figure 8.3.23:** Most common components of the Euler space alongside the ODF maps for the IM, CALH, CH, and UFH samples.



### 8.3.3.7. Tensile properties and hardness

To have complete knowledge of the effect of UFH on DP steels, tests were conducted to check the mechanical properties. Specifically, the micro-hardness and tensile tests were performed. During the tensile tests, the main issue was that with the Gleeble, the homogeneously heated zone was not large enough to cover the whole gauge length of a standard tensile sample. Therefore, smaller tensile samples were cut, in ‘dog-bone’ shape. In order to determine the homogeneously heated zone, the micro-hardness was measured along the length of the samples. As shown in **Figures 8.3.24a, b**, the homogeneously heated zone for the CH is around 15 mm, and for the UFH, approximately 10 mm in length. The deviation in these two curves is due to the constituents (martensite, ferrite) that affect the hardness. It is also observed that the hardness of the CH sample decreases due to the high fraction of recrystallized ferrite, which is expected to have decreased hardness. According to the aforementioned, the tensile samples shown in **Figure 8.3.25a** were cut with gauge length 8 mm, which is smaller than the homogeneously heated zone. To study the material's isotropy, the tensile samples were cut at different angles to the cold rolling direction, at  $0^\circ$ ,  $45^\circ$ , and  $90^\circ$ , as shown in **Figures 8.3.25b-d**, respectively.

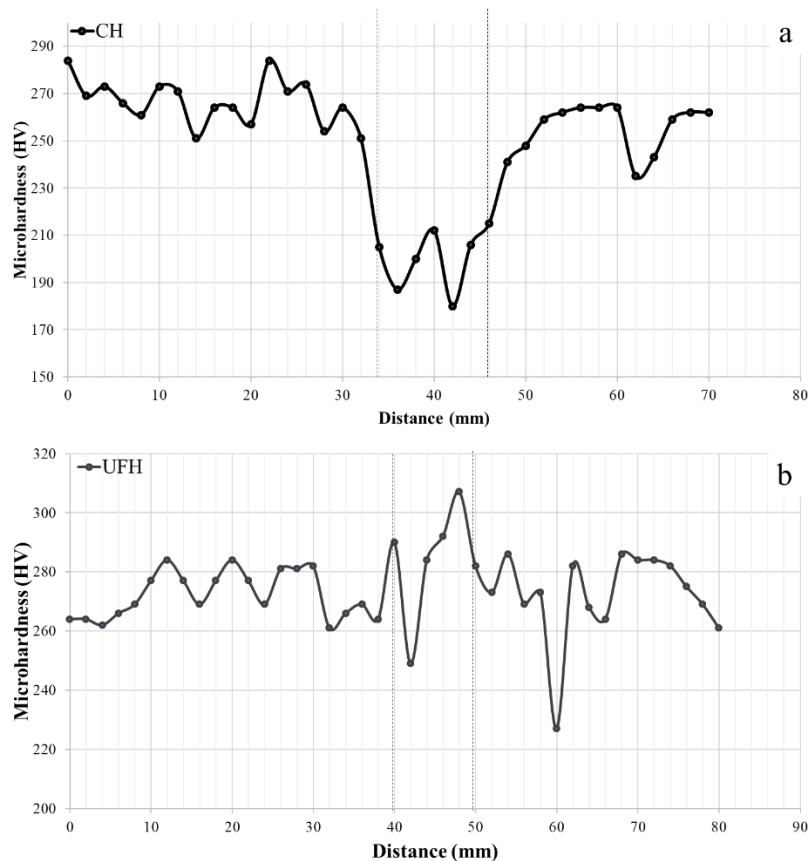


**Figure 8.3.24:** Micro-hardness profile of the (a) CH and (b) UFH samples indicating the homogeneously heated zones.

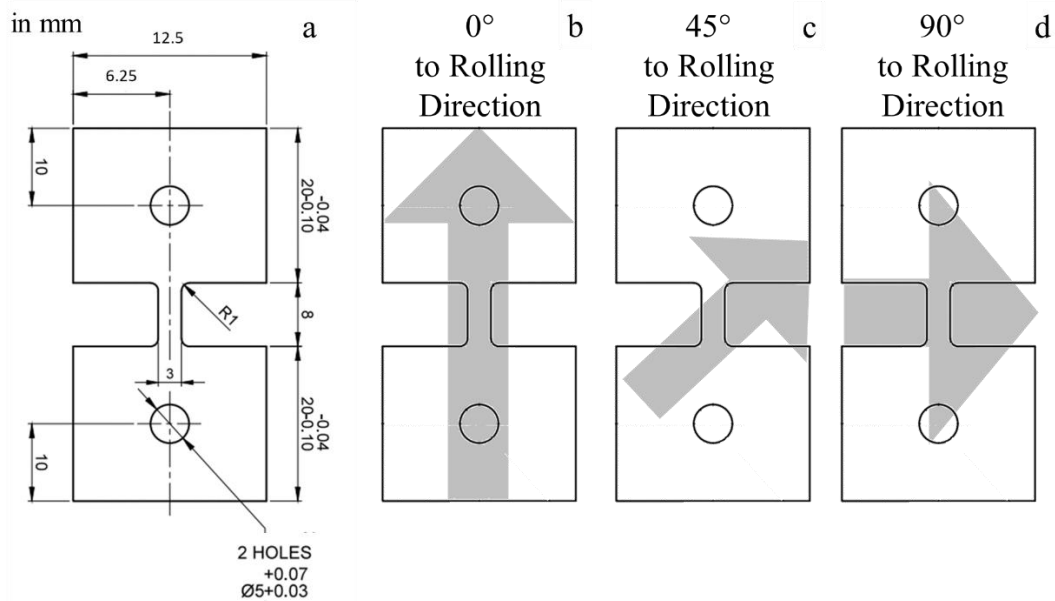


**Figure 8.3.25:** (a) The dog-bone tensile sample dimensions and their (b-d) direction in comparison to the rolling direction (grey arrows).

The samples were placed in the tensile machine with pin holders using the holes of the samples. The strain rate that was selected was 2.4 mm/min (0.007). Three samples per condition were tested to get the average properties. Tensile tests were also performed for the CALH samples, but due to manufacturing problems and lower hardness, the fracture occurred outside the gauge length, and therefore, the results were not included in the study. From the standards, the tensile properties of the initial material were measured: 400 MPa Yield Strength (YS), 640 MPa Ultimate Tensile Strength (UTS), and 23 % Total Elongation (TE). In **Table 8.3.4** below, these properties are given for the CH and UFH samples alongside the Uniform Elongation (UE) and the  $R$  and  $\Delta R$  values that indicate the normal and planar anisotropies of the material, respectively.

For the UFH sample, from the table and **Figures 8.3.26, 8.3.27**, it is shown that at 0° angle from the rolling direction, the highest UTS and YS were achieved at 973 MPa and 570 MPa, respectively. Nevertheless, the total elongation for these samples was quite low, at 14 %. The UTS and YS decrease at 45° angle from the rolling direction but are still considered higher than the IM while maintaining a considerably good elongation at 24 %. Finally, at a 90° angle from the rolling direction, the strength is slightly lower than at 0°, but the elongation is somewhat higher. The same trend is followed by the CH sample as well.

Nevertheless, both the UTS and YS are quite lower than in the UFH sample, while the elongation remains at the same levels. This increase in strength in the UFH sample is correlated to the increased fraction of martensite and pearlite calculated from EBSD analysis and from the lower fraction of recrystallized ferrite. Concerning the  $R$  and  $\Delta R$  values, both samples are anisotropic, as expected, due to the retainment of the cold-rolled microstructure. Although, the higher  $R$ -value in the UFH sample indicates that it might be less anisotropic than the CH sample. According to [119], the stronger is the  $\gamma$  (ND//{1 1 1}) texture, the stronger anti-thinning

ability can be achieved. Thus, the better R-value of the UFH sample can be attributed to its stronger ND fiber, as indicated in the ODF maps in **Figure 8.3.23**.

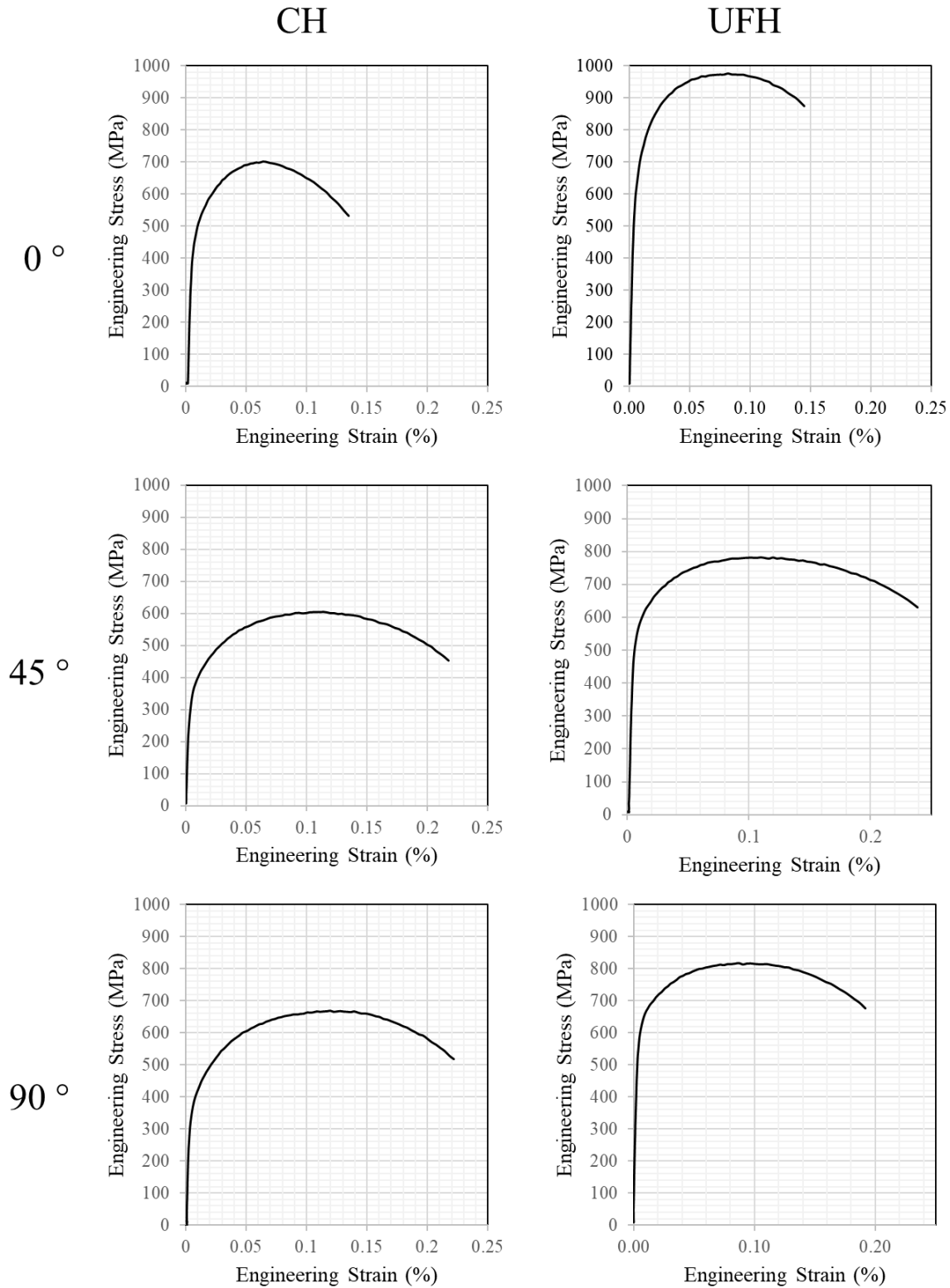


**Figure 8.3.26:** The engineering stress-strain curves for the CH and UFH samples for different tensile angles, as were plotted from the tensile tests and with the use of the DIC.

**Table 8.3.4:** The tensile properties and R-values of the CH and UFH samples.

	CH			UFH		
	0 °	45 °	90 °	0 °	45 °	90 °
<b>YS (MPa)</b>	453	355	347	570	520	562
<b>UTS (MPa)</b>	697	612	682	973	762	815
<b>UE (%)</b>	7.7	13.1	12.7	8	10	8.7
<b>TE (%)</b>	13.2	24.8	22	13.85	23.9	18
<b>r</b>	0.321	0.883	1.742	0.558	1.671	1.097
<b>R</b>	0.957			1.25		
<b><math>\Delta R</math></b>	0.149			-0.844		

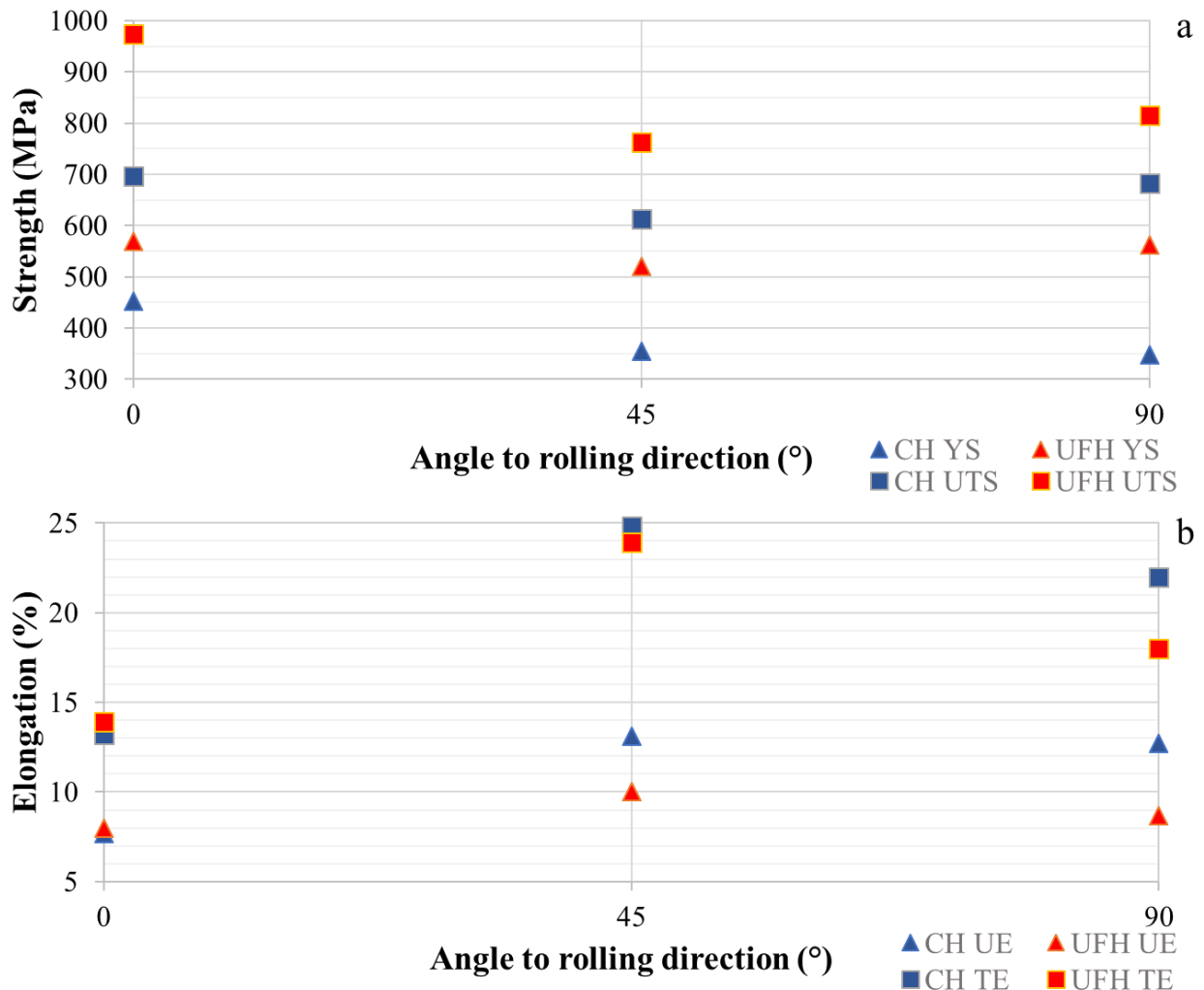


**Figure 8.3.27:** (a) Tensile and yield strengths for the CH (blue) and UFH (red) samples in relation to the angle of the tensile direction to the direction of the cold rolling. (b) The uniform and total elongations for the CH (blue) and UFH (red) samples in relation to the angle of the tensile direction to the direction of the cold rolling.

It is also observed from **Figure 8.3.27** that at 45° from the rolling direction, the elongation of the UFH sample is similar to that of the initial material, while the strength increases as well, giving probably the optimal strength to stress ratio. This can be attributed to the texture of the material. As shown in **Figure 8.3.28**, the majority (14.8 times random) of ferritic grains appear at 0° (brass orientation) on the alpha fiber, followed by 25-35° and 80-90° on the gamma fiber at 5 times random each. From the geometry of these BCC crystals [146], this means that the slip directions that are most commonly found in the material are the  $\langle \bar{1} 1 1 \rangle$  and the  $\langle 1 1 0 \rangle$ , for which the Burgers vector is parallel to the tensile direction when the load is applied at 45° angle to the rolling direction. Therefore, the grains exhibit higher elongation when pulled towards this direction, and thus the total elongation is increased for these samples.



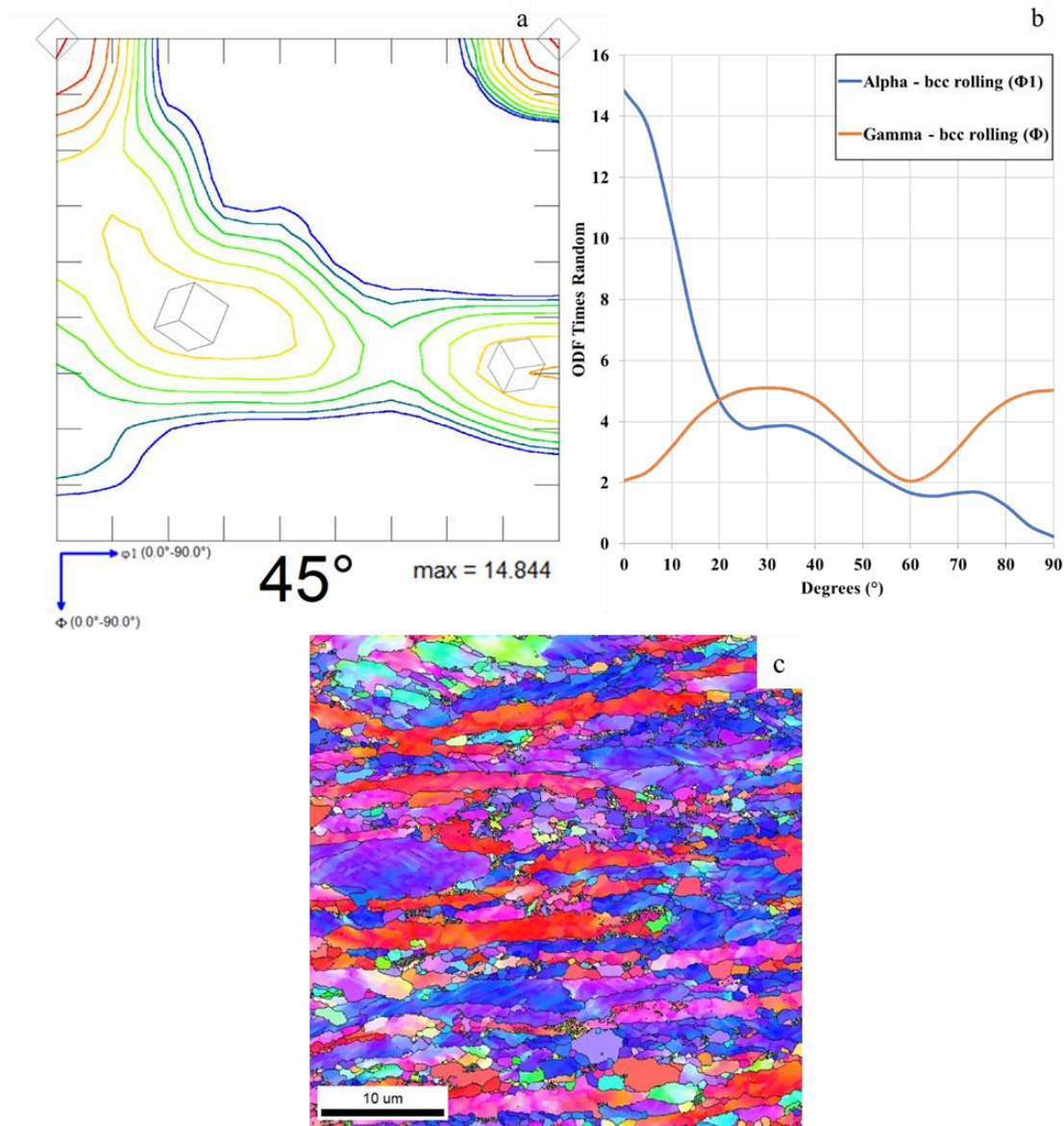


**Figure 8.3.28:** (a) ODF of the UFH sample indicating the direction of the grains. (b) Degrees – ODF times random chart indicates the density of grains that are rotated to a specific orientation. (c) IPF map of the UFH sample indicating that the highest fraction of ferrite has a similar orientation. Step size: 50 nm.

Fractography was made in the fracture surfaces of the CH and UFH samples at  $0^\circ$  from the rolling direction in SEM (**Figure 8.3.29**), in which they showed the highest UTS. At first glance, it is observed that the size, spread, and density of the dimples varies with the heating rate. In both cases, a mixed fracture can be considered with cleavage and dimple surfaces in microscale. In the CH sample, the fracture is predominantly ductile. On the other hand, the dimples are smaller in the UFH sample, but the fraction of brittle surfaces where the shear fracture occurred is higher. This can be attributed to the increased fraction of martensite calculated in the UFH sample from EBSD analysis. The larger dimple density and smaller average size observed in the UFH sample's fracture mean higher deformation capacity.

In **Figure 8.3.30**, the fracture surfaces are shown for the different angles for the UFH sample. A trend can be observed from these figures, and specifically an increase of the brittle surfaces as the angle from the rolling

direction increases. This means that at 0° from the rolling direction, the fracture appears to be more ductile, while at 90° from the rolling direction, the fracture is more brittle. At 45° from the rolling direction, an intermediate state is observed. The reason for this can be possibly attributed to the retainment of the bands from the cold rolling. As was mentioned in SEM **Figures 8.3.6, 8.3.7** at the beginning of the chapter, the martensite islands in the UFH sample mostly appear on the cold rolling bands that have been retained during the heating. Bearing in mind that those SEM images are taken at the samples' cross-section at 90° from the cold rolling direction, they correspond to **Figures 8.3.30 e, f**. Therefore, the banded martensite islands will exhibit cleavage fracture at the studied direction, which will propagate through the soft ferritic matrix. On the other hand, at 0° angle from the rolling direction, their fracture will be more ductile.

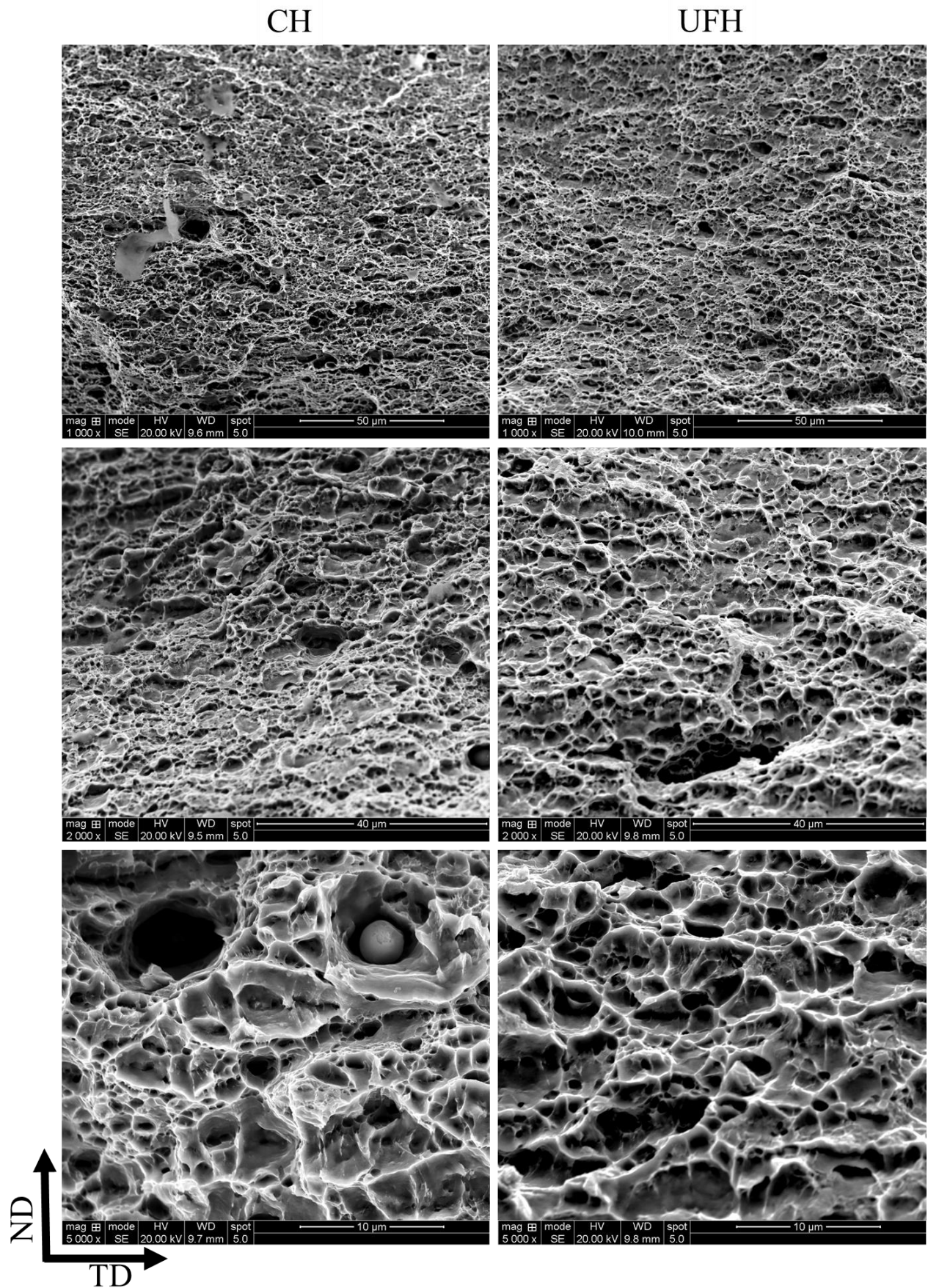


**Figure 8.3.29:** SEM fractography of the CH and UFH samples at different magnifications at 0° angle to the rolling direction indicating mixed fracture mode, primarily ductile with a few cleavage surfaces on a microscale.

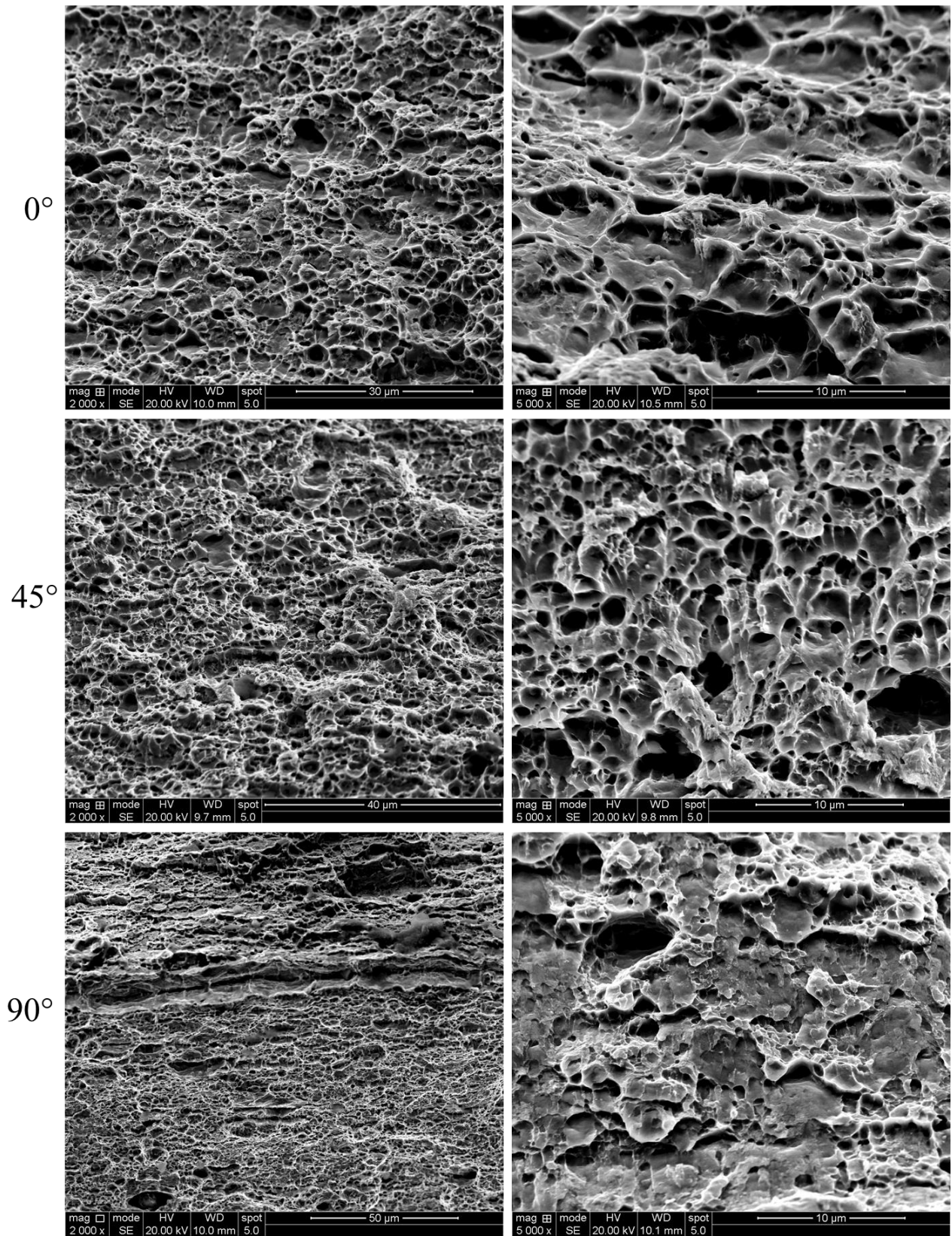


**Figure 8.3.30:** SEM fractography of the UFH sample for tensile tests at 0°, 45°, and 90° from the rolling direction.

Concerning the Vickers hardness of the material (**Table 8.3.5**), it can be observed that the hardness is lower for the CH sample than in the IM. This happens due to ferrite's recrystallization and the formation of new dislocation-free ferrite grains that exhibit lower hardness. On the other hand, for the UFH sample, the hardness

is only slightly higher than that of the IM. The main reason for this can be the presence of deformed ferrite to a great extent in the microstructure and of martensite at almost 25 % volume fraction. Compared to the IM, which consisted of 86 % deformed ferrite and 13 % pearlite/martensite, the UFH was expected to exhibit higher hardness. The reason for this can be the content of carbon in the martensite. As mentioned before, martensite can form between two ferrite grains with no apparent carbon source. This martensite is expected to have much lower carbon content than the IM's pearlite and martensite and, therefore, lower hardness and brittleness.

**Table 8.3.5:** *The average Vickers hardness of the IM, CH, and UFH samples.*

	<b>IM</b>	<b>CH</b>	<b>UFH</b>
<b>HV (average)</b>	271.2	235.2	274.8
<b>Deviation (average)</b>	2.6	2.5	4



## 9. Discussion

### 9.1. Discussion on the effect of the heating parameters

High heating rates were applied in small samples as described in **Chapter 8.1**, in order to reveal and study the effect of different heating parameters in the microstructure evolution. The initial experiments were performed in the dilatometer so that the phase transformations as affected by the ultra-fast heating could be properly monitored. The effect of alloying elements, such as Cr and Mn, was studied alongside to the effect of the heating rate. Also, a comparison was made between an ultra-fast heat treatment and a conventional heat treatment to unveil the effect of rapid heating. The initial microstructure has a great effect on the experiments. In the samples where the initial microstructure consisted of ferrite and lamellar cementite, during heating, a complete dissolution of cementite is achieved. This means that diffusion of carbon has taken place effectively and that the austenite formed is enriched in carbon. Though, the soaking time is minimal and complete homogenization of the chemical composition may not be achieved. As the homogenization occurs mostly during soaking, in the case of ultra-fast heating, gradients of carbon are expected across the microstructure. Therefore, the austenite formed inside or near the prior pearlitic colonies is expected to be enriched in carbon, while austenite formed from ferritic grains will have a lower carbon content. The same phenomenon is expected to be even more pronounced when the initial microstructure consists of ferrite and spheroidized cementite. As observed, the spheroidized cementite particles do not dissolve when high heating rates are applied. This means that the carbon content is concentrated in these particles. Furthermore, only partial dissolution of cementite was found to take place. This creates a gradient of carbon content in close proximity to the cementite spheres. The austenite formed on the  $\alpha/\theta$  interfaces or near them will be enriched in carbon, while the austenite formed at ferrite grains will have a lower carbon content. In both cases, though, austenite enriched in carbon and austenite poor in carbon is expected at peak temperature.

Concerning the effect of the chemical composition of the steel, two grades were studied. The first grade (C45 sample) had low additions of alloying elements while the other had a higher content of Cr and Mo (42CrMo4 sample). As both samples consisted of ferrite and lamellar cementite in their initial condition, complete dissolution of cementite was achieved. Both microstructures are martensitic with a very small fraction of retained austenite (1-2 %). Additionally, it was observed (see **Figure 8.1.8**) that the average grain size of the PAGs, and consequently of the final microstructure, is much more refined in the 42CrMo4 sample. This is attributed to the solute drag effect of Cr and Mo [97]. As it is also confirmed by the analysis shown in Chapter 8.3, in particular see **Figures 8.3.17-19**, Cr and Mn tend to segregate on the surface of cementite, thus, impeding its dissolution. Therefore, the growth of austenite is also impeded, due to a pinning effect applied by cementite, until it is dissolved.

As expected, the application of long soaking (more than 300 s and at high austenitization temperatures e.g., 1080 °C) in the heat treatment leads to dissolution of cementite. This results from the second experiment of this set, in which the UF&S&Q sample, contains, spheroidized cementite that has dissolved in a much greater

extent than in the UF&Q sample, where there was no soaking in the peak temperature. As these two samples consist of the same initial microstructure and chemical composition, it can be concluded that the dissolution of the spheroidized cementite depends mostly on the heating time.

In addition, when comparing the UF&Q sample with the UFHT sample, the difference in the retained austenite fraction is noteworthy, almost 3 %. These samples have the same initial microstructures, chemical compositions and heating rates while the changing parameter is the peak temperature (1080 °C to 900 °C). It is reported [123] that with increasing heating rate, the  $A_{c1}$  and  $A_{c3}$  temperatures increase. Also, it is found that the UFHT sample consists of a small fraction of ferrite [Figure 8.1.23]. Therefore, it can be concluded that in the UFHT sample, the austenitization process is not completed. In addition, the homogenization process and the diffusion of carbon is not as pronounced as in the UF&Q sample. Hence, more areas with increased carbon content are expected in the UFHT sample, leading to the retainment of more austenite.

The CCT diagrams were plotted [135–137] for the three compositions used in this chapter. As seen in Figure 9.1.1, the  $B_s$ ,  $B_f$ , and  $M_s$  curves are shown for the different grades.

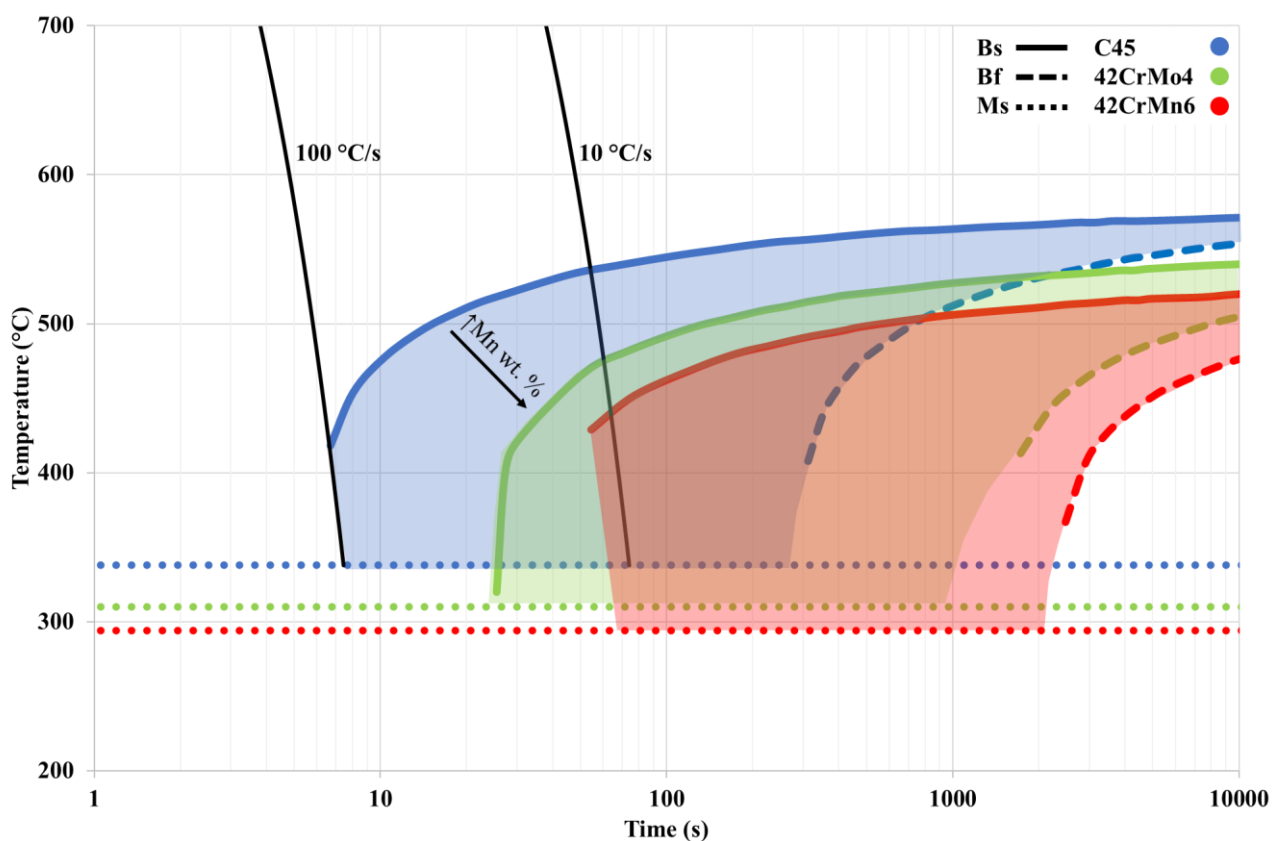
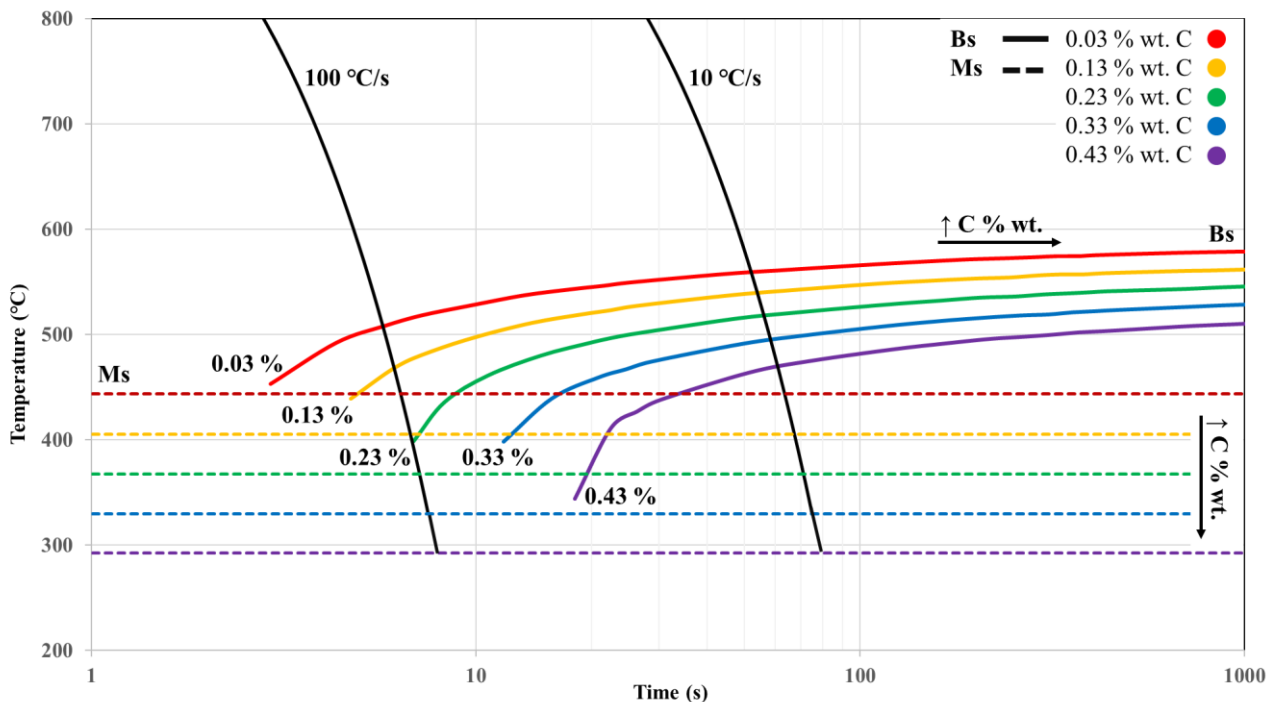


Figure 9.1.1: The CCT diagram shows the shift in the bainitic areas depending on the chemical composition.

The bainitic area is determined between the  $B_s$  and  $B_f$  curves. If the cooling rate curve (black lines) intersects the bainitic area, then bainite starts to form until the  $M_s$  is reached and the martensitic transformation begins. In the case that the cooling rate curve intersects the  $B_f$  curve, the bainitic transformation is complete, and the microstructure will fully consist of bainite. However, this would require much slower heating rates. It is

observed in this figure that the bainitic area for the C45 grade (blue lines) is shifted to the left side of the diagram, in comparison to the 42CrMo4 (green lines) and the 42CrMn6 (red lines). As the carbon content is the same in all the grades, this shift is attributed mainly to the manganese content. Mn is a  $\gamma$ -phase stabilizer that suppresses the bainitic and martensitic transformations. Therefore, the 42CrMn6 grade, which has the highest Mn content, has the lowest  $M_s$  temperature, and its bainitic area is shifted to the right.

On the other hand, the C45 grade has the lowest manganese content, and thus its  $M_s$  is higher, and its bainitic area is to the left of the diagram. As mentioned before, in all these samples, a carbon gradient in the austenite exists even after the peak temperature. Hence, the bainitic areas may shift further to the left or the right side of the CCT diagram, depending on the austenite's carbon content. The effect of the carbon content is shown below, in **Figure 9.1.2**. The composition used for this CCT diagram is that of the 42CrMo4 sample for an average PAG diameter of 15  $\mu\text{m}$  and the carbon content is deviated. Similar to the effect of Mn, shown in **Figure 9.1.1**, increased carbon content shifts the  $B_s$  curves to the right-hand side of the diagram and decreases the  $M_s$  temperature. The reason is similar, as carbon is also a  $\gamma$ -phase stabilizer and impedes the formation of bainite/martensite in the expense of austenite. Thus, according to this diagram, austenite grains in areas depleted in carbon may transform into bainite upon quenching with a cooling rate of 100  $^\circ\text{C}/\text{s}$ . Such areas can be found in the UF&Q and UFHT samples, in which the carbon is concentrated in the undissolved cementite.



**Figure 9.1.2:** CCT diagram that shows the  $B_s$  temperature curves for deviating carbon content. The composition used for the diagram is the 42CrMo4. Increasing carbon content shifts the  $B_s$  curves to the right-hand side of the diagram and the  $M_s$  temperature to lower values.

Refinement of the PAGs is observed in the ultra-fast heat-treated grades. Due to the short heating times, the growth of austenite is impeded. Also, the undissolved cementite spheres have a pinning effect on the mobility of the interfaces, further preventing the austenite growth. This may also lead to the formation of bainite, as is indicated in **Figure 9.1.3**. In this CCT diagram, the 42CrMo4 composition is used, while the PAG size is differentiated. It can be seen that with decreasing PAG size, the  $B_s$  curves shift to the left-hand side of the CCT diagram and the formation of bainite is possible for higher cooling rates. Therefore, in the samples with undissolved cementite in the microstructure, where refinement of the PAGs takes place, the formation of bainite upon quenching is possible.

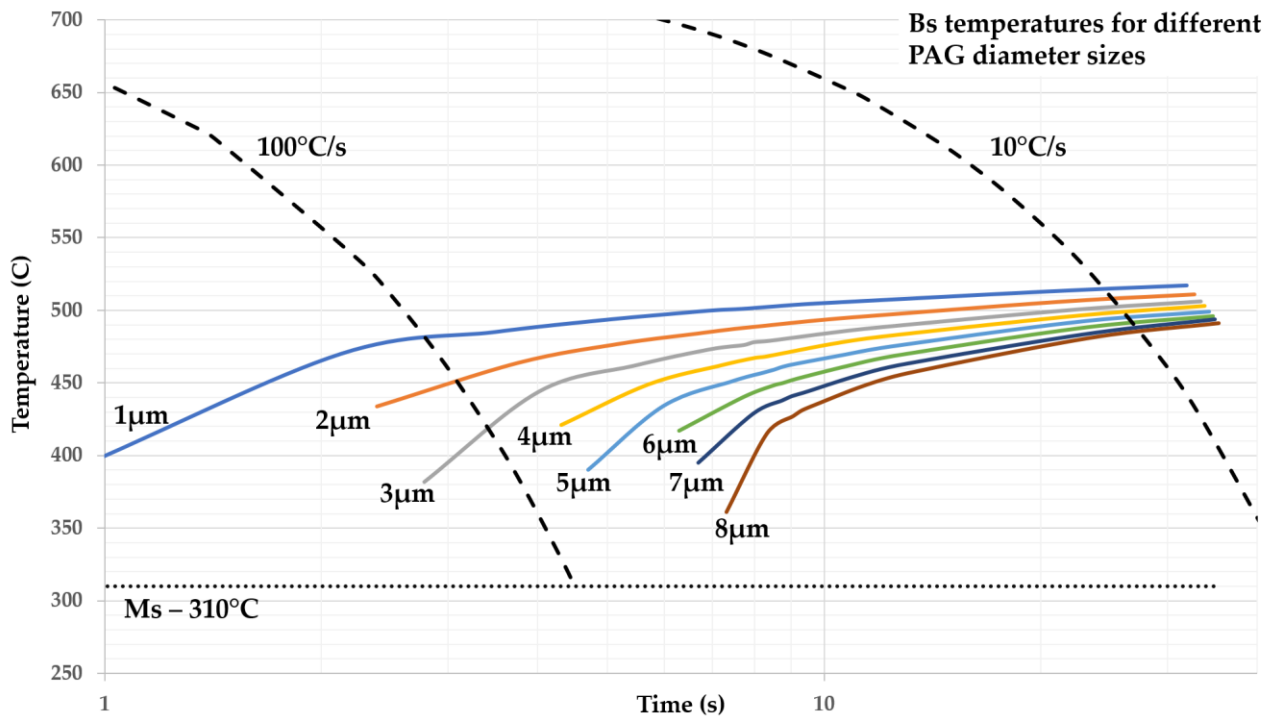


**Figure 9.1.3:** CCT diagram plotted for the 42CrMo4 composition in which the  $B_s$  temperature curves for different PAG sizes are shown. Decreasing PAG size shifts the  $B_s$  curves to the left hand-side of the diagram making the formation of bainite upon quenching possible.

## 9.2. Discussion on the formation of bainite and the retainment of austenite in large-scale samples under UFH cycles

The transformations that occur during Ultra-Fast Heating are dictated by the resulting heterogeneity in the chemical composition. It has been previously reported [97] that high heating rates impede the dissolution of cementite. Therefore, the majority of the carbon content is found in the undissolved cementite. It is particularly found [81] that partial dissolution of cementite takes place, which creates a carbon gradient in the microstructure. In the experiments of **Chapter 8.2**, complete dissolution of cementite is achieved. Nevertheless, the heating time above the  $A_{c3}$  temperature is not enough for homogenization of the chemical composition in the material's microstructure. Hence, the regions near the dissolved pearlitic colonies will be enriched in carbon. As the initial microstructure consisted of a 3/1 ratio of ferrite to pearlite, the C-rich areas

are expected to cover a similar fraction of the microstructure. In these areas, the nucleation of austenite occurs on the  $\theta/\alpha$  interfaces, with the difference in carbon being the driving force [56]. The newly formed austenite grains will be enriched in carbon due to its availability and will grow with increasing heating time. Though, due to the lack of time for the growth of austenite, some grains are expected to be refined. In these C-enriched grains, martensite laths will start to form by a shear transformation mechanism during quenching. During this shear transformation, there is no time for carbon to be partitioned [24]. Nevertheless, as indicated by **Figures 8.2.9-12**, retained austenite films were found in the microstructure (approximately 3 %) between martensite laths, indicating that the excess of carbon and manganese may decrease the  $M_s$  and  $M_f$  temperatures. Thus, the martensitic transformation is not completed.

On the other hand, the areas not adjacent to any pearlitic colony are not expected to be enriched in carbon. As the initial microstructure was not deformed, the distance carbon can travel through pipe diffusion is limited, and thus, the preferential route for its diffusion is through the ferrite grain boundaries [145]. This segregation of carbon and other alloying elements in the interfaces is the driving force for the nucleation of austenite between two ferrite grains when there is no other carbon source in proximity. This formed austenite, though, will not be enriched in carbon. The mechanism that takes place, in this case, is similar to the bainitic displacive transformation and is controlled by the movement of the interfaces [91-93]. According to the CCT diagram (**Figure 8.2.13**), such parent austenite grains may transform into bainite during quenching alongside martensite. Indeed, lower bainite was found in the microstructure via TEM (**Figure 8.2.14-19**). Due to the displacive nature of lower bainite transformation, there is not adequate time for carbon diffusion in long distances, so fine parallel cementite particles are precipitated inside the bainitic laths. Due to the higher than the  $M_s$  temperatures at which the bainitic transformation occurs, the internal energy is higher and partial carbon diffusion occurs at short distances from the super-saturated bainitic laths, and thus austenite is retained in films on the lath boundaries [78]. Nevertheless, as observed from the CCT diagram, martensite also forms in the C depleted parent austenite grains. This martensite is expected to contain less carbon and thus be less brittle than the martensite formed in the carbon-rich areas.

According to these, the final microstructure consists of martensite, lower bainite, and retained austenite. It was found (**Figure 8.2.9**) that the fraction of retained austenite in the examined region was approximately 3%. Also, from **Figure 8.2.13a**, it can be assumed that the maximum possible fraction of bainite transformed from the carbon-depleted austenite (for 100 °C/s cooling rate) is almost 50 %. As the area fraction of pearlite in the initial microstructure is approximately 25 %, due to the lack of heating time for homogenization, the carbon-depleted austenite will cover a 75 % area fraction. Thus, the bainite fraction that will occur from this austenite will cover a fraction of 37.5 % of the overall microstructure, while the rest microstructure will consist of martensite. The reason such mixed microstructures are desired is that they can achieve a good ratio of strength and ductility [147]. Bainite favors the ductility of the material, while martensite increases its strength. Retained austenite films, despite the Transformation Induced Plasticity effect, also impede the movement of dislocations, thus favoring the strength of the material [148].



### 9.3. Discussion on the application of UFH on a commercial DP steel grade

In **Chapter 8.3**, the effect of UFH is studied on the microstructure evolution of a conventional DP grade. The high heating rates have an impact on the transformation temperatures, shifting them at higher values. As mentioned before, during heating, the cementite is only partially dissolved, creating regions with higher or lower carbon content in the material. In **Chapter 8.1**, it was shown that when the initial microstructure consists of ferrite and lamellar cementite, the cementite would fully dissolve when high heating rates up to 300 °C/s are applied. In **Chapter 8.3** though, it is described that even though the cementite is in lamellar form, it is not fully dissolved. As the peak temperature is lower in these experiments, 760 °C instead of 1080 °C, and the heating rate is much higher, 780 °C instead of 1080 °C, it can be assumed that the heating temperature is more important for the dissolution of cementite than the heating time. Even though the dissolution of cementite is not completed, spheroidization occurs. According to different theories of spheroidization [82], atoms move through diffusion to the neighboring or even inside the same lamellae and eventually lead to the plate's fracture. In the areas of the lamella that carbon atoms have accumulated, the thickness increases and a sphere is formed. As the spheroidization process is a diffusion-controlled mechanism, time is required. Though, when high heating rates are applied, this time is not available and hence, the spheroidization process may not be completed. The evolution of the spheroidization process of cementite is observed in both samples and can be seen in (**Figure 8.3.9, 8.3.10**).

As homogenization of the chemical composition cannot be achieved due to the low heating time and the diffusion of carbon is impeded, the regions near the undissolved pearlitic colonies are expected to have high carbon content. A gradient of carbon and manganese is created around the undissolved cementite, as suggested by **Figures 8.3.17-19**. In contrast, in ferritic regions of the initial material that are located far from any carbon source, enrichment in carbon is averted. Again, this heterogeneity in the chemical composition is apparent in the parent austenite grains during and after the austenitization process.

In parallel, the recovery and recrystallization processes are also impeded during ultra-fast heating and overlap with the austenitization process. This is in accordance to the work of Cerda et al. [114-115]. The mobilization of dislocations in the deformed ferrite and the formation of low and high angle grain boundaries is averted locally, as shown by the TKD results (**Figure 8.3.22**). This has an important impact on the microstructure as these retained dislocations act as nucleation sites for austenite when the  $A_{c1}$  temperature is reached. More nucleation sites mean that more parent austenite grains will be formed with a smaller size leading to a refined microstructure. Another factor for the refinement of the microstructure is the undissolved cementite, either lamellar or spheroidized. It is shown (**Figures 8.3.13-14**) that this cementite has a pinning effect on the mobility of dislocations and of the grain boundaries of the parent austenite.

According to the aforementioned, for ultra-fast heating, at the intercritical peak temperature, the microstructure is expected to consist of deformed ferrite, very small fractions of recrystallized ferrite, undissolved cementite in lamellar and spheroidized forms, carbon enriched austenite near this cementite, and carbon depleted austenite. Heterogeneity is not met only in the chemical composition of the austenite but also on its grain size.

The austenite nuclei formed near or inside the former pearlitic colonies will be able to grow until cementite is found and impede the movement of the grain boundaries. On the other hand, austenite nuclei formed between ferrite grains will have the ability to grow much more as no obstacles are apparent, as long as the heating time allows it.

Concerning the crystallographic texture of the ultra-fast heated material, it is almost identical to that of the initial material as the cold rolling morphology and bands are retained. This creates a highly anisotropic material, as shown from the tensile tests with the direction parallel to the cold rolling exhibiting the highest strength (**Figure 8.3.26, 8.3.27**). The optimal balance of stress/strain ratio is achieved when the tensile axis is at an angle of  $45^\circ$  to the rolling direction with an increase in both strength and elongation. The texture of the material also explains this. The largest fraction of crystals in the ferrite grains is rotated towards the  $\langle 1\ 1\ 1 \rangle$  and  $\langle 0\ 0\ 1 \rangle$  directions (**Figure 8.3.28**). This means that their most common slip planes  $[\bar{1}\ 1\ 1]$  and  $[1\ 1\ 0]$  have Burgers vectors parallel to the tensile axis, when pulled at  $45^\circ$  to the rolling direction, exhibiting better elongations. Finally, the ultra-fast heated material shows similar hardness to the initial material due to the large fraction of deformed ferrite.

## 10. Conclusions

This thesis aims to explain the evolution of the microstructure that gives the potential to control thermal treatments and design new steel grades that can be included in the 3<sup>rd</sup> Generation of AHSS, alongside the currently used TRIP and Q&P steels. This research is part of a rather recent worldwide trend to study the overall effects of ultra-fast heating treatments, having different scopes such as the comprehension of the recrystallization processes, the dissolution and precipitation of carbides, and the production of automotive steel grades such as the Q&P.

The results of the current study explain the transformation mechanisms that occur during the heating stage when high heating rates are applied and the consequent transformations upon quenching via characterization techniques. In particular, the simultaneous formation of martensite and bainite, and the retainment of austenite that result in optimal mechanical properties.

- The dissolution of cementite depends on the addition of chromium due to the solute drag effect, as it is segregated on the  $\alpha/\theta$  interfaces. Similarly, manganese and carbon segregate on the boundaries between pearlite/ferrite and ferrite/ferrite and offer the required thermodynamic driving force for austenite nucleation. In the case that the content of such alloying elements is lower, the dissolution of cementite is faster and better homogenization of the chemical composition in the microstructure is achieved. In the dissolution of cementite, the peak temperature has a stronger effect than the heating rate. Spheroidized cementite, either from the initial microstructure or formed during the heating stage, is more energetically stable and is retained in the final microstructure. This retainment of cementite creates a gradient of carbon content in a radius around the cementite particle.
- The microstructure is also affected from the deformation of ferrite, as the dislocations act as fast-track ways to the diffusion of carbon and act as nucleation sites for austenite. Regarding ferrite, the processes of recovery and recrystallization shift to higher temperatures and, at some point, overlap with the austenitization process, when high heating rates are applied. Therefore, non-recrystallized ferrite is found in the microstructure, alongside recrystallized ferrite. The volume fraction of non-recrystallized ferrite depends solely on the heating rate. The high fraction of non-recrystallized ferrite affects the texture of the material. When the fraction of recrystallized ferrite is quite low the texture is very similar to that of the initial material and strongly affects the mechanical properties and isotropy of the material.
- The nucleation and chemical composition of the formed austenite is strongly dependent on the heating rates. Austenite nucleates once the  $A_{c1}$  temperature is reached preferentially in sites where there is enough difference in carbon content. Such sites are primarily the interfaces between ferrite and lamellar or spheroidized cementite, and secondarily dislocations or ferrite/ferrite boundaries. The nucleation of austenite will thus initiate first at the former sites, and then will initiate in the latter sites. Hence, two types of austenite will be formed, those with high carbon content in close proximity to cementite and those with lower carbon content, formed on ferrite interfaces and dislocations. The growth of austenite will be impeded due to the high heating rates and to the presence of undissolved cementite. In the case that the

cementite is fully dissolved, the austenite grains will grow more as their growth will be dependent only on the heating rate. In contrast to a conventional heat treatment, the chemical composition's heterogeneity is retained and the size of the austenite grains are refined.

- The composition and size of the austenite affects the quenching products. Martensite is formed upon quenching to room temperature from the carbon-rich austenite. The formation of bainite takes place with the same quenching rates in the carbon-depleted austenite. The presence of bainite is confirmed from the SEM, EBSD, and TEM analysis. Retainment of austenite in films also occurs in the carbon-rich areas due to a decrease in the  $M_s$  temperature.
- The UFH microstructures may consist of martensite, bainite, undissolved cementite, retained austenite, and ferrite, and are similar to those met in the 3<sup>rd</sup> Generation advanced high strength steel grades. During the tensile tests, the cold-rolled material exhibited a very good strength and elongation ratio compared to conventional steels of the same martensite volume fraction. The strength and hardness of the material are attributed to the martensite, while the good ductility is attributed to the retained austenite, bainite, and ferrite. Nevertheless, due to the specific texture of the cold-rolled samples, these properties are anisotropic, limiting the possible applications of such a grade. The fracture is mainly ductile from the fractography, with a few cleavage fractures surfaces observed.

In the pursuit for optimization of automotive steel grades, the process of UFH has a prominent position. This thesis provides a detailed explanation of the transformation mechanisms, that occur upon the heating and cooling stages when very high rates are applied. In that way, the ability to control such treatments and to design new alloys can be achieved. Therefore, this thesis can contribute to the improvement of this process for its application in the automotive industry.

## 11. References

1. European Commission Emissions in the automotive sector.  
[https://ec.europa.eu/growth/sectors/automotive/environment-protection/emissions\\_en](https://ec.europa.eu/growth/sectors/automotive/environment-protection/emissions_en). Accessed 16 Nov 2020
2. Liu Q., Zhou Q., Venezuela J. et al. (2016) A review of the influence of hydrogen on the mechanical properties of DP, TRIP, and TWIP advanced high-strength steels for auto construction. *Corrosion Reviews* 34: 127–152. <https://doi.org/10.1515/corrrev-2015-0083>
3. Singh M.K. (2016) Application of Steel in Automotive Industry. *International Journal of Emerging Technology and Advanced Engineering* 6
4. Rana R., Singh S.B. (2016) *Automotive steels: Design, metallurgy, processing and applications*. Woodhead Publishing, Oxford
5. Das S., Singh S.B., Mohanty O.N. et al. (2008) Understanding the complexities of bake hardening. *Materials Science and Technology* 24: 107–111. <https://doi.org/10.1179/174367507X247511>
6. Galibois A., Krishnadev M.R., Dubé A. (1979) Control of grain size and sub-structure in plain carbon and high strength low alloy (HSLA) steels—the problem and the prospect. *MTA* 10: 985–995. <https://doi.org/10.1007/BF02811645>
7. Chen M.-Y., Gouné M., Verdier M. et al. (2014) Interphase precipitation in vanadium-alloyed steels: Strengthening contribution and morphological variability with austenite to ferrite transformation. *Acta Materialia* 64: 78–92. <https://doi.org/10.1016/j.actamat.2013.11.025>
8. Fonstein N. (2015) *Advanced high strength sheet steels: Physical metallurgy, design, processing, and properties*. Springer, Cham
9. Katsamas A.I., Haidemenopoulos G.N., Aravas N. (2004) Modelling of Transformations in TRIP Steels. *steel research international* 75: 737–743. <https://doi.org/10.1002/srin.200405836>
10. Horvath C.D., Mallick P.K. (2010) *Advanced steels for lightweight automotive structures: Materials, design and manufacturing for lightweight vehicles*. Woodhead Publishing in materials. CRC Press; Oxford : Woodhead, Boca Raton, Fla.
11. Kuziak R., Kawalla R., Waengler S. (2008) Advanced high strength steels for automotive industry. *Archives of Civil and Mechanical Engineering* 8: 103–117. [https://doi.org/10.1016/S1644-9665\(12\)60197-6](https://doi.org/10.1016/S1644-9665(12)60197-6)



12. Taylor T., Fourlaris G., Evans P. et al. (2014) New generation ultrahigh strength boron steel for automotive hot stamping technologies. *Materials Science and Technology* 30: 818–826. <https://doi.org/10.1179/1743284713Y.0000000409>
13. Cornette D., Cugy P., Hildenbrand A. et al. (2005) Ultra High Strength FeMn TWIP Steels for automotive safety parts. *Rev Met Paris* 102: 905–918. <https://doi.org/10.1051/metal:2005151>
14. Elliott R., Coley K., Mostaghel S. et al. (2018) Review of Manganese Processing for Production of TRIP/TWIP Steels, Part 1: Current Practice and Processing Fundamentals. *JOM* 70: 680–690. <https://doi.org/10.1007/s11837-018-2769-4>
15. Cola G. (2007) Properties of bainite nucleated by water quenching in 80 ms. In: Furuhashi T, Tsuzaki K (eds) *Proceedings of the 1st International Symposium on Steel Science*. Iron and Steel, Tokyo, Japan, pp 187–190
16. Lolla S.V.T., Cola G., Narayanan B. et al. (2009 // 2010) Towards Understanding the Microstructure Development during Heating and Cooling of Steels. In: Chandra T (ed) *Proceedings of the International Conference on Processing and Manufacturing of Advanced Materials-THERMEC'2009 // THERMEC 2009: 6th International Conference on Processing & Manufacturing of Advanced Materials*, Berlin, Germany, August 25-29, 2009. Trans Tech Publications, Stafa-Zurich
17. Lolla S.V.T. (2009) *Understanding Microstructure Evolution in Rapid Thermal Processing of AISI 8620 Steel*. Master Thesis, The Ohio State University
18. Lolla T., Cola G., Narayanan B. et al. (2011) Development of rapid heating and cooling (flash processing) process to produce advanced high strength steel microstructures. *Materials Science and Technology* 27: 863–875. <https://doi.org/10.1179/174328409X433813>
19. Noor H. (2017) *Materials Science and Engineering*. International Energy and Environment Foundation
20. Papavinasam S. (2014) *Corrosion Control in the Oil and Gas Industry // Corrosion control in the oil and gas industry*. Elsevier; Gulf Professional, Oxford
21. Krauss G. (2015) *Steels: Processing, structure, and performance / George Krauss, Second edition*. ASM International, Materials Park, Ohio
22. Morito S., Nishikawa J., Maki T. (2003) Dislocation Density within Lath Martensite in Fe-C and Fe-Ni Alloys. *ISIJ International* 43: 1475–1477. <https://doi.org/10.2355/isijinternational.43.1475>
23. Pickering A. (1967) *Transformation and Hardenability in Steels*. Climax Molybdenum Company of Michigan, Michigan, USA
24. Bhadeshia, H. K. D. H. (2001) *Bainite in steels: Transformations, microstructure and properties / H.K.D.H. Bhadeshia, 2nd ed. Book, vol 735*. IOM Communications, London
25. Marder A.R., Goldstein J.I. (eds) (1984) *Phase Transformations in Ferrous Alloys*. ASM International, Cleveland, OH

26. Matas S.J., Hehemann RF (1961) The structure of bainite in hypoeutectoid steels. *Transactions of the Metallurgical Society of AIME* 221: 179–185
27. Aaronson H.I. (1969) *The mechanism of phase transformation in crystalline solids*. Institute of Metals, London, UK
28. Zajac S., Schwinn V., Tacke K.H. (2005) Characterisation and Quantification of Complex Bainitic Microstructures in High and Ultra-High Strength Linepipe Steels. *MSF* 500-501: 387–394. <https://doi.org/10.4028/www.scientific.net/MSF.500-501.387>
29. Cayron C. (2013) One-step model of the face-centred-cubic to body-centred-cubic martensitic transformation. *Acta Crystallographica Section A: Foundations of Crystallography* 69: 598-509. <https://doi.org/10.1107/S0108767313019016>
30. Pitsch W. (1962) Der orientierungszusammenhang zwischen zementit und austenit. *Acta Metallurgica* 10: 897–900
31. Kurdjumow G., Sachs G. (1930) ber den Mechanismus der Stahlhrtung. *Z Physik* 64: 325–343. <https://doi.org/10.1007/BF01397346>
32. Koumatos K., Muehlemann A. (2017) A theoretical investigation of orientation relationships and transformation strains in steels. *Acta Crystallogr A Found Adv* 73: 115–123. <https://doi.org/10.1107/S2053273316020350>
33. Bhadeshia, H. K. D. H. (2018) *Geometry of crystals, polycrystals and phase transformations*. CRC Press/Taylor & Francis Group, Boca Raton
34. Andrews K.W. (1963) The structure of cementite and its relation to ferrite. *Acta Metallurgica* 11: 939–946
35. Tyshchenko A.I., Theisen W., Oppenkowski A. et al. (2010) Low-temperature martensitic transformation and deep cryogenic treatment of a tool steel. *Materials Science and Engineering A* 527: 7027–7039. <https://doi.org/10.1016/j.msea.2010.07.056>
36. Shackleton D.N., Kelly P.M. (1967) The crystallography of cementite precipitation in the bainite tranformation. *Acta Metallurgica* 15: 979–992
37. Bhadeshia, H. K. D. H. (1980) The lower bainite transformation and the significance of carbide precipitation. *Acta Metallurgica* 28: 1103–1114
38. Pearson G.L. (1964) Diffusion in Solids. *Solid-State Electronics* 7: 274. [https://doi.org/10.1016/0038-1101\(64\)90025-5](https://doi.org/10.1016/0038-1101(64)90025-5)
39. Bocquet J.L., Brebec G., Limoge V. (1983) Diffusion in Metals and Alloys. In: Cahn R.W., Haasen P. (eds) *Physical Metallurgy*. Elsevier Science Publishers
40. Sinha A.K. (2003) *Physical Metallurgy Handbook: Chapter 2: Diffusion in Metals and Alloys*. McGraw-Hill, New York, USA

41. Papaefthymiou S. (2005) Failure mechanisms of multiphase steels, 1. Auflage. Berichte aus dem Institut für Eisenhüttenkunde, 2005/1. Shaker, Aachen
42. Landheer H. (2010) Nucleation of ferrite in austenite: The role of crystallography. Doctoral. TU Delft, Delft, NE
43. Porter D.A., Easterling K.E., Sherif M.Y. (2009) Phase transformations in metals and alloys. CRC Press, Boca Raton, FL
44. Sutton A.P., Balluffi R.W. (1995) Interfaces in crystalline materials. Monographs on the physics and chemistry of materials, vol 51. Clarendon Press, Oxford
45. Wolf D., Yip S. (1992) Materials interfaces: Atomic-level structure and properties
46. Bain E.C. (1924) The nature of martensite. Transactions of the American Institute of Mining and Metal 70: 25–46
47. Nishiyama Z. (1934) X-ray investigation of the mechanism of the transformation from face-centred cubic lattice to body-centred cubic. Science Reports of the Tohoku Imperial University, Series 1: Mathematics, 23: 637–664
48. Wassermann G. (1935) Über den Mechanismus der  $\alpha$ - $\gamma$  Umwandlung des Eisens. Verlag Stahleisen
49. Greninger A.B., Troiano A.R. (1949) Kinetics of the austenite to martensite transformation in steel. Transactions of the American Institute of Mining, Metallurgical and Petroleum Engineers 1: 590–598
50. Azizi-Alizamini H., Militzer M., Poole W.J. (2011) Austenite Formation in Plain Low-Carbon Steels. Metall and Mat Trans A 42: 1544–1557. <https://doi.org/10.1007/s11661-010-0551-5>
51. Andrade-Carozzo V., Jacques P.J. (2007) Interactions between Recrystallisation and Phase Transformations during Annealing of Cold Rolled Nb-Added TRIP-Aided Steels. MSF 539-543: 4649–4654. <https://doi.org/10.4028/www.scientific.net/MSF.539-543.4649>
52. Huang J., Poole W.J., Militzer M. (2004) Austenite formation during intercritical annealing. Metall and Mat Trans A 35: 3363–3375. <https://doi.org/10.1007/s11661-004-0173-x>
53. Dieter G.E. (1986) Mechanical metallurgy, 3rd ed. McGraw-Hill series in materials science and engineering. McGraw-Hill, New York
54. Humphreys F.J., Hatherly M. (2004) Recrystallization and related annealing phenomena, 2nd ed. Elsevier, Amsterdam, London
55. Brooks C.R. (1992) Principles of the austenitization of steels. Elsevier Applied Science, London
56. Savran V.I. (2009) Austenite Formation in C-Mn Steel. Doctoral Thesis, TU Delft
57. Roósz A., Gácsi Z., Fuchs E.G. (1983) Isothermal formation of austenite in eutectoid plain carbon steel. Acta Metallurgica 31: 509–517. [https://doi.org/10.1016/0001-6160\(83\)90039-1](https://doi.org/10.1016/0001-6160(83)90039-1)

- 
58. Datta D.P., Gokhale A.M. (1981) Austenitization kinetics of pearlite and ferrite aggregates in a low carbon steel containing 0.15 wt pct C. *Metall and Mat Trans A* 12: 443–450.  
<https://doi.org/10.1007/BF02648541>
59. Samuels L.E. (1999) *Light microscopy of carbon steels*, Rev. ed. ASM, Materials Park, Ohio
60. Dykhuizen R.C., Robino C.V., Knorovsky G.A. (1999) A method for extracting phase change kinetics from dilatation for multistep transformations: Austenitization of a low carbon steel. *Metall and Materi Trans B* 30: 107–117. <https://doi.org/10.1007/s11663-999-0011-z>
61. Schmidt E., Wang Y., Sridhar S. (2006) A study of nonisothermal austenite formation and decomposition in Fe-C-Mn alloys. *Metall and Mat Trans A* 37: 1799–1810.  
<https://doi.org/10.1007/s11661-006-0122-y>
62. Nakaoka K., Hosoya Y., Ohmura M. et al. (1979) Reassessment of the Water- Quenching Process as a Means of Producing Formable Steel Sheets. In: Morris JW, Kot RA (eds) *Structure and Properties of Dual-phase Steels: Proceedings: Symposium Sponsored by the TMS-AIME Heat Treatment Committee*. Metallurgical Society of AIME, pp 330–345
63. Hansen S.S., Pradhan R.R. (1981) Structure /Properties Relationship and Continuous Yielding Behavior in Dual-Phase Steel. In: Kot R.A., Bramfitt B.L. (eds) *Fundamentals of dual-phase steels: Proceedings of a symposium sponsored by the Heat Treatment Committee of the Metallurgical Society of AIME and the ASM/MSD Structures Activity Committee at the 110th AIME Annual Meeting, Chicago, Illinois, February 23-24, 1981*, The Metallurgical Society of AIME, Warrendale, Pa., pp 115–144
64. Enomoto M., Lange W.F., Aaronson H.I. (1986) The kinetics of ferrite nucleation at austenite grain edges in Fe-C and Fe-C-X alloys. *Metall and Mat Trans A* 17: 1399–1407.  
<https://doi.org/10.1007/BF02650121>
65. Huang W., Hillert M. (1996) The role of grain corners in nucleation. *Metall and Mat Trans A* 27: 480–483. <https://doi.org/10.1007/BF02648428>
66. Enomoto M., Aaronson H.I. (1986) Nucleation kinetics of proeutectoid ferrite at austenite grain boundaries in Fe-C-X alloys. *Metall and Mat Trans A* 17: 1385–1397.  
<https://doi.org/10.1007/BF02650120>
67. Kaufman L., Cohen M. (1956) The Martensitic Transformation in the Iron-Nickel System. *JOM* 8: 1393–1401. <https://doi.org/10.1007/BF03377892>
68. Bunshah R.F., Mehl R.F. (1953) Rate of propagation of martensite. *Transactions of the American Institute of Mining and Metallurgical Engineers* 197: 1251–1258
69. Christian J.W. (1962) The origin of surface relief effects in phase transformations. In: Zackay V.F., Aaronson H.I. (eds) *Decomposition of Austenite by Diffusional Processes: Proceedings of a Symposium Held in Philadelphia, Pennsylvania, October 19, 1960, Under the Sponsorship of the*

- Ferrous Metallurgy Committee of the Institute of Metals Division, the Metallurgical Society, American Institute of Mining, Metallurgical, and Petroleum Engineers. Interscience Publishers
70. Davenport E.S., Bain E.C. (1930) Transformation of austenite at constant subcritical temperatures. *Transactions of the American Institute of Mining and Metallurgical Engineers* 90: 117–154. <https://doi.org/10.1007/BF03037892>
  71. Fumimaru K., Toshiyuki H., Keniti A. (2000) Extremely-low carbon bainitic steels for new structural steel products. *Rev Met Paris* 97: 1235–1244. <https://doi.org/10.1051/metal:2000109>
  72. Aaronson H.I., Wells C. (1956) Sympathetic nucleation of ferrite. *JOM* 8: 1216–1223
  73. Hehemann R.F. (1970) *Phase Transformations*. ASM, OH, USA
  74. Bhadeshia, H. K. D. H., Christian JW (1990) Bainite in steels. *Metallurgical and Materials Transactions A* 21A: 767–797
  75. Aaronson H.I. (1969) *The Mechanism of Phase Transformations in Crystalline Solids*. The Institute of Metals, London, UK
  76. Honeycombe R.W.K. (1976) Transformation from austenite in alloy steels. *Metallurgical and Materials Transactions A* 7A: 915–936
  77. Ali A., Bhadeshia, H. K. D. H. (1989) Growth rate data on bainite in alloy steels. *Materials Science and Technology* 5: 398–402. <https://doi.org/10.1179/mst.1989.5.4.398>
  78. Takahashi M. (2004) Recent progress: kinetics of the bainite transformation in steels. *Current Opinion in Solid State and Materials Science* 8: 213–217. <https://doi.org/10.1016/j.cossms.2004.08.003>
  79. Wanwe A. (2019) Investigation of rapid heating on surface hardening characteristics of shotpeened Alloy steel. College of Engineering, Pune
  80. Lucas A. (2007) Production of high quality formable grades in an ultra short annealing processing line. EUR, 1018-5593, 22437 EN. Office for Official Publications of the European Communities, Luxembourg
  81. Papaefthymiou S., Goulas C., Castro Cerda F.M. et al. (2017) The Effect of Heating Rate on the Microstructure of a Soft-Annealed Medium Carbon Steel. *steel research international* 88: 1700158. <https://doi.org/10.1002/srin.201700158>
  82. Tian Y.L., Kraft R.W. (1987) Mechanisms of Pearlite Spheroidization. *Metallurgical and Materials Transactions A* 18: 1403–1414. <https://doi.org/10.1007/BF02646654>
  83. Garcia C.I., Deardo A.J. (1981) Formation of Austenite in 1.5 Pct Mn Steels. *Metallurgical and Materials Transactions A* 12A



- 
84. Castro Cerda F.M., Goulas C., Sabirov I. et al. (2016) Microstructure, texture and mechanical properties in a low carbon steel after ultrafast heating. *Materials Science and Engineering: A* 672: 108–120. <https://doi.org/10.1016/j.msea.2016.06.056>
  85. Papaefthymiou S., Banis A., Bouzouni M. et al. (2019) Effect of Ultra-Fast Heat Treatment on the Subsequent Formation of Mixed Martensitic/Bainitic Microstructure with Carbides in a CrMo Medium Carbon Steel. *Metals* 9: 312. <https://doi.org/10.3390/met9030312>
  86. Zhao Q. (ed) (2019) *Advanced nanomaterials for pollutant sensing and environmental catalysis*. Micro and nano technologies series. Elsevier, Amsterdam
  87. Liu B., Hu X. (2019) *Hollow Micro- and Nanomaterials: Synthesis and Applications*. In: Zhao Q (ed) *Advanced nanomaterials for pollutant sensing and environmental catalysis*. Elsevier, Amsterdam, pp 1–38
  88. Papaefthymiou S., Karamitros V., Bouzouni M. (2019) Ultrafast Heating and Initial Microstructure Effect on Phase Transformation Evolution of a CrMo Steel. *Metals* 9: 72. <https://doi.org/10.3390/met9010072>
  89. Papaefthymiou S. (2017) A New Opportunity for the Design of Advanced High Strength Steels with Heterogeneous-Phase Microstructures via Rapid Thermal Processing. *Journal of Nanoscience with Advanced Technology* 2: 20–23. <https://doi.org/10.24218/jnat.2017.23>
  90. Cryderman R., Garrett D., Schlittenhart Z. et al. (2020) Effects of Rapid Induction Heating on Transformations in 0.6% C Steels. *J of Materi Eng and Perform* 29: 3502–3515. <https://doi.org/10.1007/s11665-020-04632-0>
  91. Kaluba W.J., Taillard R., Foct J. (1998) The bainitic mechanism of austenite formation during rapid heating. *Acta Materialia* 46: 5917–5927. [https://doi.org/10.1016/S1359-6454\(98\)00210-9](https://doi.org/10.1016/S1359-6454(98)00210-9)
  92. Aaronson H.I., Nie J.F. (2000) Discussion to “the bainitic mechanism of austenite formation during rapid heating”. *Scripta Materialia* 42: 505–509. [https://doi.org/10.1016/S1359-6462\(99\)00388-7](https://doi.org/10.1016/S1359-6462(99)00388-7)
  93. Kaluba W.J., Taillard R., Foct J. (2000) A reply to “discussion to “the bainitic mechanism of austenite formation during rapid heating””. *Scripta Materialia* 42: 511–516. [https://doi.org/10.1016/S1359-6462\(99\)00389-9](https://doi.org/10.1016/S1359-6462(99)00389-9)
  94. Cahn J.W. (1960) *Theory of Crystal Growth and Interface Motion in Crystalline Materials*. *Acta Metallurgica* 8
  95. Hillert M. (1975) Diffusion and interface control of reactions in alloys. *Metall and Mat Trans A* 6: 5–19. <https://doi.org/10.1007/BF02673664>
  96. Castro Cerda F.M. (2017) *Third Generation Advanced High Strength Steels via Ultrafast Heating*. Doctoral Thesis, TU Delft

97. Papaefthymiou S., Bouzouni M., Petrov R.H. (2018) Study of Carbide Dissolution and Austenite Formation during Ultra-Fast Heating in Medium Carbon Chromium Molybdenum Steel. *Metals* 8: 646. <https://doi.org/10.3390/met8080646>
98. Bouzouni M., Papaefthymiou S. (2017) Modeling of the Steel Microstructure Gained after the Application of an Ultra-Fast Heat Treatment. *J Nanosci Adv Tech* 2: 15–19. <https://doi.org/10.24218/jnat.2017.22>
99. Bouzouni M., Papaefthymiou S. (2017) Preliminary Study of Carbide Dissolution during an Ultra-Fast Heat Treatment in Chromium Molybdenum Steel. *Int J Metall Met Phys* 2: 1–7. <https://doi.org/10.35840/2631-5076/9205>
100. Meshkov Y.Y., Pereloma E.V. (2012) The effect of heating rate on reverse transformations in steels and Fe-Ni-based alloys. In *Phase Transformations in Steels*. In: Pereloma E, Edmonds DV (eds) *Phase transformations in steels*. WP, Oxford, pp 581–618
101. Savran V.I., Offerman S.E., Sietsma J. (2010) Austenite Nucleation and Growth Observed on the Level of Individual Grains by Three-Dimensional X-Ray Diffraction Microscopy. *Metallurgical and Materials Transactions A* 41: 583–591. <https://doi.org/10.1007/s11661-009-0142-5>
102. Schmidt E.D., Damm E.B., Sridhar S. (2007) A Study of Diffusion- and Interface-Controlled Migration of the Austenite/Ferrite Front during Austenitization of a Case-Hardenable Alloy Steel. *Metall and Mat Trans A* 38: 698–715. <https://doi.org/10.1007/s11661-007-9208-4>
103. Liu G., Li T., Yang Z. et al. (2020) On the role of chemical heterogeneity in phase transformations and mechanical behavior of flash annealed quenching & partitioning steels. *Acta Materialia* 201: 266–277. <https://doi.org/10.1016/j.actamat.2020.10.007>
104. Goodenow R.H. (1966) Recrystallization and grain structure in rimmed and aluminum killed low carbon steel. *Trans. ASM* 59: 804–823
105. Muljono D., Ferry M., Dunne D.P. (2001) Influence of heating rate on anisothermal recrystallization in low and ultra-low carbon steels. *Materials Science and Engineering: A* 303: 90–99. [https://doi.org/10.1016/S0921-5093\(00\)01882-7](https://doi.org/10.1016/S0921-5093(00)01882-7)
106. Ferry M., Muljono D., Dunne D.P. (2001) Recrystallization Kinetics of Low and Ultra Low Carbon Steels during High-rate Annealing. *ISIJ International* 41: 1053–1060. <https://doi.org/10.2355/isijinternational.41.1053>
107. Atkinson M. (2003) On the credibility of ultra rapid annealing. *Materials Science & Engineering A* 354: 40–47
108. Atkinson M. (1999) Bifurcation of thermal restoration processes in deformed iron and steel. *Materials Science & Engineering A* 262: 33–38

- 
109. Senuma T., Kawasaki K., Takemoto Y. (2006) Recrystallization Behavior and Texture Formation of Rapidly Annealed Cold-Rolled Extralow Carbon Steel Sheets. *Mater Trans* 47: 1769–1775. <https://doi.org/10.2320/matertrans.47.1769>
110. Chbihi A., Barbier D., Germain L. et al. (2014) Interactions between ferrite recrystallization and austenite formation in high-strength steels. *J Mater Sci* 49: 3608–3621. <https://doi.org/10.1007/s10853-014-8029-2>
111. Liu G., Li J., Zhang S. et al. (2016) Dilatometric study on the recrystallization and austenization behavior of cold-rolled steel with different heating rates. *Journal of Alloys and Compounds* 666: 309–316. <https://doi.org/10.1016/j.jallcom.2016.01.137>
112. Xu D., Li J., Meng Q. et al. (2014) Effect of heating rate on microstructure and mechanical properties of TRIP-aided multiphase steel. *Journal of Alloys and Compounds* 614: 94–101. <https://doi.org/10.1016/j.jallcom.2014.06.075>
113. Petrov R.H., Kestens L., Kaluba W. et al. (2003) Recrystallization and austenite formation in a cold rolled TRIP steel during ultra fast heating. *Steel Grips* 1: 289–293
114. Castro Cerda F.M., Kestens L., Monsalve A. et al. (2016) The Effect of Ultrafast Heating in Cold-Rolled Low Carbon Steel: Recrystallization and Texture Evolution. *Metals* 6: 288. <https://doi.org/10.3390/met6110288>
115. Castro Cerda F.M., Kestens L., Petrov R.H. (2019) “Flash” Annealing in a Cold-Rolled Low Carbon Steel Alloyed with Cr, Mn, Mo, and Nb: Part II-Anisothermal Recrystallization and Transformation Textures. *steel research int* 90: 1800277. <https://doi.org/10.1002/srin.201800277>
116. Bandi B., van Krevel J., Aslam N. et al. (2019) A Model and Experimental Validation to Predict Heating Rates for Overlap Between Ferrite Recrystallization and Austenite Transformation in Dual Phase Steel Manufacture. *JOM* 71: 1386–1395. <https://doi.org/10.1007/s11837-019-03358-2>
117. Li P., Li J., Meng Q. et al. (2013) Effect of heating rate on ferrite recrystallization and austenite formation of cold-roll dual phase steel. *Journal of Alloys and Compounds* 578: 320–327. <https://doi.org/10.1016/j.jallcom.2013.05.226>
118. Reis A.C.d C., Bracke L., Petrov R. et al. (2003) Grain Refinement and Texture Change in Interstitial Free Steels after Severe Rolling and Ultra-short Annealing. *ISIJ International* 43: 1260–1267. <https://doi.org/10.2355/isijinternational.43.1260>
119. Wen P-y, Han J-s, Luo H-w et al. (2020) Effect of flash processing on recrystallization behavior and mechanical performance of cold-rolled IF steel. *Int J Miner Metall Mater* 27: 1234–1243. <https://doi.org/10.1007/s12613-020-2023-2>
120. Petrov R.H., Sidor J.J., Kestens L. (2011) Texture Formation in High Strength Low Alloy Steel Reheated with Ultrafast Heating Rates. *MSF* 702-703: 798–801. <https://doi.org/10.4028/www.scientific.net/MSF.702-703.798>

121. Arruda M.V.P., Melo T.M.F., Costa F.S. et al. (2019) Microstructural evolution during continuous annealing of a 980 MPa cold rolled steel grade. *J Phys.: Conf Ser* 1270: 12020. <https://doi.org/10.1088/1742-6596/1270/1/012020>
122. Valdes-Tabernero M.A., Vercruyse F., Sabirov I. et al. (2018) Effect of Ultrafast Heating on the Properties of the Microconstituents in a Low-Carbon Steel. *Metall and Mat Trans A* 49: 3145–3150. <https://doi.org/10.1007/s11661-018-4658-4>
123. Knijf D. de, Puype A., Föjer C. et al. (2015) The influence of ultra-fast annealing prior to quenching and partitioning on the microstructure and mechanical properties. *Materials Science and Engineering: A* 627: 182–190. <https://doi.org/10.1016/j.msea.2014.12.118>
124. Calcagnotto M., Ponge D., Raabe D. (2012) On the Effect of Manganese on Grain Size Stability and Hardenability in Ultrafine-Grained Ferrite/Martensite Dual-Phase Steels. *Metall and Mat Trans A* 43: 37–46. <https://doi.org/10.1007/s11661-011-0828-3>
125. Dai J., Meng Q., Zheng H. (2020) High-strength dual-phase steel produced through fast-heating annealing method. *Results in Materials* 5: 100069. <https://doi.org/10.1016/j.rinma.2020.100069>
126. Castro Cerda F.M., Schulz B., Celentano D. et al. (2019) Exploring the microstructure and tensile properties of cold-rolled low and medium carbon steels after ultrafast heating and quenching. *Materials Science and Engineering: A* 745: 509–516. <https://doi.org/10.1016/j.msea.2018.12.036>
127. Massardier-Jourdan V., Ngansop A., Fabrègue D. et al. (2010) Microstructure and Mechanical Properties of Low Carbon Al-Killed Steels after Ultra-Rapid Annealing Cycles. *MSF* 638-642: 3368–3373. <https://doi.org/10.4028/www.scientific.net/MSF.638-642.3368>
128. Hernandez-Duran E.I., Ros-Yanez T., Castro-Cerda F.M. et al. (2020) The influence of the heating rate on the microstructure and mechanical properties of a peak annealed quenched and partitioned steel. *Materials Science and Engineering: A* 797: 140061. <https://doi.org/10.1016/j.msea.2020.140061>
129. Vercruyse F., Celada-Casero C., Linke B.M. et al. (2020) Temperature Dependence of the Static and Dynamic Behaviour in a Quenching and Partitioning Processed Low-Si Steel. *Metals* 10: 509. <https://doi.org/10.3390/met10040509>
130. Cayron C. (2007) ARPGE: a computer program to automatically reconstruct the parent grains from electron backscatter diffraction data. *J Appl Crystallogr* 40: 1183–1188. <https://doi.org/10.1107/S0021889807048777>
131. Sutton M.A., Wolters W.J., Peters W.H. et al. (1983) Determination of displacements using an improved digital correlation method. *Image and Vision Computing* 1: 133–139. [https://doi.org/10.1016/0262-8856\(83\)90064-1](https://doi.org/10.1016/0262-8856(83)90064-1)
132. Bruck H.A., McNeill S.R., Sutton M.A. et al. (1989) Digital image correlation using Newton-Raphson method of partial differential correction. *Experimental Mechanics* 29: 261–267. <https://doi.org/10.1007/BF02321405>

133. Bailey Metal Processing Limited Support r-Value and Related Parameters.  
<http://www.baileymetalprocessing.com/techmatters/blog-category-1/2017/11/16/r-value-and-related-parameters>. Accessed 17 Nov 2020
134. Andersson J-O., Helander T., Höglund L. et al. (2002) Thermo-Calc & DICTRA, computational tools for materials science. *Calphad* 26: 273–312. [https://doi.org/10.1016/S0364-5916\(02\)00037-8](https://doi.org/10.1016/S0364-5916(02)00037-8)
135. Kirkaldy J.S., Doane D.V. (eds) (1984) *Hardenability Concepts with Applications to Steel*. AIME: Warrendale, Pa, USA
136. Bhadeshia, H. K. D. H. (1982) Thermodynamic analysis of isothermal transformation diagrams. *Metal Science* 16: 159–166. <https://doi.org/10.1179/030634582790427217>
137. Bhadeshia, H. K. D. H. (1981) Driving force for martensitic transformation in steels. *Metal Science* 15: 175–177. <https://doi.org/10.1179/030634581790426714>
138. Petrov R., Kestens L., Wasilkowska A. et al. (2007) Microstructure and texture of a lightly deformed TRIP-assisted steel characterized by means of the EBSD technique. *Materials Science and Engineering: A* 447: 285–297. <https://doi.org/10.1016/j.msea.2006.10.023>
139. Pinard P.T., Schwedt A., Ramazani A. et al. (2013) Characterization of dual-phase steel microstructure by combined submicrometer EBSD and EPMA carbon measurements. *Microsc Microanal* 19: 996–1006. <https://doi.org/10.1017/S1431927613001554>
140. Morito S., Oh-ishi K., Hono K. et al. (2011) Carbon Enrichment in Retained Austenite Films in Low Carbon Lath Martensite Steel. *ISIJ Int* 51: 1200–1202. <https://doi.org/10.2355/isijinternational.51.1200>
141. Castro Cerda F.M., Goulas C., Sabirov I. et al. (2017) The effect of the pre-heating stage on the microstructure and texture of a cold rolled FeCMnAlSi steel under conventional and ultrafast heating. *Materials Characterization* 130: 188–197. <https://doi.org/10.1016/j.matchar.2017.06.010>
142. Bouzouni M. (2020) Προσομοίωση των μετασχηματισμών φάσης και της εξέλιξης της μικροδομής σε υποευτηκτοειδείς χάλυβες κατά τη διάρκεια ραγδαίων θερμικών κατεργασιών. Doctoral Thesis, National Technical University of Athens (unpublished)
143. Peranio N., Li Y.J., Roters F. et al. (2010) Microstructure and texture evolution in dual-phase steels: Competition between recovery, recrystallization, and phase transformation. *Materials Science and Engineering: A* 527: 4161–4168. <https://doi.org/10.1016/j.msea.2010.03.028>
144. Oliveira M. (2004) Influence of strain-induced nucleation on the kinetics of phase transformation in a forging steel during warm working. *Scripta Materialia* 50: 1157–1162. <https://doi.org/10.1016/j.scriptamat.2004.01.011>
145. Love G.R. (1964) Dislocation pipe diffusion. *Acta Metallurgica* 12: 731–737
146. Weinberger C.R., Boyce B.L., Battaile C.C. (2013) Slip planes in bcc transition metals. *International Materials Reviews* 58: 296–314. <https://doi.org/10.1179/1743280412Y.0000000015>



## *11. References*

---

147. Parker S.V., Wadsworth J.E., Gutierrez I. et al. (2003) Property models for mixed microstructures: Technical steel research, Report EUR 20880. European Commission
148. Chang L.C., Bhadeshia, H. K. D. H. (1995) Austenite films in bainitic microstructures. *Materials Science and Technology* 11: 874–882. <https://doi.org/10.1179/mst.1995.11.9.874>

## 12. Curriculum Vitae

### 1. Personal Information

---

Name:	Banis Alexandros
Date and place of birth:	30.05.1993 – Athens, Greece
Nationality:	Greek
E-mail:	<a href="mailto:alex_banis@hotmail.com">alex_banis@hotmail.com</a>
Telephone:	+30 6989866095

### 2. Studies

---

03/2017 –	<b>Ph.D. Student</b>
03/2021	<i>School of Mining and Metallurgical Engineering, Division of Metallurgy and Materials Science, NTUA, Greece</i> ‘The effect of Ultra-Fast Heat treatments on the microstructure evolution of Automotive Steels’
10/2018 –	<b>Ph. D. Exchange Student via the Erasmus+ Program</b>
07/2019	<i>Department of Electrical Energy, Metals, Mechanical Constructions &amp; Systems Faculty of Engineering and Architecture, Universiteit Gent, Ghent, Belgium</i>
09/2011 - 11/2016	<b>Diploma of Mining &amp; Metallurgical Engineering</b> <i>School of Mining and Metallurgical Engineering, NTUA, Greece, Grade: 7.64</i>
02/2016 –	<b>Diploma Thesis via the Erasmus+ Program</b>
07/2016	<i>Institute of Ferrous Metallurgy, Rheinisch – Westfälische Technische Hochschule, Aachen, Germany</i> ‘Influence of heat treatment on cold-rolled high strength Dual Phase steels for application in the automotive industry’

### 3. Professional Activity

---

07/2015 – 09/2015	Internship in National Hellenic Research Foundation Raman Spectroscopy for Chemical Analysis of glass samples to offer conductive properties under the supervision of Ph.D. Kamitsos E., Director of Theoretical & Physical Chemistry Institute
07/2013 - 09/2013	Internship in N.C.S.R. Demokritos Preparation of metallic sample and observation with Scanning Electron Microscopy under the supervision of Dr. Travlos A., Director of Material Science Institute

#### 4. Publications

---

- **A. Banis**, M. Bouzouni, E. Gavalas, S. Papaefthymiou, The formation of a mixed martensitic/bainitic microstructure and the retainment of austenite in a medium-carbon steel during ultra-fast heating, *Materials Today Communications*, **2021**, Vol. 26, <https://doi.org/10.1016/j.mtcomm.2020.101994>
- **A. Banis**, M. Bouzouni, R. H. Petrov, S. Papaefthymiou, Simulation and characterisation of the microstructure of ultra-fast heated dual-phase steel, *Materials Science and Technology*, **2020**, 36:12, <https://doi.org/10.1080/02670836.2020.1777508>
- **A. Banis**, E. Hernandez Duran, I. Sabirov, V. Bliznuk, R.H. Petrov, S. Papaefthymiou, The Effect of Ultra-Fast Heating on the Microstructure, Grain Size and Texture Evolution of a Commercial Low-C, Medium-Mn DP Steel, *Metals*, **2019**, 9:877, <https://doi.org/10.3390/met9030312>
- S. Papaefthymiou, **A. Banis**, M. Bouzouni, R.H. Petrov, Effect of Ultra-Fast Heat Treatment on the Subsequent Formation of Mixed Martensitic/Bainitic Microstructure with Carbides in a CrMo Medium Carbon Steel, *Metals*, **2019**, 9:312, <https://doi.org/10.3390/met9080877>
- **A. Banis** and S. Papaefthymiou, Microstructure Characterization of an Ultra-Fast Heated Medium Carbon Chromium-Manganese High Strength Steel, *International Journal of Metallurgy and Metal Physics*, 2018, 3:021, <https://doi.org/10.35840/2631-5076/9221>

#### 5. Conference announcements

---

- **A. Μπάνης**, Μ. Μπουζούνη, Σ. Παπαευσθυμίου, Oral presentation, 7th Panhellenic Conference on Metallic Materials, 11-13 December 2019, Athens, Greece
- **A. Banis**, E. Hernandez Duran I. Sabirov, V. Bliznuk, R.H. Petrov, S. Papaefthymiou, Oral presentation, 7th Panhellenic Conference on Metallic Materials, 11-13 December 2019, Athens, Greece
- **A. Banis**, M. Bouzouni, R. Petrov, S. Papaefthymiou, Poster Presentation, EUROMAT 2019, September 01-05, Stockholm, Sweden
- **A. Banis**, E. Hernandez Duran I. Sabirov, V. Bliznuk, R.H. Petrov, S. Papaefthymiou, Oral Presentation, Rex&GG: 7<sup>th</sup> International Conference on Recrystallization and Grain Growth, August 04-09, 2019, Ghent, Belgium
- **A. Banis**, M. Bouzouni, M. Karna, A. Vazdirvanidis and S. Papaefthymiou, Poster Presentation M&M Microscopy & Microanalysis Meeting, August 05-09, 2018, Baltimore, MD, USA